Author:
Germon, Anna L

Title:
Identification of Protein Disulphide-Isomerase A3 Dependent Proteins from the Secretome of MDA-MB-231 Breast Cancer Cells

Identification of Protein Disulphide-Isomerase A3 Dependent Proteins from the Secretome of MDA-MB-231 Breast Cancer Cells

Anna L. Germon

BSc Biochemistry

M.Sc by Research in Biochemistry 2018-2019

Supervisor: Professor Josephine C. Adams

A dissertation submitted to the University of Bristol in accordance with the requirements for award of the degree of MSc by Research in the Faculty of Life Sciences.

School of Biochemistry

Date of Submission: 03:09:2019

Word Count: 27979

Abstract

Breast cancer is the most common cancer in women in the UK. In over 90% of cases mortality is due to tumour recurrence and metastasis, which are hard to treat because most tumours become resistant to conventional therapies. During tumour progression, changes to the breast cancer microenvironment and extracellular matrix result in part from altered secretomes of neoplastic cells. There is a need to identify the molecular pathways that control these changes.

Previous research in Professor Adams' laboratory showed that Protein Disulphide-Isomerase A3 (PDIA3) supports a pro-metastatic phenotype in breast cancer cell lines through effects on secreted proteins. In this study, pharmacological inhibition of PDIA3 in MDA-MB-231 invasive breast cancer cells is shown to decrease cell area, focal adhesions and to alter F-actin organisation. Formation of 3-dimensional spheroids was also decreased. By comparing the activities of conditioned media from control or PDIA3-inhibited MDA-MB-A231 cells, secreted PDIA3-dependent or heparin-binding proteins were shown to be necessary for cell spreading.

Comparative TMT-based quantitative proteomic analysis of the PDIA3-dependent, heparin-binding fractions of conditioned media identified that PDIA3 inhibition significantly decreased (≥ 2-fold) 80 proteins, 48 of which were extracellular proteins, including lysyl-oxidase like 2 (LOXL2) ($p=0.003$). However, pharmacological inhibition of LOXL2 in MDA-MB-231 cells with β-aminopropionitrile did not affect 3-dimensional spheroid formation.

Analysis by Gene Ontology and other computational tools highlighted that 20 of these proteins are components of Extracellular Structure Organisation and 17 proteins are involved in Epithelial-to-Mesenchymal Transition. The extracellular proteins also showed pathway enrichment for Platelet Degranulation. The altered abundance of selected extracellular proteins was validated by immunoblotting.

These results demonstrate a PDIA3-dependence of secreted proteins of A231 cells that have known roles in a pro-metastatic phenotype. Future investigation into the role of PDIA3 in breast cancer microenvironment and metastasis may help direct new drug targets to prevent metastasis.

Acknowledgments

I would like to thank the Wolfson Bioimaging Facility for support with microscopy, particularly to Dr. Jepson who was very helpful when running the 3-dimensional cell-based experiments.

Thank you to Dr. Kate Heemson from Bristol University's Proteomics Facility for running the TMT-based quantitative proteomics and Dr Lewis for statistical analysis on the heparin binding fraction of the PDIA3-dependent secretome.

Thank you to Professor Green from the University of Bristol's Mathematics Department for consultation on the statistical tests used in the cell-based assays of this project.

Thank you to members of my laboratory Harry Young and Dr. Hellewell for allowing access to their unpublished data which was fundamental to this project. Finally, thank you to Professor Adams for her guidance and support.

Author's Declaration

I declare that the work in this dissertation was carried out in accordance with the requirements of the University's Regulations and Code of Practice for Research Degree Programmes and that it has not been submitted for any other academic award. Except where indicated by specific reference in the text, the work is the candidate's own work. Work done in collaboration with, or with the assistance of, others, is indicated as such. Any views expressed in the dissertation are those of the author.

SIGNED: 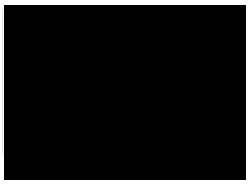 DATE: 03:09:2019

Table of Contents

List of Tables

List of Figures

List of Abbreviations

2D	2-dimensional
3D	3-dimensional
A231	MDA-MB-231
AA	Amino Acids
AR	Abundance Ratio
βAPN	3- Aminopropionitrile fumarate salt
BiP	Binding immunoglobulin protein
BO2	MDA-MB-231 osteotropic BO2 subclone
BSA	Bovine Serum Albumin
CAF	Cancer associated fibroblast
CL	Cell lysate
CM	Conditioned media
CTCs	Circulating tumour cells
CXCL12	C-X-C motif chemokine 12
DAPI	4',6-diamidino-2-phenylindole
DCIS	ductal in situ carcinoma
dH_2O	Deionised water
DMEM	Dulbecco's Modified Eagle Medium
DMSO	Dimethyl sulfoxide
DTT	DL-dithiothreitol
ECL	Enhanced Chemiluminescence
ECM	Extracellular Matrix
EDTA	Ethylenediaminetetraacetic acid
EGF	Epidermal growth factor
EGFR	Epidermal growth factor receptor
EMT	Epithelial-to-mesenchymal transition
ER	Endoplasmic reticulum
Erol1	ER-oxidoreductin 1
Erp57	Endoplasmic reticulum protein 57
ERα	oestrogen receptor
FA	Focal adhesions
F-actin	Filamentous actin
FBS	Foetal bovine serum
FGF7	Fibroblast Growth Factor 7
FGM	Fibroblast Growth Medium
FN	Fibronectin
FoxM1b	Forkhead box protein M1b
GAPDH	Glyceraldehyde-3-phosphate dehydrogenase
GO	Gene Ontology
GOBO	Gene Expression-Based Outcome for Breast Cancer Online
GOrilla	Gene Ontology enrichment analysis and visualization tool
GSEA	Gene Set Enrichment Analysis
HBP	Heparin binding protein
HGF	Hepatocyte growth factor
HIF-1	Hypoxia-Inducible Factor
HRP	Horseradish Peroxidase
IDC	Invasive ductal carcinoma
IF	Immunofluorescence
IGFBP3	Insulin growth factor binding protein 3
IGFBP7	Insulin growth factor binding protein 7
IgG	Immunoglobulin
IL-6	Interleukin 6
JAK	Janus kinase

LAMA5	Laminin Subunit Alpha 5
LAMAC1	Laminin Subunit Gamma-1
LOX	Lysyl-oxidase
LOXL2	Lysyl-oxidase like 2
MAPK	Mitogen-activated protein kinase
MEF	Mouse embryonic fibroblasts
MET	Mesenchymal-to-epithelial transition
MHC I	Major histocompatibility complex 1
M.Res	Masters by Research
MMPs	Matrix Metalloproteinases
mTOR	Mammalian target of rapamycin
MW	Molecular Weight
PDGFα	Platelet derived growth factor alpha
PDIA1	Protein disulfide-isomerase A1
PDIA3	Protein disulfide-isomerase A3
PFA	Paraformaldehyde
PLAT	Tissue plasminogen activator
PLAU	Urokinase
PR	Progesterone receptor
PTHrP	Parathyroid hormone-related peptide
PVDF	Polyvinylidene Difluoride
QSOX1	Quiescin Sulfhydryl Oxidase 1
RARRE2	Retinoic Acid Receptor Responder
RNASE4	Ribonuclease A Family Member 4
RT	Room temperature
RT-PCR	Real time polymerase chain reaction
SDS	Sodium Dodecyl Sulphate
SERPINE1	Serpin Family E Member 1
SND1	Staphylococcal Nuclease and Tudor Domain Containing 1
SOD3	Superoxide Dismutase 3
SPON1	Spondin-1
STAT3	Signal Transducer and Activator of Transcription 3
TAP	Antigen peptide transporter 1
TAZ	Transcriptional coactivator with PDZ-binding motif
TC	Tissue Culture
TEMED	N,N,N',N'-Tetramethylethylenediamine
TGFβ	Transforming growth factor beta
TME	Tumour Microenvironment
TMEM123A	Transmembrane Protein 123
TMT	Tandem mass tag
TNBC	Triple Negative Breast Cancer
Tris	Trizma Base
UPR	Unfolded Protein Response
UV	Ultraviolet
WB	Western Blot
WT	Wild type
YAP	Yes-Associated Protein

Chapter 1 Introduction

The main aim of this project is to investigate the role of Protein disulphide-isomerase A3 (PDIA3) in promoting phenotypes of breast cancer cells that are associated with pro-metastatic activity, including adhesion and F-actin organisation. To date, there is some evidence that PDIA3 is upregulated in some breast cancer cells and promotes a pro-metastatic phenotype through its effects on secreted proteins (Halperin et al., 2014; Jessop et al., 2007; Santana-Codina et al., 2013; Young, unpublished, 2018). Therefore, the introductory chapter will cover aspects of breast cancer metastasis, the tumour microenvironment, extracellular matrix and details about PDIA3.

1.1 Breast Cancer and Metastasis

Mortality from breast cancer is greater than any other cancer in women worldwide. In the UK, breast cancer causes many deaths from cancer in women, second only to lung cancer (Ferlay et al., 2015) (**Figure 1.1**). In most cases, mortality is due to tumour recurrence and metastasis, because the metastatic tumours become resistant to conventional therapies (Han et al., 2019). Cancer metastasis involves the migration of cells away from a primary tumour, to invade local tissues and lymph nodes or transport of tumour cells around the body by the hematopoietic system, namely the blood vessels or lymphatic system. At a secondary site, a migrated tumour cell can adhere to a new tissue environment and undergo rapid proliferation to form a new tumour. Common secondary sites of breast cancer colonisation include the bone, brain, liver and lungs (Patanaphan et al., 1988). To date there is no cure for metastatic breast cancer and there is an urgent need for a better understanding of the molecular mechanisms of metastasis.

1.1.1 Classification of Breast Cancer

Breast cancer is a heterogenous disease that can arise from any cell in the mammary gland. For this reason, there are many different classifications of breast cancer. Histologically, breast cancer can be divided into ductal carcinoma in situ (DCIS), which presents with tumour formation at a pre-malignant stage, or invasive ductal carcinoma (IDC), which presents as breast cancer when the basement membrane has been breached and there may have been a migration of breast cancer to local lymph nodes or other tissues (Malhotra et al., 2010).

Original molecular subclassifications of breast cancer were based on the expression of oestrogen receptor (ERα), progesterone receptor (PR) or amplification of *Erbb2* (*HER2*). Accordingly, there are three immunohistochemical subgroups: ERα-positive, HER-2-positive (HER-2 enriched) and triple-negative (Triple Negative Breast Cancer (TNBC)) which is lacking of expression of all three receptors (Perou et al., 2000). TNBC is the most prone to metastasis and has the poorest prognosis of the breast cancer subtypes (Li et al., 2017). In the past it was this classification that determined the kind of treatment a patient would receive.

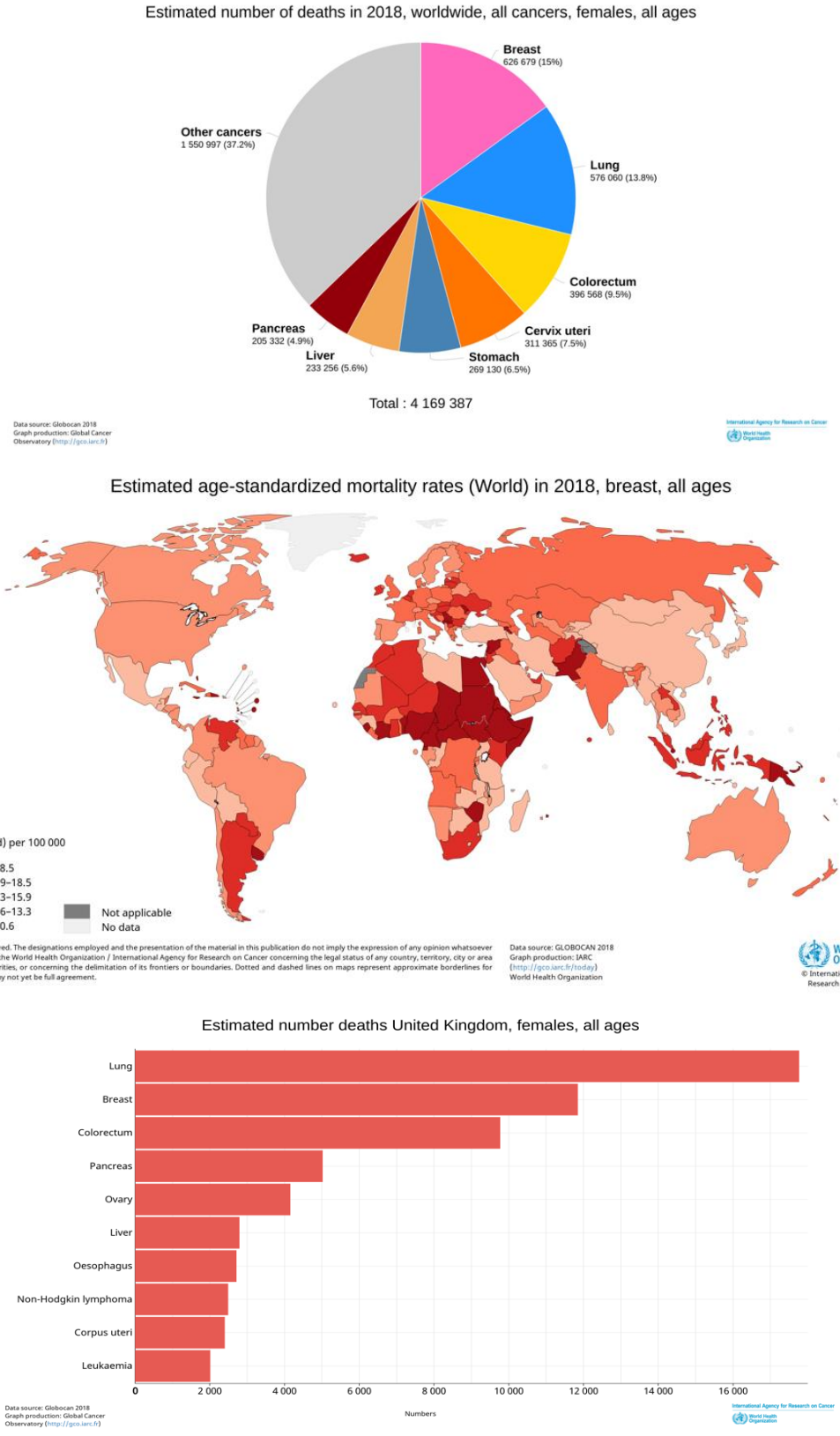

Figure 1.1 ***Mortality Statistics for Breast Cancer in Females.*** Data from The World Health Organisation. *Graphics from* https://gco.iarc.fr/today/home

More recently, breast cancer has been classified in a more detailed manner according to breast cancer gene expression signatures; the subgroups made according to gene expression and clustering. There are five subgroups of breast cancer that largely overlap with the immunohistochemical subgroups. The refined subclassifications of breast cancer are luminal A and luminal B, Her2-enriched, claudin-low, and basal-like. Luminal breast cancer arises from luminal epithelial cells in the breast duct. The basal-like subclassification of breast cancer is similar to TNBC and TNBC encompasses most basal-phenotype breast cancers (Eliyatkın et al., 2015). Amongst these subclassifications basal-like breast cancer is most prone to metastasis and relapse in chemotherapy is frequent (Carey et al., 2010).

More recently, genomic expression profiling has split TNBC into a further six subclassifications which include two basal-like, immunomodulatory, mesenchymal, mesenchymal stem-like, and luminal androgen receptor subtypes. All of these subtypes have genomic abnormalities that affect proteins with functions in cell motility, proliferation, immune cell processes and metabolism (Collignon et al., 2016).

Currently, TNBC accounts for 15% of all breast cancer cases: breast cancer mortality is dropping in all subgroups except TNBC (Al-Mahmood et al., 2018). TNBC is notoriously difficult to treat, it is clinically very aggressive and has a high propensity for brain/visceral metastasis and recurrence. Once a tumour cell has left the primary tumour, TNBC can be very hard to detect. Sometimes TNBC can lie dormant for many years and eventually reappear at a distant organ as a secondary tumour site (Irvin and Carey, 2008).

The vast genetic, cellular and extracellular matrix (ECM) changes that allow for tumour cell migration and extravasation in TNBC remain poorly understood (Neophytou et al., 2018). There is a need to identify the cellular changes that allow TNBC to metastasise. In the following sections I will discuss changes in tumour cell phenotype and microenvironment that have roles in supporting metastasis.

1.2 Epithelial-to-Mesenchymal Transition in Breast Cancer

1.2.1 Epithelial-to-Mesenchymal Transition

Based on the current understanding of cancer metastasis, for a breast cancer cell to metastasise it must first undergo an epithelial-mesenchymal transition (EMT), a reversible molecular process that allows cell migration. Normally, breast epithelial cells are held in place by an array of biological, chemical and physical barriers. These include a distinct apical-basal polarity, presence

of tight and adherens junctions based on occludins, claudins and cadherins, respectively, and an intact basement membrane linked to cells via α6β4 integrins (Saunders and McClay, 2014). The loss of the epithelial-like phenotype during EMT is accompanied by the loss of cell-surface E-cadherins. These are calcium ion (Ca^{2+})-dependent, transmembrane glycoproteins that attach adjacent epithelial cells together and also link intracellularly to the actin cytoskeleton through protein complexes, commonly containing catenin proteins (Ohashi et al., 2017). Acquisition of a mesenchymal phenotype is accompanied by gain of N-cadherin (a different type of cadherin family receptor to E-cadherin). Other markers of a mesenchymal phenotype that are increased include vimentin (an intermediate filament component of the mesenchymal cell cytoskeleton), fibronectin (normally heavily secreted by mesenchymal cells such as fibroblasts) and increased expression of matrix metalloproteinases that can degrade the basement membrane. Mesenchymal-like cells also adopt a more spindle-shaped morphology with a wide 'leading' edge and pinched 'trailing' edge (**Figure 1.2)** (Kalluri and Weinberg, 2009).

EMT is an essential process for breast cancer cells to become invasive. EMT facilitates DCIS to progress to invasive IDC and increases the chances of basement membrane breaching. In the most recent model of cancer progression, once the basement membrane has been degraded by extracellular proteases and cells have undergone an EMT, they become free to move out of the epithelial layer and into connective tissue and/or blood vessels, a process known as intravasation. Metastatic breast cancer cells in vessels then have the means to be transported to distant tissues and around the body. Circulating tumour cells (CTCs) (cells from a primary tumour that have escaped into the blood stream) then have the potential to extravasate and colonise another site, either in their tumour of origin or in a new organ (Kalluri and Weinberg, 2009). It is not well understood why certain organs are more favoured by CTCs as sites of colonisation, but there is some suggestion that it may be because of availability of growth factors or favourable microenvironment conditions. This hypothesis is known as the 'soil and seed hypothesis'; the current understanding is that some organs are 'made ready' for metastatic growth or already have a pre-metastatic niche set up (Cox et al., 2012). CTCs leave blood vessels and enter new tissues by a process called extravasation. To form a secondary tumour, CTCs must attach and regain an epithelial-like phenotype (Ramakrishna and Rostomily, 2013). A mesenchymal-epithelial transition (MET) occurs if the new stromal environment is favourable. Successful MET results in tumour cell proliferation and the development of a secondary metastatic tumour.

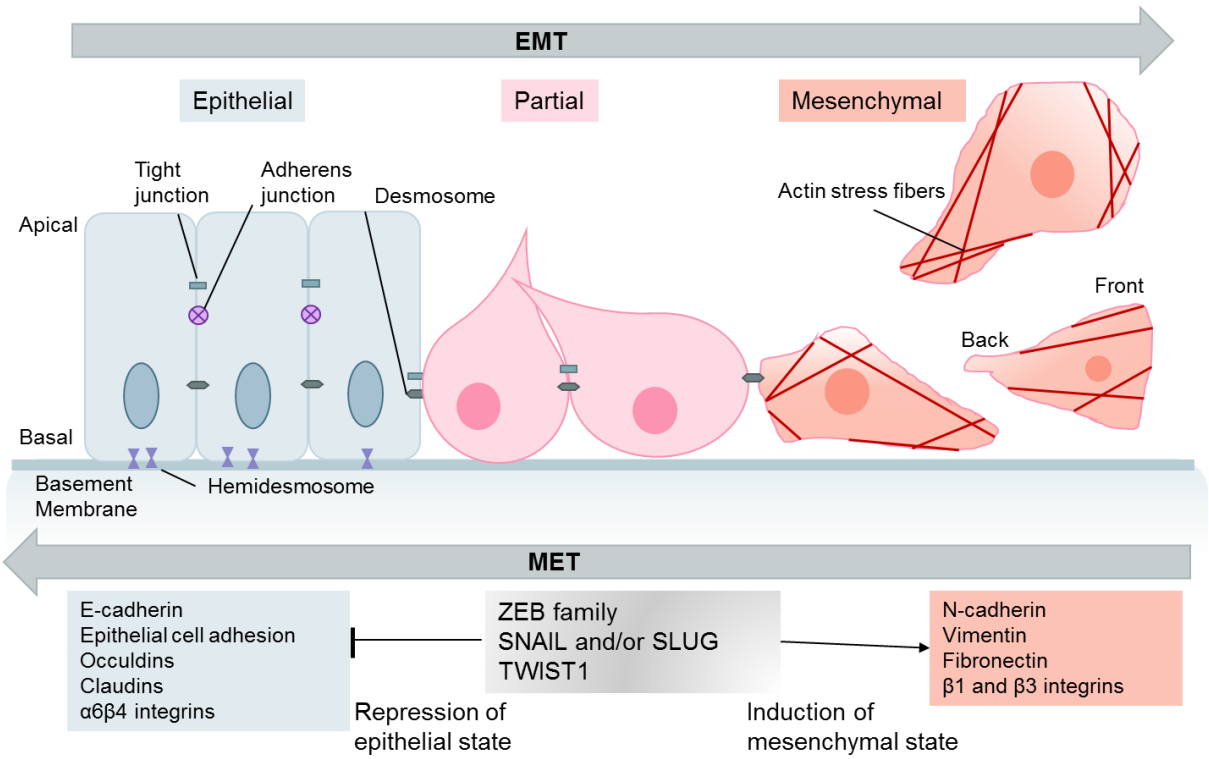

Figure 1.2. ***Epithelial-to-Mesenchymal Transition.*** *Adapted from* (Dongre and Weinberg, 2019).

1.2.2 Signalling Pathways

EMT is orchestrated by transcriptional activity. It is thought that over one hundred genes could be involved in EMT, including genes for growth factors, cell surface adhesion, proteases and cytoskeletal organisation (Goossens et al., 2017). The main transcription factors that drive EMT are repressive of genes that promote an epithelial phenotype and inducive of genes that promote a mesenchymal phenotype. There are many transcription factors involved in breast cancer EMT, the most well studied are SLUG, SNAIL, GATA3, Zeb1 and TWIST. The differing levels of EMT transcription factor expression in breast cancer has been attributed as leading to certain organ tropisms, for example, expression of SNAIL correlates with lymph node metastasis (Blanco et al., 2002).

EMT is not a cell-autonomous process. The transcription factors required for EMT are themselves activated by signalling pathways that can be initiated by extracellular ligands binding to their cognate receptors. Therefore, EMT is controlled by a cohort of ligands derived from stromal origin in the tumour microenvironment (Dongre and Weinberg, 2019).

There are several pathways that influence the EMT program. Transforming growth factor beta (TGFβ) is known to induce intracellular cell signalling in breast cancer cells that induces cell growth, motility and proliferation. TGFβ has also been shown to induce a mesenchymal-like phenotype since it increases fibronectin and vimentin abundance in breast cancer cells. This is thought to occur because binding of TGFβ to its receptor tyrosine kinase activates an intracellular downstream SMAD signalling cascade. SMAD signalling leads to a phosphorylated SMAD complex that migrates into the nucleus and activates the transcription of SLUG and SNAIL. The abundance of these transcription factors is then linked with EMT (Xu et al., 2009).

Binding of extracellular WNT to its receptor, frizzled, also causes the transcription of EMT transcription factors. WNT-induced intracellular signalling leads to stabilisation of β-catenin and increased nuclear β-catenin, which then modulates transcriptional activity. NOTCH binding to Delta-like or jagged receptors also promotes the expression of SNAIL (Xiao et al., 2016). Complexity of EMT regulation is increased because there is a degree of crosstalk between these intracellular signalling pathways. For example, phosphorylated SMAD proteins of the TGFβ signalling pathway can interact with β- catenin and intracellular NOTCH (Luo, 2017). The TGFβ pathway can activate other intracellular signalling pathways involved in EMT transcription factor control such as Ras/Raf/ Mek/Erk and the Pi3k/Akt/ mTOR/NFKβ pathways (Dongre and Weinberg, 2019).

1.2.3 Breast Cancer Stem Cells and Phenotypic Plasticity

To form a tumour at a secondary site a disseminated tumour cell must undergo MET (the reverse of EMT). This involves another extensive change in cellular phenotype. It is thought that MET occurs because EMT is controlled by changes in gene transcription, and so it is a plastic state that can be reversed (Jayachandran et al., 2016). Once MET has occurred, extensive cell proliferation and clonal expansion can lead to formation of a secondary tumour. The full process of metastasis requires vast changes in tumour cellular properties and a large degree of cellular plasticity. It has been observed that the two phenotypes needed for successful colonisation of a secondary site are very similar to the defining characteristics of a cancer stem cell (CSC). These characteristics of a CSC are self-renewal and ability to differentiate.

This has led to the idea that much of breast cancer metastasis can be attributed to the behaviour of stem cells. Indeed, EMT does increase the expression of stemness genes; the expression of EMT transcription factors Snail, Twist and TGFβ will induce stemness in immortalised human mammary epithelial cell lines (Luo et al., 2015).

More recently, it has been debated whether EMT and MET are discrete entities, because cancer cells can metastasise without fully losing an epithelial phenotype. **Figure 1.2** depicts a partial EMT where cancer cells share markers for both epithelial and mesenchymal phenotypes. It has been suggested that these cells are the most versatile and have the greatest degree of plasticity (Weidenfeld and Barkan, 2018).

Studies on solid mouse tumours showed that only a subpopulation of breast cancer cells are capable of forming a tumour at a secondary site. It was hypothesised that these cells were breast cancer stem cells (Liu et al., 2010). Further studies reported that EMT transcription factors (SLUG/Zeb1) are expressed in adult stem cells and that aberrant activation of TGFβ increases stemness in TNBC (Xu et al., 2018). These results provide evidence that breast cancer stem-like cells exist.

1.3 Tumour Microenvironment

Increasingly, the intracellular molecular mechanisms that govern cancer metastasis are being considered in the context of the tumour microenvironment (TME). The TME is the environment within and surrounding a tumour and consists of cellular and non-cellular components. Stromal cells found in the tumour microenvironment include cancer-associated fibroblasts, immune cells, endothelial cells, adipocytes and neoplastic cells. Non-cellular components include the

extracellular matrix (ECM) and cytokines. It is also important to consider blood vessel growth, pH, levels of hypoxia, hormones and cytokine signalling (Soysal et al., 2015). The tumour microenvironment has a role to play in every stage of cancer progression, which can be split into local (nearby tumour cells), regional (cells in the stroma) or distant (upon metastasis to other organs) (**Figure 1.3**) (Yuan et al., 2016).

Each cell type in the TME can influence cell behaviour through secreted proteins. Each type of stromal cell has its own unique secretome made up of signalling molecules including: chemokines, cytokines, growth factors and ECM proteins. These all contribute to the overall tumour microenvironment. In addition, each secretome can change depending on local TME conditions. Once in the TME, secreted proteins can bind to cognate receptors on recipient cells and influence downstream intracellular signalling pathways, such as NOTCH, WNT and TGFβ, that may change epigenetic or genetic programmes and affect cell behaviour. These signalling pathways also control EMT and MET and so the TME impacts on cell plasticity.

Extracellular signalling molecules can act on the same cell that secreted them or on other cells, and leads to changes in cells, known as autocrine or paracrine signalling, respectively. For example, an overabundance of TGFβ in the TME due to secretion from malignant cells can act on breast cancer cells in general and influence EMT, angiogenesis, metastasis and fibroblast activation (Bierie and Moses, 2006). IL-6 in the breast cancer tumour microenvironment increases stemness via JAK/STAT3 signalling (Sağlam et al., 2015).

Autocrine and paracrine signalling is also part of the normal physiology in the mammary gland. The TME can be protective against the development of tumours under certain circumstances and therefore can act as a tumour suppressor. For example, myoepithelial cells in the breast microenvironment lay down basement membrane, which acts as a physical barrier to slow the invasion of breast cancer cells and prevent formation of IDC (Barsky and Karlin, 2005).

However, after the origin of a tumour, the microenvironment can become ‘hijacked’ and change into an environment that favours cancer progression. For instance, favourable conditions may be generated at distant sites to support adhesion of circulating cancer cells that undergo MET and proliferate to form a secondary tumour. In this way, the TME is the soil that nourishes the seed (a circulating cancer cell) (Ramakrishna and Rostomily, 2013). The TME may also protect neoplastic cells from immune surveillance.

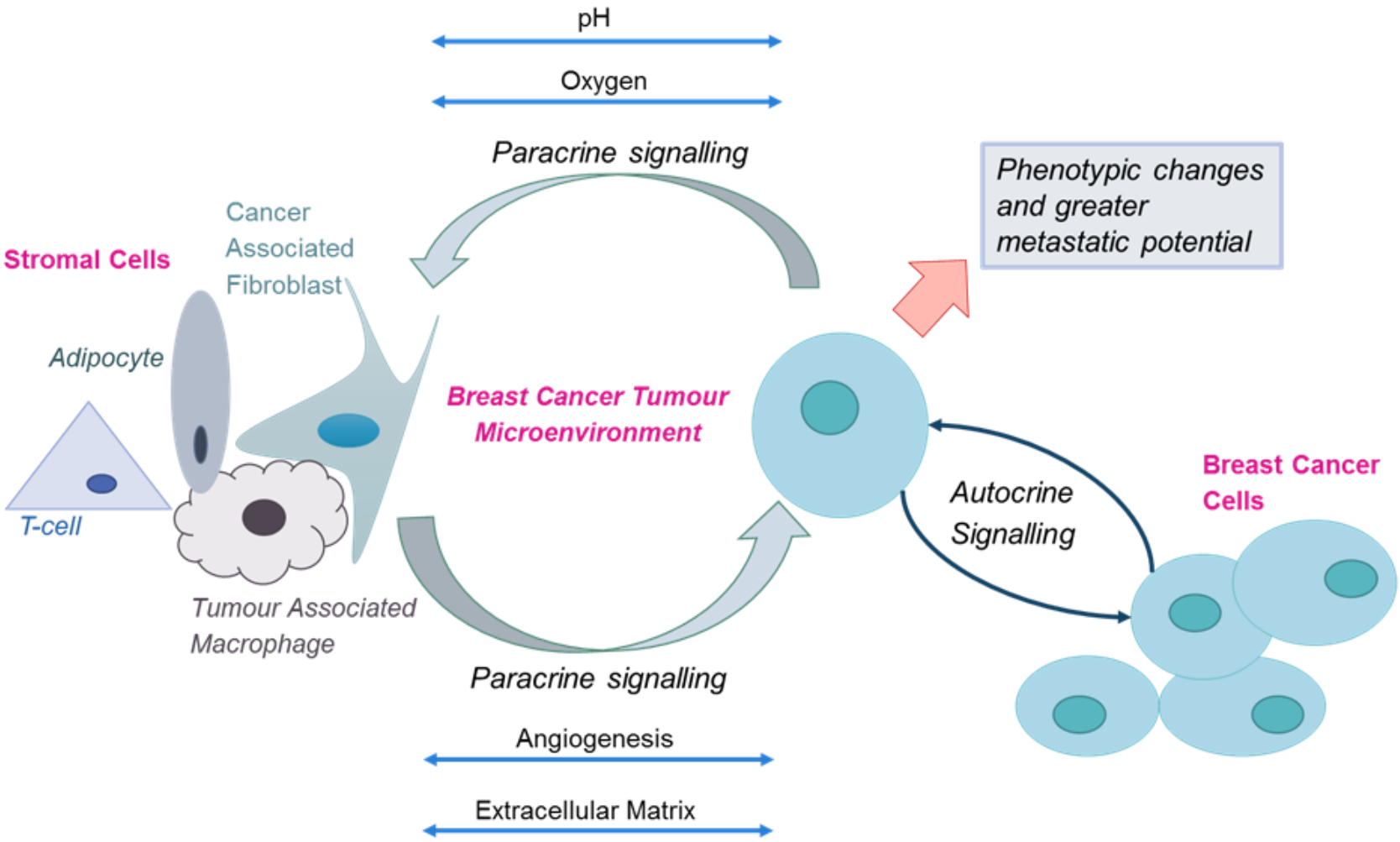

Figure 1.3 **Schematic of the Breast Cancer Tumour Microenvironment**. Conditions in the ECM and cell signalling that contribute to cancer progression and metastasis (Wang et al., 2017).

This can happen by an increase in immune suppressive cytokines or, there is also a suggestion that, immune surveillance can contribute to selective survival of dominant malignant cells that hasten the development of a solid primary tumour (Dunn et al., 2004; Kalluri and Zeisberg, 2006; Ricciardi et al., 2015).

1.3.1 Metastasis

Breast cancer tumours have tropisms to metastasise to certain organs. Common sites of metastasis include the bone, brain, liver and lungs (Kimbung et al., 2015). Specific organ tropisms occur because organs provide a microenvironment that has physical and biochemical properties that prime CTCs to create a secondary niche. One of the most important steps in forming a new colony of tumour cells is for CTCs to undergo MET. For bone tropism, it is thought that in the hemopoietic system CTCs are sustained in their mesenchymal status by autocrine signalling. However, when a CTC arrives in the bone and adheres to stromal cells in bone marrow, the adhesion favours MET (Xie et al., 2018). Then the cancer cells release parathyroid hormone-related peptide (PTHrP) that activates osteoblasts (bone-forming cells) (Soki et al., 2012). This creates a favourable environment for proliferation and differentiation of breast cancer cells and so a secondary tumour is able to form (Pulido et al., 2017)

There are also suggestions that organ tropism depends on a specific receptor-ligand interaction. C-X-C motif chemokine 12 (CXCL12) is a chemokine that is secreted by stromal cells in organs that are often targets of breast cancer metastasis. The receptor of CXCL12 is C-X-C chemokine receptor type 4 (CXCR-4) that is expressed on breast cancer cells. It has been suggested that paracrine signalling through the CXCL-12-CXCR-4 axis dictates organ tropisms by a long distance homing mechanism (Roato and Ferracini, 2018).

1.3.2 Cancer-Associated Fibroblasts

Cancer-associated fibroblasts (CAF) make up a large population of stromal cells in the TME. CAF secrete large amounts of ECM proteins, signalling growth factors and exosomes (McAnulty, 2007). CAF are recruited to tumours by cytokine and chemokine signalling from the neoplastic cells. When recruited into a tumour, CAF have a large impact on the composition of the TME, to the extent that they have been termed, ‘the architects of cancer pathogenesis” (Marsh et al., 2013). CAF-secreted products affect stromal autocrine and paracrine signalling in the TME. In turn, secreted proteins affect the immune system, angiogenesis, ECM production and surrounding neoplastic cells (Santi et al., 2018). Bidirectional paracrine signalling between cancer cells and CAF can change the transcription profile of both cells alike and is likely to enhance tumour progression. Currently, CAF are thought to promote breast cancer tumour progression and metastasis (Houthuijzen and Jonkers, 2018).

There is debate about the origin of CAF. They may arise from tissue-resident fibroblasts or from mesenchymal CSCs that have undergone an EMT (Avgustinova et al., 2016; Lee et al., 2011; Jotzu

et al., 2011). To contribute to the proteinaceous TME, fibroblasts must to be activated by paracrine signalling from cancer cells, including TGF-β1, PDGFα and IL-6 signalling (Shao et al., 2000; Giannoni et al., 2010). However, activation of fibroblasts can also happen via environmental stimuli such as hypoxia and ECM stiffness. These extracellular signals alter gene expression by epigenetic mechanisms by binding to extracellular receptors and causing intracellular signalling cascades (Hu et al., 2005). Fibroblasts may also become activated by gaining certain single nucleotide polymorphisms leading to a change in the expression and secretion of ECM components such as collagens, lysyl-oxidase (LOX) and matrix metalloproteinases (MMPs) (Du and Che, 2017; Liu et al., 2019).

CAF also secrete copious amounts of growth factors and cytokines that contribute to cancer cell proliferation. Fibroblast growth factor 7 (FGF7) and hepatocyte growth factor (HGF) are both increased in CAF compared to normal fibroblasts. FGF7 is a mammary growth factor that increases cell proliferation and HGF increases tumour growth *in vivo* (Palmieri et al., 2003; Tyan et al., 2012). Breast cancers that are ER-positive rely on oestrogen signalling for growth and there is some evidence that CAF may maintain breast cancer tumour growth by rapid oestrogen metabolism. Activity of 17 β-estradiol dehydrogenase (an enzyme involved in the metabolism of oestrogen) in the TME is increased in CAF stroma and would increase the rate of oestrogen metabolism (Adams et al., 1988). Metabolites of oestrogen can then enter cells and modulate ligand activated gene transcription that can lead to an increase in malignancy, for example, cyclin D1 is increased in abundance leading to unregulated breast cancer proliferation (Liang and Shang, 2013). IL-6 expression is increased in CAF and IL-6 is associated with cancer growth, progression and chemotherapy-resistance by fundamental roles in immune response, cell metabolism and inflammation (Masjedi et al., 2018). CXCL12 is also increased in the stroma and secreted by CAF (Orimo et al., 2005).

CAF are thought to be involved in many other aspects of cancer metastasis from enhancing the plasticity of neoplastic cells, inducing an EMT, changing ECM composition, promoting angiogenesis, dictating organ tropisms and secreting pro-inflammatory cytokines (e.g. IL-1β, IL-8, IL-10, TNFα) that orchestrate a pathological immune response (Kalluri and Zeisberg, 2006; Wang et al., 2019; Buchsbaum and Oh, 2016). The large amount of crosstalk and involvement in multiple signalling pathways of CAF means that the role of CAF in pathogenesis is complex and the precise mechanisms remain unclear (Buchsbaum and Oh, 2016).

1.3.3 Exosomes

Exosomes are extracellular vesicles of approximately 30-120nm diameter that originate from an endosomal origin. They are released by stromal cells by the multivesicular body fusing to the plasma membrane and releasing exosome cargo (Jia et al., 2017). It is thought that exosomes provide

another means of cell-cell communication in the TME, playing a complex and pivotal role in cancer progression and metastasis (Vader et al., 2014).

Exosomes contain cargo that can influence aspects of the TME, including the major histocompatibility complex class 1 (MHCI), miRNA, DNA, enzymes and molecular chaperones (Jia et al., 2017). The discovery that exosomes contained genetic information means that RNA or DNA can be transferred between cells and potentially change cell behaviour. Exosomes have been demonstrated to affect behaviour of cells in the TME, for example, upon delivery of exosome-derived miR-9 in breast cancer, fibroblasts show more CAF-like behaviour (Baroni et al., 2016). Exosomes communicate with cells by cargo release to the ECM or by binding to receptors on recipient cells, fusion to the plasma membrane and being endocytosed (Ogorevc et al., 2013).

The exact composition of exosome components reflects the status of the donor cell, for example, hypoxia in the TME enhances the release of exosomes that contain cargo that promotes metastasis (Kucharzewska et al., 2013). More specifically to breast cancer, exosomes from two different breast cancer cell lines, MCF-7 and MDA-MB-231 (subsequently referred to as A231) were found to contain different proportions of exosome cargos. MCF-7 exosomes contained more nucleic acids, whilst A231 exosomes contained a higher proportion of MMPs. Also, the miRNA content of MCF-7 and A231 exosomes was different. Gene Ontology revealed that in both cell lines the miRNAs were associated with metastasis (Kruger et al., 2014). Despite these differences there are some proteins that are characteristic of exosomes such as annexins, cytoskeletal proteins (vimentin, talin, actin, tubulin), tetraspanins and heat shock proteins. These are now viewed as markers for identifying exosomes (Jia et al., 2017).

There is also evidence that exosomes are critical in forming the pre-metastatic niche (Guo et al., 2019). In the TME, exosomes can facilitate cancer migration. Exosomes found in the conditioned media of TNBC cells induce cell proliferation, metastasis *in vivo*, and increase sensitivity to ‘anoikis’ (cell death without a home) in naïve recipient cells. Exosomes may stimulate cancer cell migration: exosomes are released after breast cancer detachment from the basement membrane and concentrate on the surface of the detached cell to mediate cell adhesion to the ECM (O’Brien et al., 2013).

Exosomes can also travel outside the TME by transportation in the lymphatics or blood vessels. This led to the notion that exosomes can ‘prime’ secondary site of tumour colonisation to form a pre-metastatic niche. Therefore, exosomes are thought to affect organ tropisms (dos Anjos Pultz et al., 2017). There is evidence that this is in part due to integrin expression on exosomes. αvβ5 integrin on exosomes enhanced exosome accumulation in the liver, whilst α6β4 integrin was associated with accumulation in the lung. Once bound to integrins, exosomes can deliver genetic information and change cell behaviour through endocytosis (Hoshino et al., 2015).

Thus, exosomes have a large impact in both early and late stage tumour development. As well as the roles discussed here, exosomes are also involved in immune suppression, angiogenesis and tumour chemoresistance (Guo et al., 2019).

1.4 Breast Cancer Extracellular Matrix

1.4.1 The Cancerous Extracellular Matrix

The ECM is an important regulator of breast cancer and part of the non-cellular aspect of the TME. The ECM is formed in part, from the combined secretomes of stromal cells (predominantly non-neoplastic cells, immune cells and CAF) (Bhowmick et al., 2004). The local composition of the ECM creates a niche environment for growth of a tumour and impacts on all stages of cancer development. Connective ECM acts as an extracellular network scaffold for stromal cells and directs many biochemical and biomechanical signals. Basement membrane ECM provides support below epithelial cells and acts as a barrier to malignant cell migration. The proteinaceous composition of breast ECM is very diverse and changes during cell proliferation or differentiation. A cancerous ECM is physiologically very different from a normal ECM. The characteristics of breast cancer ECM closely resemble breast ECM during mammary gland involution post-pregnancy or an ECM involved in wound healing (Bissell and Hines, 2011; Muschler and Streuli, 2010). The similarities to wound healing are because there is excessive ECM deposition, proliferation and recruitment of fibroblasts, and increased expression of ECM remodelling enzymes, albeit without the regulatory mechanisms that maintain long-term ECM homeostasis in the normal breast. The results of these changes tend to support breast cancer metastasis (Bissell and Hines, 2011).

Normally, physical attachment of epithelial cells to the ECM and to each other prevents cell migration. Loss or change of cell-cell, cell-basement membrane or cell-ECM adhesions are features that enable an EMT and subsequent mesenchymal-type cell migration. The normal adhesions also sustain distinct apical-basal polarity, a fundamental aspect of the epithelial phenotype. Tight and adherens junctions form cell-cell attachments at the apex of in the epithelial layer, hemidesmosomes link the base of cells to the basement membrane (BM) and other integrins link cells to ECM via focal adhesions (Lee and Streuli, 2014). Integrin expression can change according to malignancy status and cell positioning in the ECM. Through these adhesions, biomechanical cues from the ECM are transmitted to the cells and throughout the epithelial cell layer. ECM binding to integrins initiates downstream signalling pathways and affects the transcription of ECM-dependent genes (**Figure 1.4**). These functions can bolster cancer progression (Desgrosellier and Cheresh, 2010).

If normal epithelial cells are detached from their ECM they undergo anoikis, a form of programmed cell death (Paoli et al., 2013). With alterations in integrin expression, breast cancer cells can subvert these normal controls and survive in non-native ECM environments. Thus, resistance to apoptosis is important for supporting tumour cell invasion and metastasis. Breast cancer ECM is often very stiff

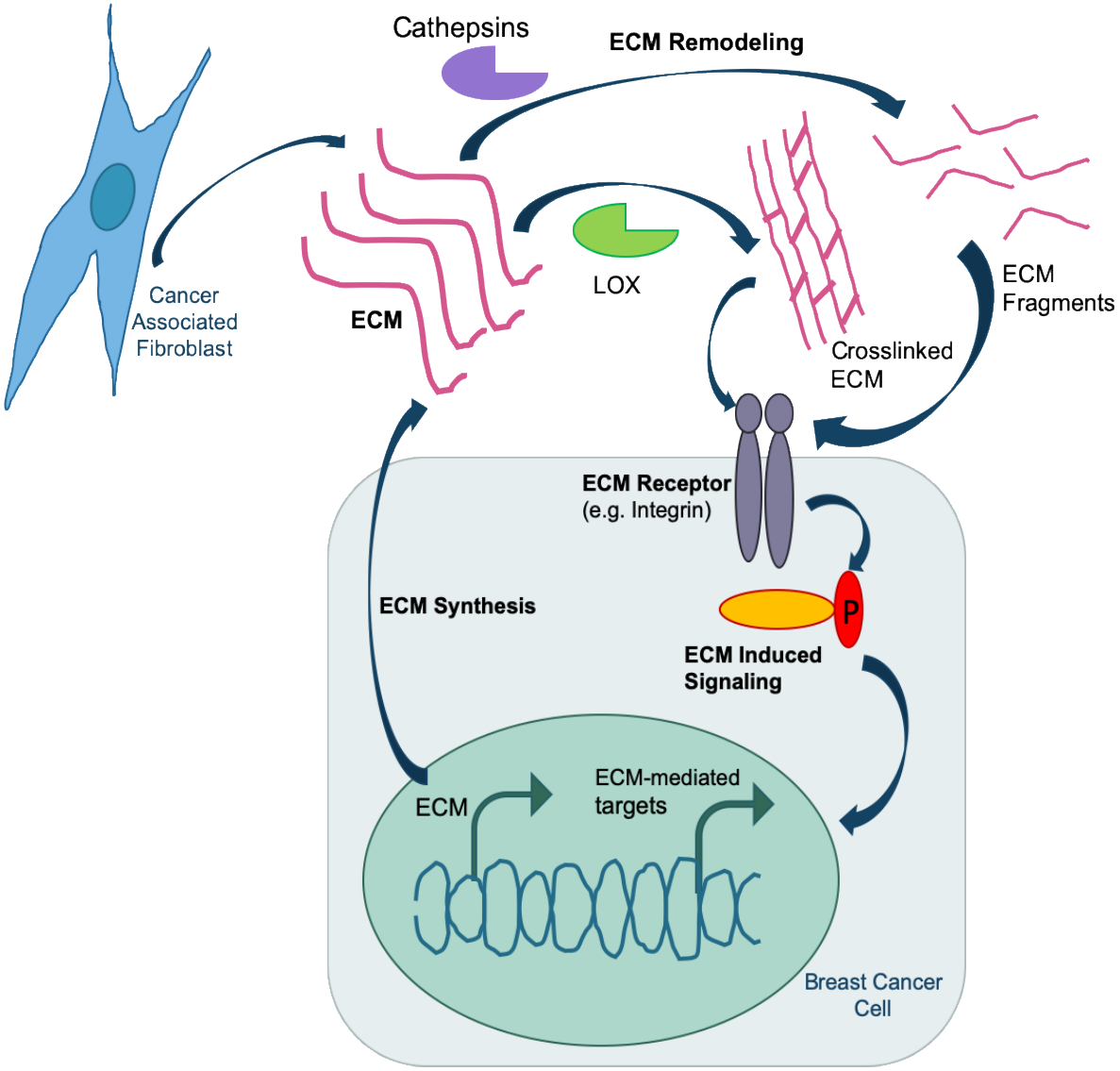

Figure 1.4. ***The extracellular matrix can affect transcription in target cells.*** *Depiction of how a cancerous ECM can modulate biological functions in cancer progression. Modified from 'The Extracellular Matrix in Breast Cancer'* (Insua-Rodríguez and Oskarsson, 2016).

compared to normal ECM. Components of the ECM that contribute to this include fibrillar collagens (I, III, V), fibronectin and adhesive extracellular glycoproteins such as thrombospondin-1 (Egeblad et al., 2010). ECM stiffness also is partly due to the abundance of collagen cross-linking enzymes of the lysyl-oxidsase (LOX) family; cross-linking results in highly aligned collagen fibres (Rodriguez-Pascual 2016). It is thought the aligned collagen fibres act like 'train tracks' to facilitate and direct cancer cell migration (**Figure 1.4**). Increased ECM stiffness aids cancer progression by enhancing the ability of cancer cells to extend actin rich protrusions whilst migrating (Berger et al., 2019). A stiffer ECM also promotes the development of blood vessels and thus supply of nutrients to a tumour, and increases the risk of extravasion (Broders-Bondon et al., 2018).

The ECM of tumours also contains increased levels of active MMPs (Radisky and Radisky, 2015). This can lead to remodelling of ECM in abnormal places, affecting stromal biochemical and biomechanical signalling pathways, cell proliferation and making accessible pathways for tumour cell migration (Benson et al., 2013).

1.4.1 Roles of ECM Glycoproteins in EMT and Cancer Progression

1.4.1.1 Collagen

Collagen is the most abundant protein in the ECM. There are 28 different types of collagens in humans with different roles in the ECM. Fibrillar collagens (I, III, V), form the largest structural fibrils of connective ECM and act as scaffolds for stromal cells. Non-fibrous collagen IV is a central part of the BM that is assembled as a flat network (Lochter and Bissell, 1995).

The abnormal breast cancer ECM included increased adjacently aligned, collagen fibres (Insua-Rodríguez and Oskarsson, 2016). The high degree of collagen alignment increases ECM stiffness, which impacts on malignant cells as discussed in **1.4.1**. In the clinic, ECM stiffness correlates with poor breast cancer prognosis and resistance to breast cancer therapy (Hayashi et al., 2012). Increased mechanical tension in the ECM induces changes in cancer cell behaviour by activating intracellular signalling pathways through integrins. For example, activation of phosphoinositide 3-kinase and mitogen-activated protein kinase (MAPK) signalling pathways regulates mammary cells invasive behaviour or proliferation (Levental et al., 2009; Klein et al., 2009). Stiffness of the ECM also has a role in cell plasticity. Mammary epithelial cell differentiation is induced by ECM tension by affecting Rho-associated protein kinase levels and by changing cellular transcriptional activity, in particular promoting transcriptional coactivator with PDZ-binding motif (TAZ) to form an active transcriptional complex with yes-associated protein (YAP) which induces stem-cell like properties (Dupont et al., 2011; Wozniak et al., 2003).

1.4.1.2 Fibronectin

Fibronectin is an ECM glycoprotein. Fibronectin is largely secreted by fibroblasts, but other stromal cells also secrete it. Fibronectin is secreted as a dimer which binds to $\alpha 5\beta 1$ integrin on the plasma

membrane. As the concentration of fibronectin dimers increase, they are assembled by tissue-transglutaminase 2 to form a mesh-like network surrounding cells (Singh et al., 2010).

Fibronectin binding has regulatory effects on cell behaviour: it relays biomechanical cues from the ECM through binding integrins and syndecan-4, which affect downstream intracellular signalling pathways (Bass et al., 2007). For example, fibronectin modulates the intracellular signal transducer and activator of transcription 3 (STAT3) signalling pathway that promotes EMT and induce invasiveness in breast cancer (Balanis et al., 2013).

Fibronectin in the ECM also influences cancer progression through effects on the biochemical signalling of other proteins. For example, insulin growth factor binding protein 3 (IGFBP3) in the presence of fibronectin increases breast cancer proliferation (McIntosh et al., 2010). Fibronectin abundance has been associated with mesenchymal phenotype and promotes EMT through TGFβ signalling(Park and Schwarzbauer, 2014). Fibronectin contributes to a pre-metastatic niche in secondary organs by increasing the recruitment of cancer stem cells (Kaplan et al., 2005). It is also a cargo of exosomes (Sung and Weaver, 2017). Therefore, fibronectin abundance has been associated with a poor prognosis in breast cancer (Bae et al., 2013).

1.4.1.3 Lysyl oxidase and Lysyl-oxidase-like Family

Lysyl oxidase (LOX) is a member of a family of extracellular, copper-dependent enzymes, that function in collagen fibril assembly. LOX oxidises peptidyl lysine on fibrillar collagen to mediate molecular crosslinking. LOX has an essential role in vascular homeostasis (Cox et al., 2016).

There are five members of the LOX family, LOX and lysyl-oxide-like 1-4 (LOXL1-4). All members share a highly conserved C-terminal domain that contains the catalytic domain, a Cu^{2+} binding site, a cytokine-like receptor domain and cofactor residues, lysyl tyrosyl quinine (LTQ). They differ in the N-terminal region. LOXL1 has a proline rich domain and LOXL2-4 have four scavenger receptor domains. The N-terminus is thought to be involved in protein-protein interactions. LOX is synthesised as a zymogen and cleaved outside cells by bone morphogenetic protein 1 to produce mature LOX and pro-protein LOX fragment (Wang et al., 2016).

LOX production is induced by the transcription factor hypoxia-inducible factor 1 (HIF-1) under hypoxic conditions. A hypoxic core is a feature of all tumours and therefore it is likely that LOX is in high abundance in the tumour core (Pez et al., 2011). Furthermore, FoxM1b, a transcription factor globally upregulated in cancer that is correlated with metastasis, also induces LOX and LOXL2 expression (Park et al., 2011). The abundance of LOX is increased in invasive basal breast cancer but not in non-invasive breast cancer, suggesting that LOX may contribute to EMT (Chu et al., 2012).

Mature LOX that has been cleaved in the ECM can become intracellular. LOX can be shuttled into the nucleus of cells and affects cancer progression by directly modulating transcriptional activity. LOX has been shown to directly influence transcription by affecting histone modifications and

chromatin structure regulation. Intracellular LOX also effects transcriptional activity by interaction with other intracellular proteins that themselves have roles in the transcription regulation (Iturbide et al., 2015).

LOX has been shown to affect cancer progression through transcriptional modulators, or platelet derived growth factor receptor -β, as well as basic fibroblast growth factor (Xiao and Ge, 2012). LOXL2 is thought to increase cancer aggression by cooperating with the transcription factor SNAIL to downregulate an epithelial phenotype (Cuevas et al., 2017).

1.5 Breast Cancer Cells *in vitro*

1.5.1 MDA-MB-231 cells

Currently there are 27 TNBC cell lines (Chavez, Garimella, Lipkowitz 2010). One of the most well characterised TNBC cell lines was derived nearly 50 years ago from a 51-year old woman. This woman had IDC that had metastasized to the lungs and the pericardial effusion after having a radical double mastectomy four years previously. The malignant cells established the MDA-MB-231 (A231) cell line (R.Cailleau 1974). A231 cells have a basal, TNBC phenotype, are highly metastatic and poorly differentiated and have migratory activity *in vitro* (Bigagli et al., 2019). This cell line is important for understanding breast cancer metastasis *in vitro* (Chavez et al., 2010).

1.5.2 2-Dimensional Cell Culture

A231 cells in 2-dimensional (2D) cell culture have a distinctive 'kite-shaped' appearance with F-actin-rich leading edges that provide tensile force to push the cell forward (Ohashi et al., 2017). Actin-rich protrusions such as lamellipodia at the leading edge or invadopodia under the cell body aid migration. Lamellipodia form cell-matrix adhesions (focal adhesions (FA)) via integrins, which exert new sites of traction for migration, whereas mature invadopodia secrete MMPs (2, 9 and 14) that digest ECM and help create a loose ECM for migration (Izdebska et al., 2018; Harris et al., 2018). At the rear 'trailing edge' of the cell, the F-actin cytoskeleton is contracted to allow forward movement (Kalluri and Weinberg, 2009).

The migratory ability of A231 cells can be characterised by assessment of cell phenotype by fluorescence microscopy. In fixed cells, fluorescently labelled antibodies for cytoskeletal proteins such as actin and tubulin can give an overall impression of cell shape or disruptions of the cytoskeleton. Fluorescent-phalloidin provides a one-step reagent to visualise filamentous actin (F-actin) structures (Chazotte, 2010). Larger cell area and dense meshwork of F-actin at leading edges are associated with greater migratory capacity (Lyons et al., 2016; Rottner et al., 2017). Indirect immunofluorescence can also show the number and location of FA, by staining for proteins such as vinculin. FA are the intracellular protein complexes associated with integrin cytoplasmic domains and include adhesion molecules that enable mechanotransduction from the ECM to F-actin. FA are critical for transducing ECM stiffness into changes in cell behaviour. An increase in FA is

characteristic of the distinctive mesenchymal phenotype (Khalili and Ahmad, 2015). Another method to analyse cell migratory ability is to grow cells to confluence and introduce a 'scratch' wound. Time-lapse imaging can be used to analyse the ability of cells to migrate and resolve the wound (Cory, 2011).

1.5.3 3-Dimensional Cell Culture

Molecular therapies for breast cancer often fail pre-clinical drug trails. One reason this may be is that, traditionally, the understanding of cancer cell mechanisms has been based on 2D cell culture models. These are increasingly being shown to be a far cry from *in vivo* tumours (Friedrich et al., 2009). Culturing cancer cells as 3-dimensional (3D) structures (spheroids) better recapitulates cell organisation in a tumour and is more physiologically relevant. Cells in 3D form cell-cell and cell-matrix adhesions and organise as a ball-like structures (Rodday et al., 2011). These 3D structures also provide a gradient for pH, hypoxia and cell waste products. The collective term for the adhered cells in 3D is a spheroid. Large spheroids (>500μm) are more representative of a tumour with the presence of a necrotic core. Spheroids can also form as co-cultures with different cell types, for example breast cancer cells and fibroblasts (Kim et al., 2015). These features make spheroids better models to understand the molecular mechanisms of EMT or tumour progression (Nath and Devi, 2016).

Spheroids can be cultured with or without a synthetic scaffold. Scaffolds in 3D culture are used to create a synthetic ECM that recapitulates an *in vivo* TME, as cell-matrix adhesions can have a large impact on cell adhesion, proliferation and migration (Gkretsi 2018). Examples of scaffold methods include Matrix Encapsulation, Spinner Flasks and Micropatterned Plates (Tan et al., 2001; Justice et al., 2009; Lee et al., 2007). A synthetic matrix can help hydration, passage of oxygen and nutrient flow. The limitations of scaffolds are that they introduce a large amount of manufacturing variability: scaffold batch variability could have a large unknown impact on cancer cell phenotypes and limit reproducibility. Scaffold-free culture relies on cancer cells self-aggregating to form spheroids. Methods to achieve this include Ultra-low attachment plates, Hanging Drop and Magnetic Levitation (Nath and Devi, 2016).

Spheroids can be characterised by microscopy, biochemical assays or flow cytometry. 3D image analysis can be done using a confocal microscope. The 3D nature of the spheroids requires consideration of the X, Y and Z axis. For smaller spheroids, immunofluorescence can be used to visualise cytoskeletal and extracellular proteins. Larger spheroids (>150μm) are more difficult to visually analyse by confocal microscopy. Large spheroids are more fragile, and the usual immunofluorescent methodology can damage the spheroid. A large diameter also makes antibody penetration more challenging (Weiswald et al., 2010). However, different microscopy techniques allow for live-imaging, high-resolution or cross-section visualisation (Lorenzo et al., 2011; Jaros et

al., 2017). Small spheroids tend to form within 48 hours whilst larger spheroids and spheroid culture with scaffolds can take 4-5 days to form spheroids. In some cases, spheroids can be kept growing long-term for weeks through media changes, which gives the ability for spheroid analysis over time (Cohen et al., 2015). Breast cancer spheroids are enriched with cancer stem cells which suggests that spheroids have the propensity to change over time (Ishiguro et al., 2017).

1.5.4 Conditioned Media

In vivo, extracellular fluids contain the combined secretomes of stromal cells (e.g. neoplastic cells, CAF and immune cells) and regulates autocrine and paracrine signalling and ECM remodelling (Dai et al., 2016). *In vitro*, the secreted products of a cell type or co-culture enter the conditioned media (CM), which will then contain proteins such as cytokines, growth factors, ECM components and enzymes (e.g. MMPs), lipids, and extracellular vesicles such as exosomes. Precise measurements of the CM proteome can be carried out using proteomics, helping to gain a greater understanding of the mechanisms that sustain malignancy. This is particularly effective for identifying pathological protein markers that could be targeted for disease treatment or as biomarkers of cancer progression or relapse (Brandi et al., 2018).

Although less physiologically relevant than body fluids, CM is advantageous for studying cancer cell secreted products since it simpler in composition, meaning that low abundance secreted proteins, that may pass unrecognised in proteomics analysis from biological fluids, can be identified (Méndez and Villanueva, 2015).

1.6 Protein Disulphide-Isomerase A3

Protein disulphide-isomerase A3 (PDIA3) is an ER-resident protein of relative molecular mass ~57kDa. It is also known as Erp57, Grp58, 125D3MARR and Grp60. PDIA3 is a multi-functional isomerase and oxidoreductase that catalyses a series of redox reactions that ultimately break or make disulphide bonds in target proteins. Disulphide bonds are often important for proteins' final tertiary structure. PDIA3 is in part responsible to ensure that newly synthesised glycoproteins, destined for secretion, reach their native folded state. PDIA3's role in protein folding and quality control is well documented (Turano et al., 2011).

The enzymatic chaperone activity of PDIA3 is mediated in conjunction with homologous lectin chaperones calreticulin and calnexin as part of the ER machinery for new protein folding and the unfolded protein response (UPR). As an important regulator of ER homeostasis, PDIA3 is upregulated during the UPR and helps to disassemble protein aggregates (Ellgaard and Frickel, 2003). PDIA3 is important in the assembly of MHCI (Raghavan et al., 2008). Its oxidoreductase activity folds MHCI, in addition to PDIA3 being a component of the MHCI complex itself along with calreticulin, ER antigen peptide transporter 1 (TAP), and tapasin (Stepensky et al., 2007). PDIA3 contains a KDEL-ER retrieval motif and, as noted above, resides in the ER, however there are

reports that PDIA3 may also locate elsewhere, including the cytoplasm, plasma membrane and in the ECM (Raykhel et al., 2007). It is not clear how PDIA3 reaches these locations from within the secretory pathway, although TGFβ1 was reported to increase PDIA3 extracellularly in renal fibrosis (Dihazi et al., 2013). Due to the fundamental nature of PDIA3 its dysregulation has been attributed in many disease aetiologies (Hatahet and Ruddock, 2009).

1.6.1 Structure and Mechanism

PDIA3 is made up of four thioredoxin domain: each thioredoxin domain is characterised by a βαβαβββα fold. Two of the thioredoxin domains are catalytically active and possess a catalytic cysteine residue within a CXXC motif (**Figure 1.5**). The catalytic domains, or the a/a' domains, flank the two redox inactive b/b' domains. The a/a' domains are more similar to each other than to the b/b' domains (Kozlov et al.). Nuclear magnetic resonance has shown that these domains form a "U-like" structure, with the b/b' domains at the base and the a/a' domains at the 'ears' parallel to one another (Pollock et al., 2004). The b'/a' domains are joined by a 19 amino acid linker sequence and are a component of prolyl-4 hydroxylase (important for a post-translation modification that stabilises the collagen triple helix) (Pirneskoski et al., 2001).

The main site for substrate binding is the b' domain. PDIA3's substrate binding pocket is very shallow. Coupled with high hydrophobicity in this pocket, substrate selection is promiscuous. During catalysis the two independent catalytic domains a/a' rotate out of the starting plane, whereas the b/b' domains remain stationary throughout the reaction. This movement positions a catalytic cysteine of the CXXC motif in the a/a' domains to attack a thiol bond in the substrate. After the reaction PDIA3 becomes reduced and must be re-oxidised to be ready to perform another round of reduction.

PDIA3 then undergoes a series of redox reactions facilitated by oxidising agents, peroxiredoxin, glutathione peroxidase 7 or 8 and ER-oxidoreductin 1 (Ero1). The reaction terminates with the reduction of molecular oxygen to hydrogen peroxide. The catalytic cysteine must be maintained at low pH (4.4 - 6.7) to keep the reduction potential high and the kinetics efficient to be favourable for thiol-disulphide exchange (Hawkins and Freedman, 1991). Alone, PDIA3 has a much slower rate of isomerase and oxidoreductase activity than other members of the PDI family (Hatahet and Ruddock, 2009).

PDIA3 is unique amongst the PDI family in that it uses cofactors, calnexin and calreticulin, to enhance substrate binding (Oliver et al., 1999). PDIA3 binds calnexin and calreticulin on its acidic C-terminal. The b' domain on a proline-rich arm and one lysine residue of the b domain contribute to this interaction (Frickel et al., 2002) (**Figure 1.5**). Both of these proteins are important in the quality control cycle that involves PDIA3 in the UPR (Hatahet & Ruddock, 2009).

1.6.2 Known Targets of PDIA3

It is well established that PDIA3 interacts with calnexin and calreticulin to form a complex that helps to regulate protein quality control in the ER. PDIA3 is then equipped to catalyse the formation of

naïve disulphide bonds. This reaction only occurs on mono-glycosylated protein substrates (Oliver et al., 1999).

Experimental identification of proteins that are targeted by PDIA3 has been done by mass spectroscopy and use of substrate trapping mutants of PDIA3. 25 proteins have been found to be targets of PDIA3. Of these proteins many contain small, disulphide rich domains (such as EGF domain, IgG domain and Kunitz domain) and many have a low level of secondary structure. All proteins identified to date are glycoproteins and have an array of cellular locations. However, secreted proteins or cell-surface proteins appear to be particularly targeted as substrates. Examples include agrin, clusterin, integrin α3 and laminin β3 (Jessop et al. 2007).

Some of the 25 proteins identified as PDIA3 substrates are known components of breast cancer ECM. For example, over-expression of LOXL2 and collagen α(VI) chain promote breast cancer metastasis (Salvador et al., 2017; Karousou et al., 2014). Agrin is upregulated in some breast cancer cell lines and has roles in stimulating focal adhesions (Chakraborty et al., 2015). Laminins are the major component of the basement membrane and fundamental for the epithelial phenotype (Holler, 2005).

Identification of these proteins showed that although PDIA3 is resident in the ER, it has a role in the secretory pathway of many glycoproteins. Therefore, through proteins that it targets PDIA3 has a far-reaching influence on cells.

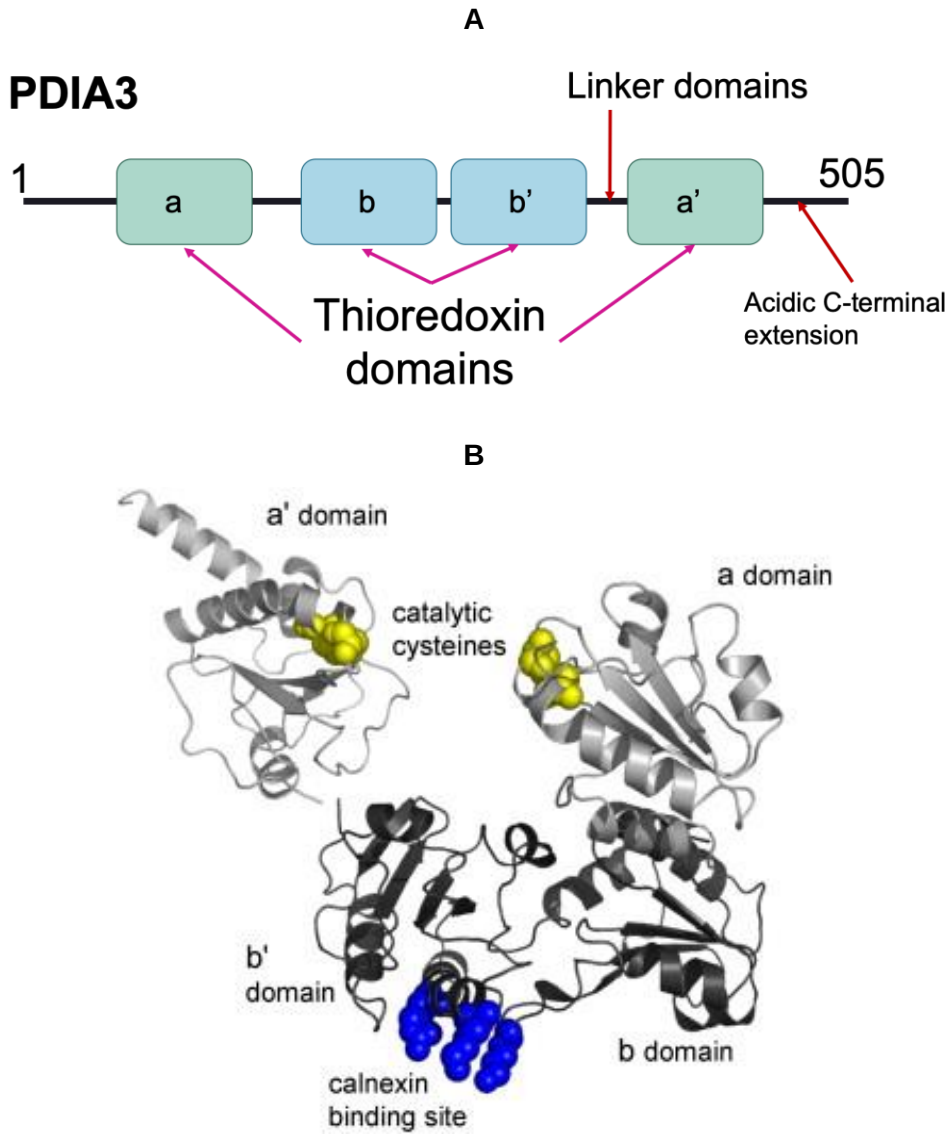

Figure 1.5 ***The Structure of PDIA3.*** **(**A) *Structural Schematic of PDIA3 Showing Four Domains. (B) Crystal Structure of PDIA3* (Kozlov et al., 2006)

1.6.3 PDIA3 and Breast Cancer

In general, PDIA3 expression is correlated with more aggressive breast cancer. Proteomic analysis taking samples from Korean women has revealed that PDIA3 is upregulated in human DCIS and IDC tissue compared to normal tissue. This study also found a comparative increase in calreticulin in breast cancer tissue (Song et al., 2012). At the transcript level, *PDIA3* is upregulated in aggressive primary ductal breast cancer and also has increased abundance in metastatic lymph-node tumours (Ramos et al., 2015). Because PDIA3 is multifunctional, it is hypothesised to affect breast cancer progression in many ways, as discussed in the following sections.

1.6.3.1 Cell Proliferation

PDIA3 has been implicated in cancer cell proliferation. In general, this is because PDIA3 is involved in the assembly process of the serine threonine kinase, mammalian target of rapamycin 1 (mTOR1), a key mediator in cell growth, proliferation, autophagy and protein synthesis. The analysis of mTOR1 and PDIA3 interaction was done by a yeast two-hybrid screen. Confirmation was performed by expression of recombinant proteins for mTOR1 and PDIA3 in HEK293T cells, cell lysates were then purified on an affinity column and proteins identified by immunoblot. It has been suggested that overexpression of PDIA3 helps to stabilize the mTOR complex and promote tumour progression (Hussmann et al., 2015).

However, the specific role of PDIA3 in breast cancer proliferation is unclear. This is largely because of the multi-functional role of PDIA3 in cellular mechanisms. Many breast cancers overexpress epidermal growth factor receptor (EGFR) and as a result have sustained proliferative signals. PDIA3 inhibits the degradation of EGFR by decreasing its cycling from the plasma membrane and inhibits dephosphorylation of EGFR. This results in copious active EGFR at the cell-surface and unchecked breast cancer cell proliferation (Gaucci et al., 2013). Conversely, PDIA3 expression in the MCF-7 breast cancer cell line was shown to modulate vitamin D signalling. This was achieved with a ribozyme construct for PDIA3 mRNA knockdown and levels of 1,25 dihydroxyvitamin D3 expression were measured by real time PCR and western blotting. Vitamin D signalling is often anti-tumorigenic and protective against cancer progression (Richard et al., 2010).

1.6.3.2 Chemoresistance

Increased activity of PDIA3 may help cancerous cells survive adverse tissue conditions and promote chemoresistance. One aspect of this is that an increased abundance of PDIA3 correlated with reduction of MHCI receptors, which may help cancer cells to escape immune surveillance (Antoniou et al., 2002). In addition, PDIA3 may assist cancer survival under conditions of cell stress, reducing the impact of hypoxia, high pH or depletion of nutrients by inducing UPR. Overexpression of PDIA3 has been shown to be a marker of aggressiveness in breast cancer IDC (Da Costa et al., 2015).

1.6.3.3 Bone Metastasis of Breast Cancer

Transcriptomic and proteomic profiling of breast cancer cells (MDA-MB-231 and its osteotropic BO2 subclone (BO2)) was used to identify the functional characteristics that promote breast cancer metastasis to the bones. This study revealed that PDIA3 functions as a 'hub' that mediates a range of cancer-associated cellular phenotypes. The study suggested that PDIA3 regulates human MHCI expression in BO2 and A231 cells, and in BO2 cells PDIA3 has an inverse relationship with MHCI expression at the plasma membrane. The study also suggested that there is an inverse relationship between vimentin (an intermediate filament mainly found in mesenchymal cells) and PDIA3 abundance, suggesting that PDIA3 may have substrates with roles in breast cancer cell MET. Subcellular location analysis and abundance of proteins of interest (MHCI, PDIA3 or cytoskeletal proteins) was done by immunofluorescence and RT-PCR, knock-down of proteins was done with small interfering RNA. There is also a suggestion that PDIA3 interacts with cytoskeletal proteins like galnetin-1, cytokeratin-19 and stathmin-1 from online curated databases that include databases on disease-gene associations (Guney and Oliva, 2012). Finally, PDIA3 knockdown by short hairpin RNA reduced bone-specific metastasis in the BO2 breast cancer subclone variant in mice, as measured by mouse whole body analysis of tumour formation with non-invasive bioluminescence imaging (Santana-Codina et al., 2013). Taken together, these results support that PDIA3 contributes functionally by unknown mechanisms in breast cancer metastasis.

1.6.4 Chemical Inhibition of PDIA3

One commercially available small molecule inhibitor of PDIA3 is 16F16. Like all PDI-targeted inhibitors, 16F16 functions to inhibit PDIA3's catalytic cysteine. The chloroacetyl moiety of 16F16 covalently and irreversibly binds to the catalytic cysteine of the CXXC motif in the active thioredoxin domain of PDIA3 (**Figure 1.6**) (Hatahet and Ruddock, 2009)**.** However, because of the high degree of conservation of the thioredoxin domains of the PDI family, specific inhibition of PDI family members is hard to achieve (Hoffstrom et al., 2010). The efficacy of intracellular 16F16 has been debated;16F16 was originally described as a PDIA1 inhibitor, yet recent studies comparing 16F16 to PACMA31 (a known PDIA1 inhibitor with no off-target binding) on breast cancer cell spreading, attachment and migration assays proved to elicit very different outcomes (Xu et al., 2012; Young, unpublished, 2018; Chen et al., 2018). These data suggest that 16F16 is probably an inhibitor of PDIA3. With lack of truly specific, commercially available pharmacological inhibitors and the recent evidence in Adams laboratory for the action of 16F16 on breast cancer cells, 16F16 was chosen as the PDIA3 inhibitor to use in this project.

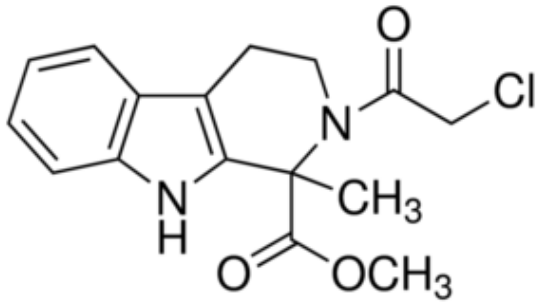

Figure 1.6 ***Structure of 16F16.*** *Skelton diagram retrieved from the Sigma-Aldrich website: catalogue number- SML0021, PubChem- CID-329825093.*

1.7 The PDIA3-Dependent Secretome of Mouse Embryonic Fibroblasts

As discussed, PDIA3 is up-regulated in metastatic forms of breast cancer (Santana-Codina et al., 2013). Because PDIA3 could have effects on the TME by directing the folding of secreted glycoproteins (Jessop et al., 2007, Halperin 2014), Professor Adams' laboratory has begun to investigate a potential role of the PDIA3-dependent secretome in the TME. Research carried out by Dr. Hellewell (under Medical Research Council- K018043) showed that *Pdia3*$^{-/-}$ mouse embryonic fibroblasts (MEF) had a reduced migratory phenotype compared to wild type (WT) MEF, as assessed by cell area, F-actin organisation and number of FA. It was also found that a normal migratory phenotype could be restored in *Pdia3*$^{-/-}$ MEFs by plating with CM from WT-MEF. Tandem mass tag (TMT)-based quantitative proteomics on the CM from *Pdia3*$^{-/-}$ and WT-MEF revealed a set of proteins that were decreased in the *Pdia3*$^{-/-}$ secretome. These proteins included cytokines, growth factors and ECM proteins (unpublished data). A subsequent M.Res project carried out by Harry Young examined the effects of PDIA3 inhibition by 16F16 on several breast cancer cell lines. Cell spreading and migration was decreased upon PDIA3 inhibition and this effect depended on the conditioned medium. The stronger phenotypic changes were obtained with A231 cells. The data indicated that PDIA3 activity affects cell morphology of these breast cancer cell lines through secreted products (Young, unpublished, 2018). This M.Res project starts from these findings.

1.8 Aims of this M.Res Project

The central objective of this project is the identification of the PDIA3-dependent secretome in A231 breast cancer cells.

Specific goals are:

1. To characterise the effect of secreted PDIA3-dependent proteins on F-actin, cell spreading and focal adhesions in naïve A231 cells and to identify if these effects depend on heparin-binding secreted proteins.

2. To identify the PDIA3-dependent, heparin-binding proteins in A231 breast cancer cells by quantitative TMT-based proteomics and to analyse the dataset and validate selected proteins.

3. To examine the effect of pharmacological inhibition of PDIA3 on spheroid formation by A231 cell in 3D culture.

Chapter 2 Materials and Methods

2.1 Cell Culture

2.1.1 MDA-MB-231 Cells

The entirety of this project has used MDA-MB-231 cells (described originally by Caileau et al.1973) that were purchased from American Type Culture Collection.

2.1.2 Cell Culture Media

DMEM containing 44.5μM of phenol red was used throughout the project to sustain and grow cells and was supplemented with 10% foetal bovine serum (FBS). Some experiments used Fibroblast Growth Medium (FGM) (**Table 2.1**) which is a complete medium that contains 3.3μM of phenol red.

2.1.3 Recovery and Expansion of Cells

Cells were removed from long term storage in liquid nitrogen (-196°C), then rapidly warmed in their cryovial in a 37°C water bath, to avoid dimethyl sulfoxide (DMSO)-induced toxicity. Cells were then diluted 1:10 in Dulbecco's Modified Eagle Medium high glucose (DMEM) (**Table 2.1**), which had been warmed to 37°C and supplemented with 10% foetal bovine serum (FBS) (**Table 2.1**). Cells were then centrifuged at 1000rpm for 5 minutes, resuspended in DMEM with 10% FBS, and placed in a T25 flask for culture (**Table 2.4**). at 37°C in a sterile, humidified, copper-lined incubator gassed with 5% CO_2. Medium was changed every Monday, Wednesday and Friday: depending on confluence (≥80%) and experimental requirements, cells were either passaged or used in experiments.

2.1.4 Passaging of Cells

As required, cells were rinsed briefly with 0.05% trypsin/EDTA (1x) (**Table 2.1**) to remove dead cells and cell debris. Cells were then incubated at 37°C with a small volume of 0.05% trypsin/EDTA for 2/3 minutes to detach adherent cells from plastic. Trypsin was collected and then inactivated by resuspending the cells in DMEM containing 10% FBS to be re-plated according to requirements or used in experiments.

2.2 Chemicals and Inhibitors

Table 2.1 and **Table 2.2** list all the chemicals and inhibitors used in this project.

Table 2.1. *Chemicals used in project*

Name	Supplier	Catalogue Number
Acrylamide (40%)	Bio-Rad	1610140
Ammonium Persulfate powder (APS)	BDH (now VWR life science)	BDH9214-500G
Bromophenol Blue	Sigma	B0126
Bis-acrylamide(2%) Solution	Bio-Rad	161-0142
Dimethyl sulphoxide (DMSO)	GPR™	282164K
DL-dithiothreitol (DTT)	Sigma	D9779
Dulbecco's Modified Eagle's Medium	Sigma- Aldrich	D6429
Enhanced Chemiluminescence (ECL) ™ WB detection agent	Amersham	RPN2209
Ethanol (100%)	Sigma-Aldrich	32221
Ethylenediaminetetracetic acid (EDTA)	Sigma	ED2SS
Foetal Bovine Serum	Sigma-Aldrich	F7524
Fibroblast Growth Medium	Promocell	C-23010
Glycerol	Sigma	G5516
Glycine	Sigma	G8898
Heparin−Agarose in aqueous ethanol suspension	Sigma-Aldrich	H0402
Hydrocholoric acid	Sigma	H1758
L-Ascorbic Acid	Sigma	A4544
Methanol	Sigma	322415
Milk Powder	Sainsbury's	7742528
N,N,N′,N′-Tetramethylethylenediamine (TEMED)	Sigma	T9281
Paraformaldehyde (PFA) 16% (w/v)	Alfa Aesar	43368
Phalloidin–Atto 565	Sigma	94072
Pierce™ Control Agarose Resin	Thermo Scientific	26150
Ponceau S Stain	Sigma	P71701
Precision Plus Protein ™ Dual Colour Standards	BIO-RAD	#1610374
Sodium Dodecyl Sulphate (SDS)	Fischer Scientific	28906
Triton X-100	Sigma	T6066
Trizma Base (Tris)	Sigma	T6066

Trypsin-EDTA	Sigma- Aldrich	T3924
Tween-20	Sigma	P2287
VectaMount	Vector	H5000
VectaShield with 4',6-diamidino-2-phenylindole (DAPI)	Vector	H1200

***Table 2.2**. Inhibitors used in project*

Inhibitor	**Mechanism of action**	**Supplier**	**Catalogue Number**	**CAS**
16F16	Irreversible inhibitor of PDIA3 and PDIA1	Sigma	SML-0021	922507-80-0
3-Aminopropionitrile fumarate salt (β-APN)	Irreversible inhibitor of LOX and LOXL2	Sigma	A3134	2079-89-2
Pierce™ Protease inhibitor tablets-mini	Broad spectrum inhibitors of cellular proteases	ThermoFisher Scientific	88665	30827-99-7

2.3 Buffers

Buffers were prepared in the laboratory using the solutions detailed in **Table 2.3**.

Table 2.3*. Solutions used in project. Key: WB= Western Blot*

Buffer	Abbr.	Working Composition	Experiment
10 X Tris buffered saline	10 X TBS	80g NaCl, 25g KCl, 30g Tris base, 5M HCl made up with 800ml dH_2O	General Use
1X Tris buffered saline	1X TBS	900mL dH_2O; 100mL 10x TBS	Proteomics; Staining, fixing
20% SDS stock solution	20% SDS	20g SDS dissolved in 100ml dH_2O	WB
Immunoblot Blocking Buffer		PBS containing 2% (w/v) semi-skimmed dried milk and 0.2% (v/v) Tween 20	WB
Phosphate buffered Saline	PBS	NaCl 0.138M; KCl- 0.0027 M; pH 7.4 in dH_2O.	Cell lysate; staining; fixing; WB; proteomics
Phosphate buffered saline, 0.2% Tween	PBS, 0.2% Tween	PBS containing 0.2% (v/v) Tween 20	WB
Resolving Gel 10% acrylamide Final		5ml of 40% Acrylamide, 1.5ml of 2% Bis solution, 7.4ml of 1M Tris base pH 8.7, 6.55 ml of H_2O, 190µl of APS (w/v in dH_2O), 90µl 20% SDS, 72µl of TEMED	WB
10X SDS-PAGE Running Buffer		151g Trizma base; 720g glycine; 5ml 20% SDS, made up to 1l in dH_2O	WB
SDS-PAGE Sample Buffer	SDS-SB	100mM Tris pH 6.8, 4% SDS, 0.2% bromophenol blue, 20% glycerol	WB
Stacking Gel 4% acrylamide Final		1.28 ml of 40% Acrylamide, 0.65 ml of 2% Bis solution, 1.25 ml of 1M Tris base pH 6.8, 6.77ml of dH_2O, 150µl of 10% APS, 20 µl of TEMED	WB
Transfer Buffer	TB	100ml 10X SDS-PAGE Running Buffer; 200ml Methanol, made up to 1l in dH_2O	WB

2.4 Plasticware

Table 2.4. *The plasticware used in this project. Key: PVDF= Polyvinylidene Difluoride, TC= Tissue Culture*

Supplier	Type	Abbreviation	Catalogue Number
Falcon ®	50mL polypropylene conical tube	-	352070
Falcon ®	Tissue Culture Treated Flasks 250ml	T75	35316
Greiner Bio-one	Cell culture microplate, 96 well, F-bottom (chimney well), black, CellStar® TC	-	655079
Alpha Laboratories	Transfer Pipettes	-	LW4141
Amersham	PVDF (0.2µM) membrane	-	10600021
Anachem	20-200µl sterile filter tips		ABA2005
ATTO Corporation	Slab Gel Casting Stand	-	AE6200
Corning®	96-well Clear Round Bottom Ultra-Low Attachment Microplate	96-well spheroid plate	7007
Falcon ®	Cell scraper	-	35386
Falcon ®	100mm TC-treated cell culture dishes	P90	353003
Falcon ®	60mm TC-treated cell culture dishes	P60	353002
Falcon ®	6-well Cell Clear Flat Bottom TC-treated Multiwell Culture Plate	6-well plate	353934
Millex	Syringe Filter Unit, 0.22 µm, polyethersulfone, 33 mm, gamma sterilized	-	SLGP033RB
Millipore	Stericup and Steritop 0.45µm	-	SCHV U01 RE
SARSTEDT	15ml centrifuge tube	-	62.554.002
Thermo Scientific™	Nunc™ Cell Culture Treated Flasks with Filter Caps	T25	136196

2.5 Centrifuges

Table 2.5*.Centrifuges used in this project.*

Name	Model Number	Rotator	Volumes
Eppendorf Centrifuge	5804 R	FA-45-6-30	2.5 -50ml
Eppendorf Centrifuge	5424 R	FA-45-24-11	< 2.5 ml

2.6 Antibodies

The primary and secondary antibodies used are shown in **Table 2.6** and **Table 2.7.**

Key: IF: Immunofluorescence, IgG: Immunoglobulin G, RT: Room temperature, WB: Western blot, HRP: Horseradish Peroxidase

***Table 2 6**. Primary Antibodies*

Antigen	Antibody	Supplier	Cat. Num.	Dilution		Incubation time (h) WB/IF	Incubation Temp WB/IF
				WB	IF		
Binding immunoglobulin protein (BiP)	Rabbit Polyclonal IgG	abcam	Ab21685	1:2000	-	Overnight/-	4ºC/-
Fibronectin (FN)	Rabbit Polyclonal IgG	Sigma	F3648	1:600	-	Overnight/-	4ºC/-
Glyceraldehyde-3-phosphate dehydrogenase (GAPDH)	Mouse monoclonal IgG	abcam	Ab9484	1:600	-	Overnight/-	4ºC/-
Insulin Growth Factor Binding Protein-7(IGFBP7)	Rabbit Polyclonal IgG	abcam	Ab74169	1:1000	-	Overnight/-	4ºC/-
Lysyl oxidase-like 2 (LOXL2)	Rabbit Polyclonal IgG	abcam	Ab96233		-	Overnight/-	4ºC/-
Protein Disulphide Isomerase (PDIA3/Erp57)	Mouse monoclonal IgG1	abcam	Ab13506	1:2000	-	Overnight/-	4ºC/-
Vinculin	Mouse monoclonal IgG	Sigma	V4505	-	1:300	-/1.5	-/RT

Table 2.7*.Secondary Antibodies*

Antigen	Antibody	Supplier	Cat. Num.	Dilution	
				WB	IF
Mouse IgG	Alexafluor®488 conjugated polyclonal goat IgG	Life Technologies	A11001	-	1:200
Mouse IgG, IgA, IgM	HRP-conjugated goat IgG	LI-COR	926-80010	1:50000	-
Rabbit IgG, IgA, IgM	HRP-conjugated goat IgG	LI-COR	926-80011	1:50000	-

2.7 Cell Culture: Experimental Setup of Cells

2.7.1 Experimental Setup of Cells with 16F16 Inhibitor

MDA-MB-231 cells were trypsinised as described in **2.1.4**. Cells were collected into a 15ml centrifuge tube (**Table 2.4**) containing 8ml of DMEM and 10% FBS (**Table 2.1**). If experiments used more than one dish of cells, all cells were collected into one 15ml centrifuge tube (**Table 2.4**). The cell suspension was centrifuged at 1000rpm for five minutes to pellet the cells. Spent medium was discarded, and cells were resuspended in 8ml of FGM (**Table 2.1**) and mixed very thoroughly before being centrifuged again at 1000rpm. According to the experimental design, p90 dishes were set up with a total volume of 8ml of FGM and $1.5x10^6$ cells. L-Ascorbic acid was diluted from 10mg/ml stock (**Table 2.1**) and added to give a final concentration of 50µg/mL to promote collagen synthesis. Ascorbic acid is a cofactor for prolyl-4-hyroxylase, a key enzyme for collagen hydroxylation and is essential for collagen to reach its tertiary structure (Pihlajaniemi et al., 1991). Plates were incubated at 37°C 2-3 hours to allow cells to attach, then 5µM of 16F16 (**Table 2.2**) was added or an equivalent volume of DMSO as solvent-only control, and cells incubated for 48 hours at 37°C.

2.7.2 Preparation of Conditioned Media (Small Scale)

After 48 hours of incubation of cells with either DMSO or 16F16, medium was removed from each p90 dish using a transfer pipet and put in a 50ml polypropylene conical tube (**Table 2.4**). Cell lysates were collected according to **2.7.3.** The medium was centrifuged at 1000rpm for 5 minutes to pellet any cell debris, and the supernatant then passed through a 0.22µm pore Syringe Filter Unit (**Table 2.4**) to sterilize and remove particles larger than 0.22µm, and then collected into a fresh 50ml polypropylene conical tube.

2.7.3 Preparation of Cellular Samples for Western Blotting

After conditioned medium was removed from p90 dishes as described in **2.7.2**, cells were gently rinsed three times in PBS to remove any detached cells or residual medium. Then 200µl of SDS-PAGE sample buffer containing 100mM of DTT was added and the cell lysate scraped into a 1.5mL Eppendorf tube (**Table 2.4**) and stored at -20°C.

2.8 SDS-PAGE and Immunoblotting

All samples were stored at -20°C in SDS-PAGE-SB containing 100mM DTT. Prior to gel loading, samples were heated at 95°C for 5 minutes. Samples that contained heparin-agarose or control-agarose beads were centrifuged at 1000rpm for 1 minute to pellet beads and the supernatant loaded onto the gel. Precision Plus Protein™Dual Colour Standards (**Table 2.1**) was diluted 2:5 with SDS-PAGE-SB containing 100mM DTT and provided molecular weight references on the gel. Gels were cast as 10% SDS-polyacrylamide resolving gels overlain with 4% polyacrylamide stacking gel (**Table 2.4**). Proteins were stacked at 80V for 1 hour then

separated in the resolving gel at 140V for 4 hours. For immunoblotting, proteins were transferred onto 0.2µm pore PVDF membrane at 15V for 1.5 hour using a Trans-Blot®SD Semi-Dry Transfer Cell (Biorad). The membrane was stained with Ponceau S (**Table 2.1**) to visualise transferred proteins. The membrane was then washed three times in dH_2O to increase band clarity and a digital image was taken using a Syngene G:BOX Chemi XRQ. The membrane was then cut into segments according to the experimental design and blocked for 30 minutes in immunoblot blocking buffer (**Table 2.3**). Proteins of interest were probed for with specific primary antibodies (**Table 2 6**). Primary antibody dilutions were made in blocking buffer and incubated at 4°C overnight with rotation to bind to antigen. The membrane was then washed three times (10 minutes each) in blocking buffer to remove non-specific bound antibody and then incubated with the appropriate diluted secondary antibody (**Table 2.7**) for one hour at room temperature with rotation. The membrane was washed in blocking buffer as described above, with two additional 10-minute washes in PBS. Bound antibodies were visualised by adding equal volumes of Amersham ECL Western Blot detection reagent (**Table 2.1**) to provide chemiluminescence at the band location and imaged in a Syngene G:BOX Chemi XRQ. A digital image was taken with the GeneSys software and the file exported to GeneTools for quantitative band analysis and normalisation to loading control.

2.9 3-Dimensional Spheroid Cell Culture

2.9.1 Experimental Setup and Quantification

Breast cancer spheroids were grown in 96-well Clear Round Bottom Ultra-Low Attachment Microplates (**Table 2.4**). Each well contained 100µl of DMEM with 10% FBS. To minimise the time cells were not at 37°C, the total volume in the wells was made up in halves: the first half containing 50 µl of DMEM with 20% FBS and double the final concentration of 16F16; the second half containing 50 µl of DMEM with the correct number of cells to be seeded. To begin, a stock solution of 20mM 16F16 which had been dissolved in deionised water was thawed from storage at -20°C and the correct volume diluted in 8ml of DMEM with 20% FBS to make final concentrations of either 1, 2.5, 5, 10, 12.5, 17.5, 25 or 50µM (depending on experimental design/requirements) in a 15ml centrifuge tube. A further 8ml DMEM with 20% FBS was made up individually with DMSO at an equivalent total volume to the highest volume used for 16F16. A stock of DMEM with 20% FBS only was made up for control wells. Once made up and mixed well, 50µl aliquots were put into the allocated wells. The 96-well plate was then left in the humidified 37°C incubator until the cells had been prepared. One T75 of stock cells was trypsinised as described in **2.1.4** and cells collected into a 15ml centrifuge tube and counted in a haemocytometer. A volume of cell suspension was then taken into an Eppendorf tube (**Table 2.4**) that contained the total number of cells needed to plate all the wells - over one 96-

well plates this included 400, 200, 1000, 2500, 5000, 7500 and 10000 cells/100µl. For experiments with varying concentrations of 16F16 there were 6 replicate wells per condition, except the third experiment which has 2 replicate wells. For experiments investigating seeding cell number there were 6 replicate wells for the 50µM 16F16 and 0µM 16F16 conditions, and 3 replicate wells for the control. This volume was further diluted as needed with DMEM such that the desired number of cells was present in a 50µl volume. After remixing, 50µl of cell suspension was then added to allocated wells containing 50µl DMEM, 20%FBS and 16F16 and mixed well. The 96-well plate was then placed in a humidified chamber at 37ºC 5% CO_2, and within a maximum of 15 minutes taken to the Wolfson Bioimaging Facility to be put in the EssenBiosciences IncuCyte® ZOOM Live-Cell Analysis System. Here, cells were incubated in a humidified chamber at 37ºC with 5% CO_2 whilst being live-imaged. A phase contrast digital image of each well was taken every 2 hours for 72 hours under control of the IncuCyte Software. After images had been collected, the 96-well plate was removed from the IncuCyte® ZOOM incubator and the spheroids were fixed for further inspection of 3D character. Control wells or wells with DMSO seeded at 10000 cells/100µl were chosen since spheroids could be seen by eye in these wells and under a light microscope appeared to have 3D quality. Being careful not the damage the spheroid and drawing liquid from the edges of wells, 70µl of spent media was discarded, and wells washed gently in 70µl of PBS. The spheroids were then submersed in freshly made 4% PFA in PBS (**Table 2.1**) for 30 minutes for fixation. The 4% PFA was removed and the spheroids left in 100µl of PBS. The 96-well plate was wrapped in parafilm and stored at 4ºC until staining (**2.10.5**).

Spheroid formation was quantified using the IncuCyte ® ZOOM System Software. A phase-contrast image of every well, for every timepoint was exported as a TIFF file. Spheroid area was then defined using ImageJ tools (https://imagej.net/Welcome), (threshold > binary> measure particles (particles size above 10000µm)). The spheroid area was analysed and recorded by region-of-Interest (ROI) manager on ImageJ. The TIFF files were processed by ImageJ by a batch macro; once all the spheroid areas had been collected for a plate, they were exported from the ROI into Microsoft Excel. The processed spheroid TIFF files that showed the threshold images of quantified area were also saved in a separate folder and were checked visually that the batch ImageJ macro had worked correctly on all images. If the macro had incorrectly measured a spheroid, the phase-contrast TIFF was loaded into ImageJ and the spheroid area measured by freehand outline. The average spheroid area for each time-course, reciprocal data and ratios were calculated in Microsoft Excel and then exported to GraphPad Prism 7.0 for presentation.

2.9.2 Experimental Setup of Cells with β-aminopropionitrile Inhibitor

A T75 flask of cells was treated with 500μM of β-aminopropionitrile (βAPN) (**Table 2.2**) and incubated at 37ºC for 72 hours. Then, 1M βAPN dissolved in deionised water was diluted to 5mM in DMEM containing 20% FBS under sterile conditions. This concentration was chosen because βAPN has been shown to be most effective at inhibiting LOXL2 around 300μM, 1M was prepared for a βAPN serial dilution (Rodriguez et al., 2010). Breast cancer cells were setup for spheroid formation in a 96-well plate as described in **2.9.1**. The media was again set up in two parts to minimise cell-handling time. First, fresh 5mM βAPN was diluted to 10, 100, 200, 500, 1000 or 2000μM in DMEM 20%FBS and 50μl of each was added to its allocated wells. Secondly, the prepared cells were trypinised as described in **2.1.4** and an aliquot of cell suspension at 400cells/μl was diluted in DMEM to give either 5000 or 10000 cells/50μl. Next, 50μl of either cell suspension was added to 50μl DMEM/ 20% FBS/ βAPN in the 96-well plate making final concentrations of βAPN of 5, 50, 100, 250, 500 or 1000μM, with 6 replicate wells per condition. The plate was then imaged as described in **2.9.1**.

2.10 Fluorescence Microscopy

2.10.1 Effect of the PDIA3-Dependent Secretome on Cell Spreading

Cells for experiments were trypsinised as described in **2.1.4** from a T75 flask. The cell suspension was centrifuged at 1000rpm for 5 minutes to pellet cells, and cells resuspended and washed three times in FGM. Conditioned media were prepared as in **2.7.2**. In the laminar flow tissue culture cabinet 4 sterile glass coverslips (VWR- 631-0149) were added per well in wells of a 6-well plate containing either 3ml FGM or 3ml conditioned media (**2.7.2**) and incubated with 16F16 or DMSO for 48 hours. A total of 1.5 $x10^5$ cells (in 100μl) was added per well, mixed and incubated at 37ºC for 4 hours or 20 hours to allow cells to attach and spread on the glass coverslips. At end of either incubation, medium was gently removed from each well and the cells gently washed three times in PBS to remove non-adherent cells. Freshly made 4% PFA in PBS was added to wells to completely cover the coverslips and left for 10 minutes to fix the cells. Wells were then washed three times in PBS and, if necessary, stored for a maximum 3 days before permeabilization and staining according to the experimental procedures described in **2.10.2** or **2.10.4**.

2.10.2 Quantification of Cell Attachment and Vinculin Staining

Cells were seeded at $1.5x10^6$ in a p90 dish containing glass coverslips and then treated and fixed after 4 or 20 hours as detailed in **2.10.1,** then permeabilised with 0.5% Triton X100 as described in **2.10.4**. Cells were blocked in 1% Bovine Serum Albumin (BSA) in PBS for 30 minutes, washed three times in a PBS bath, and then incubated with anti-vinculin primary antibody (**Table 2 6**) in PBS containing 1% BSA for 90 minutes. All incubations/ blocking was carried out at room temperature in a humidified chamber. After washing three times in PBS,

coverslips were incubated with Alexafluor® 488 secondary antibody (**Table 2.7**) in 1% BSA in PBS for 45 minutes. Finally, coverslips were washed thrice in PBS followed by deionised water before mounting on slides in VectorShield® with DAPI. Slides were examined as described in **2.10.4**, with a 100mW 488nm Argon laser to detect the Alexafluor® 488 secondary antibody. Images were saved as TIFF files and the Z-stack merged to give MaxIntensity in ImageJ as described in **2.10.4**, then converted to red-green-blue (RGB) TIFF images for display.

2.10.3 Role of Secreted Heparin-Binding Proteins in Cell Spreading

First, heparin-agarose affinity beads or agarose-beads (**Table 2.1**) were prepared. Keeping the beads on ice as much as possible, a total volume of beads corresponding to 20µl of heparin-agarose or control-agarose beads, per p90 dish of cells, was resuspended as 1:1 (v/v) suspensions in chilled 1x TBS (**Table 2.3**) and centrifuged for 30 seconds at 7500rpm. Beads were washed twice more in large volumes of TBS, finally leaving the beads in TBS as a 1:1 (v/v) suspension. After 48 hours culture of cells prepared as described in **2.7.1**, the conditioned medium was collected and prepared as described in **2.7.2**. 16ml of conditioned media was put into a 50mL polypropylene conical tube for each condition. 90µl of either heparin-agarose beads or 90µl of control-agarose beads (each 1:1 v/v in TBS) was added, respectively, to a tube, and incubated on a rotatory wheel at 4^{o}C for 1.5 hours, to allow binding of proteins from the media. Each medium was then centrifuged at 1000rpm for 5 minutes to pellet the beads. Each supernatant conditioned medium was transferred to a fresh tube. Beads were discarded. In the laminar flow cabinet, a 6-well plate was prepared with glass coverslips as in **2.10.1**. Cells were prepared as in **2.1.4** and added at 1.5 x10^{5} cells per well along with either fresh FGM, control conditioned media (after incubation with control-agarose beads) or conditioned media depleted of heparin-binding proteins (after incubation with heparin-agarose) to a final volume of 3ml. The attachment assays then proceeded in accordance with **2.10.1**.

2.10.4 Quantification of Cell Area

After fixation on glass coverslips (as in **2.10.1** or **2.10.3**), cells were permeabilised with 0.5% Triton- X100 in PBS for 10 minutes, then re-immersed in PBS. Coverslips were drained and placed cell-side up in a humidified chamber. Cells were stained with Phalloidin-Atto565 fluorescent compound (**Table 2.1**) diluted 1:100 in PBS, for 50 minutes at room temperature. Then the coverslip was passed three times through a bath of PBS and then deionised water to remove salts. Coverslips were mounted cell-side down on slides using VectaShield with DAPI (**Table 2.1**) and left overnight at room temperature to harden before being examined by microscopy. All slides were examined under a Lecia SP5-AOBS confocal laser scanning microscope attached to a Lecia DM I6000 inverted epifluorescence microscope with an HCX

PL APO lambda blue 63x 1.4NA oil objective. Using Lecia Application Suite AF software 2.7.3.9723, Z-stack images were taken with approx. 0.50μm z-slice thickness, over 2.5-3μm total Z-stack thickness from the base of the cells upwards. Two lasers were used to detect immunofluorescence, 20mW solid state yellow laser (561nm) was used to detect Phalloidin-Atto565 and a 50mW 405nm diode laser for 4′,6-diamidino-2-phenylindole (DAPI) (**Table 2.1**). Three coverslips were imaged per condition per experiment and enough Z-stack-stack images collected so that at least 50 cells could be scored. All files were saved as TIFF files and were loaded into ImageJ as composite images (DAPI and Phalloidin stain) and all Z-stacks were merged using Image> Stacks> Z-Project (Max Projection). Stacked images were processed using Image> Adjust> Threshold following Process>Binary> Make Binary. Cell area was measured using Analyse> Analyse Particles. These steps were combined into an automated macro in which most cell areas were extracted and added to the Region of Interest (ROI) manager. Occasionally cell area was determined using ImageJ freehand outline tool if the macro failed to quantify cell area correctly.

2.10.5 Phalloidin Staining of Breast Cancer Spheroids

After spheroid fixation as described in **2.9.1,** PBS was removed and 100μl of 0.5% Triton X100 added to each well with a fixed spheroid and permeabilised for 15 minutes. After washing in PBS, 100μl of Phalloidin-Atto565 fluorescent compound (**Table 2.1**), (diluted 1:60 in PBS) was added and spheroids incubated at room temperature for 1.5 hours. After washing three times in PBS and storing in 100μl of PBS, each spheroid was delicately transferred to a flat-bottomed 96-well plate with copious PBS and left overnight before imaging. The plate transfer was necessary because the confocal microscope can only focus correctly with flat-bottomed plates. Images were taken using a Lecia SP5-AOBS confocal laser scanning microscope attached to a Lecia DM I6000 inverted epifluorescence microscope with an HCX PL APO lambda blue with a 10x HCX PL Fluotar lens. Using Lecia Application Suite AF software 2.7.3.9723, Z-stack images were taken with approx. 1μm z-slice thickness. The total Z-stack thickness from the base of the spheroid upwards was 80-100μm. A 20mW solid state yellow laser (561nm) was used to detect Phalloidin-Atto565 fluorescence. Images were saved as TIFF files using Volocity® 3D Analysis Software. 3D reconstruction of the Z-stack images was made using the default settings. A total of seven spheroids were imaged.

2.11 Preparation for Tandem Mass Tag-Based Quantitative Proteomics

2.11.1 Experimental Setup

Confluent cells in four T75 flasks were trypsinised as described in **2.1.4** and cells prepared as in **2.7.1**, except for some minor changes to decrease serum proteins from the medium. Cells were collected into a 15ml centrifuge tube containing 10ml of DMEM and 5% FBS (rather than

10% FBS). This was repeated for a further 4x T75 flasks, so collecting all the cells into one tube. The cell suspension was then centrifuged at 1000rpm for five minutes in 10mL of FGM and the pellet resuspended in FGM. This was repeated twice more to remove all traces of DMEM. Then eight p90 dishes were set up with a total volume of 8ml of FGM and $1.5x10^6$ cells per plate. The rest of cellular setup was the same as described in **2.7.1**.

2.11.2 Heparin Affinity Pull-Down from Conditioned Media (Large Scale)

Heparin-affinity pulldown from conditioned media was carried out as described in **2.7.2,** but with some alterations to increase purity for TMT-proteomics. Since 8x p90 dishes were prepared in total (four per condition), in total 160µl of Heparin-agarose beads and 230µl control-agarose beads were prepared for this experiment. In the laminar flow cabinet cell, each conditioned medium (+DMSO or +5µM 16F16; 32ml each) was filtered through a 150mL Stericup filtration unit (**Table 2.4**) with a 0.45µm filter made of Durapore (PVDF) low-protein-binding membrane. This removed particulate material and ensured sterility. Each filtered medium was added to a fresh 50ml polypropylene conical tube and 3 tablets of Pierce™ Protease inhibitor tablets-mini (**Table 2.2**) added. Next, 100µl of 1:1 (v/v) control agarose-bead suspension was added to each tube, to absorb any non-specific agarose-binding proteins from the medium. Each tube was rotated on a rotatory wheel for 1 hour at 4°C. The tube was then centrifuged at 1000rpm for 5 minutes to pellet the control beads. Each supernatant medium was then placed in a fresh 50mL tube and 80µl of heparin-beads/TBS suspension added. The two tubes were rotated on the rotatory wheel at 4°C for 1.5 hours, this time to allow heparin-binding proteins to attach to the heparin-beads. The suspensions were then centrifuged at 1000rpm for 5 minutes to pellet the heparin-agarose beads. The beads were washed three times in TBS and then each moved into a 1.5mL Eppendorf tube and washed once more, with all liquid removed from the final pellets. 50µl of SDS-PAGE SB containing 100mM DTT was added to the heparin-beads to dissociate bound proteins, heparin-beads then centrifuged at 10,000rpm for 30 seconds and stored at -20°C before being taken to the Proteomics Facility. Four independent experiments were carried out.

2.11.3 Tandem Mass Tag-Based Quantitative Proteomics

This method was conducted at Bristol University's Proteomics Facility by Dr. Kate Heesom. The samples prepared in **2.11.2** were resolved on a 1D SDS-PAGE gel to facilitate removal of buffer components which would interfere with downstream LCMS analysis. Electrophoresis was carried out until the dye front had moved approximately 1cm into the separating gel. Each gel lane was then excised and the proteins in one gel slice were digested with trypsin (which cleaves C-terminal to lysine and arginine residues) using a DigestPro automated digestion unit. Resulting peptides were then extracted and labelled with Thermo Fisher Scientific TMT reagent (Cat# 88323) using the manufacturer's protocol. Free tags were quenched using

hydroxylamine and then all labelled peptide samples were pooled. The pooled sample was analysed by LCMS using an Orbitrap Fusion Tribrid mass spectrometer with data analysis performed using Thermo Scientific™ Proteome Discoverer™ Software. All proteins with a Unique Peptide Score over one was included in analysis. Data were exported to Microsoft Excel and underwent statistical analysis by Dr. Phil Lewis, Research Associate, School of Cellular and Molecular Medicine (**2.14**). Proteins were picked for statistical analysis if they were present with a fold difference in all four independent experiments. Of these proteins, only those with a ≥2-fold-change and statistical significance $p<0.05$ between the +DMSO and +16F16 conditions were taken for further bioinformatics analysis.

2.12 Bioinformatic Tools: Computational Analysis of the PDIA3 Dependent Secretome

All proteins found to be significantly ($p\leq0.05$) different across 4 independent repeats by statistical analysis of the control and 16F16 samples in the TMT-Based Quantitative Proteomics (**2.11.3**) were taken forward for further investigation. Each accession number was converted to gene-name using https://www.uniprot.org/uploadlists/. If the gene-name could not be found automatically, it was found manually using Uniprot. The final list of gene-names was analysed manually and then split by known intracellular or extracellular location of the proteins. **Table 2.8** shows the bioinformatic tools used. The outputs from STRING (Szklarczyk et al., 2019) and GOrilla (Eden et al., 2009) tools were saved as JPEG files for visual interpretation. For Gorilla, the background protein list used was the entire list of proteins not significantly altered (341) from the TMT-based quantitative proteomics. FASTA sequences (retrieved from the National Centre for Biotechnology Information, https://www.ncbi.nlm.nih.gov/protein/) for each protein were analysed in InterProScan (Mitchell et al., 2019) using default settings. Protein domains with disulphide bonds or cysteine-rich regions were identified and results presented as mosaic plots made in R. This plot was also used to display the top 10 enriched molecular signatures from the GSEA database (Subramanian et al., 2005). Enrichment in gene sets from GSEA was displayed using GraphPad Prism 7.0. GOBO (Ringnér et al., 2011) was used to analyse the extracellular gene set in relation to breast cancer cell lines and Reactome (Fabregat et al., 2018) was used as a secondary pathway enrichment analysis tool; the visual outputs were saved for visual interpretation.

Table 2.8. *The bioinformatic tools used in this project*

Name	Abbreviation	Reference	Website
Gene Expression-Based Outcome for Breast Cancer Online	GOBO	Ringnér, Fredlund, Häkkinen, Borg, & Staaf, 2011 & Fredlund et al., 2012	http://co.bmc.lu.se/gobo/coexpressed_genes.pl
Gene Ontology enrichment analysis and visualization tool	Gorilla	Eden, Navon, Steinfeld, Lipson, & Yakhini, 2009	http://cbl-gorilla.cs.technion.ac.il/
Gene Set Enrichment Analysis	GSEA	Subramanian et al., 2005	http://software.broadinstitute.org/gsea/msigdb/index.jsp
InterProScan	-	Mitchell et al., 2019	https://www.ebi.ac.uk/interpro/
Reactome	-	Fabregat et al., 2018	https://reactome.org/
STRING	-	Szklarczyk et al., 2019	https://string-db.org/https://string-db.org/cgi/input.pl?sessionId=Bi6pWKQCy41F&input_page_active_form=multiple_identifiers

2.13 Replication of Experiments

Three independent experiments were carried unless otherwise stated. This included the control and technical repeats.

2.14 Statistical Analysis

All statistical significance tests were performed in GraphPad Prism 7.0 except for the proteomics experiments.

Immunoblots involving two conditions were analysed by unpaired Student's t.test.

For cell area plots and final spheroid area (at 50 hours) plots, data were analysed by two-way ANOVA with Tukey's multiple comparison post-hoc test.

For the rate of spheroid formation, reciprocal plots (Time vs. 1/Area) were prepared for the time period 20 to 50 hours. Multiple linear regression was performed to find the gradient of the line of best fit for each condition and the goodness of fit (R^2). This analysis was decided after consultation with Professor Green, a statistician at the University of Bristol.

Each protein abundance was normalised by log(2) transformation and a log(2)Mean and a log(2)Median was calculated. It was decided that because of the similarity between the log(2)Mean and the log(2)Median, and the high number of independent repeats (n=4), the statistical significance between protein abundance in the two experimental conditions could be calculated using a paired Student's t-test (paired because the control and 16F16 samples were pooled in the mass spectrometer). Analysis was only performed on proteins identified in all four repeats. Statistical testing and consultation was carried out by Dr. Phillip Lewis from Bioinformatics Support at the University of Bristol's Proteomics Facility.

Chapter 3 Results

3.1 The Role of PDIA3 in Promoting a Pro-Metastatic Phenotype

3.1.1 PDIA3 is present in MDA-MB-231 Cells

Before starting the investigations, it was confirmed whether PDIA3 is present in MDA-MB-231 cells (referred to hereafter as A231 cells) by use of immunoblot. Cell lysates and CM were prepared as described in the Methods **2.7**. Cells were grown for 48 hours in serum-free media with the addition of either DMSO or 5μM 16F16 at 0 hours. Previous experiments in this laboratory have shown that 5μM 16F16 induces phenotype changes in A231 cells without causing toxicity (H.S.Young, unpublished, 2018). All cells were grown in the presence of 50μM ascorbic acid. Ascorbic acid is an antioxidant and acts as a cofactor of prolyl-4-hyroxylase, an enzyme that catalyses the hydroxylation of proline in collagen's GXY triple helical sequence (Gly-Pro-Y is frequent) (Pihlajaniemi et al., 1991). Thus, addition of ascorbic acid promotes assembly of collagen molecules and thus collagen secretion and ECM assembly. A 48-hour timepoint was chosen to give time for global biochemical effects of PDIA3 inhibition to take place before collecting cell lysates or CM.

Immunoblots revealed a band at apparently 57kDa (**Figure 3.1A**), the expected molecular weight for PDIA3, in cell lysates of both control and 16F16-treated cells. PDIA3 protein abundance was lower in the 16F16 condition relative to DMSO-treatment, when PDIA3 abundance was normalised against GAPDH (35kDa) (**Figure 3.1B**). The graph may also give some insight into 16F16 induced toxicity showing less protein in 16F16 treated samples, but this would need to be tested with replicate experiments. PDIA3 was not detected in the CM in either condition.

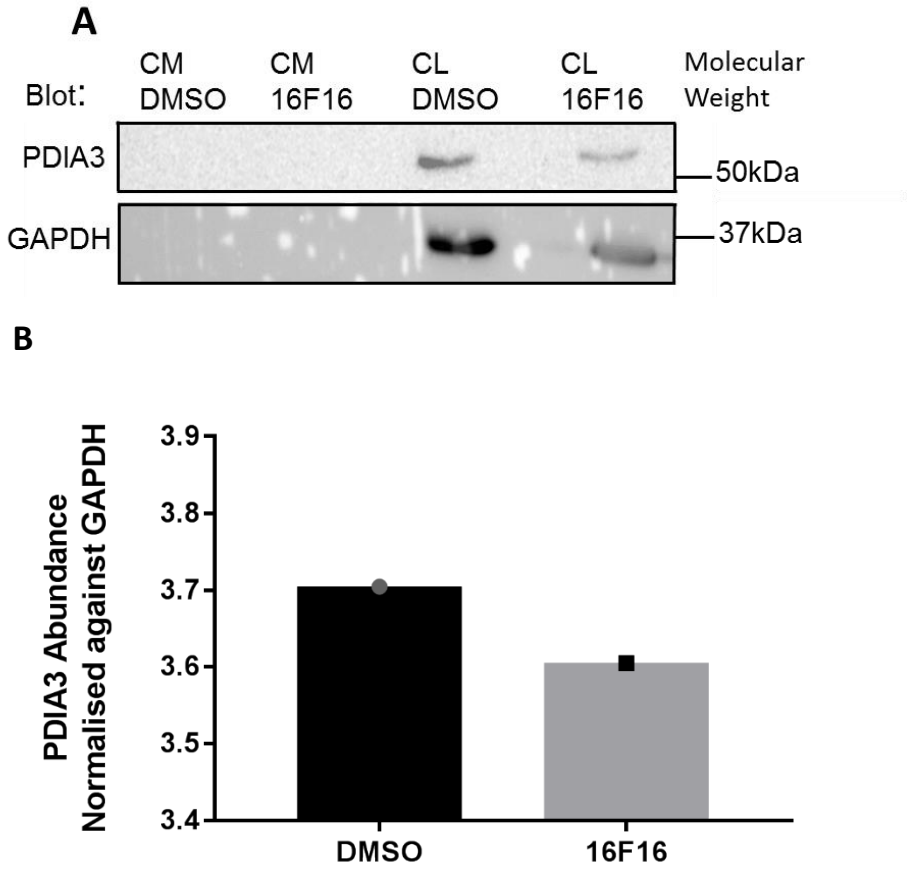

Figure 3.1. ***Presence of PDIA3 in MDA-MB-231 cells.*** *(**A**) Proteins were separated on a 10% polyacrylamide gel under reducing conditions, transferred to a PVDF membrane and probed with antibodies to PDIA3 or GAPDH. n=1 experiment. Key: CL: Cell Lysate, CM: Conditioned Media. (**B**) Automated quantification using Synegene GeneTools© of bands for PDIA3 normalised against loading control GAPDH.*

3.1.2 Fibronectin is a Target of PDIA3 and Present in MDA-MB-231 Conditioned Media

Some of PDIA3's known substrate glycoproteins are destined for secretion to the ECM, including important structural glycoproteins such as fibronectin and collagen VI (Jessop et al., 2007b). We hypothesised that a change in PDIA3's redox activity would alter the ECM of A231 cells by affecting secretion of some of these proteins. To validate that the concentration of 16F16 used was effective against the known substrate fibronectin in A231 cells, PDIA3 was inhibited by 16F16 and fibronectin protein abundance in the CM was analysed by immunoblot.

The immunoblot showed a band at around 220kDa for fibronectin in the control condition (treated with DMSO) and no band in the CM treated with 16F16 (**Figure 3.2**). This result was reproduced in two experiments (**Figure 2A**, experiments 1 and 2), but not in a third experiment (**Figure 2A**, experiment 3) where CM treated with 16F16 showed a small band at 220kDa for fibronectin. In every sample the fibronectin band was diffuse which is typical as fibronectin is heavily glycosylated. A limitation of the blots of CM is that an internal normalisation control could not be used as the protein concentration of the samples were too low to produce clear bands by Ponceau S stain. Therefore, for quantitation, fibronectin abundance in CM was compared between control and 16F16 conditions. The means of each condition were compared using an unpaired Student's t-test and this showed that the abundance of fibronectin was not significantly different between the CM treated with DMSO and the CM treated with 16F16. Bands were not normalised using GAPDH, since GAPDH was only present in cell lysates it cannot be assumed that its protein abundance would be proportionate to fibronectin in the CM. The results showed that 5μM of 16F16 decreased secretion of a known PDIA3 target, fibronectin, in A231 cells.

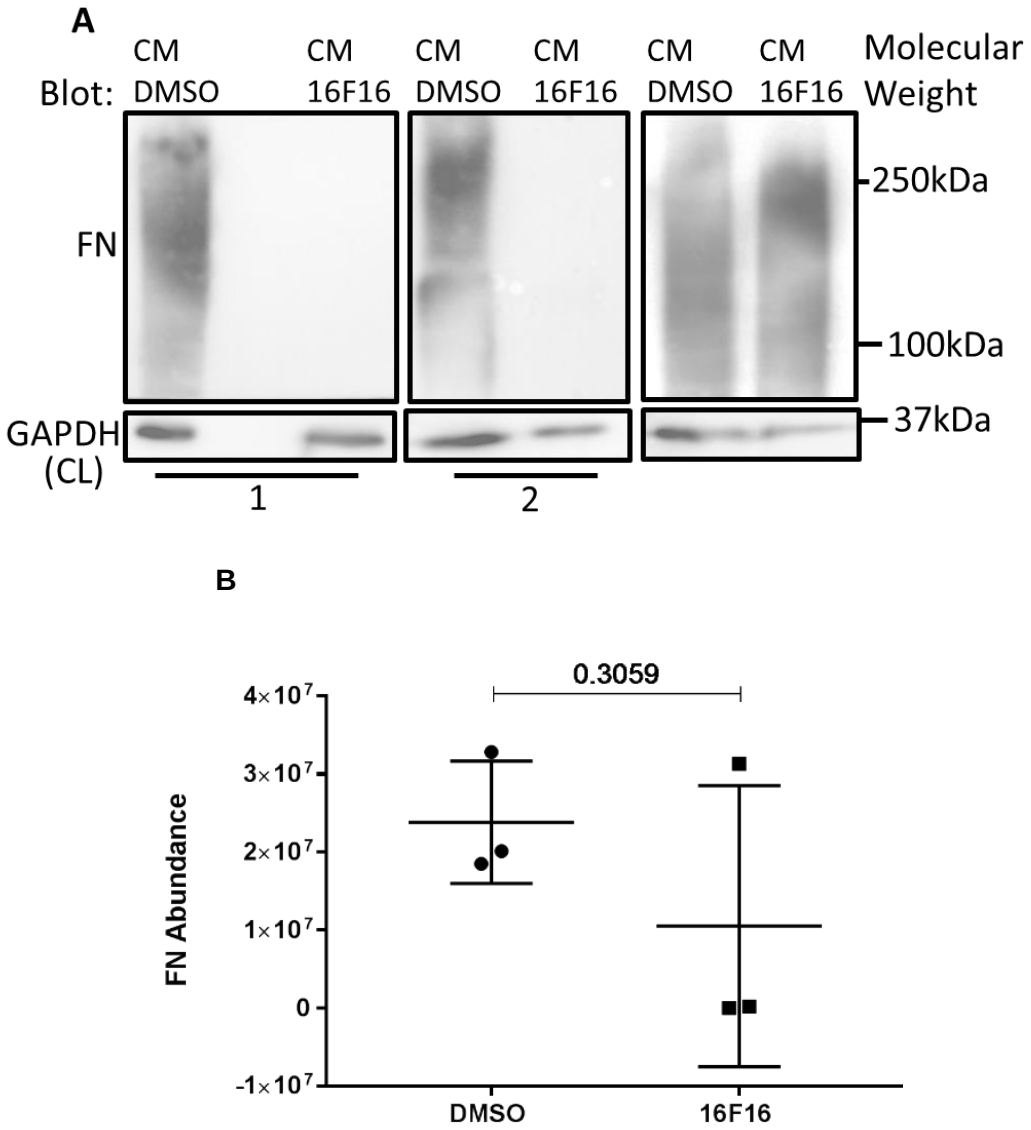

Figure 3.2. ***Effect of PDIA3 Inhibition on Fibronectin (FN) Abundance in the CM of MDA-MB-231 Cells.*** *(**A**) Immunoblot of cell lysates and conditioned media after treatment with 5μM 16F16 or equivalent volume of DMSO. Samples were resolved on a 10% polyacrylamide gel under reducing conditions, transferred to PVDF membrane and blotted for the indicated proteins. Automated quantification using Synegene GeneTools© bands for fibronectin for (**B**) all three independent repeats. Key: CL: Cell Lysate, CM: Conditioned Media.*

3.1.3 Assessment of Cell Spreading and F-Actin Organisation

It has been reported that in culture highly metastatic cells have a larger area that their counterparts (Shen et al., 2012). Previous research in the Adams laboratory (Hellewell.et.al., manuscript in preparation & Young, unpublished, 2018) has shown that pharmacological inhibition of PDIA3 in breast cancer cells (including A231 cells) and in fibroblasts, leads to an altered cell morphology and reduced cell spreading. This effect has been shown to depend on secreted proteins (Introduction **1.7**).

In this project, the effects of a PDIA3-dependent secreteome on the morphology and attachment of A231 cells was analysed by fluorescence microscopy methods. The CM was prepared by from A231 cells by incubating $1.5x10^6$ cells in serum-free media (FGM) for 48 hours after treatment with either 5µM 16F16 or equivalent volume of DMSO at 0 hours. All 2-dimensional cell-based assays were performed in FGM because as well as being a well-defined serum-free medium, it has been consistently used for inhibitor-based experiments involving breast cancer cells and fibroblasts in Professor Adams' Laboratory. Serum-free medium was also used to avoid including serum proteins in the CM. It was hypothesised that 48 hours was enough time for global effects of 16F16 in view of the result with fibronectin. Also, in 48 hours nutrients would not become too depleted or possible effects on cell toxicity high. To examine the impact that CM alone may have on A231 cells, a third condition was included using only fresh FGM. Next, $2.5x10^5$ naïve recipient cells were plated onto glass coverslips and exposed separately to each of the three different serum-free CM conditions. The cells were left for 4 or 20 hours to attach and spread. Two time points were used to give an indication of whether the secreted products of the naïve A231 cells could overcome the effects of an PDIA3-inhibited CM at 20 hours. At each time point, cells were fixed and stained with phalloidin to visualise the F-actin cytoskeleton or with antibody to vinculin to visualise focal adhesions (Methods **2.9**). The different outputs of these experiments are detailed in the separate following sections.

3.1.3.1 The Effect of a PDIA3-dependent Secretome on F-actin Organisation

Naïve A231 cells plated in fresh-FGM for both 4 and 20 hours showed a typical migratory A231 breast cancer cell phenotype with bright F-actin at the leading edges of the cells. Also visible were mesh-like lamellipodia and F-actin stress-fibers extending throughout the cells (**Figure 3.3** & **Figure 3.4**). The A231 cells plated in CM from cells that had been treated with DMSO had also strong F-actin arrays at leading edges and phenotypic features consistent with a migratory phenotype at both 4 and 20 hours (**Figure 3.3** & **Figure 3.4**).

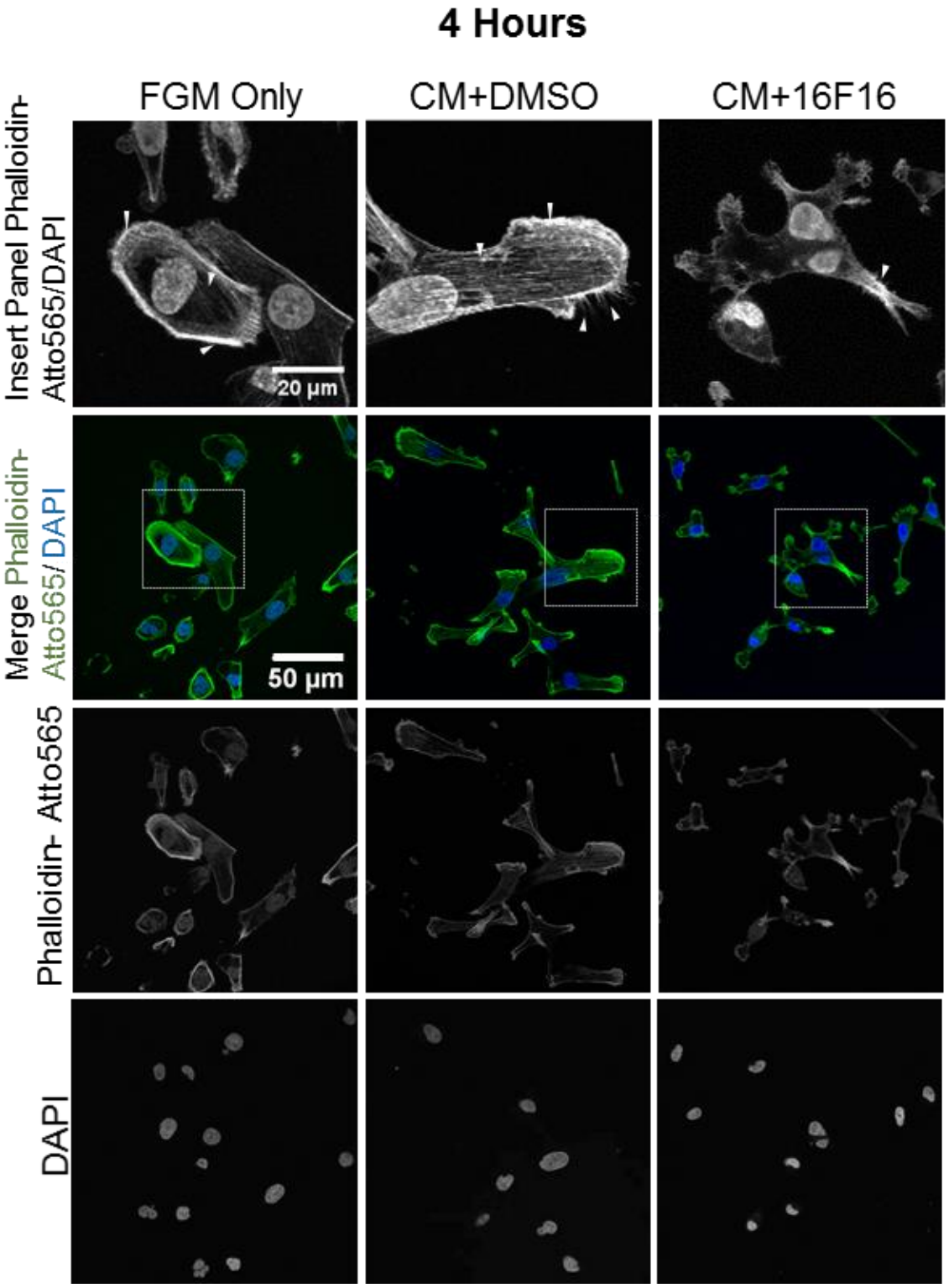

Figure 3.3 ***F-actin localisation in MDA-MB-231 Cells Plated in CM from Cells Treated with 5µM 16F16 or DMSO for 48 hours.*** *Cells were fixed 4 hours after plating with respective media and stained with Phalloidin-Atto565 to visualize F-actin.* ***Top Row*** *displays higher magnification of the boxed area from* ***Second Row*** *(63x frame), to show details. Confocal Images are displayed as Maximum Intensity Z-Projection. Representative of 3 independent experiments.*

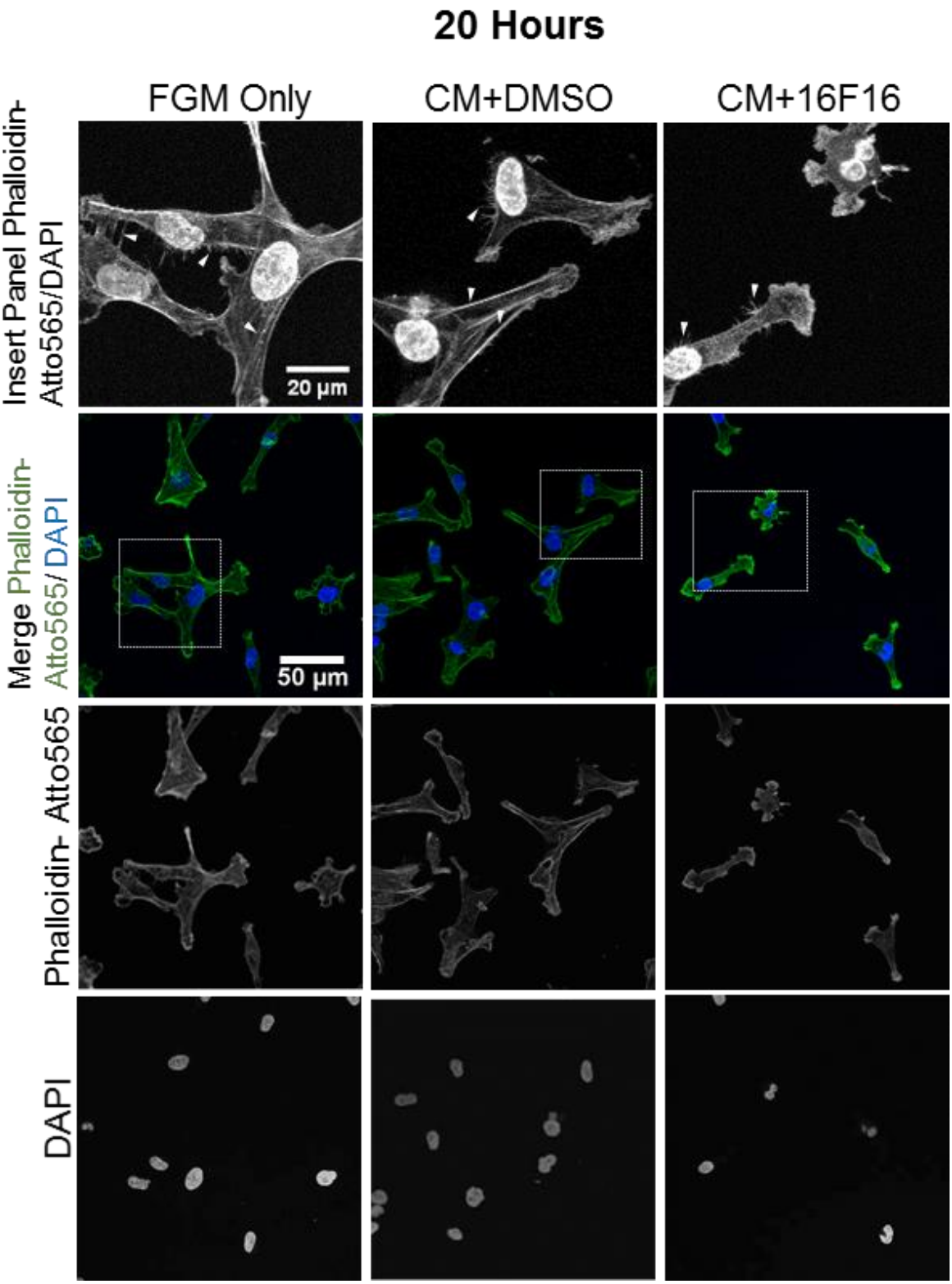

Figure 3.4. ***F-actin Localisation in MDA-MB-231 Cells Plated in CM from Cells Treated with 5µM 16F16 or DMSO for 48 hours.*** *Cells were fixed 20 hours after plating with respective media and stained with Phalloidin-Atto565 to show F-actin organisation.* ***Top Row*** *displays higher magnification of the boxed area from* ***Second Row*** *(63x frame). Confocal Images are displayed as Maximum Intensity Z-Projection. Representative of 3 independent experiments.*

However, cells plated in CM from 16F16-treated cells did not display F-actin stress fibers and overall appeared to have smaller areas. After 4 hours of incubation with CM from cells treated with 16F16, cells did not display the distinct networks of bright F-actin that indicate lamellipodia (**Figure 3.3**). After 20 hours of incubation, the A231 cells showed lamellipodia but these were not as extensive or as numerous as in the A231 cells plated in fresh-FGM or CM from cells treated with DMSO (**Figure 3.4**).

3.1.3.2 The Effect of a PDIA3-Dependent Secretome on Area of MDA-MB-231 Cells

To quantify cell areas, the images of phalloidin-stained cells were imported to ImageJ and cell areas measured. As many cells were measured as possible in each experiment; within the image frames collected, the only reasons a cell was not measured was because it overlapped so heavily with another cell its boundaries were hard to identify, or it was undergoing cell division. The plot of cell areas is shown in **Figure 3.5.**

At the 4 hour timepoint, the mean cell area of naïve A231 cells plated in CM from cells treated with DMSO was not statistically difference from the mean area of cells plated in fresh FGM. However, after 20 hours of adhesion, the mean cell area in these conditions was significantly different (**Figure 3.5**).

At 4 hours and at 20 hours, the mean cell area of cells plated in CM from 16F16-treated cells was significantly different from either cells plated in fresh FGM or cells in CM from DMSO-treated cells (**Figure 3.5**).

Thus, A231 cells plated in CM from cells treated with 16F16 had a reduced ability to spread. Analysis by immunofluorescence (**3.1.3.1**) revealed that these cells had a reduced number of F-actin stress fibers, lamellipodia, or other features of a migratory breast cancer phenotype. Collectively, these results suggest that PDIA3-dependent proteins secreted to the medium support the cell spreading and F-actin organisation of A231 breast cancer cells.

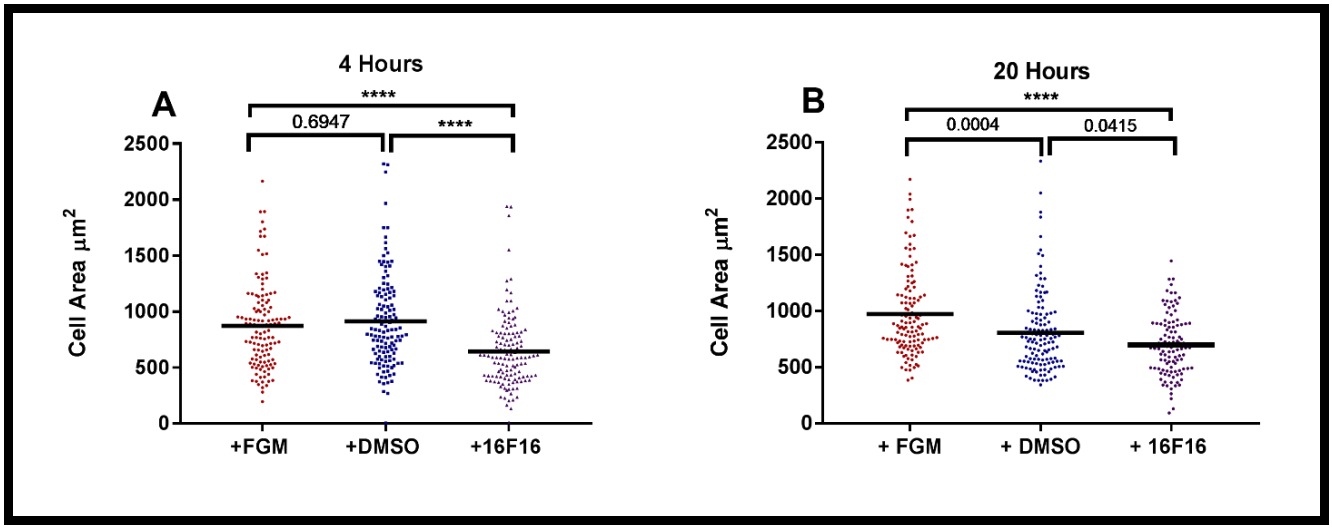

Figure 3.5. ***Quantified Comparison of MDA-MB-231 Cell Areas after Plating in CM of Cells Treated with 5µM 16F16 or Equivalent Volume of DMSO for 48 hours.*** *Cells were fixed after 4 hours (A) or 20 hours (B) adhesion. Dot plots show the cell areas; mean value (**black line**). Areas were measured from confocal Maximum Intensity Z-Projections of phalloidin-stained cells. Cell areas are from 3 independent experiments with at least 30 cells measured per condition per experiment.*

3.1.4 Assessment of Focal Adhesions

Another aspect of a migratory phenotype is the localisation of proteins that link the actin cytoskeleton via integrins to the ECM. Focal adhesions include assemblies of proteins that are mechanosensory, they transduce force from either side of the plasma membrane to elicit movement (Introduction **1.5.2**). An important protein of focal adhesions is vinculin (Harris et al., 2018). Vinculin was stained for by immunofluorescence as another indicator of the adhesive status of the cells. A231 cells and images were prepared as described in Methods **2.7** & **2.10**. The images presented are from a single experiment due to time constraints.

Naïve A231 cells plated in fresh FGM for 4 or 20 hours showed vinculin faintly distributed throughout the cytoplasm and more concentrated at the leading edges of cells. In A231 cells plated with CM from cells treated with DMSO, vinculin was found throughout the cells but not clearly concentrated at the leading edges after 4 hours. After 20 hours vinculin was strongest around the leading edges (**Figure 3.7**). In A231 cells plated in CM from cells treated with 16F16, vinculin staining was very low throughout cells at the 4-hour timepoint with no concentration of staining at cell edges. At 20 hours there was little vinculin localised to focal adhesions (**Figure 3.6** & **Figure 3.7**). Thus, the A231 cells plated in CM from cells treated with 16F16 showed less vinculin localised to focal adhesions. This suggests that cells plated in CM from cells treated with 16F16 have limited capacity to assemble focal adhesions compared with cells plated in control CM.

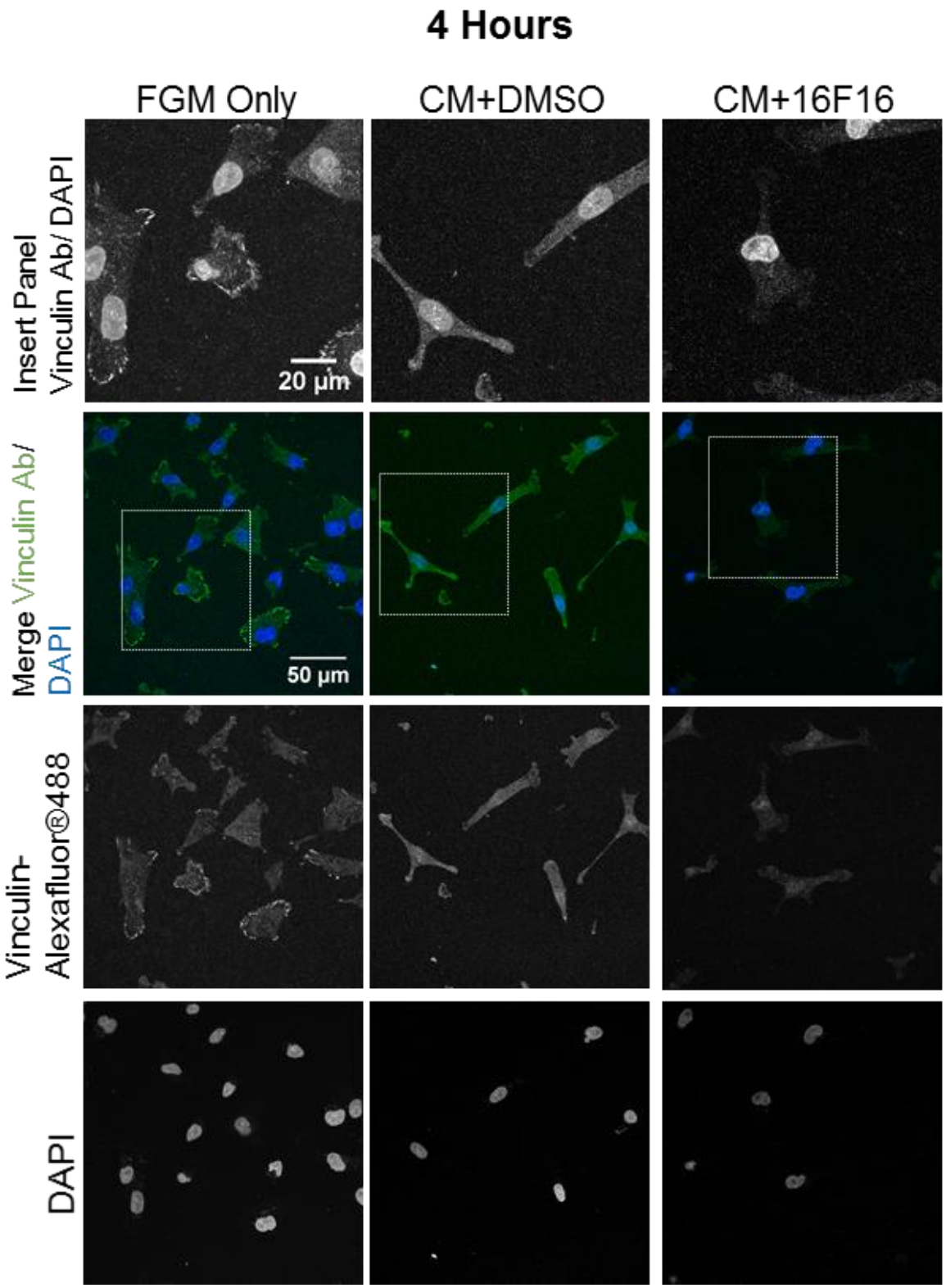

Figure 3.6. ***Vinculin Localisation in MDA-MB-231 Cells Plated in CM from Cells Treated with 5µM 16F16 or Equivalent Volume of DMSO for 48 hours.*** *Cells were fixed 4 hours after plating with respective media and stained for vinculin.* ***Top Row*** *displays higher magnification of the boxed area from* ***Second Row*** *(63x frame). Confocal images are displayed as Maximum Intensity Z-Projection. From one experiment.*

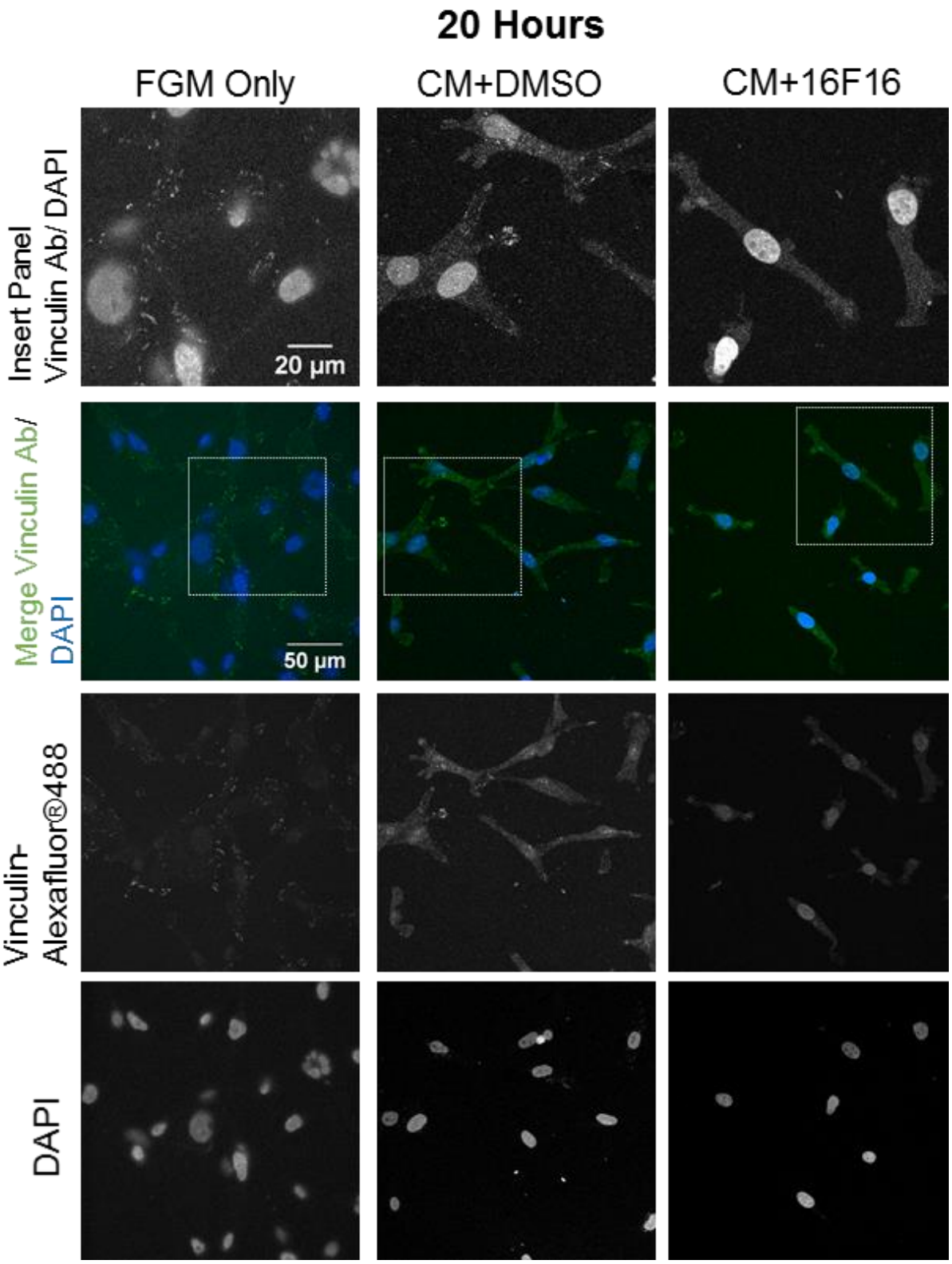

Figure 3.7. ***Vinculin Localisation in MDA-MB-231 Cells Plated in CM from Cells Treated with 5μM 16F16 or Equivalent Volume of DMSO for 48 hours.*** *Cells were fixed 20 hours after plating with respective media and stained for vinculin.* ***Top Row*** *displays higher magnification of the boxed area from* ***Second Row*** *(63x frame). Confocal Images are displayed as Maximum Intensity Z-Projection. From one experiment.*

3.2 Examination of the Effect of 16F16 on Endoplasmic Reticulum Stress in MDA-MB-231 Cells

It is well established that if misfolded proteins accumulate in the endoplasmic reticulium (ER) an unfolded protein response (UPR) is triggered (Ojha and Amaravadi, 2017). Misfolded proteins can build up during adverse conditions in pH, temperature, oxygen and nutrience levels. The UPR affects global translation and protein abundance: proteins that are particularly upregulated during UPR are those involved in protein folding or chaperone function because PDIA3 is an ER-resident oxidoreductase that adds disulphide bonds into proteins. Inhibiting PDIA3 with 16F16 might increase missfolded proteins in the ER and cause an UPR (Rellmann and Dreier, 2018; Yoo et al., 2019). If this is the case, phenoptypic changes seen when using 16F16 could be due to an elevated UPR. Therefore, immunoblotting was used to analyse A231 cells that had been pre-treated with 5µM 16F16 or DMSO for 48hours as described in **3.1.1**. Binding immunoglobulin protein (BiP) was used as a proxy for UPR. BiP is a molecular chaperone residing in the ER that is upregulated during an UPR (Sano and Reed, 2013). Three independent repeats were carried out and BiP bands were normalised against GAPDH to quantify protein abundance (**Figure 3.8**). BiP was detected in control cells and no significant difference in BiP abundance was found between the lysates from DMSO or 16F16-treated A231 cells ($p=0.8479$). The equal abundances of BiP suggest that UPR is not activated by these conditions of 16F16 treatment. This shows that the observed phenotypic differences of cells upon 16F16 treatment are not due to an elevated UPR.

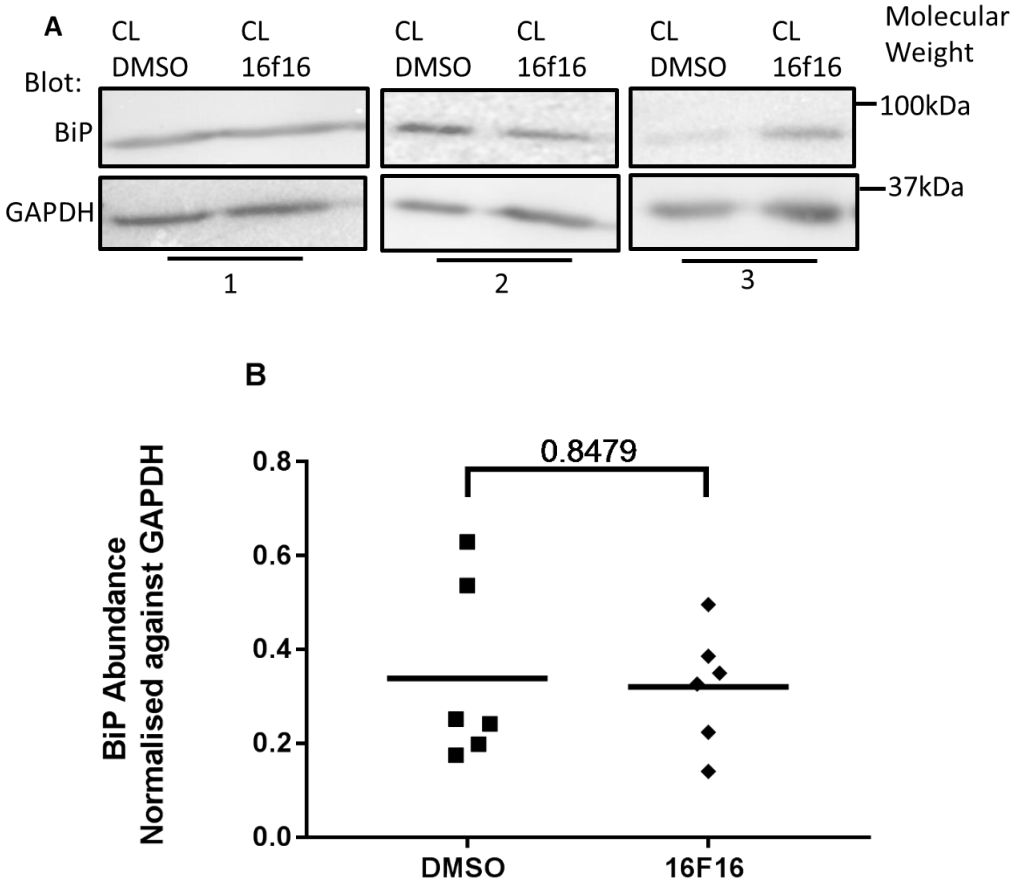

Figure 3.8. ***Assessment of ER Stress in MDA-MB-231 Cells****. (**A**) Immunoblots of A231 cell lysates and conditioned media after treatment with 5μM 16F16 or equivalent volume of DMSO. Samples were resolved on a 10% polyacrylamide gel under reducing conditions, transferred to a PVDF membrane and blotted for the indicated proteins. Key: CL: Cell Lysate, CM: Conditioned Media. (**B**) Automated quantification of BiP band intensities normalised against GAPDH loading control. Black bar shows mean abundance. From n=3 experiments.*

3.3 The Role of Heparin-Binding Secreted Proteins in MDA-MB-231 Cell Adhesion

3.3.1 Assessment of Cell Spreading and F-Actin Organisation

Previous experiments in the laboratory with mouse embryonic fibroblasts (MEF) have identified secreted, PDIA3-dependent, heparin-binding proteins (HBP) to be functionally important for adhesion and spreading (Hellewell et.al., manuscript in preparation). Because many ECM proteins or cytokines contain heparin-binding domains, heparin-affinity binding is a convenient way to isolate these proteins from CM. The experiments described in **3.1.2** and **3.1.3** showed that PDIA3-dependent secreted proteins have a role in promoting the spreading and F-actin organisation of A231 cells. To examine the contribution of secreted HBP, CM from A231 cells was examined on naïve A231 cells. $2.5x10^5$ A231 cells were plated in fresh FGM or CM prepared as in **3.1.2**, but this time the control CM was compared with CM depleted for HBP. HBP were depleted from the CM by an hour-long pre-incubation with high affinity heparin-agarose beads. At the end, CM was centrifuged to pellet the heparin-agarose beads with associated HBP. Evidence that this procedure results in effective binding of proteins to the heparin-agarose beads will be provided in the proteomics section of the results (**3.4**). The HBP-depleted CM were then added to naïve A231 cells, whilst the pellet that contained the HBP was discarded. Control CM was prepared by pre-incubation with plain-agarose beads, to control for proteins in the CM that may bind non-specifically to agarose-beads and processed in the same way as for the CM without HBP. The fresh A231 cells were plated under the various conditions for either 4 or 20 hours, and cell morphologies examined by staining for F-actin. A231 cell phenotypes were analysed as described in **3.1.3.** The experiments are described below.

3.3.2 The Role of Secreted Heparin-Binding Proteins in F-actin Organisation

From the fluorescent images, the A231 cells plated in fresh FGM for 4 hours displayed classic ‘kite’ shaped morphologies of migratory cells. The cells displayed F-actin-rich leading edges with a dense mesh-network of actin-like lamellipodia. Clear F-actin bundles were seen that spanned the cells; these are typical of F-actin stress fibres. Naïve A231 cells plated for 20 hours in fresh FGM displayed the same F-actin phenotypes (**Figure 3.10**). Likewise, the naïve A231 cells plated in control CM for 4 hours showed strong F-actin leading edges and an abundance of F-actin stress fibers and lamellipodial actin networks (**Figure 3.9**). These F-actin phenotypes were also seen in naïve A231 cells plated in control CM for 20 hours. Overall, these results suggest that in fresh-FGM and control CM, naïve A231 cells display a typical migratory phenotype, as seen in the previous experiment (**3.1.2**).

In general, A231 cells plated for 4 hours in CM depleted of HBP displayed fewer of the F-actin structures associated with a migratory phenotype. The A231 cells appeared much smaller. As shown in detail in the Insert Panel, F-actin appeared mostly more diffuse throughout the cells with little concentration of F-actin at cell boundaries. The Insert Panel (bottom right) shows one cell with F-

actin stress fibers (**Figure 3.9**). At the 20 hour timepoint, A231 cells plated in CM depleted for HBP appeared more spread. The F-actin generally appeared more diffuse than in cells plated in the control conditions. A231 cells plated in CM without HBP also had fewer F-actin stress fibres spanning the cells and limited evidence of lamellipodia network on the edges of the cells (**Figure 3.10**)**.**

Thus, the depletion of HBP from CM of A231 cells appeared to reduce A231 cell spreading and the organisation of F-actin. This effect on F-actin was most clear at the 4-hour timepoint and was less clear at 20 hours.

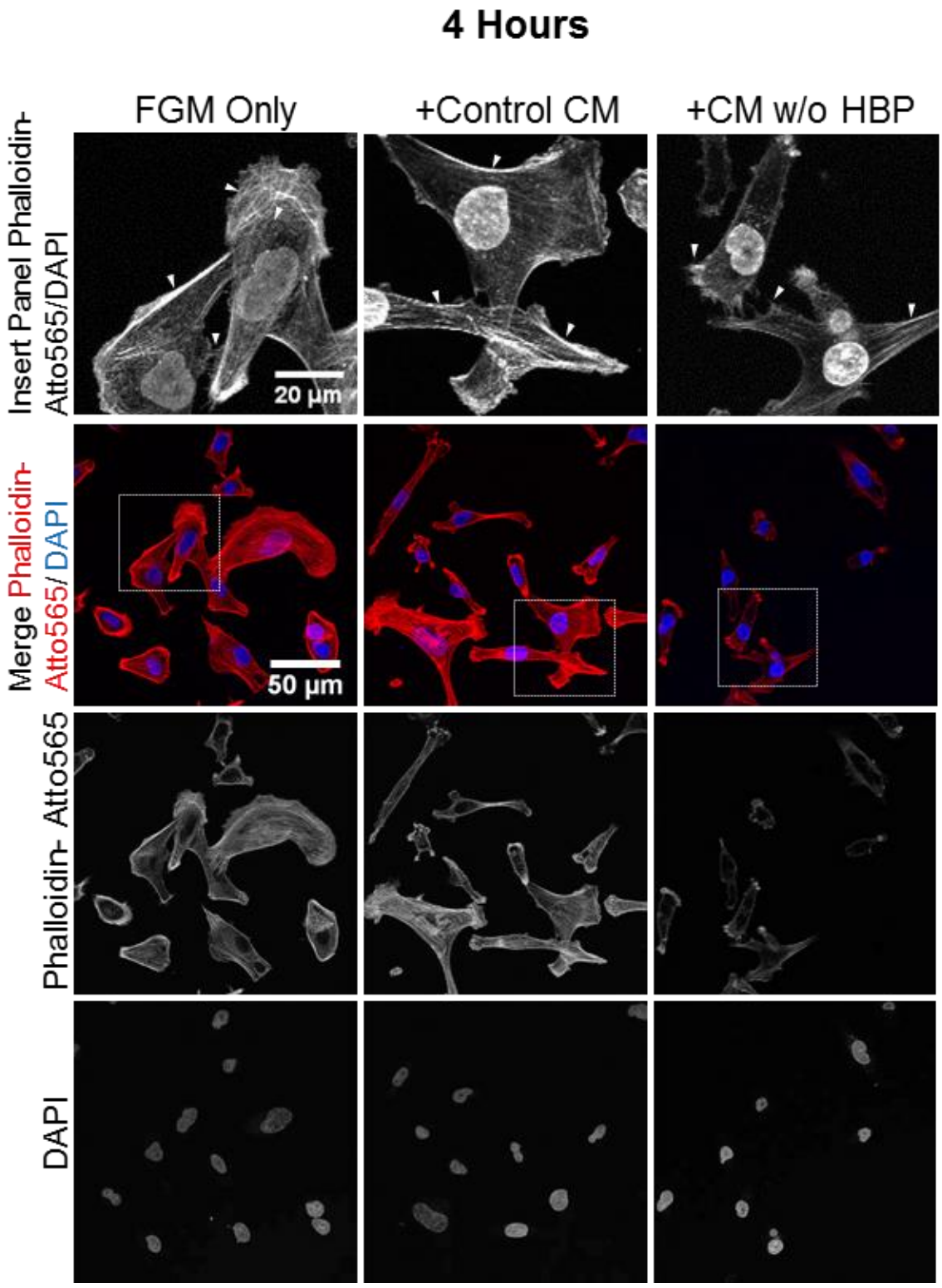

Figure 3.9. ***F-actin Localisation in MDA-MB-231 Cells Plated in Control CM, CM without Heparin-Binding Proteins (w/o HBP) or Fresh FGM for 4 hours.*** *Cells were fixed after 4 hours stained with Phalloidin-Atto565 to show F-actin organisation.* ***Top Row*** *displays higher magnification of the boxed area from* ***Second Row*** *(63x frame). Confocal Images are displayed as Maximum Intensity Z-Projections. Representative of 3 independent experiments.*

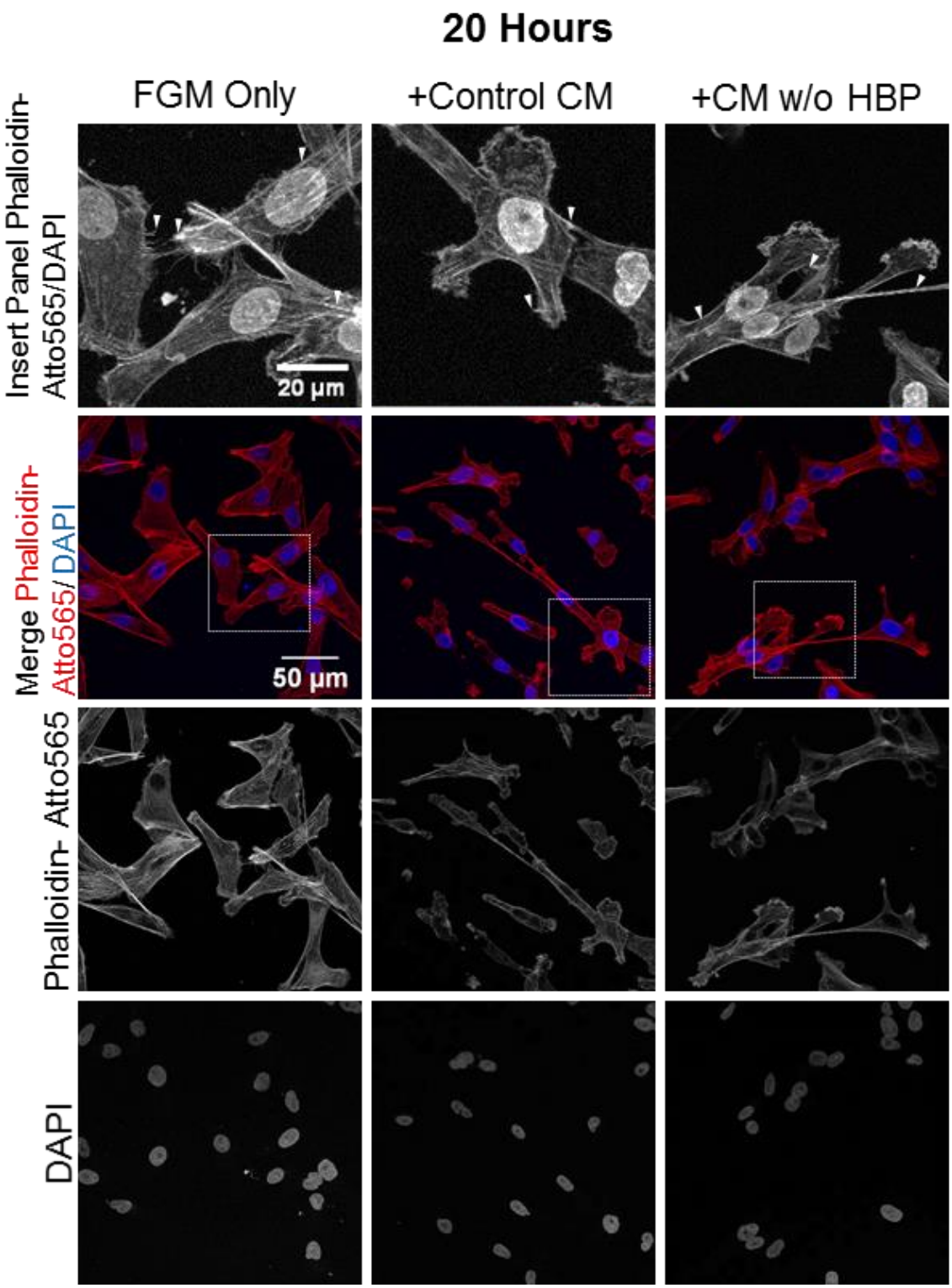

Figure 3.10. F-actin Localisation in MDA-MB-231 Cells Plated in Control CM, CM without Heparin-Binding Proteins (w/o HBP) or Fresh FGM for 20 hours. *Cells were fixed after 20 hours and stained with Phalloidin-Atto565 to show F-actin organization. Top Row displays higher magnification of the boxed area from Second Row (63x frame). Confocal Images are displayed as Maximum Intensity Z-Projection. Representative of 3 independent experiments.*

3.3.3 The Effect of Depletion of Heparin-Binding Proteins on MDA-MB-231 Cell Area

Images from the above experiments were also used to quantify effects of depleting HBP on cell areas, as in **3.1.3**. The quantification of cell areas for each condition is presented in **Figure 3.11**.

The data showed that the mean cell areas of A231 cells were not significantly different when plated in fresh FGM or control CM, either at 4 hours or 20 hours. In contrast, the A231 cells plated in CM depleted of HBP had reduced cell areas and this reduction in cell area was significantly different from that of cells plated in control CM or fresh FGM. This difference was consistent at 4 and 20 hour plating times.

Overall, the results show that when CM is depleted of HBP it has reduced activity to stimulate cell spreading in A231 breast cancer cells. Thus, the presence of HBP in the CM promotes A231 cell spreading (**3.3.2**).

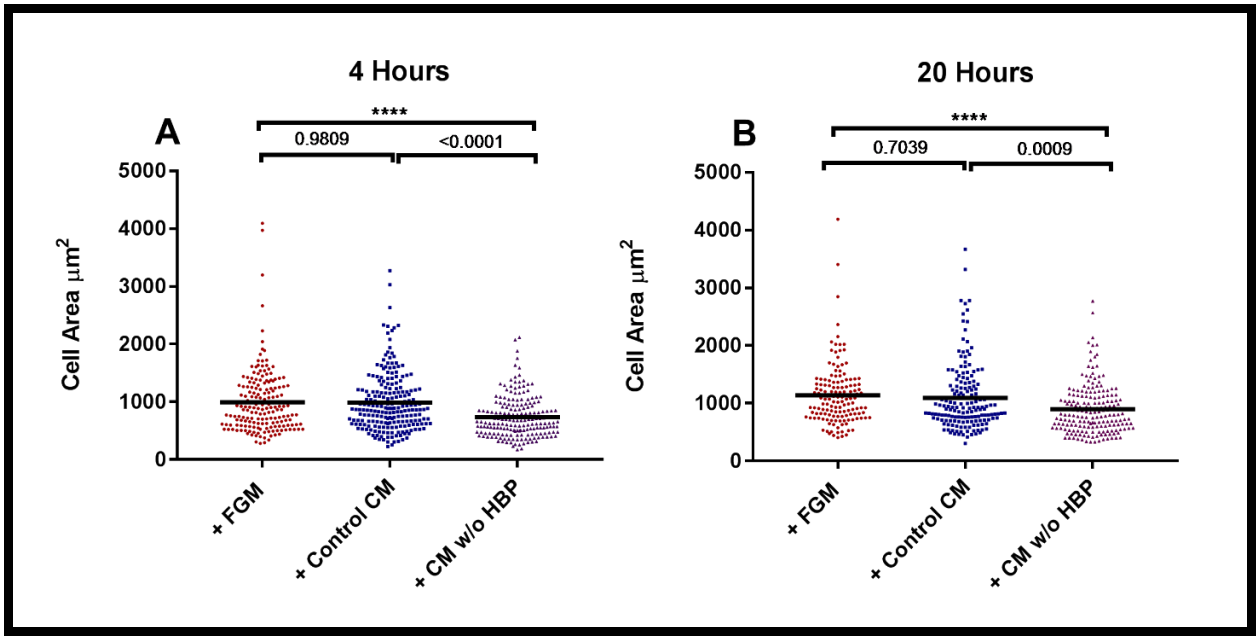

Figure 3.11. ***Quantified Comparison of MDA-MB-231 Cell Areas After Plating for 4 hours (A) or 20 hours (B) in CM Depleted for HBP.*** *Dot plots shows the cell areas;* ***black line*** *the mean values. Areas were quantified from confocal Maximum Intensity Z-Projection images. Cell areas are taken from 3 independent experiments with at least 30 cells measured per condition per experiment.*

3.4 Analysis of the PDIA3-Dependent Secretome of MDA-MB-231 Cells by TMT-Based Quantitative Proteomic

As shown in section **3.1** and **3.3,** analysis by immunofluorescence after treatment of naïve A231 cells with A231 CM, showed that secreted PDIA3-dependent proteins or secreted heparin-binding proteins each had activity to promote cell spreading and pro-migratory organisation of F-actin. The next line of investigation sought to identify what heparin-binding proteins are in the PDIA3-dependent secretome.

Identification of proteins was carried out by TMT-based quantitative proteomics on serum-free conditioned media (CM) from A231 cells. However, TMT-proteomics requires a more concentrated protein sample than CM itself can provide. To concentrate the secreted proteins, only the heparin-binding fractions of the CM was used in TMT-proteomics. As explained in **3.3,** the heparin-binding proteins (HBP) from the CM of A231 cells was shown to have activity to promote spreading and F-actin organisation in naïve recipient cells. Based on previous experiments on fibroblasts (Hellewell et.al., manuscript in preparation), it is likely that proteins in the PDIA3-dependent secretome include heparin-binding proteins and so the heparin-binding fraction of the A231 CM would be enriched for the PDIA3-dependent proteins that can promote cell spreading and a migratory phenotype. The heparin-binding fraction of CM was used in TMT-proteomics, by binding proteins to high affinity heparin-agarose beads as in section **3.3**.

CM was prepared as described as in Methods **2.7.2**, but at larger scale to produce 32ml of each CM. The use of serum-free media was to avoid the complexity of having heparin-binding proteins from foetal calf serum included in the analysis, as stated in **3.1.1**. In addition, non-specific agarose-binding proteins were removed from CM by a first incubation with plain (unconjugated) agarose beads. Extra precaution was taken to very thoroughly wash cells in serum-free medium after trypsinisation to remove FBS and any other contaminants. Each CM was also filtered through a 0.45µm Stericup-HV Sterile Vacuum Filtration System to remove all cell debris that had not been removed during washing of cells. The full protocol is given in Methods **2.11.2**. The final heparin-bead affinity sample were resuspended in SDS-PAGE sample buffer with 100mM DTT and then prepared for TMT-proteomics (Methods **2.11.3**). Four independent repeated experiments were carried out. Each pair of control and test samples were run as a pair in the LCMS using an Orbitrap Fusion Tribrid mass spectrometer (Methods **2.11.3**).

From the lists of proteins identified (by at least 1 unique peptide per protein) in each experiment, the proteins identified in all four biological repeats were pooled and a paired Student's t.test was used to compare each protein's abundance in the DMSO and 16F16 conditions (**Appendix I**) and then the significance was normalised ($-\log_{10}$p.value) around zero. Change in protein abundance was considered significant for ±2-fold difference. A total of 345 proteins were identified to be PDIA3-dependent and 107 of these proteins were statistically significantly less abundant in the PDIA3-

inhibited condition ($p \leq 0.05$ and at least 2-fold decrease in abundance). There were no proteins that increased significantly in the CM of cells treated with 16F16 (**Figure 3.12**).

The proteins were then filtered to those with a significant false discovery rate of under 0.05 ($q \leq 0.05$). It was important to remove proteins that could be false positives to improve reproducibility. This left 80 proteins that were decreased by at least 2-fold in the CM of cells treated with 16F16, here collectively termed the PDIA3-dependent, heparin-binding secretome. The names of genes encoding the 80 proteins are displayed in **Figure 3.13.**

The 80 reproducible and significantly decreased proteins (filtered protein dataset) were then split by their subcellular location according to UniProt's curated database. In total there were 48 extracellular proteins, 30 intracellular proteins and two proteins that are both intracellular and extracellular (**Figure 3.14**). The proteins found in both subcellular locations were treated for further analysis as intracellular proteins.

It was also examined whether any of the 80 proteins are known HBP or known PDIA3 substrates. 12 of the proteins were known to be heparin-binding and 4 are known substrates of PDIA3 (**Table 3.1**). The 48 extracellular proteins were then split by function according to UniProt. They covered a variety of functions, the most numerous being structural ECM (**Figure 3.15**).

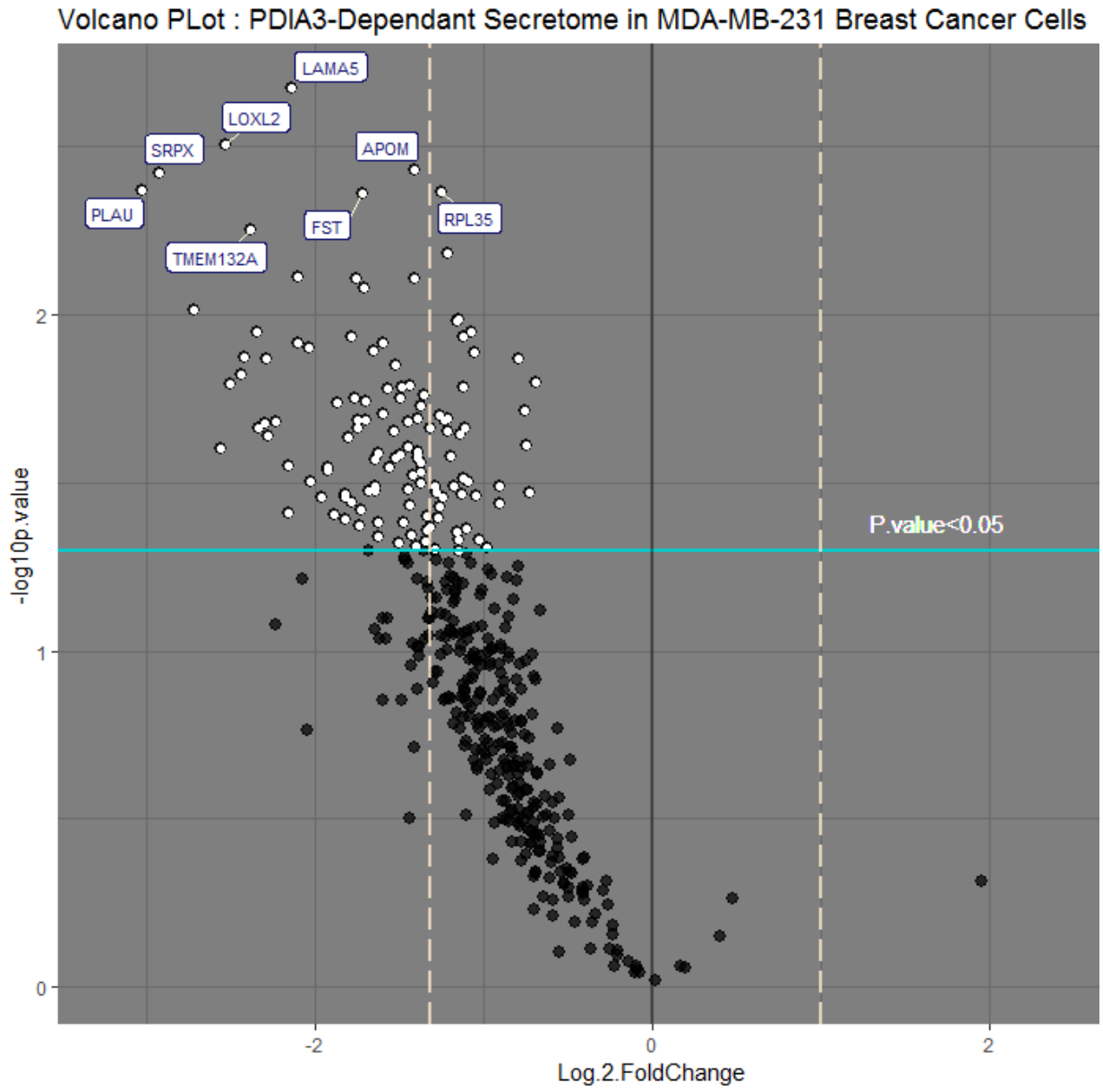

Figure 3.12. ***PDIA3-Dependent, Heparin-Binding Secreted Proteins of MDA-MB-231 Breast Cancer Cells.*** *Cells were treated with either 5µM 16F16 or equivalent volume of DMSO and the heparin-binding fractions of the CMs collected for TMT-Base Quantitative Proteomic Analysis. Dashed vertical lines represent ±2-fold change, vertical green line represents P=0.05 and vertical black line marks 0-fold change. White points represent the 107 proteins with a p-value significance over p≤0.05. Results pooled from four independent repeats. Gene names are given for the most significantly decreased proteins*

.

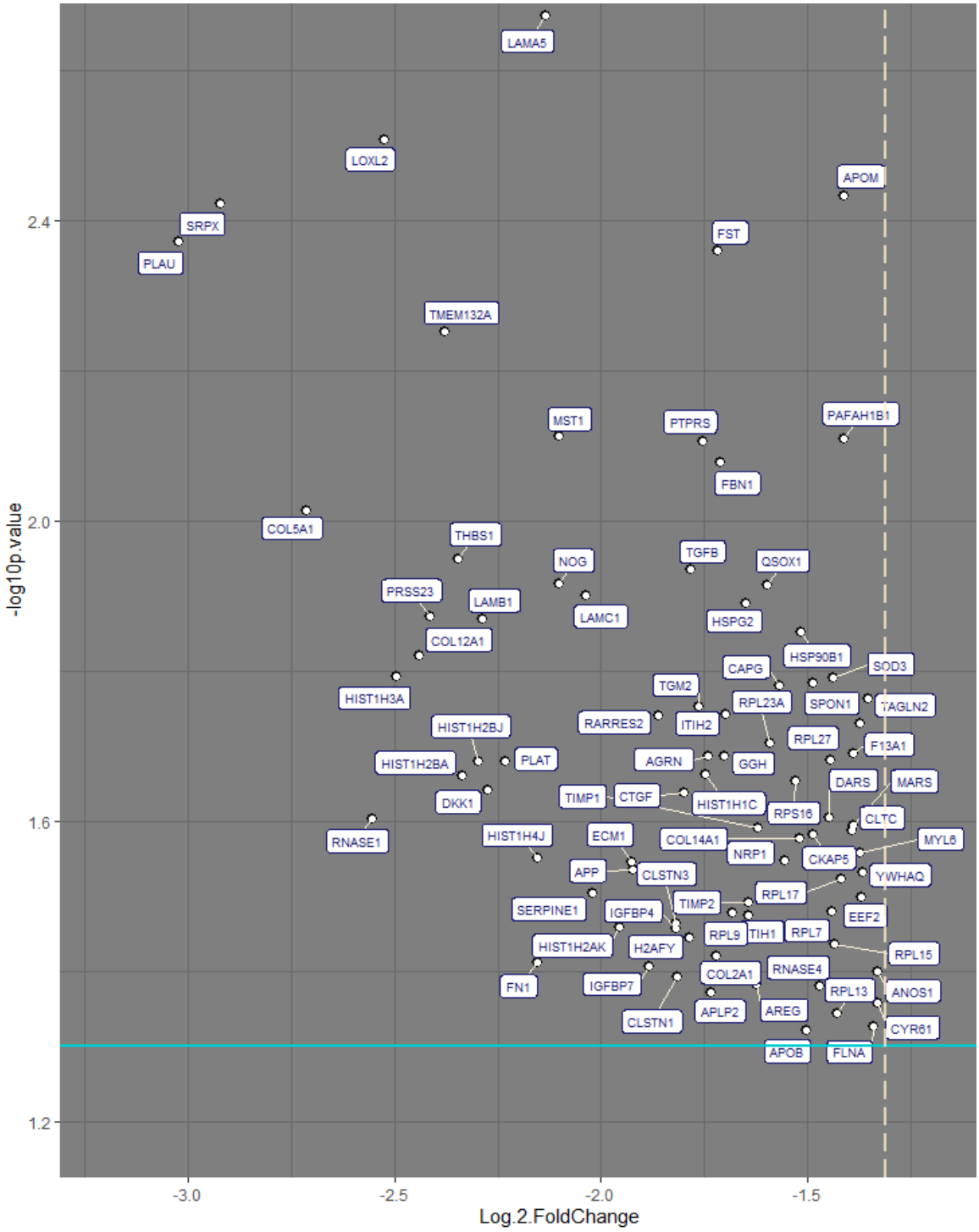

Figure 3.13. ***Zoom in of Volcano Plot: The 80 Proteins Significantly Decreased in the PDIA3-Dependent, Heparin-Binding Secretome.*** *Enlarged area of Figure 3.12 to show gene name for all the proteins decreased significantly (p≤0.05) by at least 2-fold. Results compiled from four independent repeats.*

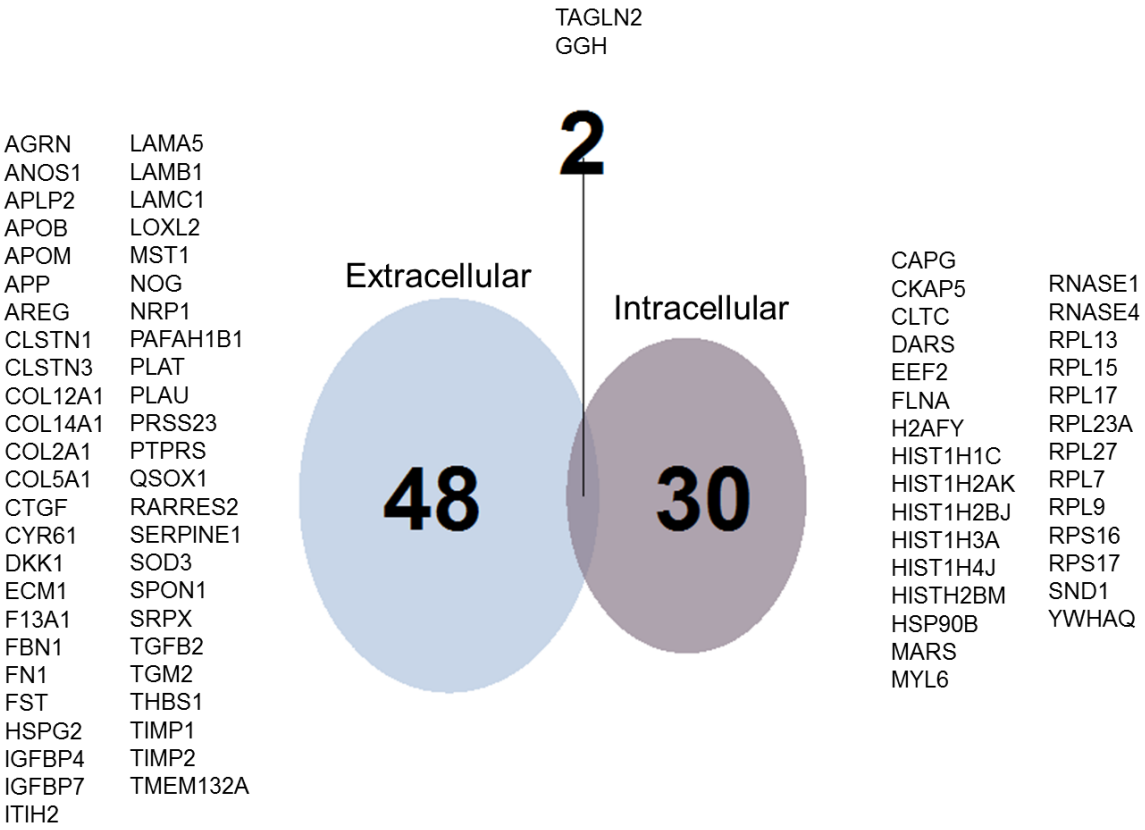

Figure 3.14 ***Venn Diagram of the Subcellular Locations of the 80 Filtered PDIA3-Dependent, Heparin-Binding Proteins from TMT-based Quantitative Proteomics.*** *Analysis performed using UniProt's curated databases (https://www.uniprot.org/).*

Table 3.1. Known ***Heparin-binding and PDIA3 Substrates within the 48 Extracellular Proteins in the Filtered TMT-Proteomics dataset.*** *These proteins were identified with p≤0.05 and ±2-fold change. Information from* (Jessop et al., 2007b; Carbon et al., 2009).

Gene Name	*Log2FoldChange*	*Adjusted p.Value*	*Heparin Binding*	*Known PDIA3 Substrate*
AGRN	-1.740031244	0.020564834		X
ANOS1	-1.328769116	0.039878104		
APLP2	-1.7325747	0.042460678	X	
APOB	-1.503851602	0.047603722	X	
APOM	-1.410774935	0.003684174		
APP	-1.921346147	0.029152123	X	
AREG	-1.622976813	0.041399566		
CLSTN1	-1.816571703	0.04049051		
CLSTN3	-1.819656719	0.034326707		
COL12A1	-2.440656945	0.015074592		
COL14A1	-1.518770853	0.026510089		
COL2A1	-1.721441198	0.037981018		
COL5A1	-2.714191378	0.009684439	X	
CTGF	-1.798645462	0.023037412	X	
CYR61	-1.331412956	0.043869839	X	
DKK1	-2.273822434	0.022797747		
ECM1	-1.926160999	0.028414135		
EEF2	-1.370068307	0.031692122		
F13A1	-1.394352844	0.048796574		
FBN1	-1.710491537	0.008340685	X	
FN1	-2.154812212	0.038767829	X	
FST	-1.716793348	0.004366334		
HSPG2	-1.650667918	0.012861		
IGFBP4	-1.818854668	0.034951891		
IGFBP7	-1.88504472	0.039242523		
ITIH2	-1.698212016	0.018107777		
LAMA5	-2.135670205	0.002123124		
LAMB1	-2.286367447	0.01352354		X
LAMC1	-2.037300052	0.012577036		
LOXL2	-2.525054697	0.003104902		X
MARS	-1.389855912	0.025437063		
MST1	-2.101881659	0.00771543		
NOG	-2.103324073	0.012112559		
NRP1	-1.555604049	0.028277882	X	
PLAT	-2.233689247	0.020869607		
PLAU	-3.023536975	0.004244137		
PRSS23	-2.416079339	0.013401314		
PTPRS	-1.755153917	0.007818062	X	
QSOX1	-1.596009923	0.012145822		
RARRES2	-1.861788834	0.018172451		
SERPINE1	-2.020721715	0.031316122		
SOD3	-1.439321413	0.016155273	X	
SPON1	-1.484953201	0.016398411		
SRPX	-2.921942411	0.003772864		
TGFB2	-1.782004114	0.011589291		
TGM2	-1.763084349	0.017637331		X
THBS1	-2.346490206	0.011240091	X	
TIMP1	-1.618457234	0.025661055		
TIMP2	-1.641731253	0.032189028		
TMEM132A	-2.378741874	0.005597112		

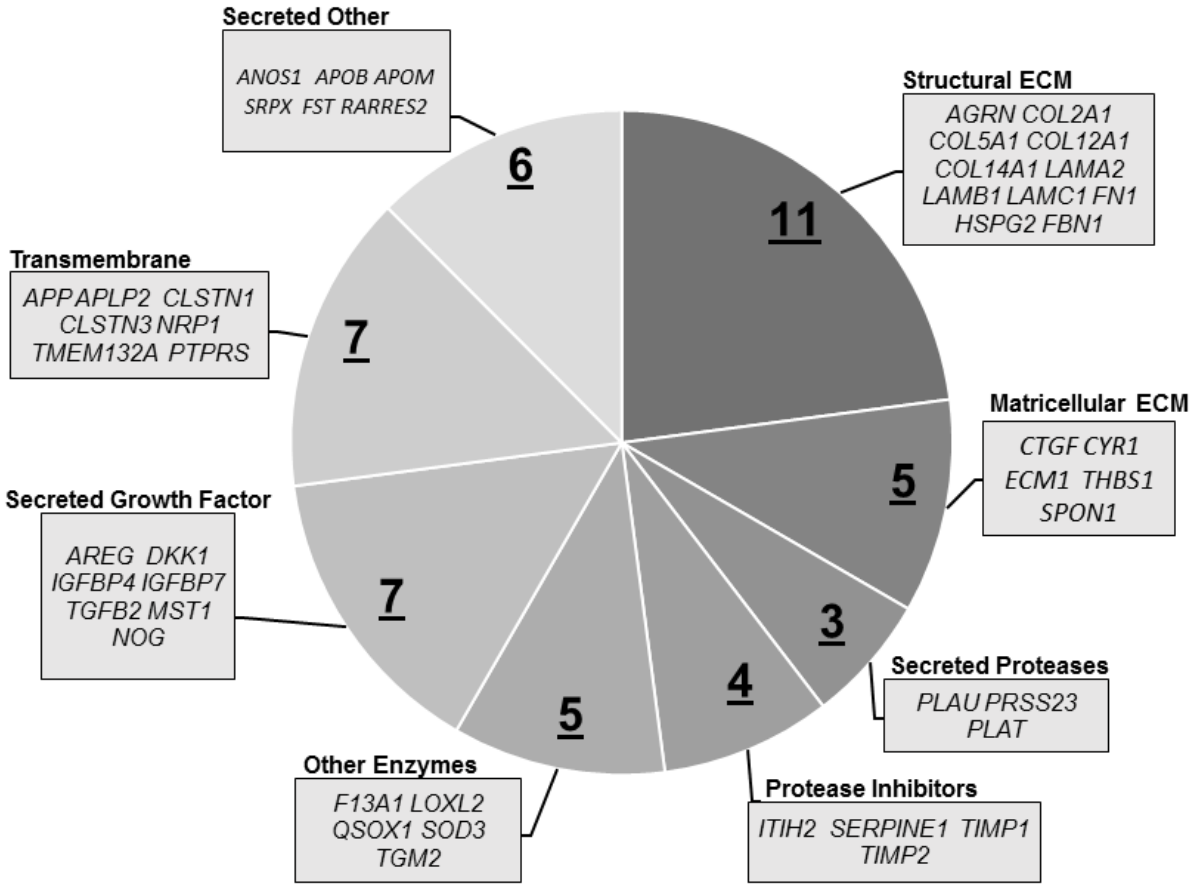

Figure 3.15. ***Pie Chart of the Functions of the 48 Extracellular Proteins in the PDIA3-Dependent, Heparin-binding Filtered Dataset identified by TMT-Proteomics.*** *Analysis was done by UniProt and by manual curation (https://www.uniprot.org/).*

3.4.1 Analysis of the Filtered Protein Dataset by Gene Ontology and Other Bioinformatics Tools

The PDIA3-dependent, heparin-binding secretome was then analysed by online curated databases. PDIA3 is an oxidoreductase and its substrate glycoproteins are likely to contain disulphide bonds in their tertiary structure. The domains in the 80 protein, filtered protein dataset were investigated by InterProScan. The domains were recorded if they were cysteine-rich or contained a critical disulphide bond; the results were then displayed as a mosaic plot (**Figure 3.16**). Nearly all the extracellular proteins from the TMT-proteomics dataset contained at least one domain that fulfilled the criteria stated above, with 6 exceptions (quiescin sulfhydryl oxidase 1 (QSOX1), retinoic acid receptor responder 2 (RARRE2), serpin family E member 1 (SERPINE1), superoxide dismutase 3 (SOD3), spondin-1 (SPON1) and transmembrane protein 123 (TMEM123A)). The most common domain was an EGF-like domain. Only one of the intracellular proteins from the TMT-proteomics dataset (ribonuclease A family member 4 (RNASE4)) contained cystine-rich domains or a disulphide bond.

Extracellular Set (48 Proteins)

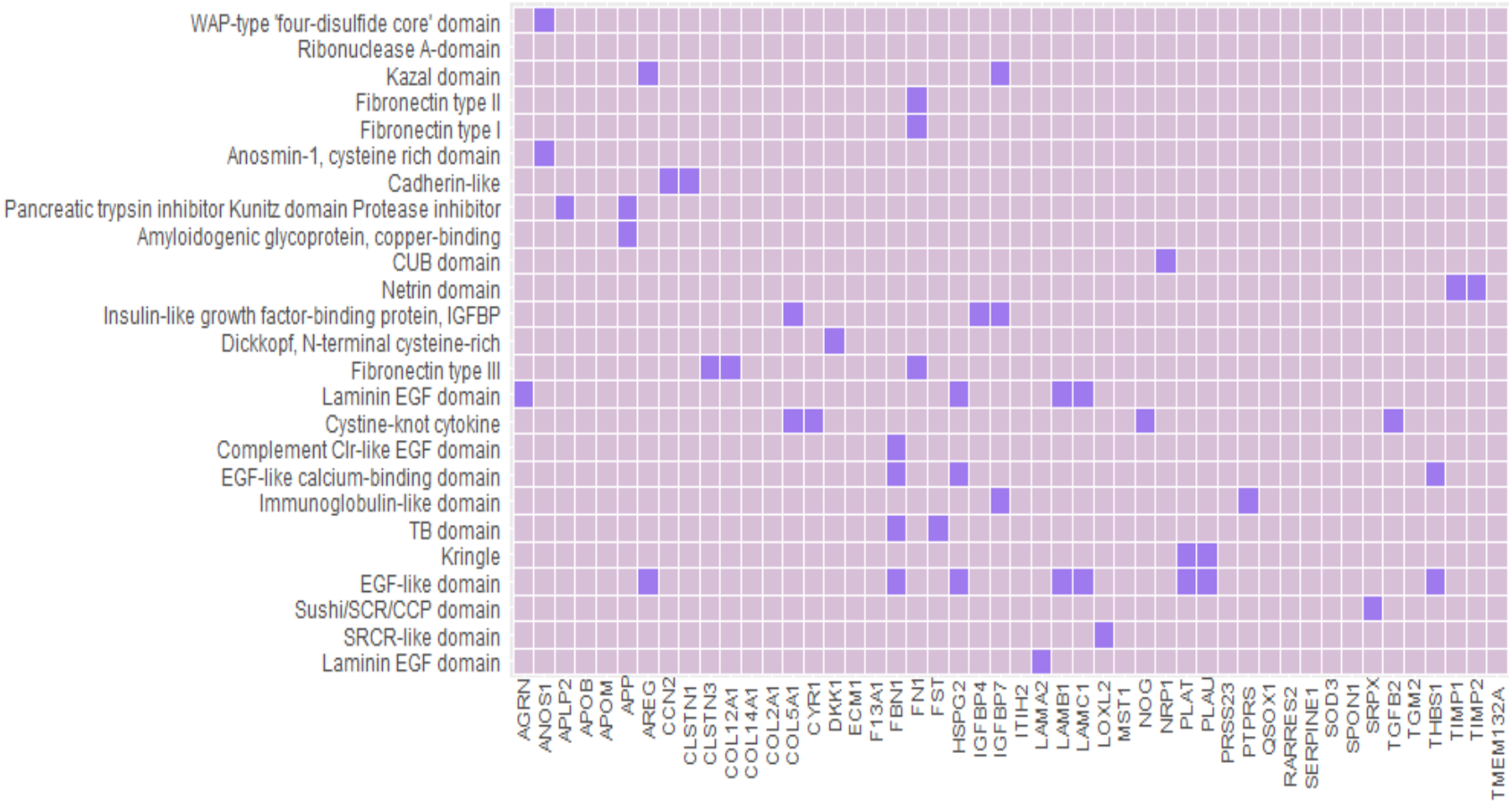

Figure 3.16. ***Mosaic Plot Displaying Extracellular, PDIA3-Dependent, Heparin-Binding Proteins with Cysteine-Rich Domains.*** *Domains were identified using InterProScan and those displayed are either cysteine-rich or contain a critical disulphide bond (https://www.ebi.ac.uk/interpro/search/sequence-search). Tiles in dark purple show which proteins have the respective domain. The Mosaic Plot was constructed in R.*

Intracellular Set (32 Proteins)

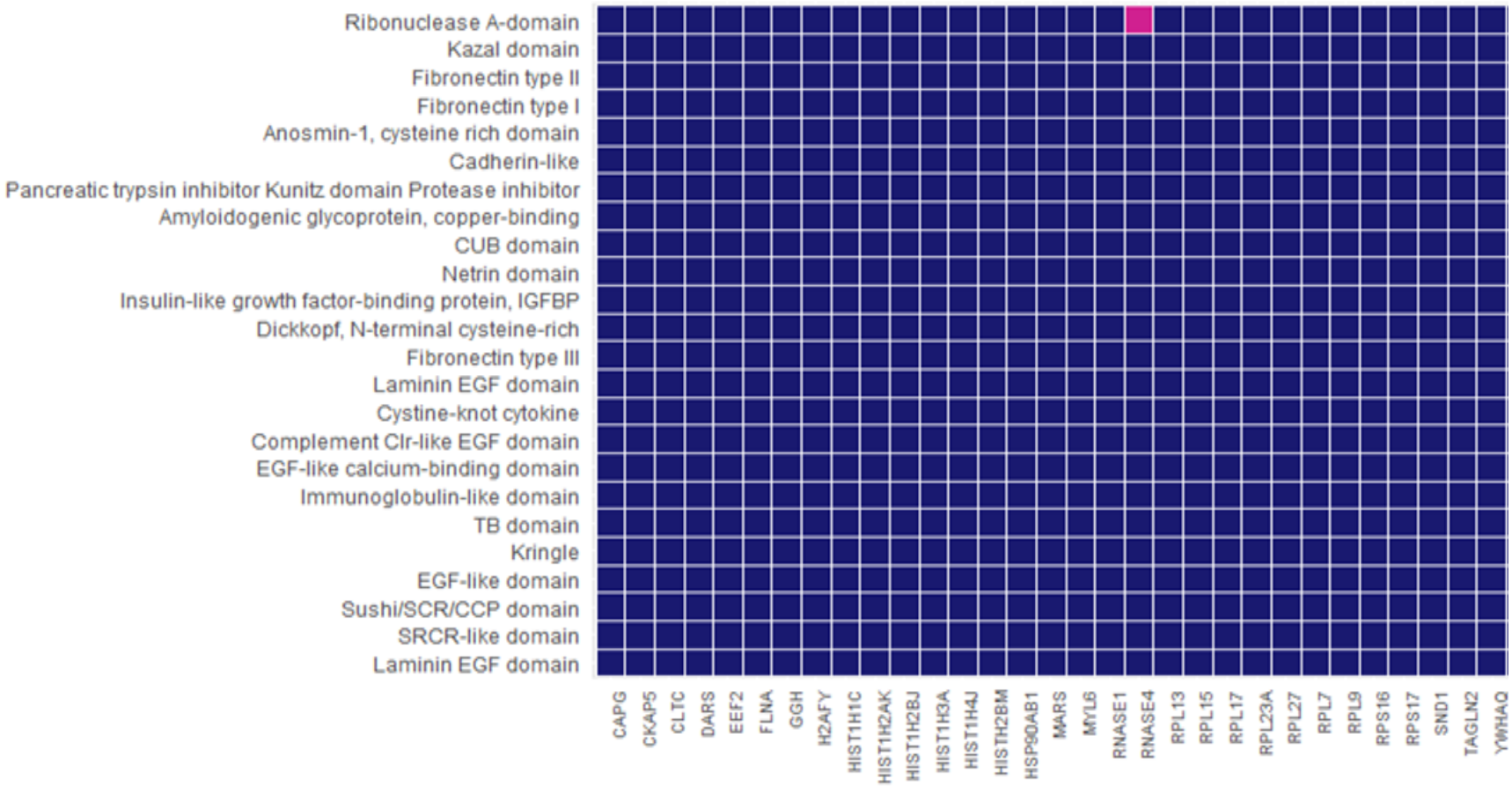

Figure 3.17. ***Mosaic Plot Displaying Intracellular PDIA3-Dependent, Heparin-binding Proteins with Cysteine-Rich Domains.*** *Domains were identified using InterProScan and those displayed are either cysteine-rich or contain a critical disulphide bond (https://www.ebi.ac.uk/interpro/search/sequence-search). Tiles in pink show which proteins have the respective domain. The Mosaic Plot was constructed in R.*

3.4.2 Gene Ontology

To understand the cellular relevance of the identified PDIA3-dependent, heparin-binding proteins, the 80-protein filtered dataset was further analysed by Gene Ontology (GO). GO gives reliable cellular attributes of genes and proteins (Subramanian et al., 2005). The Gene Set Enrichment Analysis (GSEA) database was used to find the top 10 GO terms of the three main GO domains (Biological Process, Cellular Component and Molecular Function) that were significantly enriched in the protein dataset (**Figure 3.18**, **Figure 3.19** & **Figure 3.20**). GO can also analyze the enrichment of one or more genes for a GO term.

A second independent GO tool was used to confirm the findings from the GSEA database. This was done with Gene Ontology Enrichment Analysis and Visualization Tool (GOrilla) (Eden et al., 2009). This tool reports on significance through shade coding and was used to investigate the main GO domains: GO Biological Process, GO Cellular Component and GO Molecular Function for the extracellular and intracellular proteins.

First the 48 extracellular proteins were analysed at both portals and many GO terms that relate to cancer metastasis were found. At GSEA, the extracellular proteins were enriched for terms Extracellular Space, Receptor Binding, Regulation of Multicellular Organismal Development and Locomotion (**Figure 3.18** & **Figure 3.19**). The GOrilla analysis of the extracellular proteins found many of the same GO terms for all three major GO domains. Only the most significant GO Biological Process terms from GOrilla are shown in **Figure 3.21**. These include Extracellular Matrix, Endoplasmic Reticulum Lumen, Locomotion, Integrin Binding and Extracellular Matrix Structural Constituent. Likewise, GO Cellular Component showed many significantly-enriched GO terms, particularly significant was Collagen-Containing Extracellular Matrix (**Figure 3.21** & **Figure 3.22**).

The 32 intracellular proteins were analyzed by the same procedures. There was no overlap in any of the top 10 significantly enriched GO terms between the extracellular and intracellular proteins using the GSEA curated database. Most of the enriched GO terms were associated with ribosomal proteins (**Figure 3.23, Figure 3.24** & **Figure 3.25**). The GO terms identified by GOrilla were very similar to the GO terms found enriched in GSEA, such as Ribosomal Subunit and DNA Packing Complex. Overall, the intracellular proteins were associated with fewer GO terms and with lower significances than the extracellular proteins (**Figure 3.26**).

Extracellular

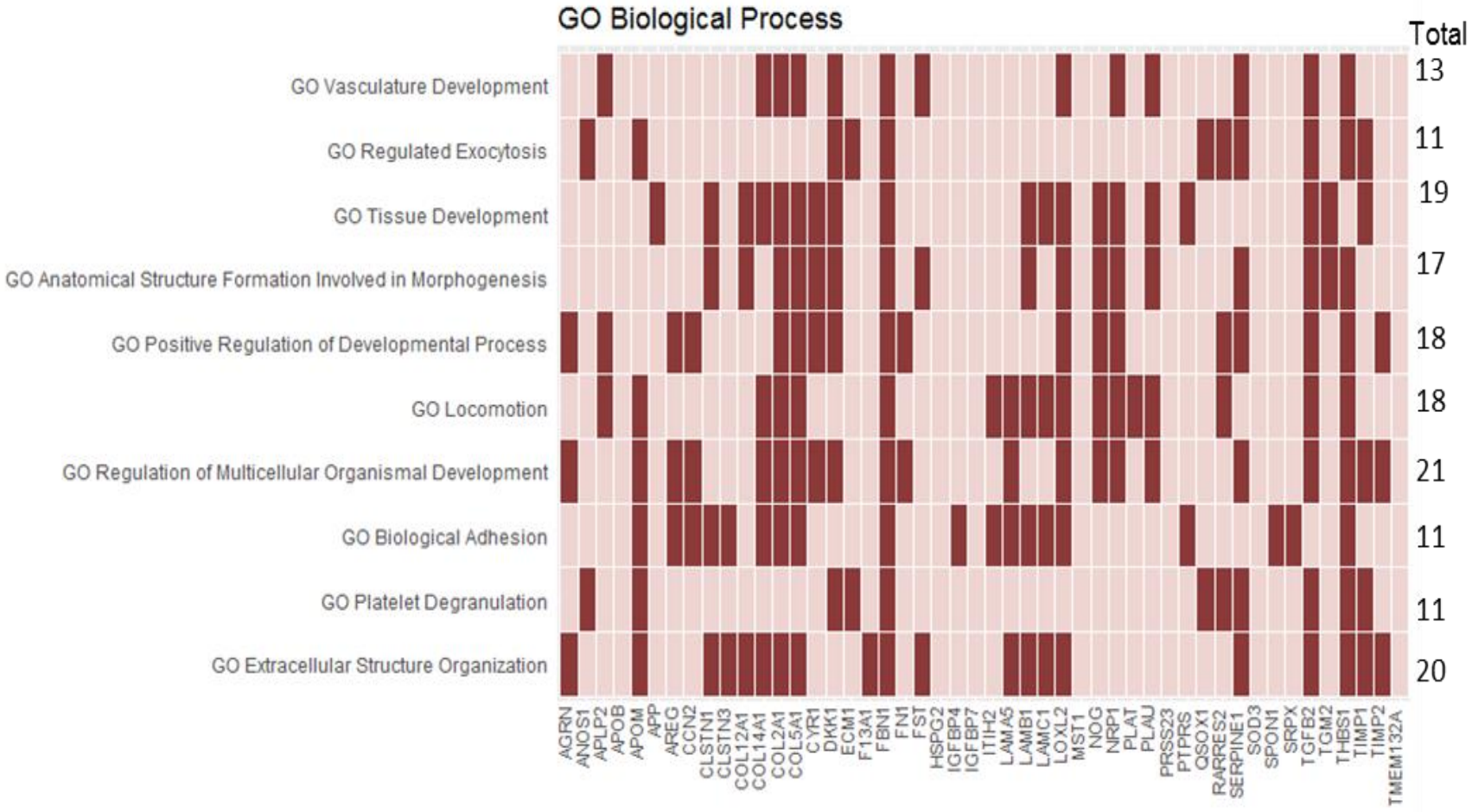

Figure 3.18. ***Mosaic Plot: Gene Set Enrichment Analysis of the Extracellular Proteins in the 80-protein dataset.*** *Analysis of the Molecular Signature Database (http://software.broadinstitute.org/gsea/index.jsp) showing the top 10 terms identified as significant for each protein (red boxes) within GO Biological Process. Mosaic Plot was constructed in R. Key: GO; Gene Ontology*

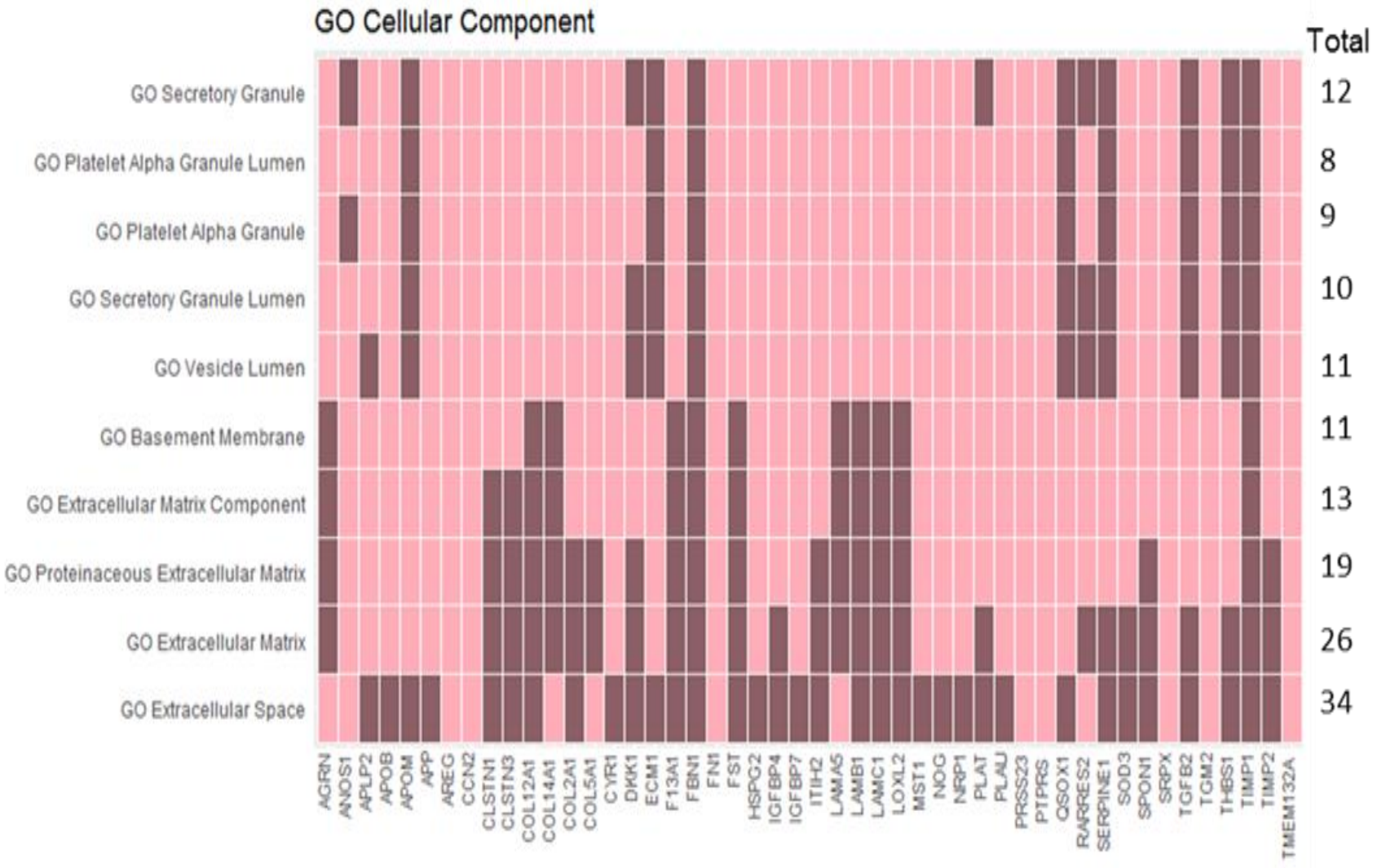

Figure 3.19. ***Mosaic Plot: Gene Set Enrichment Analysis of the Extracellular Proteins in the 80 protein dataset.*** *Analysis of the Molecular Signature Database (http://software.broadinstitute.org/gsea/index.jsp) showing the top 10 terms identified as significant for each protein (dark purple boxes) within GO Cellular Component. Mosaic Plot was constructed in R. Key: GO; Gene Ontology*

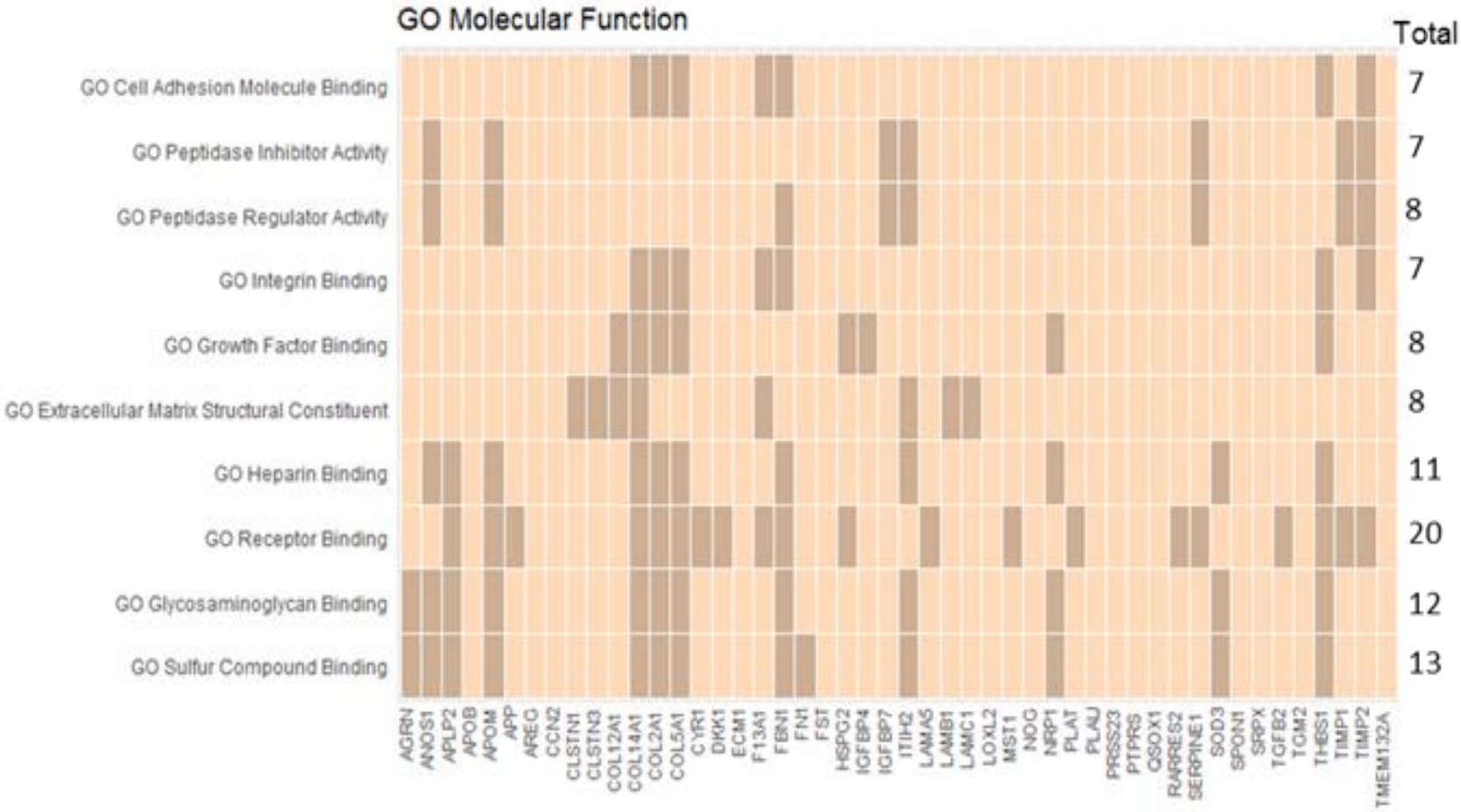

Figure 3.20. ***Mosaic Plot: Gene Set Enrichment Analysis of the Extracellular Proteins in the 80 protein dataset.*** *Analysis of the Molecular Signature Database (http://software.broadinstitute.org/gsea/index.jsp) showing the top 10 terms identified as significant for each protein (dark yellow boxes) within GO Molecular Function. Mosaic Plot was constructed in R. Key: GO; Gene Ontology*

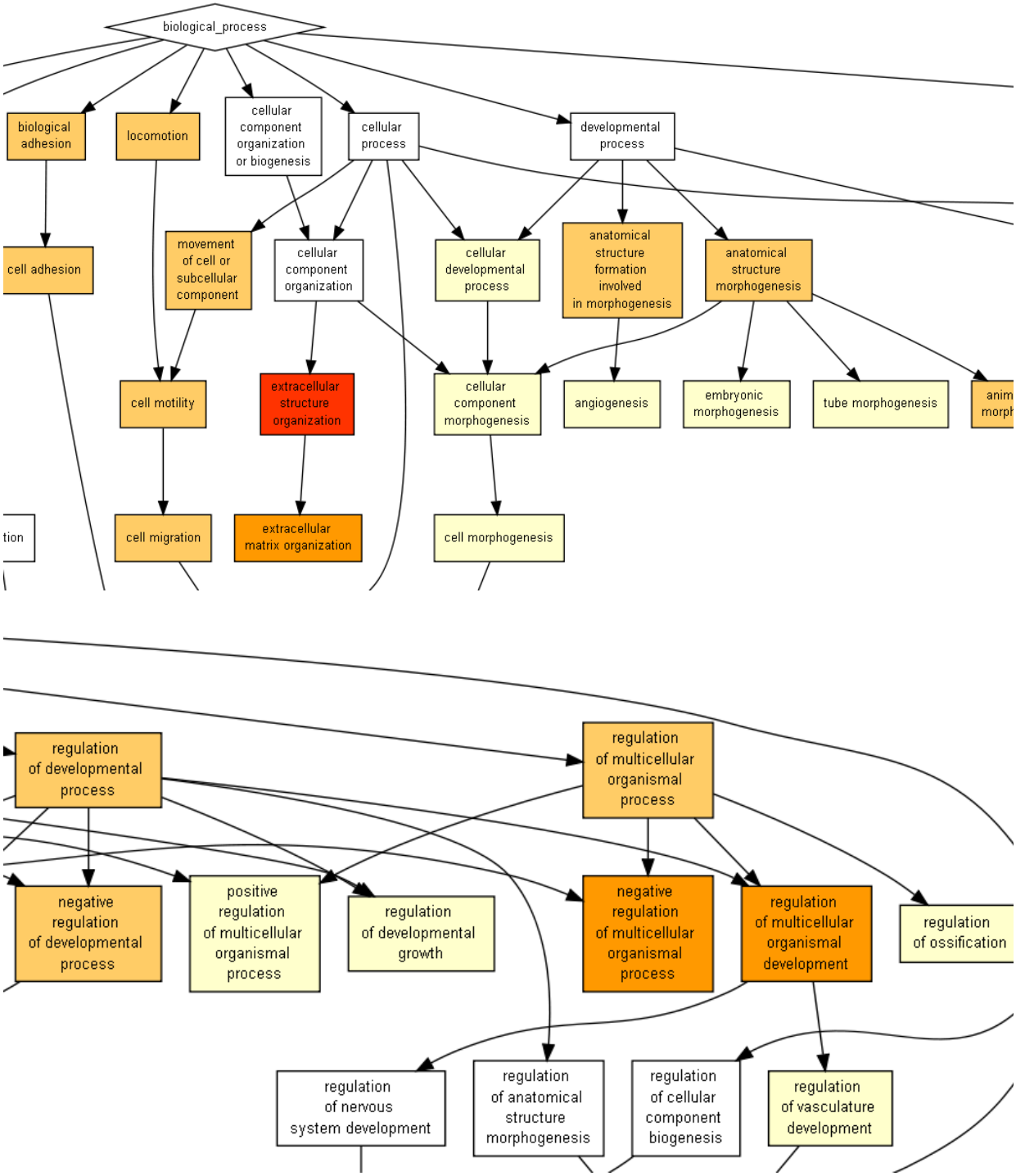

Figure 3.21. ***Gene Ontology Enrichment Analysis and Visualization Tool Analysis (GOrilla) on the Extracellular Proteins for the GO Domain Biological Process***. *http://cbl-gorilla.cs.technion.ac.il/. 48 extracellular proteins from TMT-Proteomics 80 protein dataset. Colour key: White $p>10^{-3}$; Yellow $10^{-3}< p>10^{-5}$; Light Orange $10^{-5}< p>10^{-7}$; Dark Orange $10^{-7}<p>10^{-9}$; Red $<10^{-9}$. Image cropped to fit on A4 page.*

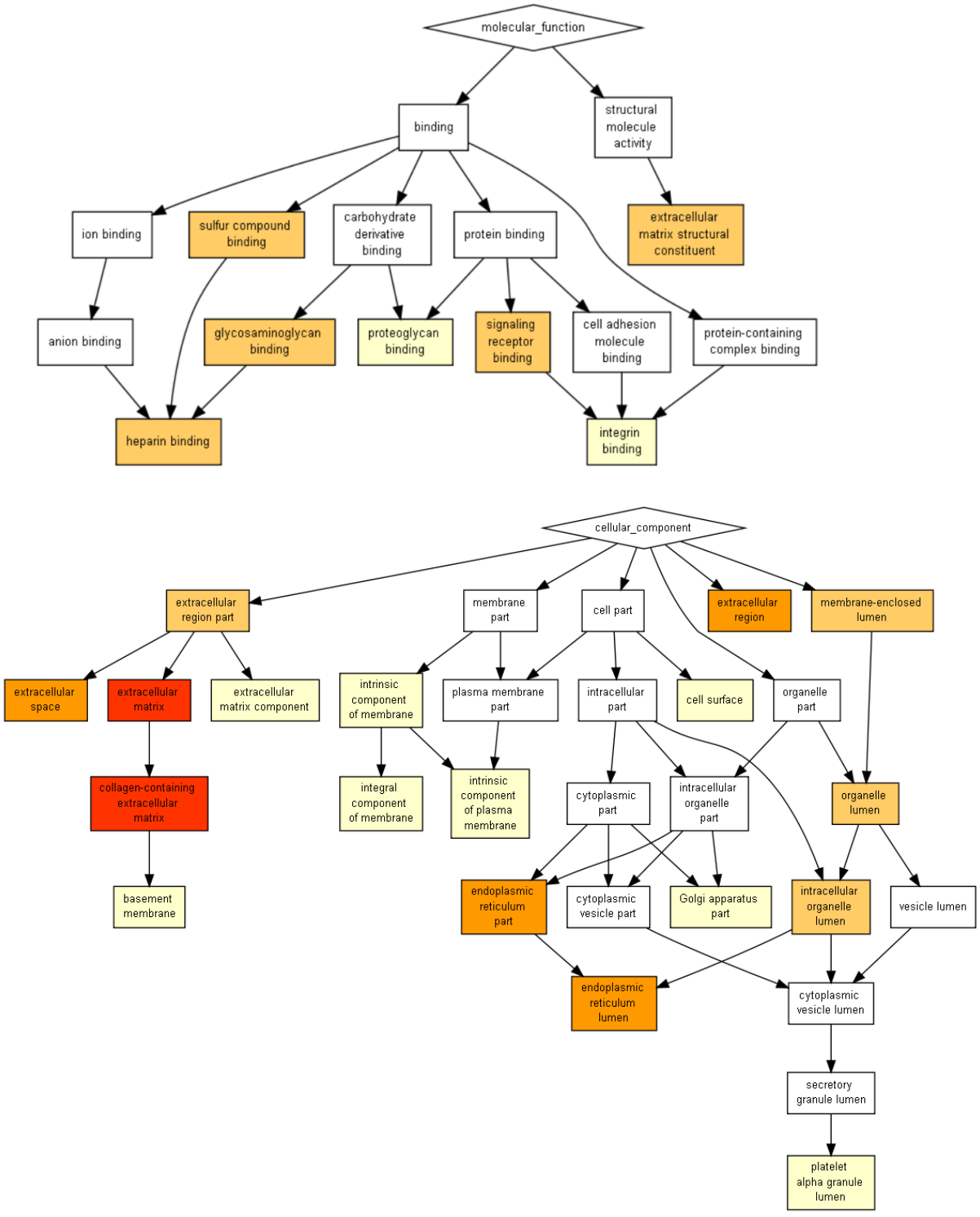

Figure 3.22. ***Gene Ontology Enrichment Analysis and Visualization Tool (GOrilla) on the Extracellular Proteins for the GO domain Cellular Component (Top) and Molecular Function (Bottom).*** *http://cbl-gorilla.cs.technion.ac.il/. 48 extracellular proteins from TMT-Proteomics 80 protein dataset. Colour key: White $p>10^{-3}$; Yellow $10^{-3}< p>10^{-5}$; Light Orange $10^{-5}< p>10^{-7}$; Dark Orange $10^{-7}<p>10^{-9}$; Red $<10^{-9}$*

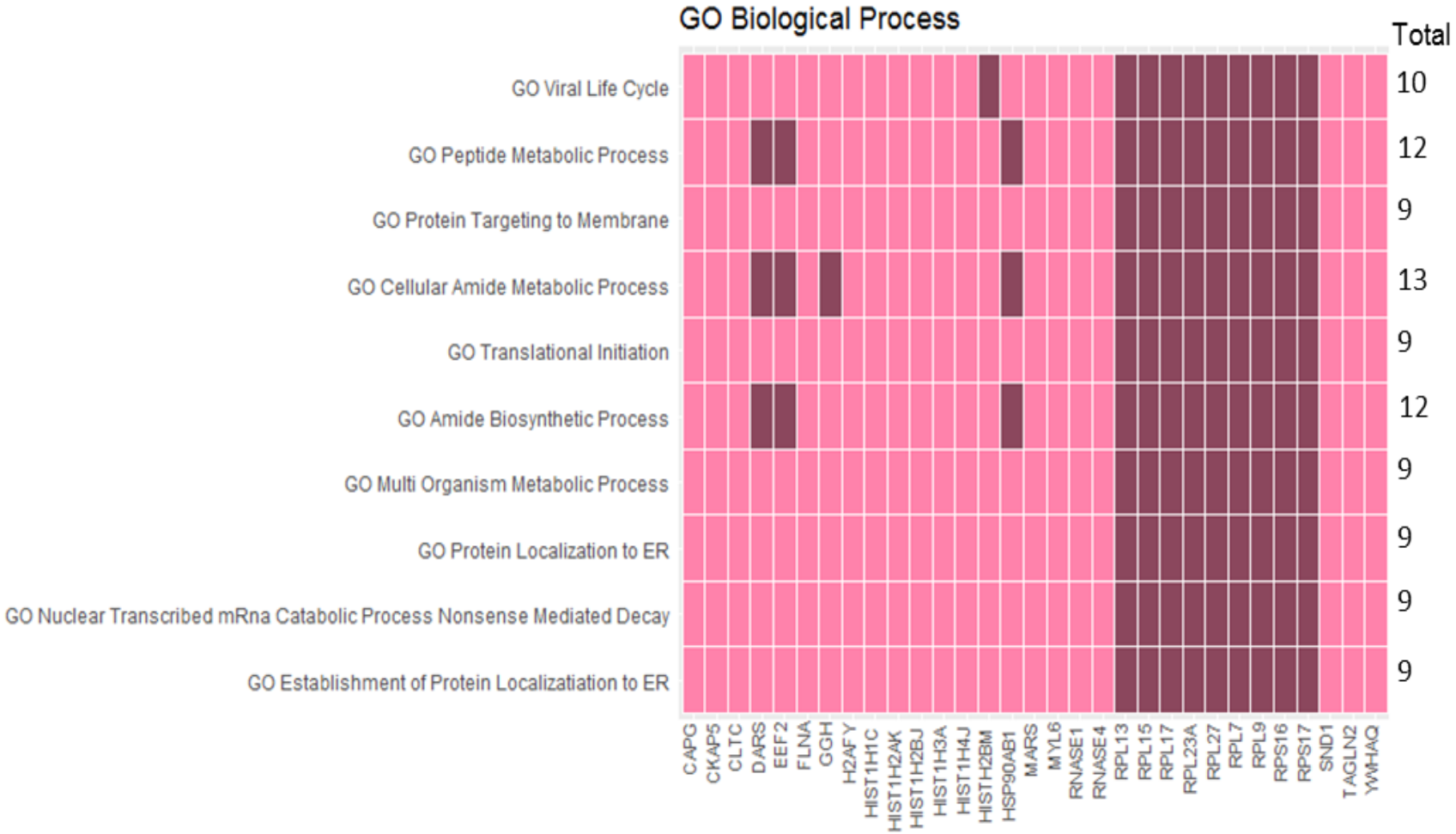

Figure 3.23 ***Mosaic Plot: Gene Set Enrichment Analysis of the Intracellular Proteins from the 80 protein dataset.*** *Analysis of the Molecular Signature Database (http://software.broadinstitute.org/gsea/index.jsp) showing the top 10 terms identified as significant for each protein (dark red boxes) within GO Biological Process. Mosaic Plot was constructed in R. Key: GO; Gene Ontology.*

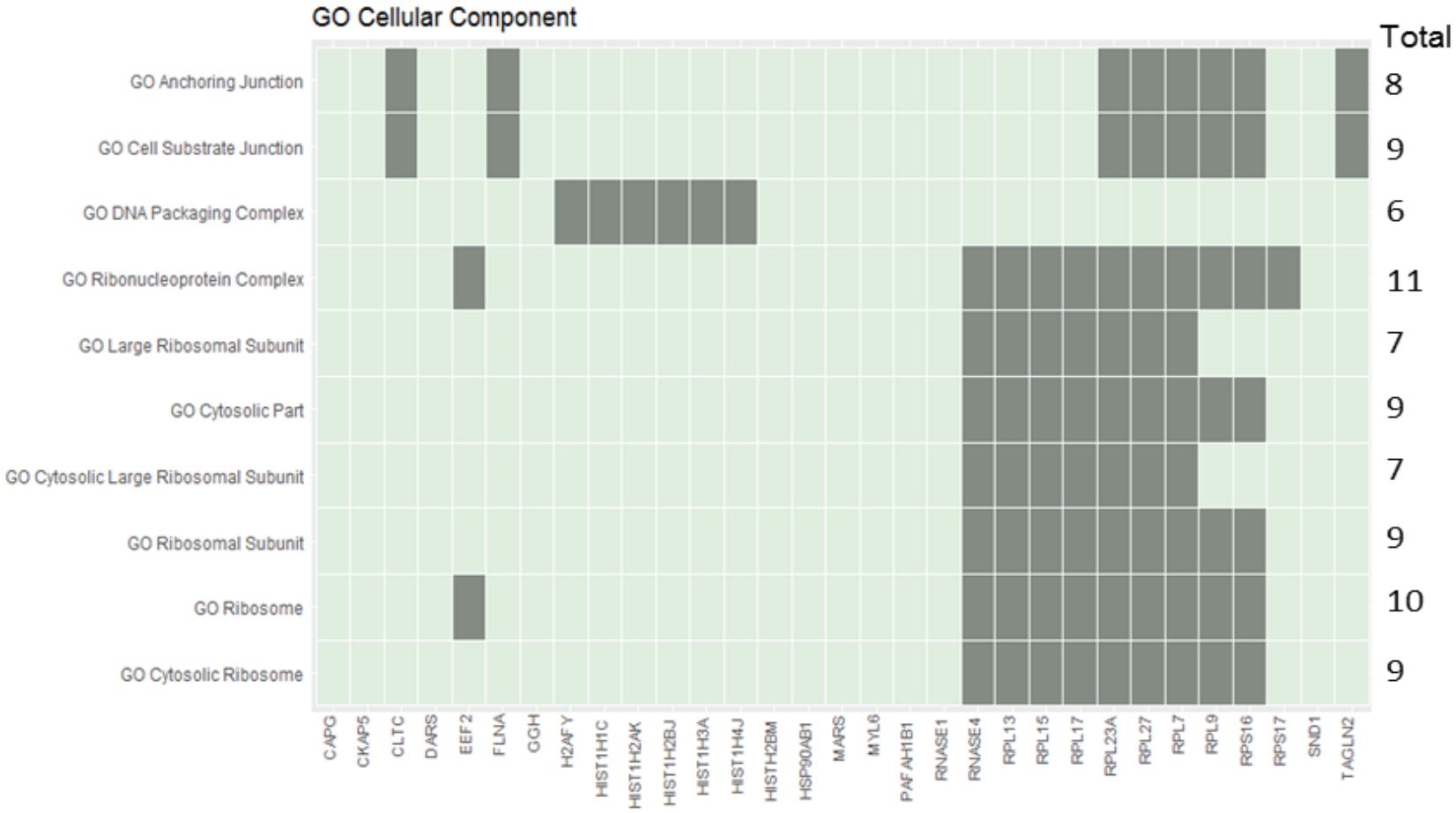

Figure 3.24. ***Mosaic Plot: Gene Set Enrichment Analysis of the Intracellular Proteins in the 80 protein dataset.*** *Analysis of the Molecular Signature Database (http://software.broadinstitute.org/gsea/index.jsp) showing the top 10 terms identified as significant for each protein (dark green boxes) within GO Cellular Component. Mosaic Plot was constructed in R. Key: GO; Gene Ontology*

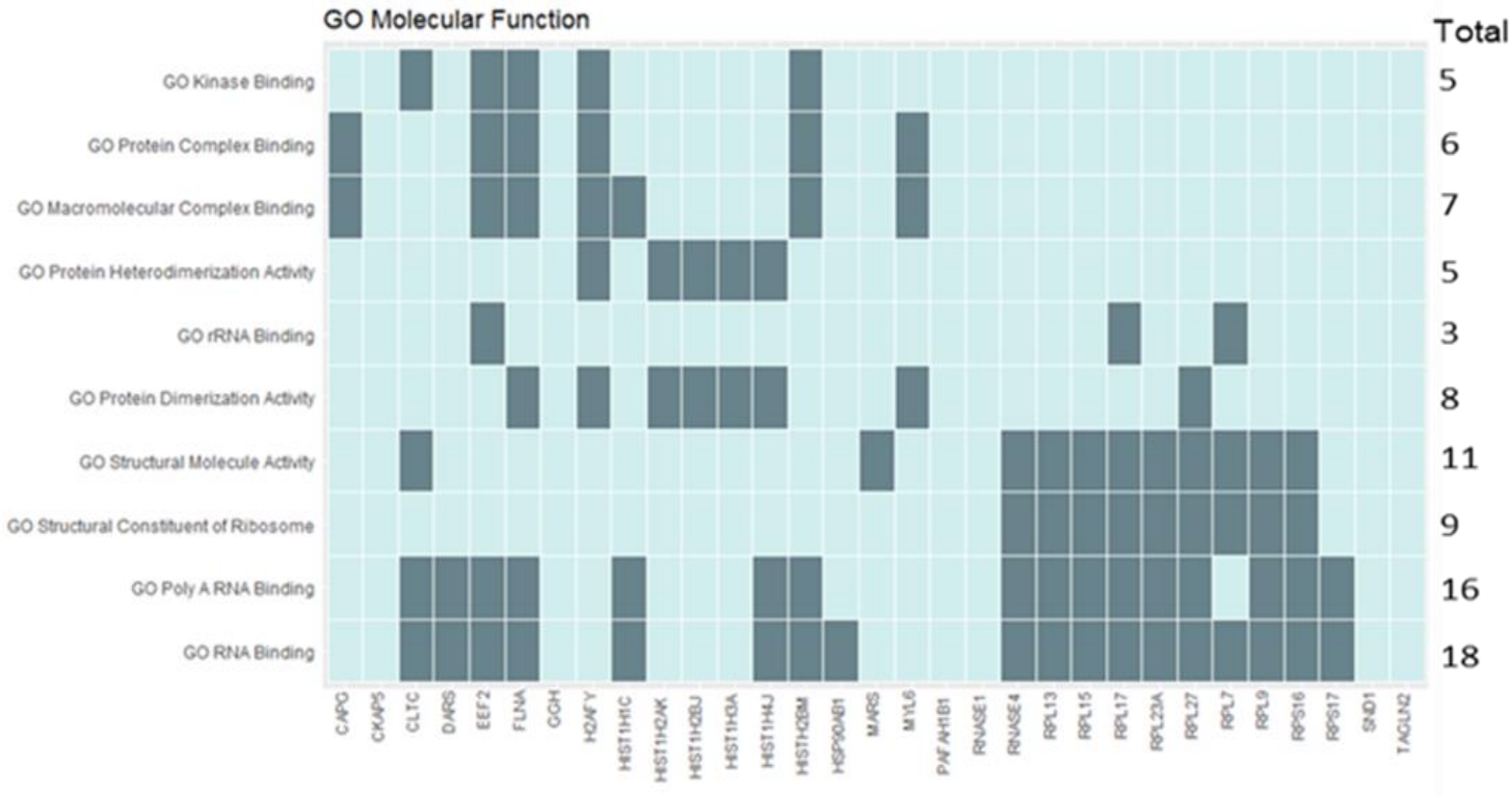

Figure 3.25 ***Mosaic Plot: Gene Set Enrichment Analysis of the Intracellular Proteins in the 80 protein dataset.*** *Analysis of the Molecular Signature Database (http://software.broadinstitute.org/gsea/index.jsp) showing the top 10 terms identified as significant for each protein (dark blue boxes) within GO Molecular Function. Mosaic Plot was constructed in R. Key: GO; Gene Ontology.*

Biological Process

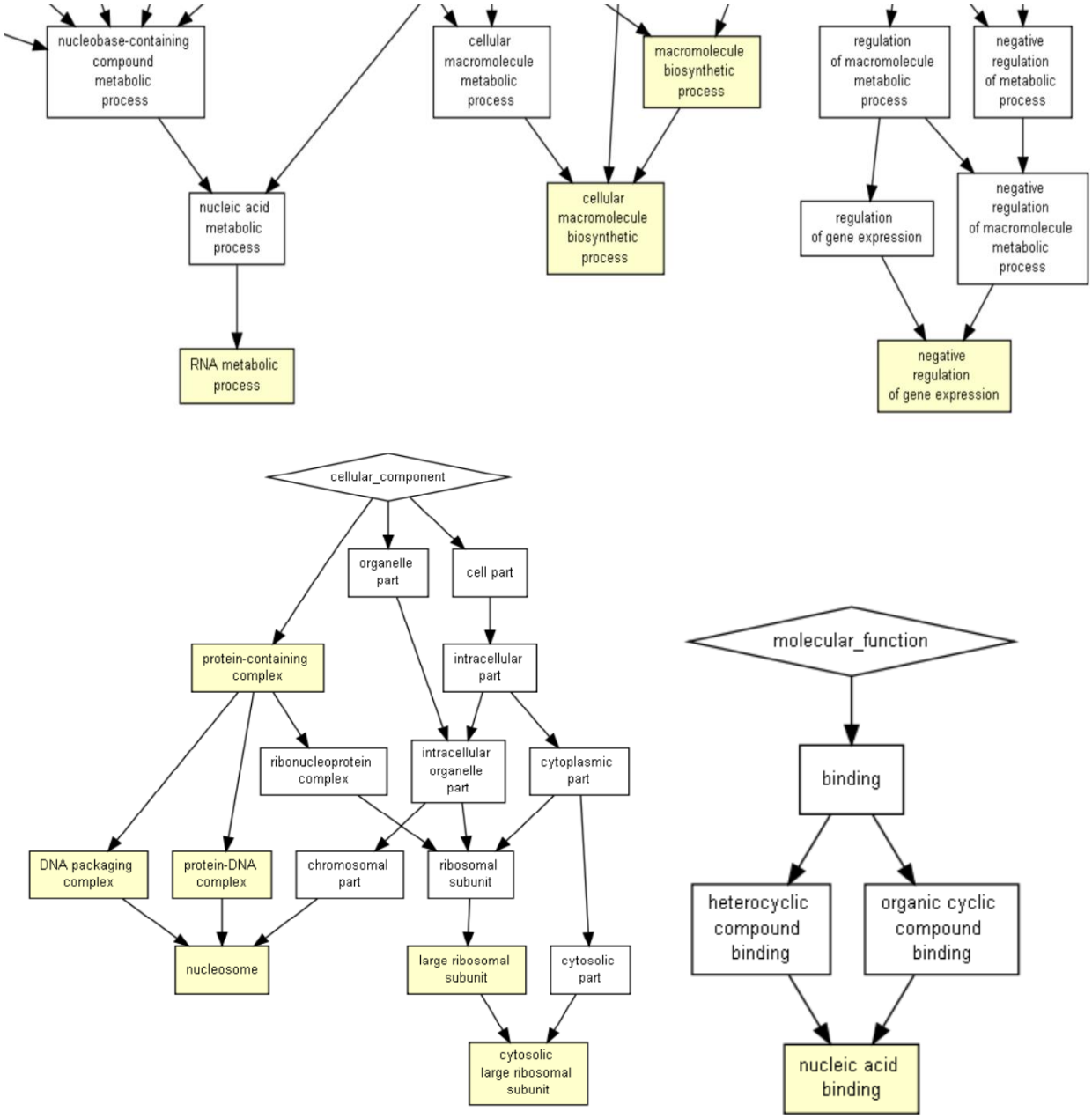

Figure 3.26. ***Gene Ontology Enrichment Analysis and Visualisation Tool (GOrilla) on the Intracellular Proteins from the 80 protein dataset.*** *GO domains Biological Process (Top), Cellular Component (Bottom Left) and Molecular Function (Bottom Right)(http://cbl-gorilla.cs.technion.ac.il/). 32 intracellular proteins were included from the TMT-Proteomics dataset. Colour key*: *White* $p>10^{-3}$; *Yellow* $10^{-3}< p>10^{-5}$; *Light Orange* $10^{-5}< p>10^{-7}$; *Dark Orange* $10^{-7}<p>10^{-9}$; *Red* $<10^{-9}$.

In GSEA, every identified GO term was very significantly enriched, enrichment scores are summarised displayed in **Figure 3.27** and enrichment significance (p.values) are displayed in **Figure 3.28**. For the extracellular proteins, every GO term for Biological Process, Cellular Component and Molecular Function was very significant, with the least significant GO term having a p.value of $<2.31 \times 10^{-9}$ (GO Molecular Function: Peptidase Inhibitor Activity). The most significant GO term was Extracellular Space ($p= 1.01 \times 10^{-41}$). The GO Cellular Component domain had the highest enrichment score, especially for the terms Platelet Alpha Granule Lumen and Basement membrane (**Figure 3.27**). The GO domain Molecular Function showed 11 proteins known to be heparin-binding proteins, validating the enrichment of the CM by heparin-binding affinity.

The intracellular proteins had less enrichment and less significant GO correlations than the extracellular proteins. The most highly enriched GO terms for the intracellular proteins were Protein Complex Binding and Cytosolic Part (**Figure 3.27**). The intracellular GO Molecular Function had less significant p values; the least significant being Kinase Binding ($p= 5.02 \times 10^{-5}$) (**Figure 3.28**).

In GSEA, the GO domains “Hallmarks” and “Cancer Modules” were also investigated for the extracellular protein set. These domains were not investigated for the intracellular proteins because there was no significant association of the intracellular proteins with GO terms in these categories. The Hallmarks domain revealed enrichment of 18 proteins involved in Epithelial-Mesenchymal Transition (EMT) (**Figure 3.29 & Figure 3.31A**), with p value of 8.79×10^{-29} (**Figure 3.31B**)**.** Many of the proteins were also associated with Cancer Modules (**Figure 3.30**). The GO Hallmarks associations were less significant: the least significant was TGFβ signaling with p.value $=2.4 \times 10^{-5}$ (**Figure 3.31 3.31B**).

Thus, two separate GO-based tools (GSEA and GOrilla) produced very similar outputs for analysis of the intracellular and extracellular proteins of the TMT dataset. The extracellular proteins had a high correlation with an array of GO terms relating to cancer, but in this set no individual GO term was obviously more significant than the others.

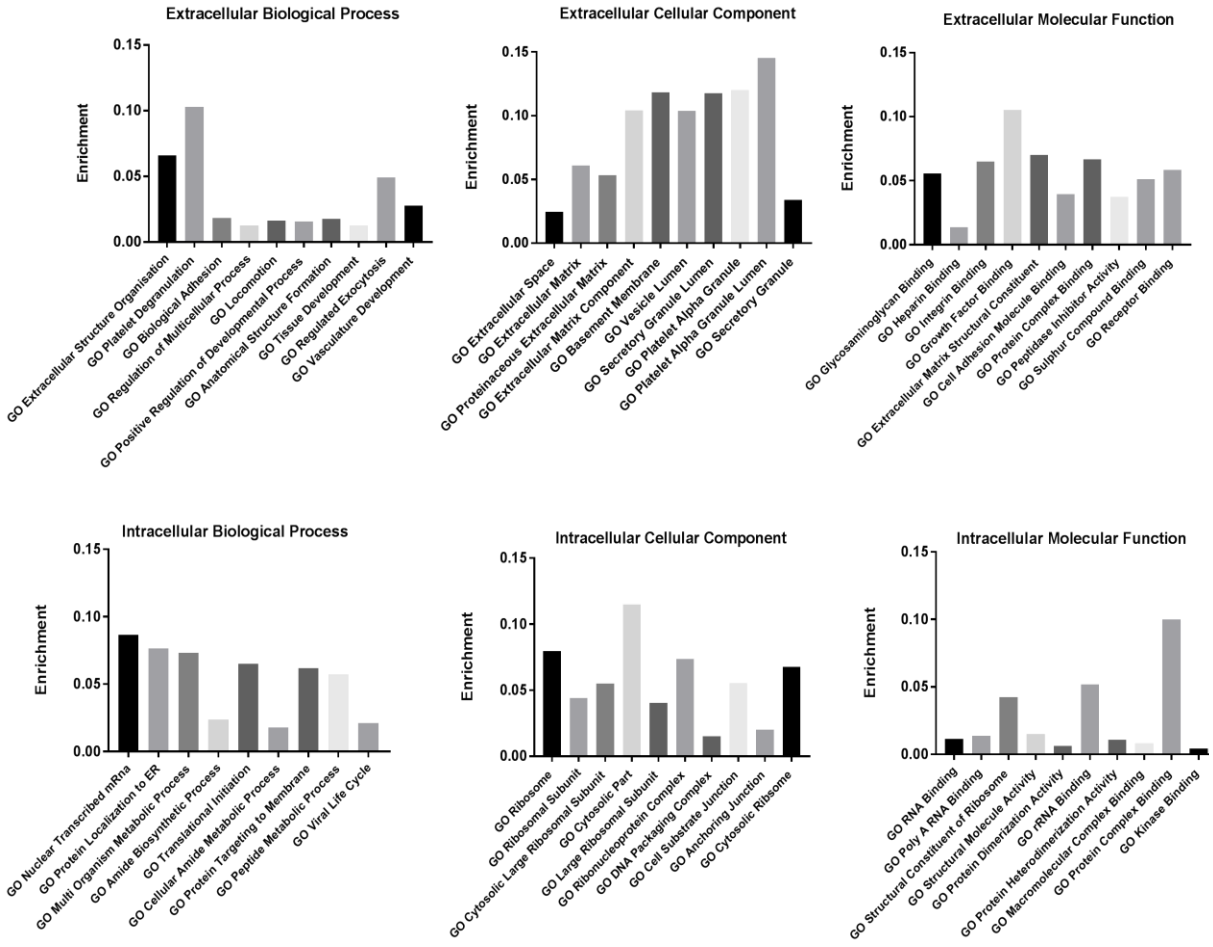

Figure 3.27. ***Gene Set Enrichment Analysis of Extracellular and Intracellular Proteins.*** *Bar charts of the top 10 terms from the analysis of the Molecular Signature Database (http://software.broadinstitute.org/gsea/index.jsp) with the* 48 extracellular (top row) or 32 intracellular proteins (bottom row) of the 80 protein dataset, according to *enrichment of GO terms within the 3 categories of GO classification. In each chart, the GO terms are plotted in order of significance (considering p.value, false-discovery rate and enrichment) Key: GO: Gene Ontology.*

	Extracellular		Intracellular	
	Gene Ontology Term	p.value	Gene Ontology Term	p.value
Biological Process	Extracellular Structure Organisation	1.14 x10-31	Nuclear Transcribed mRNA	6.83 x10-17
	Platlet Degranulation	1.04 x10-19	Establishment og Protein Localisation to ER	2.11 x10-17
	Biological Adhesion	1.2 x10-18	Protein Localisation to ER	1 x10-16
	Regulation of Multicellular Process	2.7 x10-18	Multi Organism Metabolic Process	2.9 x10-16
	Locomotion	4.51 x10-18	Amide Biosynthetic Process	3.33 x10-16
	Positive Regulation of Developmental Process	8.82 x10-18	Translation Initiation	4.88 x10-16
	Anatomical Structure Formation	2.65 x10-17	Cellular Amide Metabolic Process	5.55 x10-16
	Tissue Development	2.75 x10-17	Protein Targetting to Memrbane	9.5 x10-16
	Regulated Exocytosis	4.3 x10-17	Peptide Metabolic Process	1.37 x10-15
	Vasculature Development	4.41 x10-17	Viral Life Cycle	3.38 x10-15
Cellular Component	Extracellular Space	1.01 x10-41	Cytosolic Ribsome	4.57 x10-17
	Extracellular Matrix	9.09 x10-39	Ribsome	2.74 x10-16
	Proteinaceous Extracellular Matrix	2.44 x10-26	Ribsomal Subunit	1.34 x10-15
	Extracellular Matrix Component	3.05 x10-23	Cytosolic Large Ribsomal Subunit	1.3 x10-14
	Basement Membrane	2.07 x10-20	Cytosolic Part	2.33 x10-14
	Vesicle Lumen	9.36 x10-20	Large Ribsomal Subunit	3.25 x10-13
	Secretory Granule Lumen	1.33 x10-18	Ribonucleoprotein Complex	8.37 x10-13
	Platlet Alpha Granule	6.47 x10-17	DNA Packing Complex	1.03 x10-10
	Platlet Alpha Granule Lumen	7.49 x10-16	Cell Substrate Junction	1.96 x10-10
	Secretory Granule	1.39 x10-15	Anchoring Junction	9.88 x10-10
Molecular Function	Receptor Binding	5.14 x10-18	RNA Binding	5.92 x10-18
	Sulphur Compound Binding	1.02 x10-17	Poly A RNA Binding	1.47 x10-14
	Glycosaminoglycan Binding	1.61 x10-16	Structural Consitiuent of Ribsome	9.85 x10-13
	Heparin Binding	7.52 x10-16	Structural Molecule Acitvity	7.05 x10-7
	Intergrin Binding	1.65 x10-13	Protein Dimerization Activity	8.36 x10-6
	Growth Factor Binding	6.02 x10-13	rRNA Binding	9.99 x10-6
	Extracellular Matrix Structural Constituent	1.52 x10-12	Protein Heterodimerisation Complex Binding	1.46 x10-5
	Cell Adhesion Molecule Binding	1.7 x10-11	Macromolecular Complex Binding	3.31 x10-5
	Protein Complex Binding	2.08 x10-9	Protein Complex Binding	3.33 x10-5
	Peptidase Inhibitor Activity	2.31 x10-9	Kinase Binding	5.02 x10-5

Figure 3.28. ***Enrichment p.values for Gene Set Enrichment Analysis of Extracellular and Intracellular Proteins.*** *Table of the top 10 terms from the Molecular Signature Database (http://software.broadinstitute.org/gsea/index.jsp) with the* 48 extracellular or 32 intracellular proteins of the 80 protein dataset, according to *enrichment of GO terms within the 3 categories of GO classification.*

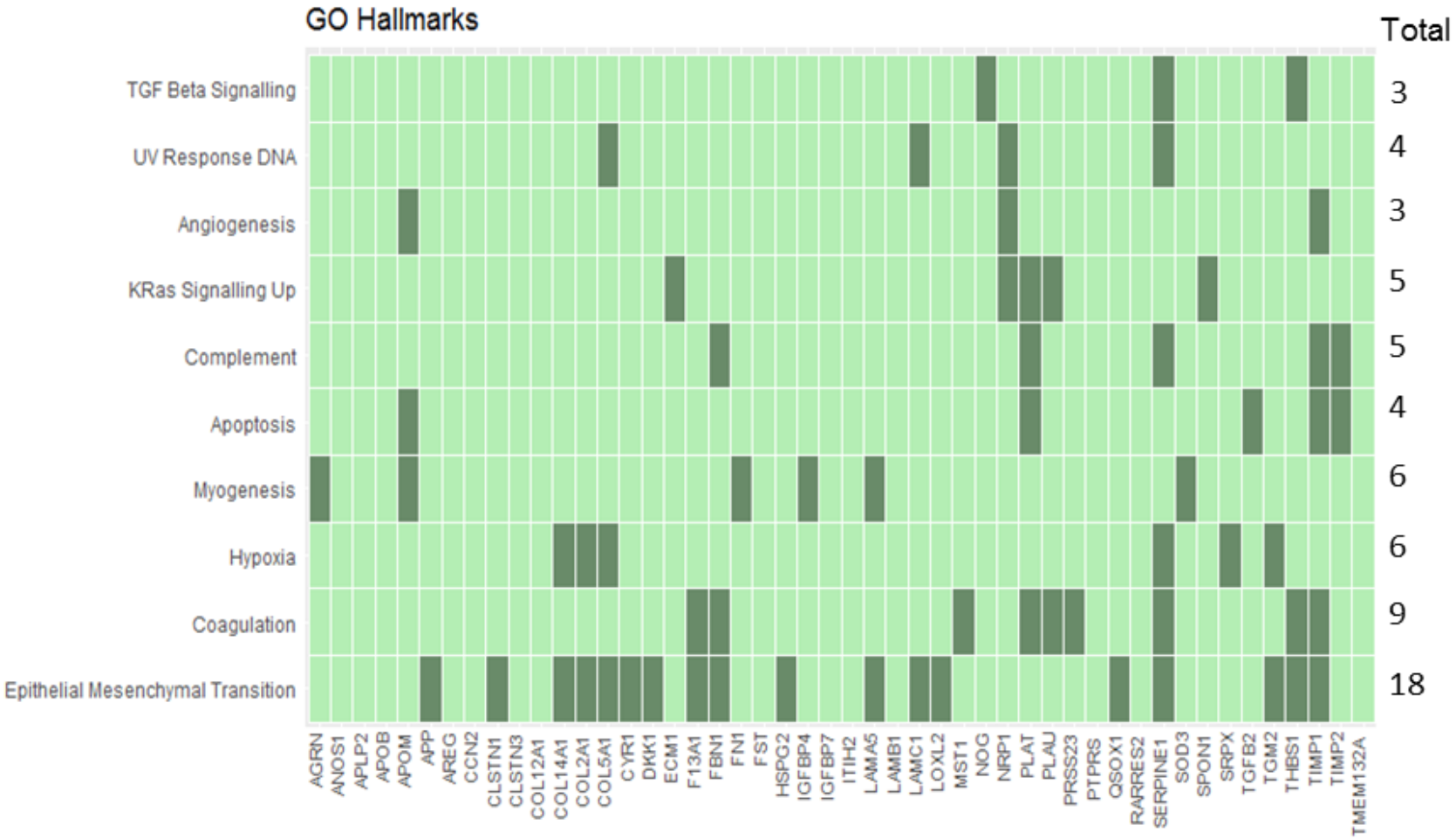

Figure 3.29. **Mosaic Plot: Gene Set Enrichment Analysis of the Extracellular Proteins in the 80 Protein Dataset.** Analysis of the Molecular Signature Database (http://software.broadinstitute.org/gsea/index.jsp) showing the top 10 terms identified as significant for each protein (dark green boxes) within GO Hallmarks. Mosaic Plot was constructed in R. Key: GO; Gene Ontology.

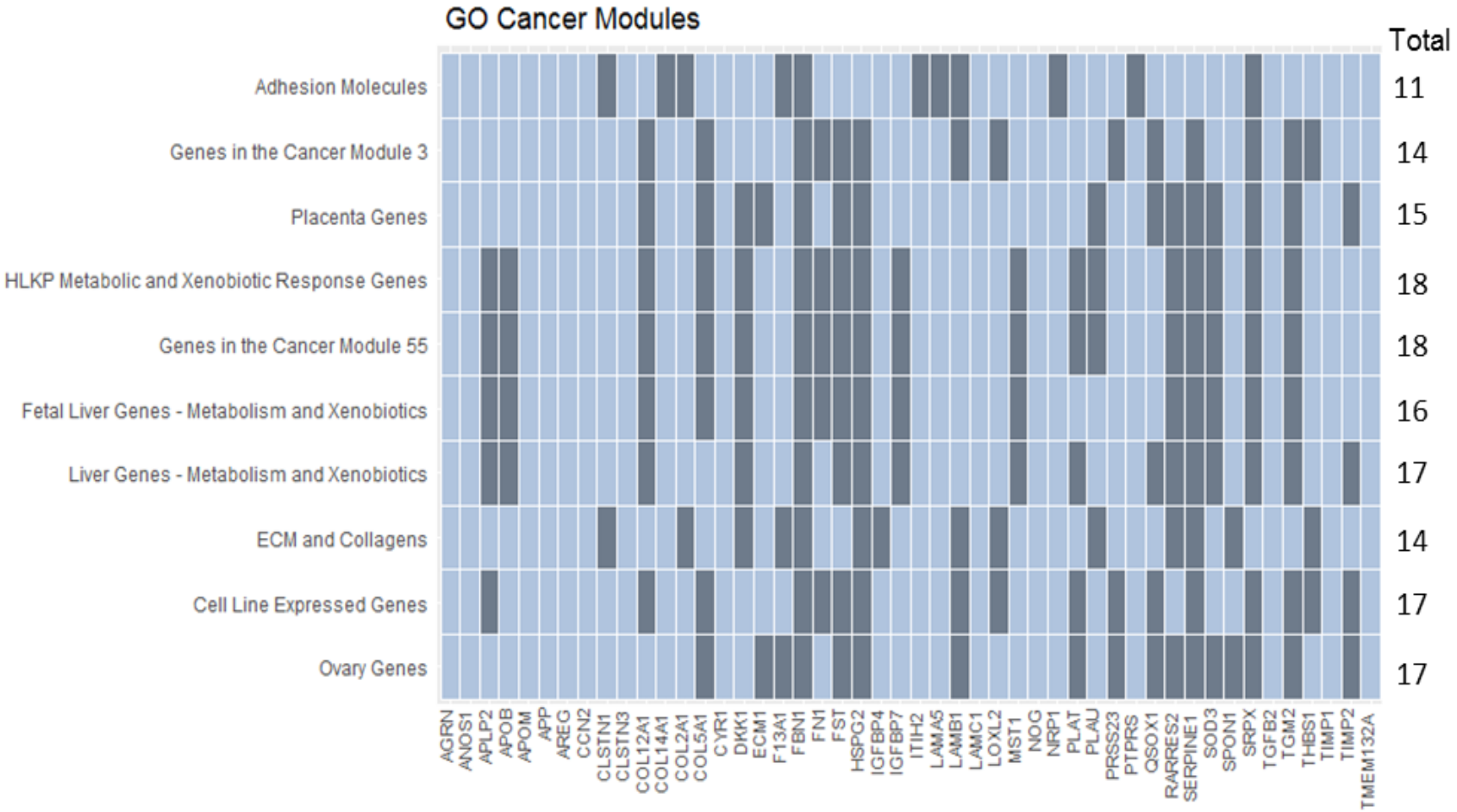

Figure 3.30. **Mosaic Plot: Gene Set Enrichment Analysis of the Extracellular Proteins in the 80 Protein Dataset.** Analysis of the Molecular Signature Database (http://software.broadinstitute.org/gsea/index.jsp) showing the top 10 terms identified as significant for each protein (dark blue squares) within GO Cancer Modules. Mosaic Plot was constructed in R. Key: GO; Gene Ontology.

A

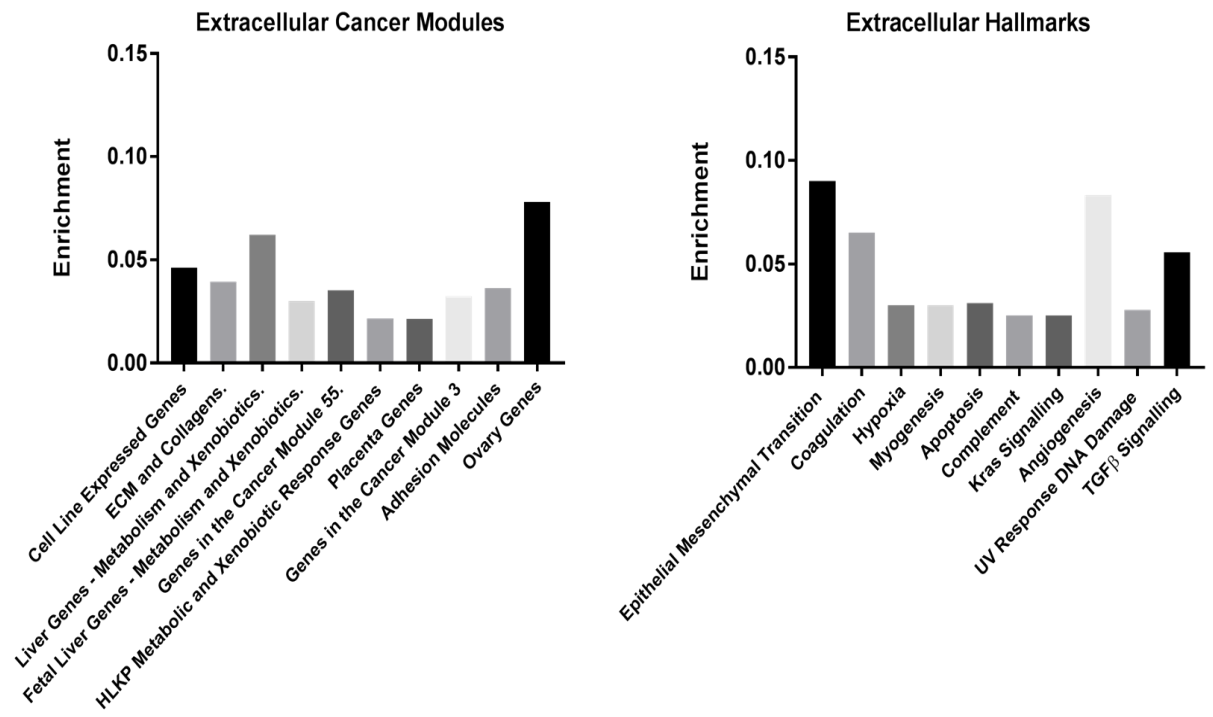

B

	Gene Ontology Term	p.value		Gene Ontology Term	p.value
Cancer Modules	Cell Line Expressed Genes	5.62 x10-23	Hallmarks	Epithelial-to-Mesenchymal Transition	8.79 x10-29
	ECM and Collagens	8.94 x10-22		Coagulation	1.88 x10-14
	Liver Genes- Metabolism and Xenobiotics	5.14 x10-21		Hypoxia	5.83 x10-8
	Fetal Liver Genes- Metabolism and Xenobiotics	6.93 x10-21		Myogenesis	6.75 x10-7
	Genes in Cancer Module 55	1.05 x10-20		Apoptosis	1.96 x10-6
	HLKP Metabolic and Xenobiotic Response Genes	1.06 x10-19		Complement	1.96 x10-6
	Placenta Genes	1.16 x10-19		Kras Signalling	1.96 x10-6
	Genes in the Cancer Module 3	1.76 x10-18		Angiogenesis	6.99 x10-6
	Adhesion Molecules	4.24 x10-18		UV Response DNA Damage	1.48 x10-5
	Ovary Genes	3.48 x10-24		TGFβ Signalling	2.4 x10-5

Figure 3.31. ***Gene Set Enrichment Analysis of Extracellular Proteins.*** *(A) Bar charts of the top 10 terms enriched from the Molecular Signature Database analysis (http://software.broadinstitute.org/gsea/index.jsp) of the indicated categories with the* 48 extracellular proteins from TMT-Proteomics dataset*. In each chart, the GO terms are plotted in order of significance (considering p.value, false-discovery rate and enrichment); on the left is the most significant GO term and on the right is least significant GO term. (B) Enrichment p.values for Gene Set Enrichment Analysis*

3.4.3 Analysis of the Extracellular, PDIA3-Dependent, Heparin-binding Proteins by Protein Association Networks

It was also important to consider how the proteins in the PDIA3-dependent 80 protein dataset might be interacting. This was investigated using Search Tool for the Retrieval of Interacting. Genes/Proteins (STRING) (Szklarczyk et al., 2019). STRING uses a curated database of protein interactions such as co-expression and protein homology. STRING extracts protein database associations from either Biocarta, BioCyc, GO, KEGG or Reactome. A STRING analysis was first done on all 80 proteins in the filtered dataset and carried out at medium confidence (0.40 interaction score). The interaction map appeared to have three focal networks: an extracellular protein cluster, a histone protein cluster and a ribosomal protein cluster, that was linked by a few proteins from the curated database (cyan line). Only 11 of the 80 proteins had no interactions (**Figure 3.32**).

The STRING analysis was repeated on either the 32 intracellular or the 48 extracellular proteins, again using medium confidence, with no text or database interactions included. The extracellular interaction map showed three distinct networks. The plasminogen activator, tissue type(PLAT)/ plasminogen activator, urokinase(PLAU)/SERPINE1 network included the proteins that account for the enrichment in the Platelet Alpha Granule Lumen GO term and the laminin subunit alpha-5 (LAMA5)/ laminin subunit gamma-1(LAMAC1)/ laminin subunit beta-1(LAMB1) were the proteins involved in GO terms relating to the basement membrane (**Figure 3.33**). The largest network included 15 proteins, 9 of which were associated with the GO term Epithelial-Mesenchymal Transition. LAMA5 and LAMAC1 were also included in the GO EMT but were not linked to the extensive protein network (**Figure 3.33**).

The intracellular proteins split into two main interaction groups, one representing ribosomal proteins and the other histone interactions, these groups did not link together (**Figure 3.33**). There was only one mapped protein interaction between the intracellular proteins and an extracellular protein: staphylococcal nuclease and tudor domain containing 1 (SND1) had an experimentally determined and a curated database interaction with fibronectin (FN1) (**Figure 3.33**) (Humphries et al., 2009).

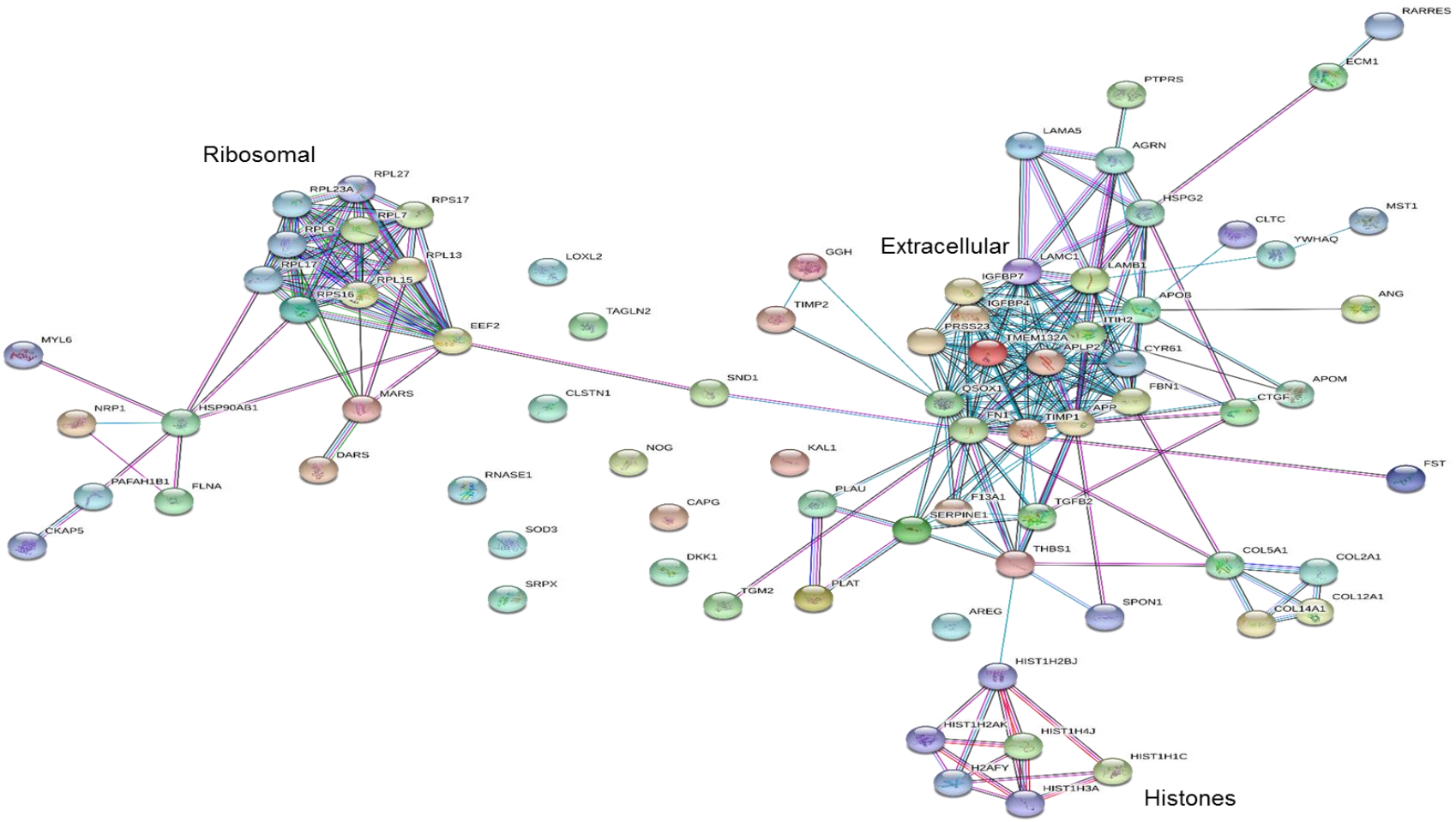

Figure 3.32. ***Output of Search Tool for the Retrieval of Interacting Genes/Proteins (STRING) for the 80 Protein Dataset*** *(https://string-db.org/). All the proteins are identified by gene name. Line Colour Key: Black: Co-expression, Cyan: Curated from Database, Green: Gene Neighborhood, Lilac: Protein Homology, Pink: Experimentally Determined, Red: Gene Fusion, Royal Blue: Gene Cooccurrence.*

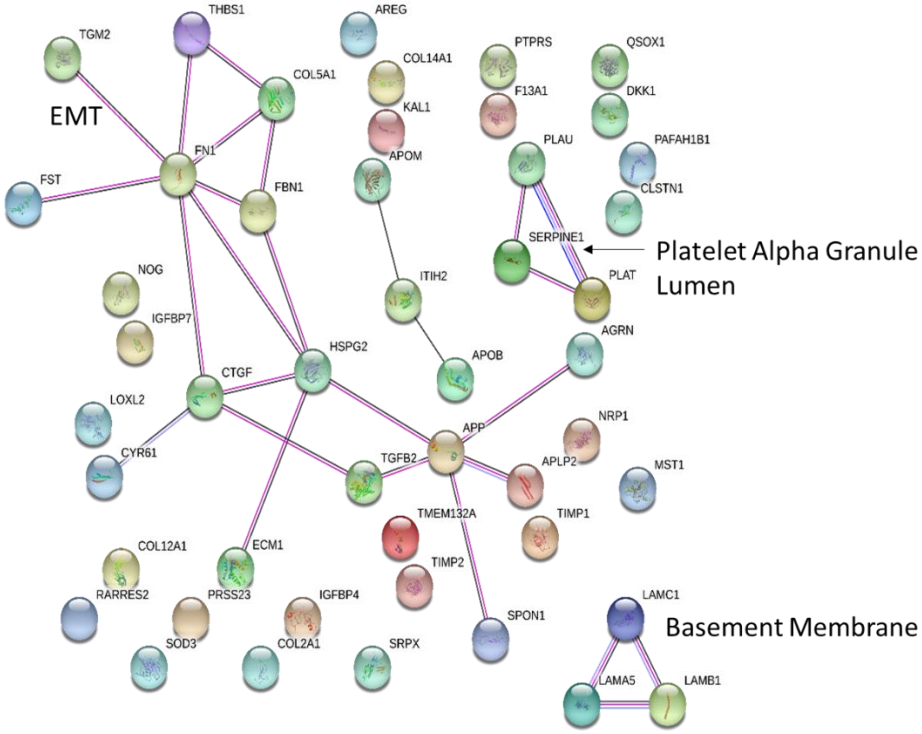

Intracellular Proteins

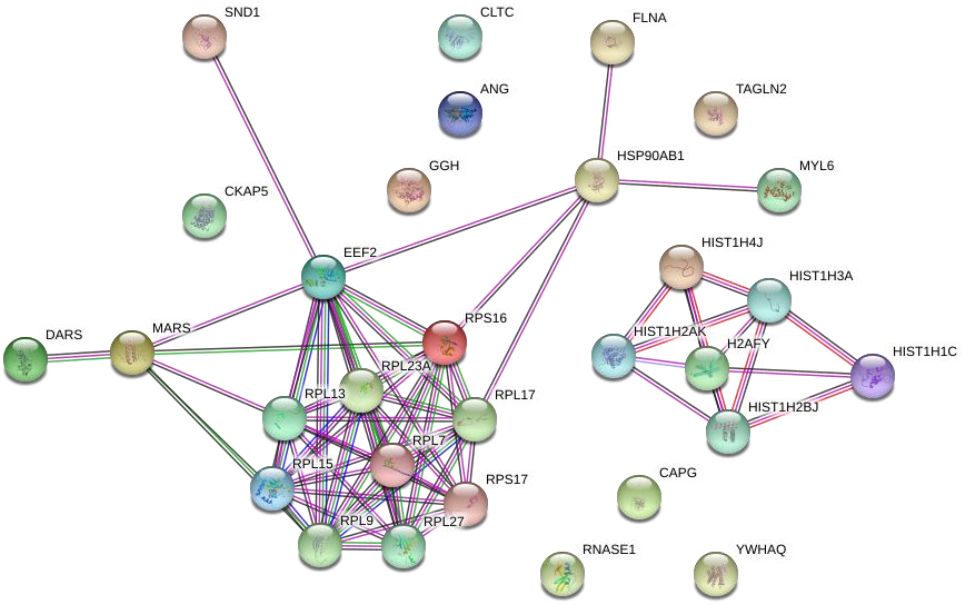

Figure 3.33. **Output of separate STRING analyses for the Extracellular or Intracellular Proteins Identified from the 80 Protein TMT-Proteomics Dataset** (https://string-db.org/). Line Colour Key: Black: Co-expression, Green: Gene Neighborhood, Lilac: Protein Homology, Pink: Experimentally Determined, Royal Blue: Gene Co-occurrence.

Overall the analysis by GO and other bioinformatics showed evidence that the extracellular proteins in the PDIA3-dependent, heparin-binding secretome are involved in many biological, cellular and molecular processes associated with cancer metastasis, such as Locomotion, Integrin Binding and Structural Extracellular Matrix. GO analysis also validated the CM experimental protocol, showing that many of the identified proteins were known heparin-binding proteins found in the ECM or the ER lumen. Also, many of the extracellular proteins contained disulphide bonds. The analysis by STRING highlighted that the major interaction network associated with these proteins included proteins associated with the process of EMT.

3.4.4 Validation of Selected PDIA3-Dependent, Heparin-binding Proteins in the CM of A231 Cells by Immunoblotting

The proteins identified in the TMT-proteomics dataset were identified with a range of protein abundance changes and significances (p.value) (**Figure 3.13**). Insulin Growth Factor Binding Protein 7 (IGFBP7) (p=0.0392) was an extracellular protein close to the p=0.05 significance cut-off. Lysyl-Oxidase Like 2 (LOXL2, p=0.0031), also an extracellular protein, was amongst the most significant identifications with the greatest fold change. To confirm results from the TMT-based quantitative proteomics, immunoblotting experiments were carried out on these selected proteins, IGFBP7 and LOXL2.

Cell lysates and CM were prepared as described in Methods **2.7.** The CM preparation was identical to the TMT-quantitative proteomics workflow. The immunoblots were repeated on three independent samples.

The immunoblots for IGFBP7 (30kDa) revealed a band at 30kDa across all three repeats, with a much stronger band in the CM from cells treated with DMSO (**Figure 3.34**). Repeat one also showed the presence of IGFBP7 in the cell lysates. Quantification of the bands in the CM showed that IGFBP7 abundance was significantly different between the CM from cells treated with DMSO or 16F16, albeit that a loading control was not available to normalise the CM loading. This result was consistent with the TMT-proteomics identification that IGFBP7 is a PDIA3-dependent, heparin-binding protein in the A231 secretome.

All blots for LOXL2 (87kDa) showed a band at just under 100kDa and a second band around 75kDa in the CM but no band in the cell lysates (**Figure 3.34**). Extracellular LOXL2 can be cleaved by serine proteases into a 65kDa protein (Okada et al., 2018) and cleaved LOXL2 is very likely the second band at around 75kDa. Only one blot showed a clear reduction of LOXL2 in the CM after treatment of 16F16. Two blots showed an equally visible band for LOXL2 in the CM treated with 16F16. When quantified there was no statistically significant difference between the abundance of LOXL2 in the two samples.

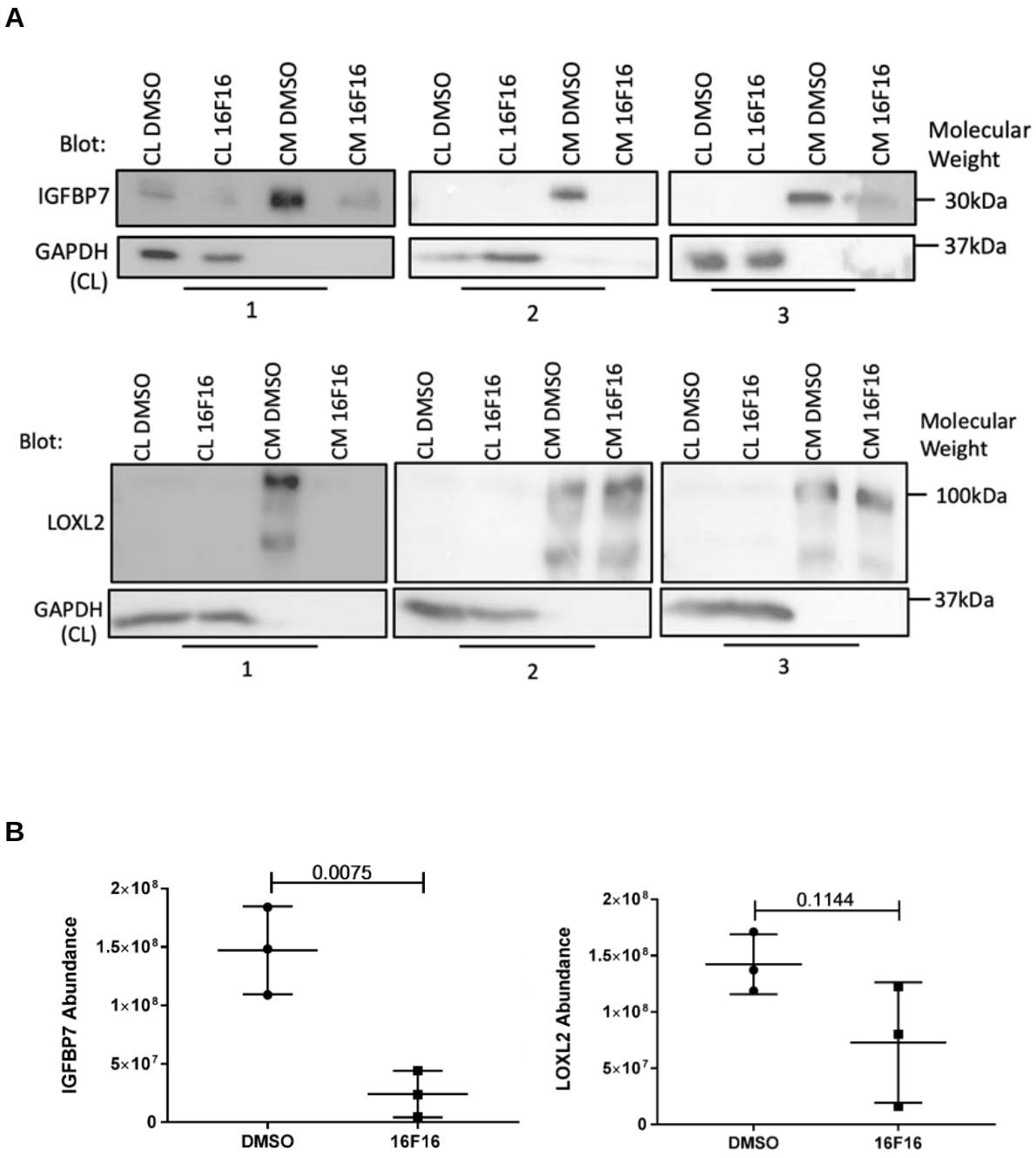

Figure 3.34. ***Assessment of IGFBP7 and LOXL2 in the CM of A231 Cells.*** *(**A**) Proteins were separated on a 10% polyacrylamide gel under reducing conditions, transferred to PVDF membrane and probed with antibodies to IGFBP7 or LOXL2. Images shown from 3 experimental repeats for each protein. Key: CL: Cell Lysate, CM: Conditioned Media. (**B**) Band quantification using Synegene GeneTools© for either IGFBP7 or LOXL2.* Central bar shows the mean, outer bars the range.

3.5 Impact of PDIA3 inhibition on MDA-MB-231 Tumor Cell Spheroid Formation

Culturing cancer cells in 3-dimensions better reflects *in vivo* tumours (Nath and Devi, 2016). To obtain 3D cultures, cells can be grown on non-adherent surfaces, meaning that cells will adhere to each other, rather than the plastic surface, and therefore form a spheroid. To address whether PDIA3 also has a role in A231 phenotype in a 3D culture*,* A231 cells were cultured in scaffold-free 3D conditions (Methods **2.9**) and the rate of spheroid formation was investigated by live-cell imaging under control conditions or after addition of 16F16 to inhibit PDIA3.

3.5.1 Cell Seeding Density and Spheroid Formation

It was first important to consider the plating density of cells suitable to form a spheroid and how long a spheroid would take to form. Based on prior publications, A231 cells were seeded at 40, 200, 1000, 5000 or 10000 cells per well in a scaffold-free, 96-well round bottom ultra-low attachment plate. These are coated with an inert substrate that prevents cell adhesion to the surface and forces the cells to adhere to each other. This plate was imaged over 3 days in an IncuCyte Microscope which has integral heating, gassing and humidity (Methods **2.9.1**). At each cell density, the effect of DMSO (0µM 16F16 control), 50µM 16F16, or medium with supplement only (general control) on the rate of spheroid formation was measured. A digital phase contrast image of each well was taken by the IncuCyte® System every 2 hours for at least 66 hours.

The images of cells at the end of the 66-hour incubation are displayed in **Figure 3.35**. At cell densities of 5000 and 10000 cells/well, the control and DMSO-only conditions showed a grey ‘haze’ in the centre of the cell cluster. This is because the cells in the centre are above the plane of focus of the image and so appear out of focus. In these conditions, one spheroid was formed per well. There was no indication of spheroid formation at other seeding densities. There was no evidence of spheroid formation at any cell density for cells treated with 50µM 16F16, yet the cell sheet appeared healthy in the images.

The area occupied by cells was then quantified using ImageJ software. As a spheroid forms the area of the visible “patch” of cells decreases (Elliott and Yuan, 2011; Härmä et al., 2014; Sodek et al., 2012). Change in area with time is displayed in **Figure 3.36**. For conditions of 40 and 200 cells/well there was no decrease in area over 66 hours incubation, in agreement that these cells did not form visible spheroids. Cell densities above 1000 cells/well all showed a decrease in “patch” area. For 1000 cells/well the decrease occurred in the first 20 hours, for 5000 cells/well over the first 40 hours, and for 10000cells/well, “patch” area decreased between 20 and 50 hours. In general, adding DMSO alone seemed to reduce spheroid compaction compared to the general control. More strikingly, cells treated with 50µM 16F16 did not form spheroids: all seeding cell-densities maintained a high area throughout the 66-hour incubation. This supports the endpoint phase contrast images, which showed no spheroids in wells treated with 16F16 (**Figure. 3.35**).

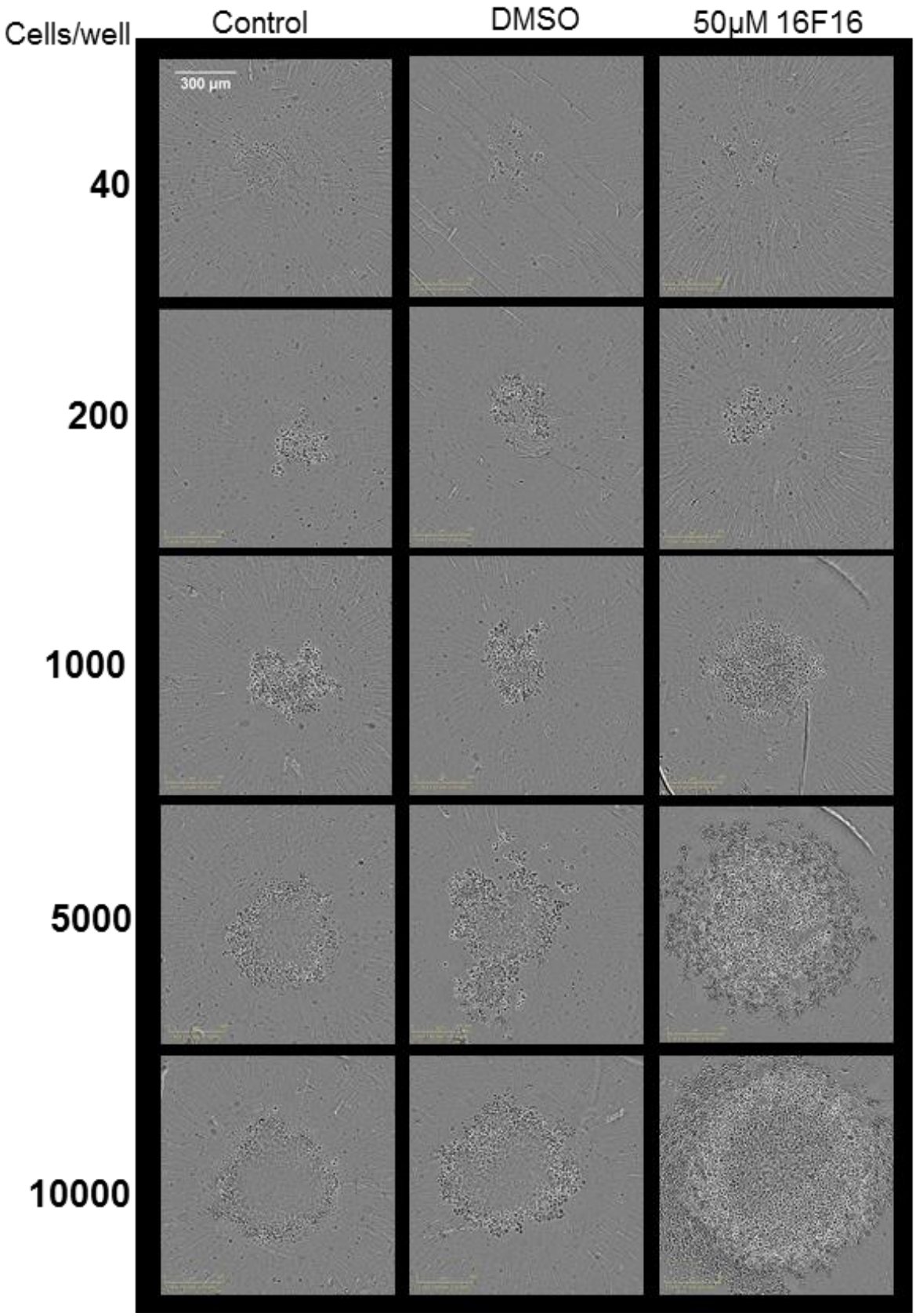

Figure 3.35. ***End Point Phase Contrast Images of A231 Cell Spheroid Formation.*** *Defined number of cells were plated in wells of a scaffold-free 96-well round bottom ultra-low attachment plate in media supplemented with serum and either 50 µM 16F16 or DMSO only. Images were taken on an IncuCyte® S3 Live-Cell Analysis System from 0 hours and then every 2 hours until 66 hours.*

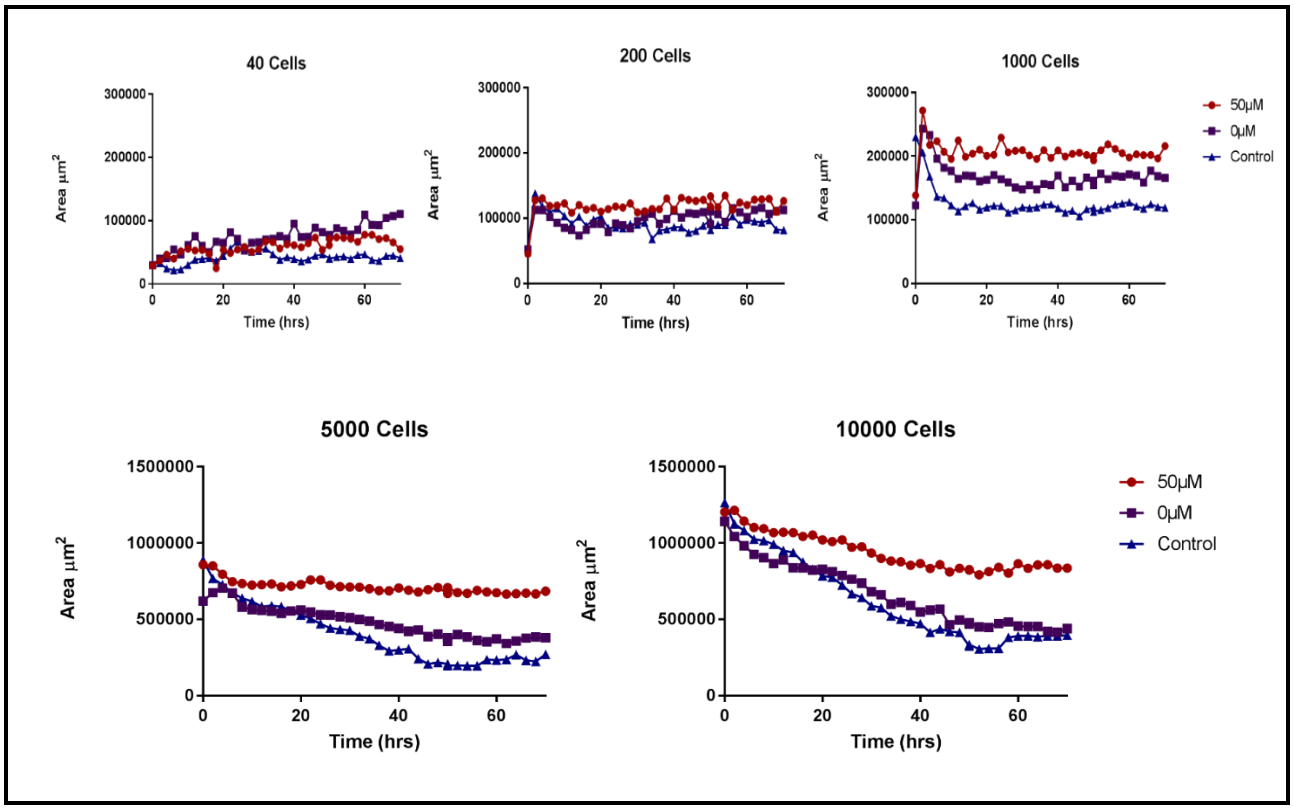

Figure 3.36. ***Rate of Spheroid Formation at Different Seeding Densities.*** *MDA-MB-231 cells were seeded as shown in wells of a scaffold-free 96-well round bottom ultra-low attachment plate and incubated for 66 hours with an image taken every 2 hours. Each line shows the mean area of cells from 6 replicate wells (3-replicate wells for Control) from one experiment.*

The phase contrast images did not provide enough detail to demonstrate clearly that spheroids had formed as 3D objects. When analysing cells in 3D culture it is important to consider the Z-axis. Therefore, spheroids were stained for F-actin and imaged by a confocal laser scanning microscope. Six spheroids grown from 10000 cells/well, under control conditions, were fixed after 66 hours of incubation, transferred to a flat-bottomed 96-well plate using a pipette and then permeabilised and stained with Phalloidin. The spheroids were moved to a 96-well flat bottom plate since the confocal microscope cannot focus accurately on structures in round-bottomed wells. Z-stack images were taken through the depth of each spheroid and 3D image reconstructions were made in Volocity®. The Z-axis of the spheroids was around 80-100μm. The spheroids looked slightly disrupted, this could be because cells on the exterior were damaged during washing and transfer steps (**Figure 3.37**). The image reconstructions confirmed that the spheroids were 3D objects.

3.5.2 Effect of Inhibition of PDIA3 on Rate of Spheroid Formation

The seeding densities of 5000 and 10000 cells/well were taken forward to investigate the effect of PDIA3 inhibition on spheroid formation in more depth. The 96-well spheroid plate was set up for spheroid analysis as described in **3.5.1**, but this time including a range of concentrations of 16F16. Cells were incubated and imaged as before, and spheroid area quantified using ImageJ. At both cell densities, cells treated with DMSO-only decreased in area, in agreement with results from **3.5.1** that spheroids have formed (**Figure 3.38 A**&**B**). However, at 10000 cells/well, there was a clear separation of areas between cultures treated with 10, 17.5 or 25 μM 16F16, which did not decrease in area with time, and the other concentrations tested (**Figure 3.38 B**). However, 16F16 concentration did not have a linear relationship to area decrease. At 5000 cells/well, 5μM and 12.5μM 16F16 resulted in similar final areas, and 10μM- and 25μM-treated cells had closer final areas than cells treated with 25μM or 17.5μM 16F16 (**Figure 3.38 A**). Overall, above a threshold of about 10μM 16F16, PDIA3 inhibition blocked spheroid formation.

The decrease in area of cells (i.e. compaction of cells) was most pronounced most between 20 and 50 hours (**Figure 3.38 A**&**B**). **Figure 3.39** shows phase contrast images of the cells over this period. Between 20 and 50 hours after plating, cultures treated with DMSO only showed a clear reduction in “patch” area, gain of a circular form and an out of focus centre, indicating 3D-spheroid formation. With increasing concentration of 16F16, this phenotype was not apparent at 50-hours, with cells more closely resembling the phenotype of control cells at 20 hours.

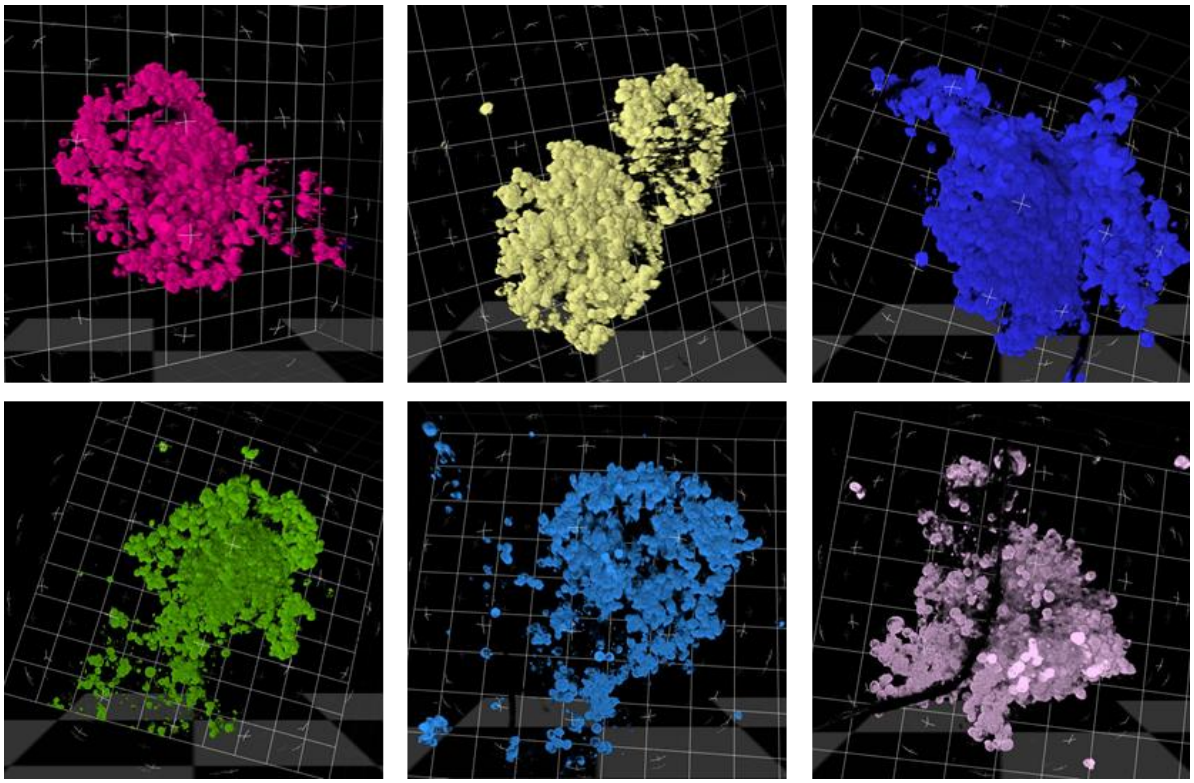

Figure 3.37. ***Fluorescence Microscopy Images of MDA-MB-231 Cell Spheroids.*** *10000 cells/well were plated in a scaffold-free 96-well round bottom ultra-low attachment plate and incubated for 72 hours**.** Cells were then fixed, permeabilized and stained with Phalloidin. 6 spheroids represent 6-replicates from one experiment. Images were taken on a confocal laser scanning microscope (10x objective). The 3D-spheroid reconstruction was made from the Z-stack in Volocity® Software.*

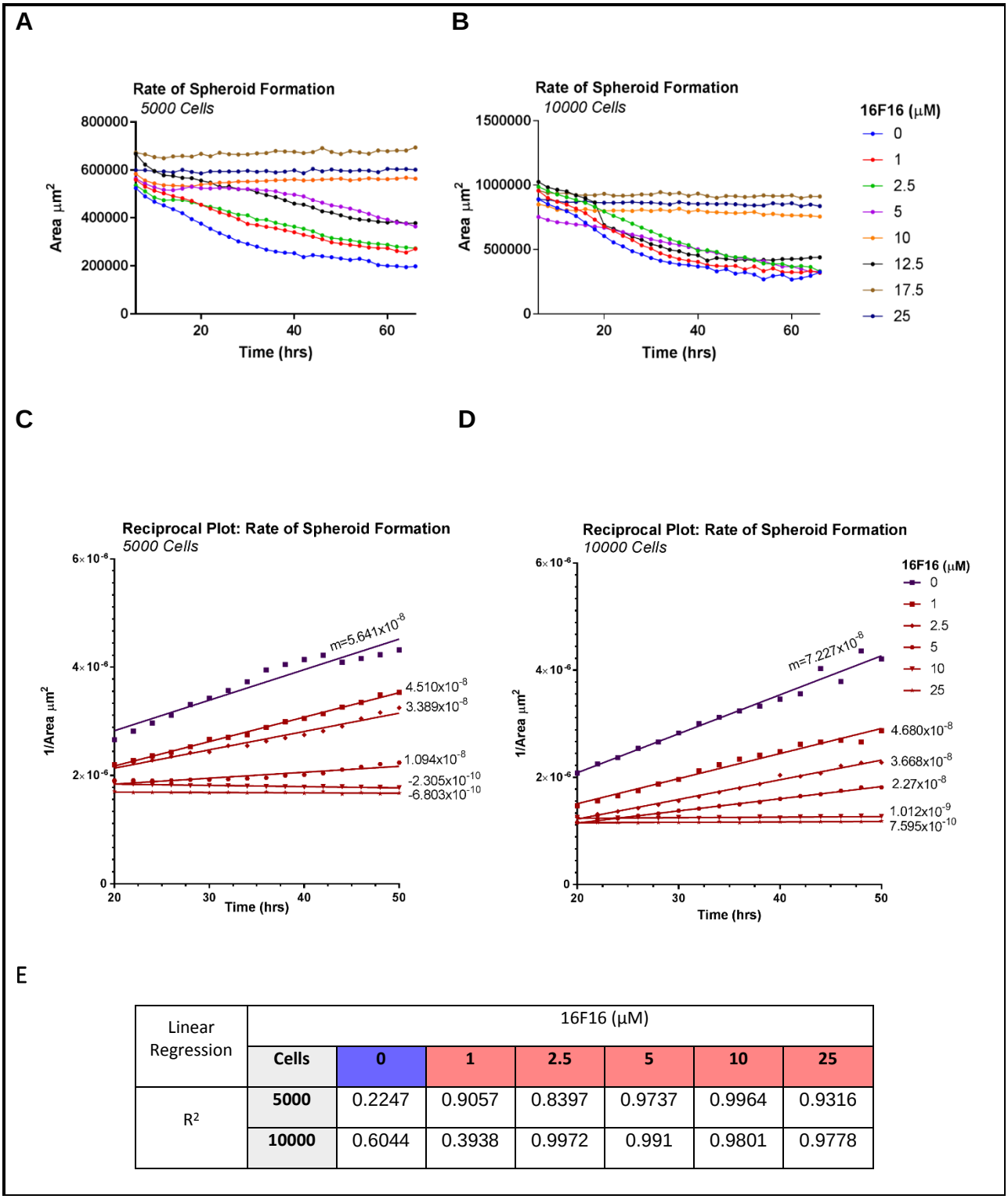

E

Linear Regression	16F16 (µM)						
	Cells	**0**	**1**	**2.5**	**5**	**10**	**25**
R^2	**5000**	0.2247	0.9057	0.8397	0.9737	0.9964	0.9316
	10000	0.6044	0.3938	0.9972	0.991	0.9801	0.9778

Figure 3.38. ***The Effect of PDIA3 Inhibition on the Rate of Spheroid Formation by MDA-MB-231 cells.*** *Defined number of cells were plated in wells of a scaffold-free 96-well round bottom ultra-low attachment plate in DMEM media supplemented with serum and either 1, 2.5, 5. 10 or 25 µM 16F16, or DMSO only. Images were taken using a IncuCyte® S3 Live-Cell Analysis System from 0 hours when cells were seeded and then every 2hours until 66 hours. (**A&B**) Spheroid formation with increasing 16F16 concentration. (**C&D**) Reciprocal plots of spheroid area against time with Line of Best Fit and slope gradient (m). The line of best fit was calculated by Linear Regression. (**E**) Table of goodness of fit (R^2). n=3 experiments, one spheroid per well over 6 replicate wells per experiment except for the third experiment which had two replicate wells.*

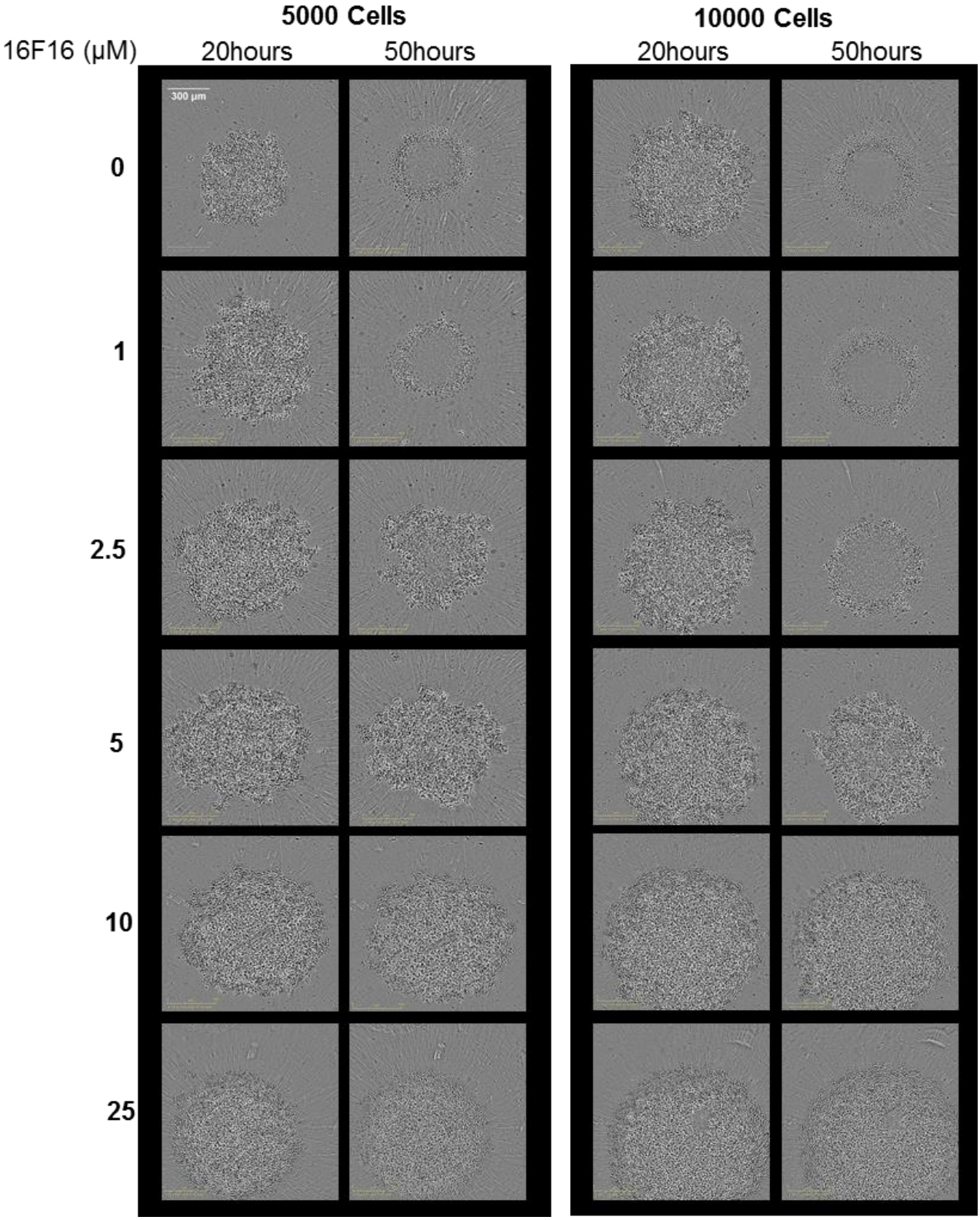

Figure 3.39. ***Phase Contrast Images of A231 Cell Spheroid Formation at 20 and 50 hours.*** *Defined number of cells were plated in wells of a scaffold-free 96-well round bottom ultra-low attachment plate in media supplemented with serum and either 1, 2.5, 5. 10 or 25 μM 16F16, or DMSO only. Images were taken using a IncuCyte® S3 Live-Cell Analysis System from 0 hours when cells were seeded and then every 2hours until 66 hours.*

To better understand the rate of area change, i.e rate of spheroid formation, a reciprocal plot of cell area against time was plotted (**Figure 3.38 C**&**D**). To capture the initial rate of change, these plots were made for the period 20 hours to 50 hours only. The slopes of the lines were then calculated (m = (y2 − y1)/ (x2 − x1)). At both seeding densities, cells treated with DMSO only had the steepest gradient, i.e., the fastest rate of change (5000 cells/well: m= $5.641x10^{-8}$, 10000 cells/well: m= $7.227x10^{-8}$). As 16F16 concentration increased, the rate of spheroid formation decreased (shown by a smaller gradient). This agrees with observations from the phase-contrast images that spheroid formation was reduced at high concentrations of 16F16.

The line of best fit was calculated using Linear Regression. The goodness of fit (R^2) shows how well the line of best fit matches the data and is most accurate when R^2=1. Higher concentrations of 16F16 (5µM, 10µM, 25µM) had R^2 values closer to 1 (R^2>0.80) for both cell seeding densities. This shows that the line of best fit is likely to be representative of the data. At 1µm 16F16, the line of best fit for 5000 cells/well fit the data well (R^2>0.90) but for 10,000 cells/well the fit was very low. This was also true for the line of best fit representing the DMSO condition, R^2 values were 0.2247 and 0.6044 for 5000 or 10000 cells/well (**Figure 3.38 E**). These results may indicate variability in cell plating steps or inaccuracies in the image processing.

The final cell area at 50 hours was also compared between each condition (**Figure 3.40 A**&**B**). Statistical analysis was performed with two-way ANOVA with Tukey's multiple comparison post-hoc test, this showed that 16F16 concentrations of 5µM and above had a statistically significant effect on the final spheroid cell area compared to the DMSO condition. Combining this result with information from the phase contrast images suggests that 5 µM is the threshold concentration of 16F16 to inhibit spheroid formation.

3.5.3 Effect of LOX Inhibition on MDA-MB-231 Spheroid Formation

The TMT-proteomics experiments (**3.4**) revealed that Lysyl-Oxidase Like 2 (LOXL2) was one of the most significantly decreased proteins in the heparin-binding, PDIA3-dependent secretome dataset (**Figure 3.12**). LOXL2 is also a known substrate of PDIA3 (Jessop et al., 2007b) and in GO LOXL2 is part of an Epithelial-to-Mesenchymal Transition signature. Its abundance is also highly associated with metastatic breast cancer ECM (Salvador et al., 2017). To investigate the possible contribution of LOXL2 to spheroid formation by A231 cells, LOXL2 was inhibited using β-aminopropionitrile (βAPN). βAPN is not LOXL2-specific but is an irreversible inhibitor of the LOX and LOX-like family of enzymes (Hutchinson et al., 2017).

To attempt substantial LOXL2 inhibition, cells were pre-treated with 500µM βAPN for 3 days before being plated into the 96-well spheroid plate. This time and βAPN concentration were used for prior experiments with fibroblasts (Rosini et al., 2018). Spheroids were then grown as described in **3.5.1** with the addition of either 0, 5, 50, 250, 500 or 1000µM βAPN to wells seeded with 5000 or 10000 cells per well, and incubated for 66 hours.

Spheroids were formed in all conditions regardless of the βAPN concentration (**Figure 3.42**). The phase contrast images of the spheroids display the change in phenotype indicating a spheroid: an out-of-focus centre and circular, compacted arrangement of cells (**Figure 3.41**).

The rate of area change was the same in all wells at both 5000 and 10000 cells/well, with the greatest area change between 20 and 50 hours (**Figure 3.42**). Thus, every well formed a spheroid regardless of βAPN concentration.

A

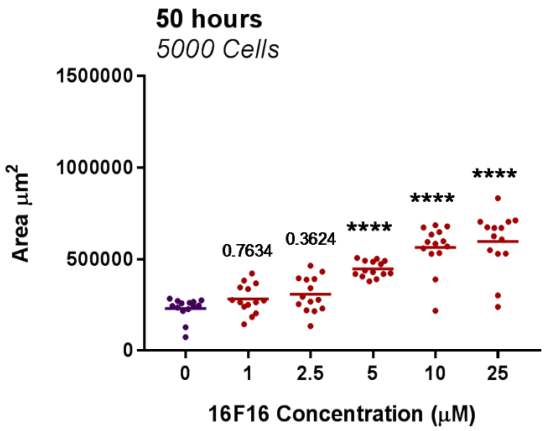

B

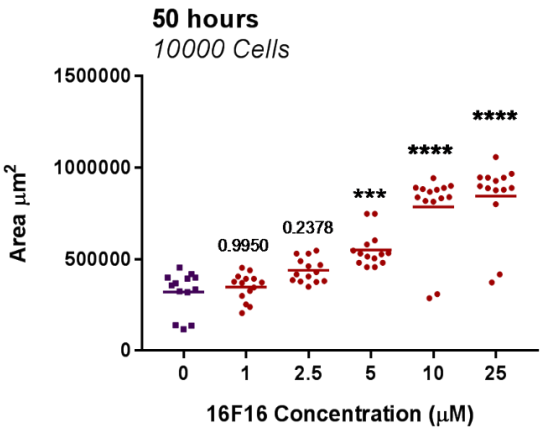

C

Tukey's Multiple Comparison Test		
Cell Number	5000	10000
16F16 (µM)	Adjusted p.value	
0 vs. 1	0.7634	0.995
0 vs. 2.5	0.3624	0.2378
0 vs. 5	<0.0001	0.0007
0 vs. 10	<0.0001	<0.0001
0 vs. 25	<0.0001	<0.0001

Tukey's Multiple Comparison Test		
Cell Number	5000	10000
16F16 (µM)	Adjusted p.value	
1 vs. 2.5	0.9872	0.5138
1 vs. 5	0.0008	0.0031
1 vs. 10	<0.0001	<0.0001
1 vs. 25	<0.0001	<0.0001
2.5 vs. 5	0.0071	0.2851
2.5 vs. 10	<0.0001	<0.0001
2.5 vs. 25	<0.0001	<0.0001
5 vs. 10	0.0378	0.0004
5 vs. 25	0.0029	<0.0001
10 vs. 25	0.9562	0.8714

Figure 3.40. ***Analysis of Final Spheroid Area from MDA-MB-231 Cells Grown in Different Concentrations of 16F16. (A&B)*** *Defined number of cells were plated in wells of a scaffold-free 96-well round bottom ultra-low attachment plate in DMEM media supplemented with serum and either 1, 2.5, 5. 10 or 25 µM 16F16, or DMSO only. Images were taken using the IncuCyte® System and area quantified using ImageJ. Results show spheroid area at 50 hours. Plotted significance compares spheroid area to DMSO only spheroid area at 50hours.* ***(C)*** *Tables shows Tukey's Multiple Comparison test of ANOVA results. Adjusted p.values highlighted (yellow) compare the spheroid area at 50 hours against the spheroid area treated with DMSO only. Non-highlighted (white) shows pairwise multiple comparison of spheroid area. n=3 independent experiments.*

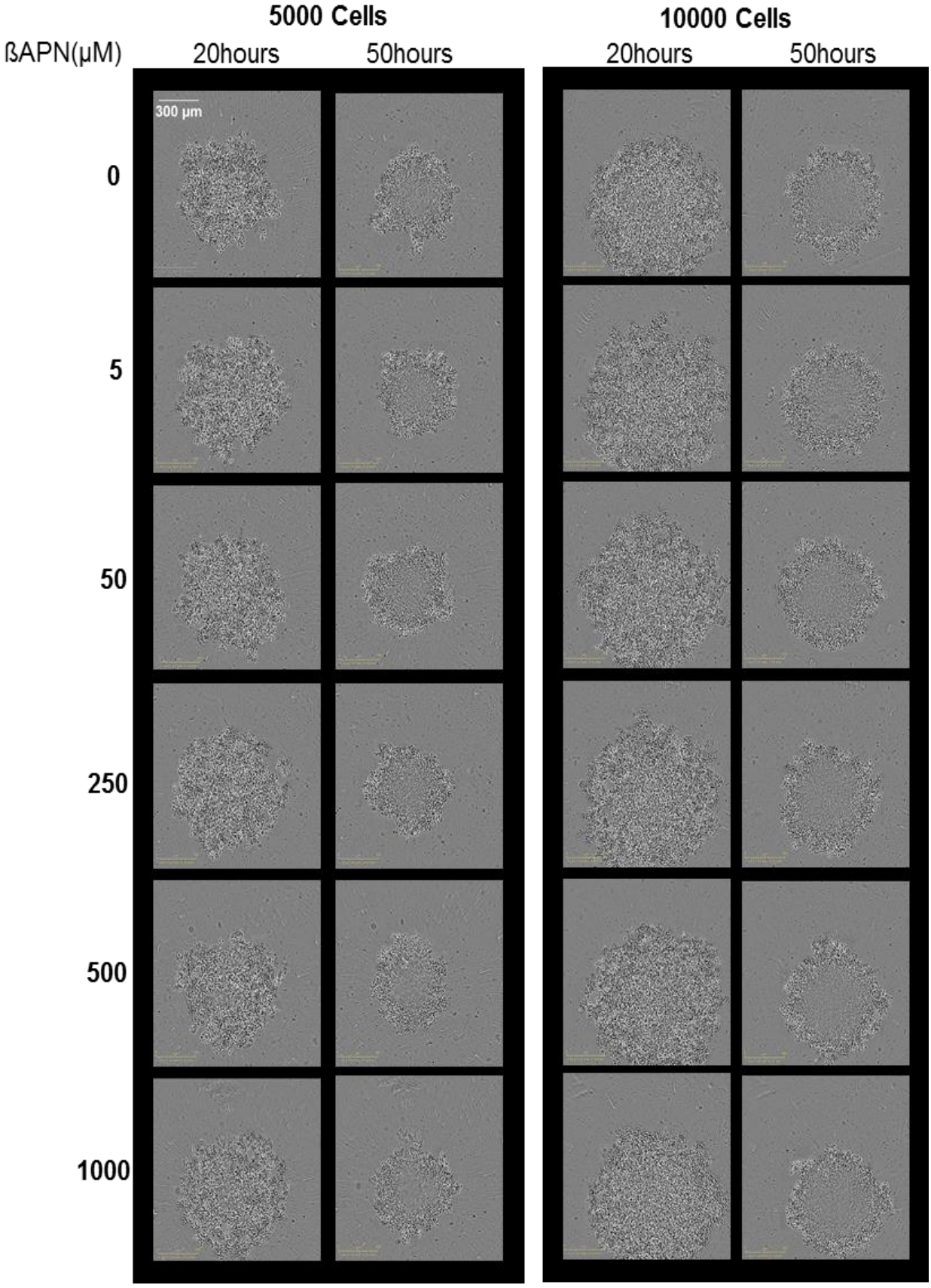

Figure 3.41. ***Phase Contrast Images of MDA-MB-A231 Cell Spheroids after βAPN Treatment.*** *Cells were plated in 96-well round bottom ultra-low attachment plate with different βAPN concentrations for 66 hours. Images were taken by the IncuCyte® System at 0 hours and then every 2 hours.*

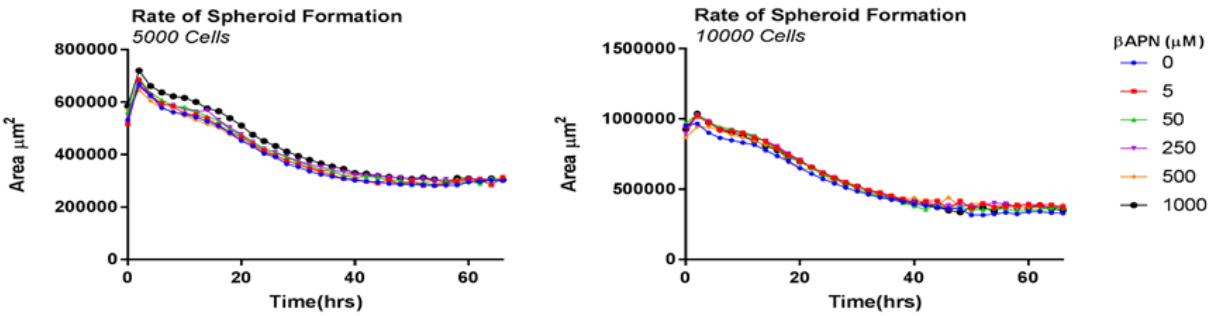

Figure 3.42. ***The Effect of βAPN on the Rate of Spheroid Formation by MDA-MB-231 cells.*** *Cells were seeded at either 5000 or 10000 cells/well in the presence of the indicated concentration of βAPN or DMSO-only control. Spheroid area was analyzed by the IncuCyte® System and quantified by ImageJ.*

Chapter 4 Discussion

The main goal of this project was to identify the PDIA3-dependent secretome of A231 human breast cancer cells. The effect of PDIA3 on A231 breast cancer cells was investigated with a combination of 2D and 3D cell-based assays. Identification of the heparin-binding fraction of the PDIA3-dependent secretome was then carried out by TMT-proteomics and validated by immunoblots. In-depth bioinformatic analysis then suggested that the heparin-binding fraction of the PDIA3-dependent secretome was associated with many Gene Ontology (GO) terms related to cancer metastasis such as cell-adhesion, EMT, ECM, locomotion and integrin binding (Subramanian et al., 2005; Eden et al., 2009).

Limitations of the research are that in each experiment PDIA3 was inhibited pharmacologically only with 16F16. 16F16 has not been proven to specifically target PDIA3 and potentially targets PDIA1 and other proteins in the thioredoxin superfamily (Hoffstrom et al., 2010). It would be advantageous for further analysis of the PDIA3-dependent secretome to be achieved with a CRISPR-mediated PDIA3 gene editing or with siRNA to PDIA3, or other specific pharmacological inhibitors as they become available (Altieri et al., 2019).

Furthermore, analysis of the PDIA3-dependent secretome has only been performed using one cell line (A231). There are a total of 26 basal breast cancer cell lines that can be divided into into basal A or basal B phenotypes depending on transcriptional profile: A231 represents only 1/14 of basal B breast cancer cell lines (Dai et al., 2017). Future analysis should analyse the PDIA3-dependent secretome in other basal cell lines (such as MDA-MB-157, BT549 and MCF10A). It may also be important to assess the impact of PDIA3 in explant cultures, as these organotypically cultured cells better represent *in vivo* conditions and present a more accurate ECM model (Marino et al., 2016). Specific outcomes of the research are discussed below.

4.1 Cell-Based Experiments

4.1.1 2D Cell Culture

The results from all the 2D cell-based experiments are summarised in **Table 4.1A**.

Generally, the results from the 2D cell-based experiments suggest that the activity of PDIA3 promotes phenotypes in A231 cells that are associated with *in vitro* metastatic behaviour-cell spreading and pro-migratory F-actin structures. Immunofluorescence was used to observe cell features that indicate pro-migratory capacity. Naïve A231 cells incubated with conditioned media (CM) from cells that had been pre-treated with 16F16 had fewer lamellipodia and stress fibres compared to cells grown in fibroblast growth medium (FGM) or CM from cells that had been pre-treated with DMSO only. Average cell area and the apparent number of focal adhesions, both at 4 and 20 hours of adhesion, was also significantly lower than for the two control conditions. The results also showed less focal adhesions in naïve A231 cells incubated in CM that had been pre-treated with 16F16.

A

2-Dimensional Assays: Cell Features Indicative of a Greater Migratory Capacity						
	Conditioned Media	F-actin Organisation (L+ SF)		Cell Spreading		Cell Attachment (Focal Adhesions)
		4 hrs	20 hrs	4 hrs	20 hrs	
Effect of PDIA3	Fresh FGM Only	✓	✓	✓	✓	✓
	+ DMSO	✓	✓	✓	X	✓
	+ 16F16	X	L / X	X	X	X
Effect of HBP	Fresh FGM Only	✓	✓	✓	✓	N/A
	+ Control CM	✓	✓	✓	✓	N/A
	+ CM w/o HBPs	X	✓	X	X	N/A

B

3-Dimensional Cell Based Assay: Spheroid Formation							
Inhibitor (μM)	16F16	0	1	2.5	5	10	25
	Spheroid	✓					X
	βAPN	0	5	50	250	500	1000
	Spheroid	✓	✓	✓	✓	✓	✓

Table 4.1. **Summary of Data from the Cell-Based Experiments**. Each feature is compared to the Fresh FGM Only condition. Key: HBP- Heparin Binding Proteins, L- lamellipodia, N/A- experiment not performed, SF-Stress fibres.

The latter experiment was only performed once, and results would become clearer upon repetition. The naïve A231 cells incubated in CM that had been pre-treated with DMSO seemed to have less focal adhesions that when grown in fresh FGM. This shows that incubation with CM alone may have affected focal adhesions. It is also noteworthy that naïve A231 cells incubated for 20 hours in CM pre-treated with DMSO showed a significant decrease in cell spreading compared cells grown for 20 hours in FGM. Perhaps the reason for the disparity is because the CM contains cellular waste products and apoptotic bodies that could be stressful or toxic to naïve cells, whilst the FGM is fresh and engineered for optimal cell growth. Efforts to remove cell debris were done by passing CM through a 0.22μM syringe filter, allowing only proteins and small vesicles to pass through (Moussay et al., 2011). Despite this limitation, the CM of cells treated with 16F16 had a significantly different effect on cell behaviour, implicating PDIA3 activity in promoting phenotypic features characteristic of a pro-metastatic phenotype.

The same type of 2D cell adhesion experiment was used to access the contribution of heparin-binding proteins in the cell secretome. Although assessment of focal adhesions is a good parameter for measuring contractile migration, this was not carried out due to project time constraints. A231 cells incubated with CM depleted of HBP showed a decrease in the number of lamellipodia but not of actin stress fibres. These cells also showed a significant decrease in cell area at both 4 and 20 hours compared to A231 cells incubated with fresh FGM or CM depleted of non-specific, agarose bead-binding proteins.

At this stage of the project it was unknown whether the heparin-agarose beads were effectively removing heparin-binding proteins from the CM. Validation on a small scale could be achieved by collecting the heparin-agarose beads (post incubation with the CM), dissociating proteins from heparin-agarose beads and separating the proteins on SDS-PAGE and then carrying out a western blot. Proteins could then be identified by probing with antibodies against common heparin-binding proteins in the CM e.g. thrombospondin-1 (TSP1) or fibronectin (FN) (Carbon et al., 2009). However, in the timeline of the project, validations were made through identification of proteins by TMT-proteomics.

4.1.2 3D Cell Culture

Cell culture in 3-dimensions better represents *in vivo* conditions and makes results more physiologically relevant. The results in these experiments showed an inverse correlation between the rate of spheroid formation and the concentration of 16F16 applied to A231 cells, when cells were seeded into low-attachment wells at 5000 or 10000 cells per well (**Table 4.1B**).

Although the phase contrast images of spheroids showed evidence of being 3D (**Figure 3.39**), the Z-axis of the spheroids was not measured. The ‘flattened’ phase contrast digital images of spheroid areas could be misleading because these do not show spheroid height. Therefore results from a 2D spheroid image for total spheroid area cannot be conclusive (Costa et al., 2016). Potential methods

to resolve this issue would include measuring the spheroid Z-axis using high content screening, for example, Perkin Elmer Opera LX System (Opera System) attached to a confocal microscope, allowing high resolution for 3D phase contrast imaging (Foitzik et al., 2016). This would allow 3D image analysis of all 96 spheroids to be measured in one experiment. However, the Opera System is incompatible with the round bottomed wells of the 96-well plate used in the spheroid experiments. Therefore, the 3D nature of the spheroids was assessed by transfer of 6 spheroids grown in control conditions to wells of a flat-bottomed 96-well plate, staining for F-actin, and collection of 3D images of these spheroids via confocal microscopy Z stacks.

Considering the 2D spheroid measurements from the phase contrast images, PDIA3 seemed to have a contribution in the rate of spheroid formation. A line of best fit was calculated for the rate of spheroid formation at each concentration of 16F16 applied to the A231 cells. Coefficient of determination (R^2) was used to measure how well the data fitted the line of best fit; an R^2 closer to 1 is a good fit. Most of the lines of best fits for the different 16F16 concentrations were over 0.90. Conditions with an R^2 much lower than 1 were with DMSO-only at both cell seeding densities and 1μM 16F16 at 10000 cells seeded. It is clear from **Figure 3.36 C, D & E** that the data do not fit the line of best fit well. The results were presented with one axis (area) plotted as a reciprocal; this was done to make the data more linear. Possible reasons for less correlation to a linear trend at lower concentrations of 16F16 could be that the rate of spheroid formation is more non-linear under these conditions than spheroid formation at high 16F16 concentrations (as shown in **Figure 3.36 C & D**). The deviance in R^2 may just be a reflection that these are the most non-linear rates of spheroid formation. Other reasons for variations in R^2 could include inaccuracies in cell plating or inaccuracies in thresholding the digital image in ImageJ.

All concentrations of 16F16 caused a significant change in the final spheroid areas at 50 hours compared to the DMSO-only condition, apart from 0μM vs. 1μM and 0μM vs. 2.5μM 16F16 which were not significantly different. There was also no significant difference in final spheroid area between 1μM and 2.5μM 16F16. The incremental rise in increase in final spheroid area with 16F16 concentration may suggest that PDIA3 inhibition has a proportional effect on spheroid formation. However, 16F16 is toxic at high concentrations (10μM and 25μM) and perhaps spheroid formation is inhibited because normal cellular activities are being affected by 16F16 induced-toxicity making the cells more stressed (Hoffstrom et al., 2010).

Formation of a 3D spheroid involves the coordinated compaction of many cells and is accompanied by a change in phenotype, for example, cells in 3D form different cell-cell and cell-matrix adhesions that make a different ECM environment (Costa et al., 2016). With concentrations of 16F16 above 12.5μM A231 cells were unable to form a spheroid, which suggests that PDIA3 has some role in cell plasticity. It would be interesting to analyse the cytoskeletal structure of cells (proteins markers for

actin, vimentin and vinculin) in a spheroid to see if they are more epithelial or mesenchymal and test for E- and N-cadherin expression (Konstantinovsky et al., 2012; Iglesias et al., 2013).

Spheroid formation seemed unaffected by lysyl-oxidase like 2 (LOXL2) inhibition, LOXL2 will be discussed in **4.3.**

4.2 The PDIA3-Dependent Secretome

To relate the results from inhibition with 16F16 to the similar effects of depletion of heparin-binding proteins, the heparin-binding fraction of the PDIA3-depdendent secretome was identified by TMT-based proteomics. This experiment identified 80 heparin-binding proteins reproducibly decreased in CM after inhibition with 16F16. 48 of these are extracellular proteins. The majority of bioinformatic analysis focused on the extracellular protein subset. Primarily, this was because extracellular proteins would be expected to be found in the CM. Analysis by Gene Ontology (GO) was performed on two bioinformatic platforms to increase confidence of association.

The first investigations began with Gene Set Enrichment Analysis (GSEA) and showed that only the extracellular proteins were significantly related to GO cancer terms; these included Biological Adhesion, EMT and Extracellular Structure Organisation (Subramanian et al., 2005). Related GO terms were identified when analysed with a second GO tool - Gene Ontology Enrichment Analysis and Visualisation (Gorilla) (Eden et al., 2009).

The extracellular proteins were also related to significant GO Cancer Module terms, whilst the intracellular proteins were not. The most significant GO term that described the extracellular proteins in the PDIA3-dependent secretome was EMT ($p= 8.79x10^{-29}$) which involved 18 of the extracellular proteins. Protein association network analysis with STRNG showed that many of the extracellular proteins were associated in a large network of 15 proteins, mainly by experimental determination or co-expression (Szklarczyk et al., 2019). Six of the proteins in this network were classified in EMT.

There were 32 significantly decreased intracellular proteins found in the heparin-binding fraction of the PDIA3-dependent secretome, which included many ribosomal and histone proteins. These were significantly related to GO terms in Protein Localisation to ER, Ribsome and RNA binding. It is interesting to speculate why intracellular proteins were found in the heparin-binding fraction of the PDIA3-dependent secretome. Intracellular proteins could arise in the CM after cell necrosis or cell damage that might result as part of experimental protocol, however both test and control conditions were treated in the same manner and so this doesn't explain the difference in intracellular protein composition. It is more likely that cell damage may arise from slight 16F16 induced toxicity, however, analysis of BiP protein did not provide evidence that 16F16 increased UPR (Hoffstrom et al., 2010). Also, the cell images did not show evidence of nuclear fragmentation.

The CM for proteomics was filtered through a 0.45µm pore size membrane and would exclude large cell debris. One possible explanation for the presence of intracellular proteins is that they arise from

exosomes. Exosomes are from endosomal origin and carry intracellular proteins, they are small, typically 100nm in diameter and would pass through the 0.45µm pore size membrane into the CM. The occurrence of proteins with transmembrane domains in the dataset could also be explained by exosomes- amyloid-like protein 2 (APLP2) and receptor-type tyrosine-protein phosphatase S (PTPRS) are both transmembrane proteins known to be present in exosomes (Keerthikumar et al., 2016; Mathivanan 2009).

The intracellular proteins showed no significant associations with GO terms related to an unfolded protein response (UPR). This is in agreement with immunoblot of binding immunoglobulin protein (BiP) on A231 cell lysates. After inhibition of PDIA3 with 16F16 the abundance of BiP was unchanged which suggests no induction of UPR with PDIA3 inhibition.

Further investigations into the PDIA3-dependent secretome may consider enriching the CM by other methods such as immunodepletion (selecting the top six most abundant proteins in the CM to be removed) or by ligand-based enrichment, instead of enrichment with heparin-beads (Severino et al., 2013; Paulus et al., 2009).

4.3 Validation of the PDIA3-Dependent Secretome

The results from TMT-based proteomics revealed that proteins from the CM were successfully captured by the heparin-beads and that a heparin-binding fraction of the PDIA3-dependent secretome had been identified. GO revealed that the extracellular proteins were significantly related to Heparin Binding (11 proteins) using GSEA analysis (**Figure 3.20**). However, not all proteins in the heparin-binding fraction of the PDIA3-dependent secretome may be direct targets of PDIA3. Indeed, none of the intracellular proteins (except RNASE4) contained disulphide bonds or cysteine-rich domains and therefore seem unlikely to be targets of PDIA3. Validation that a protein is a target of PDIA3 could have been achieved by adding a fluorescent mass-tag PDIA3 and treating cells with N-Ethylmaleimide (NEM) to prevents thiol exchange (Jessop et al., 2007). This results in a fluorescently labelled mass-tagged PDIA3 becoming irreversibly, covalently linked to a target protein during oxidoreductase exchange. PDIA3 can then be purified from cell lysates with an affinity isolation column of agarose beads conjugated to an antibody complementary to the mass-tag that was added to PDIA3. PDIA3 and associated target proteins can be eluted out the column, separated by SDS-PAGE and visualised by immunoblot. Precise PDIA3 targets identification can be achieved by taking protein bands from the gel and analysing the protein content by mass spectroscopy.

Validation of selected proteins found by TMT-based proteomics in this study was done by immunoblotting. Two proteins were selected; insulin growth factor binding protein 7 (IGFBP7) because TMT-based proteomics suggested that it had a high p.value near to the significance cut-off threshold (p=0.392), and LOXL2 because it had a very low p.value (p=0.003). On blots, IGFBP7 was significantly reduced in the CM from cells treated with 16F16 but LOXL2 was not. The TMT-proteomics entailed a more precise methodology that was repeated four independent times. It would

be worth repeating LOXL2 immunoblot a fourth time since there is a large disparity between the results from experiments one and two and experiment three. Alternatively, the LOXL2 antibody specificity was not validated. It is possible that the antibody recognises other LOX family members that are not PDIA3-dependent.

LOXL2 is a known target of PDIA3 (Jessop et al., 2007) and was amongst the most significant and most greatly changed (Log2FoldChange = -2.525) proteins in the heparin-binding fraction of the PDIA3-depedent secretome. It has roles in cross-linking collagens and associations with cancer (Salvador et al., 2017; Cuevas et al., 2017; Wang et al., 2019a). For these reasons, LOXL2 was inhibited with beta-aminopropionitrile (βAPN) and the effect on 3D spheroid formation by A231 cells was analysed. Inhibition of LOXL2 did not reproduce the results of 16F16 treatment on 3D spheroid formation. At all βAPN concentrations tested, A231 cells were able to form spheroids (**Figure 3.40**). This may give some indication that a network of proteins in the heparin-binding fraction of the PDIA3-dependent secretome is necessary for spheroid compaction. However, βAPN is a general LOX-family inhibitor and might not effectively inhibit LOXL2 (Chang et al., 2017). Few specific inhibitors of LOXL2 exist. Recently 2-chloropyridin-4-yl)methanamine was shown to be selective and effective for irreversible LOXL2 inhibition over LOX and could be a candidate inhibitor for future investigation (Hutchinson et al., 2017). LOXL2 could also be diminished by using antibodies against LOXL2 to block or deplete it in the CM of A231 cells, or by CRISPR-mediated *LOXL2* gene-editing (Ikenaga et al., 2019). These methods might yield a more profound impact on 3D spheroid formation, and as mentioned in **4.1.2**, consideration of the Z-axis should be taken into account in future measurements (Friedrich et al., 2009).

4.4 Implications for Future Research on PDIA3 and Breast Cancer Metastasis

The heparin-binding fraction of the PDIA3-dependent secretome was identified from 2D-based cell culture assays and therefore may only be representative of *in vitro* 2D cell culture. Future experiments could focus on identifying the PDIA3-dependent secretome from 3D culture, this would be more physiologically relevant and may lead to successful identification of cancer biomarkers (Brandi et al., 2018b). Future experiments could involve CM that better represents the tumour microenvironment by analysis of the PDIA3-dependent secretome from *in vitro* co-cultures of A231 cells with fibroblasts (Arrigoni et al., 2016).

Bioinformatic analysis of the heparin-binding fraction of the PDIA3-dependent secretome revealed three protein association networks in the extracellular protein subset (**Figure 3.32**). All three are linked with aspects of breast cancer metastasis. The first large network represents EMT as described in **4.2**. The second network consists of three laminin chains (LAMA5, LAMB1 and LAMC1) and represents components of the basement membrane (BM). BM was the second most enriched GO term in the heparin-binding fraction of the PDIA3-dependent secretome. The BM has a complex role in breast cancer metastasis; it acts as a tumour suppressor and must be breached before cancer

becomes invasive, however, there are some reports that some types of laminin can promote anchorage-independent proliferation by influencing autocrine signalling in the TME by other cancer cells, acting through integrins (Chang et al., 2017; Zahir et al., 2003; Carpenter et al., 2009). Some laminins have also been linked to EMT (Kim et al., 2011). The precise role of PDIA3 in maintaining the BM and the effect of laminins on breast cancer progression is unclear, but laminin β1, β3, γ1 and γ2 have been identified as PDIA3 substrates (Jessop et al., 2007).

The third network displayed on **Figure 3.32** represents proteins that were enriched in the GO term Platelet Alpha Granule Lumen. This GO term was the most enriched of all the GO terms found for the heparin-binding fraction of the PDIA3-dependent secretome and contains urokinase (PLAU) which had the highest fold change (Log2FoldChange= -3.024). Upon further inspection of the extracellular proteins with Reactome (https://reactome.org/PathwayBrowser/#TOOL=AT) it became clear that Fibrin Clot Dissolution was very highly enriched (**Figure 4.1**). A protein found in this pathway, SERPINE1, is a poor prognosis marker for breast cancer (Duffy, 2002; Janicke et al., 2001). This pathway includes the urokinase plasminogen activator system (uPAR). Activation of this pathway is thought to be an essential part of breast cancer metastasis. Cascading activation of serine proteases (including PLAU) catalyses the conversion of plasminogen to plasmin. Active plasmin is able to degrade and remodel ECM, enhancing cell migration and invasiveness (Tang and Han, 2013). It is a novel finding that PDIA3 is related to the uPAR system and future work may seek to investigate this relationship.

Previous research on PDIA3 in the Adams laboratory suggested that basal breast cancer cell lines may be more dependent of PDIA3 for 2D migration (H.S.Young, unpublished data, 2018). My own analysis of gene expression in breast cancer cell lines and tumours from clinical datasets suggests that the many of the transcripts encoding proteins of the heparin-binding fraction of the PDIA3-dependent secretome are more highly expressed in basal B breast tumours and cell lines (**Figure 4.2**) (Ringnér et al., 2011). In future, perhaps some of these proteins may be valid biomarkers for early detection of aggressive breast cancer. However, research on PDIA3 in breast cancer metastasis is still in its early stages and further work is needed to elucidate its role in malignancy.

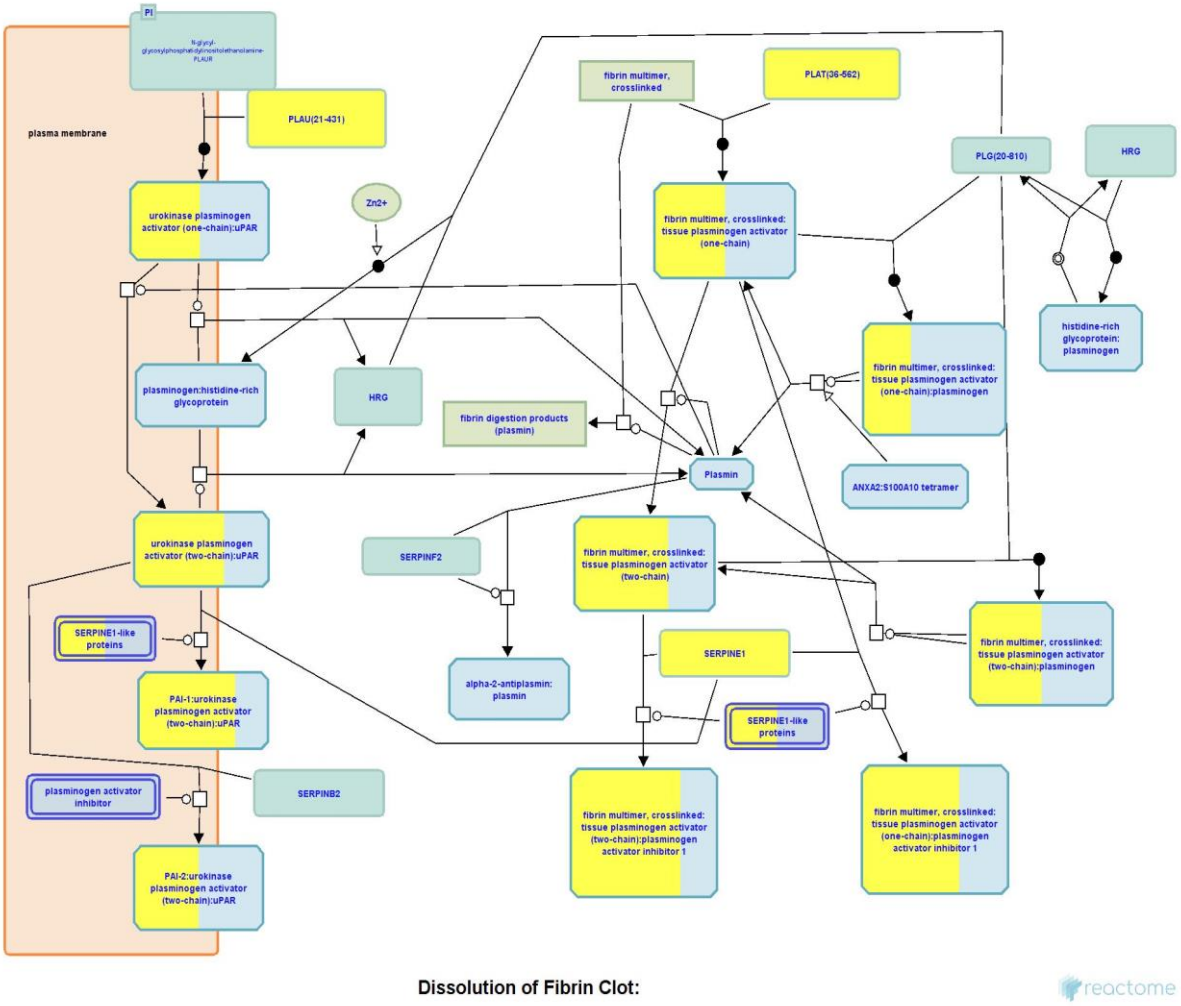

Figure 4.1. ***Dissolution of Fibrin Clot Markers Identified by Reactome*** *(https://reactome.org/PathwayBrowser/#TOOL=AT). The 48 extracellular proteins from the heparin-binding fraction of the PDIA3-dependent secretome were analysed.* ***Colour Key****: Blue Box; Protein Complex, Green Box; Protein, Green Circle; Small Molecule, Orange; Cell Compartment, White; Extracellular Space, Yellow; Enrichment in Pathway.* ***Line Key****: Arrow end; Positive Regulation, Black circle; Binding, Circle end; Catalyst, White Square; Transition.*

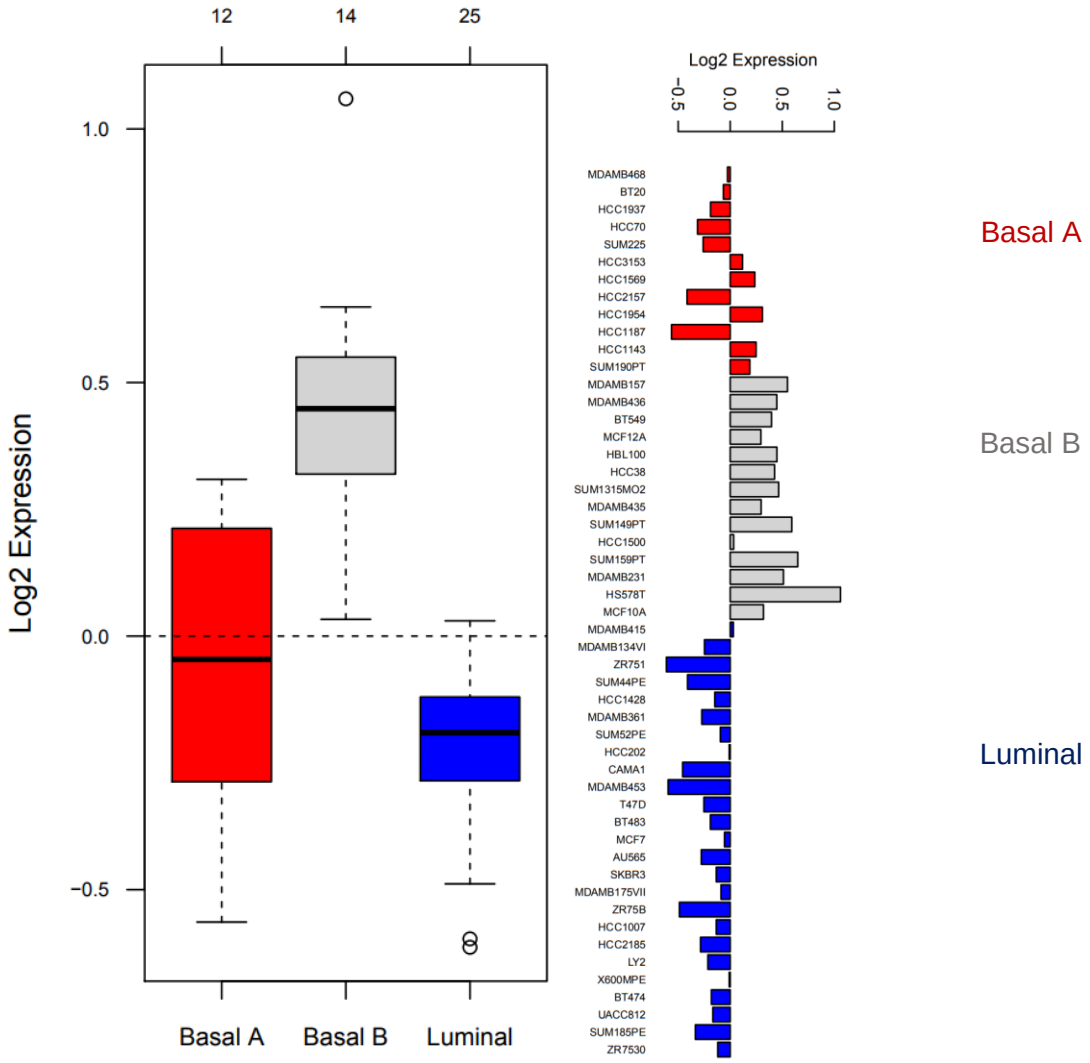

Figure 4.2. ***Conditions of mRNAs Encoding Extracellular Proteins of the Heparin-Binding Fraction of the PDIA3-Dependent Secretome of A231 Cells (48 proteins).*** *Breast Cancer Tumours (left) or Cell Lines (right). Results identified from Gene expression-based Outcome for Breast cancer Online. (*http://co.bmc.lu.se/gobo/gobo.pl*)* (Ringnér et al., 2011).

4.5 Contribution to Knowledge

The novel research contributions of this research are:

1. Analysis in A231 cells of effects of the PDIA3-dependent secretome and the heparin-binding fraction of the secretome on cell spreading, focal adhesions and F-actin organisation.

2. Assessment of the role of PDIA3 in scaffold-free 3D spheroid formation.

3. Identification of proteins of the heparin-binding fraction of the PDIA3-dependent secretome in A231 breast cancer cells and a strong suggestion for roles in aspects of cancer biology (migration, adhesion, extracellular matrix) from Gene Ontology and other bioinformatic tools.

Overall the results suggest a role for the PDIA3-dependent secretome in promoting a pro-metastatic phenotype in A231 cells.

These investigations into the role of the PDIA3-dependent secretome of MDA-MB-231 breast cancer cells are summarised in **Figure 4.3**.

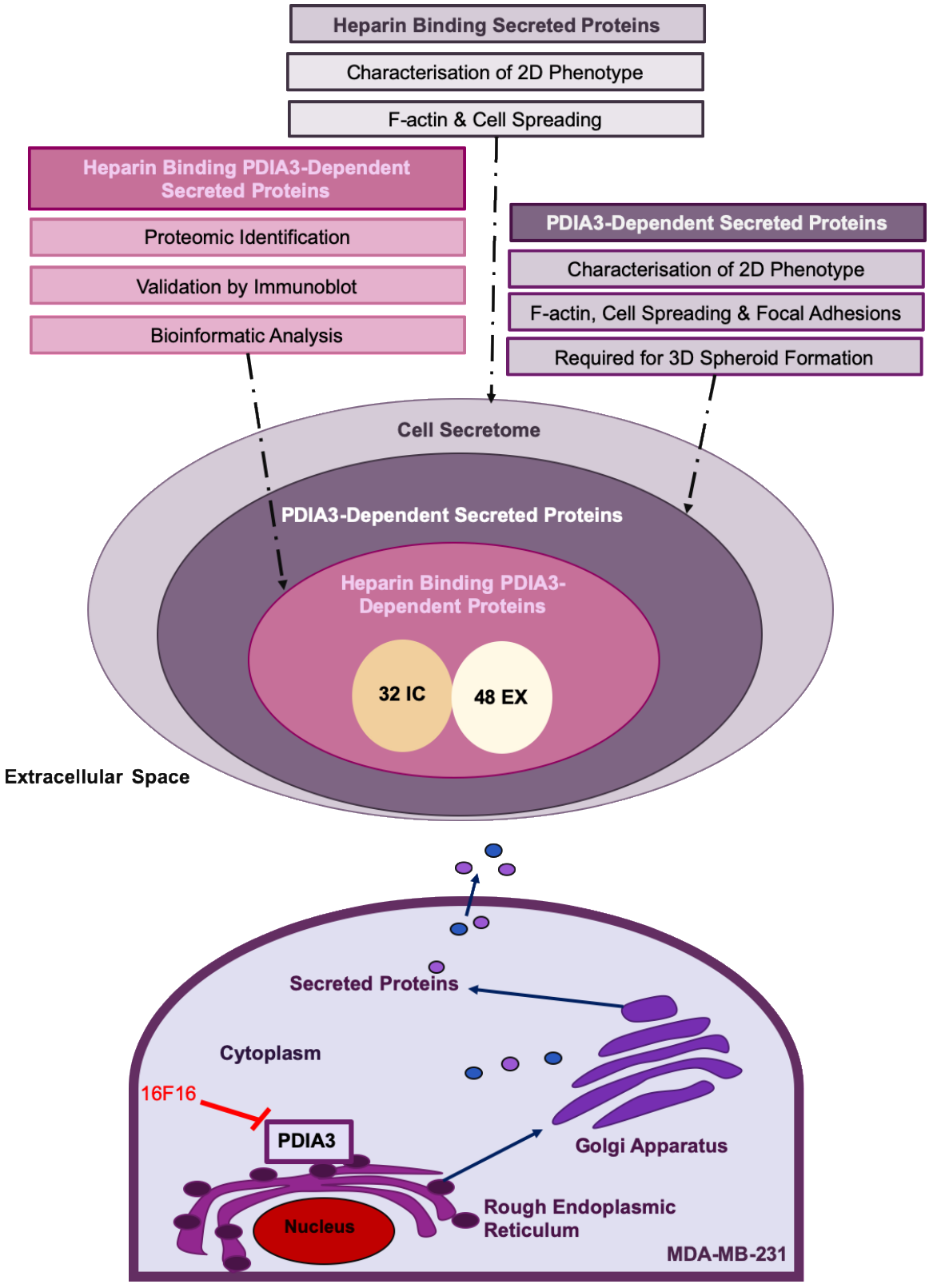

Figure 4.3 ***Summary Figure.*** *Figure summarises the achievements of the project and contribution to knowledge of the effects of PDIA3 in vitro. Key: EX; extracellular, IC; intracellular.*

Chapter 5 Appendix

***Table 5.1. Global Protein Changes identified from Four TMT-Proteomics Experiments**. Ranked by t-test value. Colour Gradient Key (for Log(2)Mean and Log(2)Median)): Red: More negative in +16F16 condition. Blue: Increased in +16F16 condition. Key: AAs, Amino Acids; AR, Abundance Ratio; MW, Molecular Weight.*

	AR(16F16/DMSO)				Log(2) AR(16F16/DMSO)				Log(2)Mean	Log(2)Median	Log(2)	Two-tailed	Exp.				# Unique		
Gene Name	n=1	n=2	n=3	n=4	n=1	n=2	n=3	n=4	AR	AR	Std.Dev	T.Test	q-value	Coverage	# Peptides	# PSMs	Peptides	# AAs	MW [kDa]
LAMA5	0.148	0.278	0.276	0.236	-2.75	-1.849	-1.856	-2.082	-2.1356702	-1.9693897	0.427	0.002123	0	15.88633	45	81	45	3695	399.5
LOXL2	0.114	0.145	0.192	0.287	-3.14	-2.786	-2.377	-1.8	-2.5250547	-2.5816899	0.575	0.003105	0	37.4677	27	68	27	774	86.7
APOM	0.284	0.484	0.342	0.427	-1.81	-1.047	-1.553	-1.229	-1.4107749	-1.3913348	0.341	0.003684	0.006	7.978723	2	3	2	188	21.2
SRPX	0.142	0.179	0.066	0.186	-2.81	-2.486	-3.958	-2.431	-2.9219424	-2.6491495	0.711	0.003773	0	17.4569	7	9	7	464	51.5
PLAU	0.061	0.218	0.144	0.119	-4.04	-2.195	-2.797	-3.066	-3.023537	-2.9316466	0.766	0.004244	0	44.2029	19	38	19	414	46.9
RPL35	0.323	0.47	0.389	0.534	-1.63	-1.088	-1.363	-0.906	-1.2472808	-1.2255956	0.318	0.004316	0.001	9.467456	2	5	2	169	17.8
FST	0.215	0.419	0.363	0.262	-2.22	-1.254	-1.46	-1.934	-1.7167933	-1.6969326	0.44	0.004366	0	55.23256	16	26	16	344	38
TMEM132A	0.109	0.176	0.331	0.215	-3.2	-2.508	-1.596	-2.215	-2.3787419	-2.3617713	0.664	0.005597	0	11.82796	9	16	9	1023	110
EBNA-2	0.168	0.309	0.402	0.301	-2.57	-1.696	-1.313	-1.731	-1.8275192	-1.7136018	0.53	0.006235	0	26.86722	23	37	23	964	107.4
MST1	0.204	0.447	0.155	0.208	-2.29	-1.161	-2.689	-2.267	-2.1018817	-2.2788487	0.656	0.007715	0	7.310345	5	7	5	725	81.9
PAFAH1B1	0.296	0.473	0.508	0.282	-1.75	-1.079	-0.983	-1.827	-1.4109131	-1.4168677	0.441	0.007755	0	7.073171	3	5	3	410	46.6
PTPRS	0.188	0.327	0.469	0.267	-2.41	-1.614	-1.091	-1.907	-1.7551539	-1.7606185	0.551	0.007818	0	10.83162	14	22	14	1948	216.9
FBN1	0.173	0.362	0.375	0.371	-2.53	-1.464	-1.414	-1.43	-1.7104915	-1.447239	0.549	0.008341	0	6.443748	17	19	17	2871	312
COL5A1	0.06	0.18	0.239	0.21	-4.07	-2.471	-2.064	-2.252	-2.7141914	-2.3614838	0.919	0.009684	0	7.834603	12	20	12	1838	183.4
TLN1	0.337	0.378	0.56	0.582	-1.57	-1.405	-0.839	-0.78	-1.1479049	-1.1219334	0.398	0.010323	0	3.010164	8	10	8	2558	271.3
THBS1	0.088	0.192	0.263	0.335	-3.5	-2.38	-1.928	-1.576	-2.3464902	-2.1536795	0.838	0.01124	0	63.93162	71	294	53	1170	129.3
TGFB2	0.162	0.47	0.339	0.277	-2.62	-1.09	-1.561	-1.853	-1.7820041	-1.7073757	0.643	0.011589	0	23.91304	11	21	10	414	47.7
HSP90AB1	0.315	0.447	0.52	0.608	-1.67	-1.16	-0.944	-0.718	-1.1219743	-1.0520877	0.405	0.011615	0	41.98895	36	75	17	724	83.2
NOG	0.11	0.355	0.228	0.329	-3.18	-1.495	-2.134	-1.603	-2.1033241	-1.8683305	0.771	0.012113	0	11.2069	2	5	2	232	25.7
QSOX1	0.195	0.435	0.473	0.299	-2.36	-1.202	-1.079	-1.741	-1.5960099	-1.4714309	0.586	0.012146	0	22.22222	14	23	14	747	82.5
LAMC1	0.127	0.225	0.455	0.27	-2.97	-2.151	-1.135	-1.891	-2.0373001	-2.020967	0.757	0.012577	0	25.48167	34	60	34	1609	177.5
HSPG2	0.185	0.284	0.391	0.5	-2.43	-1.817	-1.355	-1	-1.6506679	-1.5857854	0.619	0.012861	0	5.351856	17	28	17	4391	468.5

	AR(16F16/DMSO)				Log(2) AR(16F16/DMSO)				Log(2)Mean	Log(2)Median	Log(2)	Two-tailed	Exp.				# Unique		
Gene Name	n=1	n=2	n=3	n=4	n=1	n=2	n=3	n=4	AR	AR	Std.Dev	T.Test	q-value	Coverage	# Peptides	# PSMs	Peptides	# AAs	MW [kDa]
RAB15	0.338	0.489	0.66	0.496	-1.57	-1.032	-0.601	-1.01	-1.0527681	-1.0213837	0.396	0.012998	0.001	8.943089	2	3	1	246	27.9
PRSS23	0.087	0.283	0.143	0.35	-3.52	-1.821	-2.809	-1.516	-2.4160793	-2.3150395	0.919	0.013401	0	30.28721	9	14	9	383	43
PSMC2	0.467	0.77	0.553	0.565	-1.1	-0.376	-0.866	-0.824	-0.7911196	-0.8451277	0.302	0.013479	0.001	7.621247	3	3	3	433	48.6
LAMB1	0.097	0.165	0.38	0.289	-3.36	-2.597	-1.396	-1.793	-2.2863674	-2.1947993	0.873	0.013524	0	11.98895	22	34	22	1810	200.3
HSP90	0.211	0.305	0.526	0.442	-2.25	-1.715	-0.927	-1.18	-1.5170403	-1.4473228	0.587	0.014045	0	20.67248	16	21	14	803	92.4
COL12A1	0.112	0.095	0.347	0.311	-3.16	-3.388	-1.528	-1.686	-2.4406569	-2.4229085	0.969	0.015075	0	32.02742	84	154	84	3063	332.9
PRDX6	0.488	0.663	0.771	0.601	-1.04	-0.593	-0.375	-0.735	-0.6844709	-0.663697	0.277	0.015858	0	20.08929	4	7	4	224	25
HIST1H3A	0.07	0.379	0.167	0.221	-3.83	-1.398	-2.582	-2.177	-2.4970574	-2.3798074	1.016	0.016109	0	28.67647	5	12	5	136	15.4
SOD3	0.238	0.611	0.305	0.416	-2.07	-0.712	-1.713	-1.264	-1.4393214	-1.4887592	0.586	0.016155	0	42.91667	8	18	8	240	25.8
SPON1	0.201	0.345	0.441	0.533	-2.31	-1.534	-1.184	-0.909	-1.4849532	-1.3594091	0.608	0.016398	0	6.69145	5	7	5	807	90.9
CAPG	0.219	0.462	0.528	0.241	-2.19	-1.114	-0.921	-2.055	-1.5695783	-1.5845247	0.645	0.016559	0	11.49425	4	5	4	348	38.5
TAGLN2	0.232	0.365	0.531	0.525	-2.11	-1.455	-0.914	-0.93	-1.3523447	-1.1929173	0.564	0.017233	0.001	9.547739	2	2	2	199	22.4
TGM2	0.142	0.325	0.475	0.343	-2.81	-1.619	-1.074	-1.544	-1.7630843	-1.5817583	0.741	0.017637	0	28.52984	17	29	17	687	77.3
ITIH2	0.176	0.234	0.5	0.439	-2.51	-2.098	-0.999	-1.189	-1.698212	-1.6438549	0.721	0.018108	0	6.969377	7	21	7	947	106.5
RARRES2	0.18	0.28	0.191	0.593	-2.47	-1.834	-2.387	-0.753	-1.8617888	-2.1104577	0.791	0.018172	0	25.76687	4	7	4	163	18.6
RPL23A	0.176	0.294	0.493	0.476	-2.5	-1.768	-1.021	-1.071	-1.5905264	-1.4191983	0.697	0.019757	0	26.28866	5	8	5	194	21.9
RPS25	0.246	0.521	0.584	0.404	-2.03	-0.942	-0.774	-1.308	-1.2623533	-1.124691	0.556	0.019985	0	21.6	4	6	4	125	13.7
TKT	0.254	0.453	0.595	0.514	-1.98	-1.142	-0.757	-0.96	-1.2092816	-1.0510047	0.536	0.020349	0.001	4.333868	2	2	2	623	67.8
RPS17	0.211	0.383	0.462	0.57	-2.24	-1.385	-1.113	-0.812	-1.3879816	-1.2486368	0.616	0.020404	0	10.10274	6	9	6	584	64.5
AGRN	0.161	0.278	0.598	0.299	-2.63	-1.846	-0.743	-1.741	-1.7400312	-1.7935973	0.774	0.020565	0	7.398453	14	18	14	2068	217.2
BQ8482_100073	0.283	0.647	0.525	0.346	-1.82	-0.629	-0.924	-1.53	-1.2261558	-1.2272878	0.546	0.020581	0.028	1.827676	1	2	1	383	41
GGH	0.142	0.407	0.354	0.44	-2.82	-1.298	-1.5	-1.186	-1.7007781	-1.3987747	0.757	0.020587	0	32.38994	11	24	11	318	36
RPL27	0.189	0.432	0.493	0.453	-2.41	-1.211	-1.02	-1.143	-1.445244	-1.1770752	0.646	0.020782	0	41.17647	5	7	5	136	15.8
PLAT	0.1	0.168	0.52	0.235	-3.33	-2.578	-0.944	-2.086	-2.2336892	-2.3319686	1	0.02087	0	29.89324	13	23	13	562	62.9
HIST1H2BJ	0.074	0.396	0.252	0.231	-3.76	-1.337	-1.988	-2.114	-2.2989619	-2.0508764	1.03	0.020922	0	57.93651	9	26	2	126	13.9
HIST1H1C	0.146	0.54	0.274	0.364	-2.78	-0.889	-1.865	-1.457	-1.7465709	-1.6608583	0.794	0.021771	0	23.47418	6	12	1	213	21.4
HIST1H2BA	0.077	0.462	0.194	0.223	-3.7	-1.113	-2.368	-2.162	-2.335328	-2.264785	1.062	0.021812	0	43.9759	9	27	2	166	18
RPS16	0.176	0.517	0.462	0.344	-2.51	-0.953	-1.113	-1.541	-1.5291117	-1.3266751	0.7	0.022139	0	45.20548	9	14	9	146	16.4
LOXL4	0.386	0.613	0.617	0.294	-1.37	-0.705	-0.702	-1.766	-1.1366365	-1.0389833	0.525	0.022728	0	5.15873	3	5	3	756	84.4
DKK1	0.073	0.351	0.211	0.336	-3.77	-1.51	-2.24	-1.574	-2.2738224	-1.9068098	1.052	0.022798	0	32.33083	9	21	9	266	28.7
CTGF	0.138	0.553	0.264	0.34	-2.86	-0.856	-1.922	-1.556	-1.7986455	-1.7386296	0.835	0.023037	0	51.86246	15	31	15	349	38
DARS	0.239	0.599	0.251	0.51	-2.06	-0.739	-2.012	-0.97	-1.4465135	-1.4911632	0.691	0.024792	0	11.57685	4	6	4	501	57.1
RAC1	0.074	0.124	0.548	0.167	-3.76	-3.01	-0.874	-2.582	-2.5559649	-2.7959034	1.222	0.024881	0.001	14.74359	1	2	1	156	17.6
MARS	0.272	0.272	0.727	0.395	-1.88	-1.881	-0.461	-1.338	-1.3898559	-1.6087943	0.67	0.025437	0.001	4.666667	3	4	3	900	101.1

	AR(16F16/DMSO)				Log(2) AR(16F16/DMSO)				Log(2)Mean	Log(2)Median	Log(2)	Two-tailed	Exp.				# Unique		
Gene Name	n=1	n=2	n=3	n=4	n=1	n=2	n=3	n=4	AR	AR	Std.Dev	T.Test	q-value	Coverage	# Peptides	# PSMs	Peptides	# AAs	MW [kDa]
TIMP1	0.147	0.497	0.387	0.399	-2.77	-1.01	-1.37	-1.326	-1.6184572	-1.3480533	0.783	0.025661	0	32.36715	5	14	5	207	23.2
CLTC	0.24	0.408	0.708	0.304	-2.06	-1.294	-0.496	-1.716	-1.3916507	-1.5052237	0.674	0.025798	0	3.871352	6	7	6	1679	191.9
CKAP5	0.205	0.268	0.6	0.49	-2.28	-1.9	-0.74	-1.027	-1.487524	-1.4635032	0.724	0.026117	0.001	2.214567	4	4	4	2032	225.4
RPS20	0.25	0.438	0.629	0.538	-2	-1.191	-0.67	-0.895	-1.1894264	-1.0431419	0.582	0.026484	0	19.32773	2	5	2	119	13.4
COL14A1	0.162	0.433	0.495	0.427	-2.62	-1.208	-1.014	-1.228	-1.5187709	-1.21815	0.744	0.02651	0	2.951002	6	12	6	1796	193.4
MYL6	0.195	0.403	0.537	0.522	-2.36	-1.311	-0.888	-0.938	-1.3739248	-1.1243688	0.683	0.027613	0.001	8.823529	2	3	2	238	26.7
TFPI	0.359	0.782	0.553	0.435	-1.48	-0.355	-0.856	-1.202	-0.9724703	-1.0287297	0.484	0.027672	0	11.18421	3	5	3	304	35
HIST1H4L	0.085	0.48	0.324	0.192	-3.56	-1.06	-1.628	-2.377	-2.1553382	-2.0024541	1.079	0.028094	0	52.42718	7	24	7	103	11.4
NRP1	0.162	0.328	0.555	0.455	-2.63	-1.609	-0.849	-1.136	-1.555604	-1.3723724	0.781	0.028278	0	17.6598	11	18	11	923	103.1
ECM1	0.107	0.26	0.324	0.533	-3.23	-1.944	-1.627	-0.908	-1.926161	-1.7856141	0.968	0.028414	0	25	12	22	12	540	60.6
APP	0.146	0.148	0.495	0.454	-2.78	-2.754	-1.016	-1.14	-1.9213461	-1.9470212	0.976	0.029152	0	34.67532	25	78	24	770	86.9
YWHAQ	0.229	0.687	0.469	0.307	-2.13	-0.541	-1.091	-1.705	-1.3660859	-1.3980099	0.696	0.029384	0	16.73469	3	8	2	245	27.7
RPL17	0.189	0.544	0.553	0.342	-2.4	-0.878	-0.855	-1.546	-1.4196243	-1.2119873	0.728	0.029903	0	25	5	7	5	228	26.4
PLK4	0.253	0.528	0.564	0.597	-1.98	-0.921	-0.826	-0.745	-1.1184735	-0.8736185	0.58	0.030773	0.002	1.237113	1	3	1	970	108.9
SERPINE1	0.1	0.602	0.25	0.244	-3.32	-0.733	-2.002	-2.032	-2.0207217	-2.017128	1.055	0.031316	0	49.25373	16	43	16	402	45
EEF2	0.201	0.493	0.637	0.354	-2.31	-1.02	-0.65	-1.496	-1.3700683	-1.2579805	0.718	0.031692	0	11.18881	8	12	8	858	95.3
TIMP2	0.132	0.383	0.431	0.484	-2.92	-1.384	-1.213	-1.046	-1.6417313	-1.2986287	0.866	0.032189	0	27.27273	10	21	10	220	24.4
RARS	0.202	0.547	0.502	0.509	-2.3	-0.871	-1	-0.972	-1.2868402	-0.986047	0.681	0.032406	0.001	4.393939	3	3	3	660	75.3
LECT2	0.233	0.596	0.542	0.506	-2.1	-0.746	-0.882	-0.983	-1.1784994	-0.9327118	0.624	0.032473	0.001	11.25828	2	4	2	151	16.4
RPL7	0.178	0.585	0.512	0.344	-2.49	-0.773	-0.965	-1.54	-1.441263	-1.2526984	0.769	0.033177	0	35.90734	10	14	10	259	30.4
RPL9	0.273	0.676	0.343	0.15	-1.88	-0.565	-1.546	-2.74	-1.681409	-1.7105966	0.899	0.03331	0.001	7.272727	2	3	2	220	25
RPS7	0.213	0.547	0.401	0.617	-2.23	-0.87	-1.32	-0.695	-1.2796285	-1.0947965	0.689	0.033881	0	23.71134	5	8	5	194	22.1
eEF1a1	0.485	0.708	0.818	0.48	-1.04	-0.498	-0.29	-1.059	-0.7230816	-0.7714625	0.389	0.033945	0	37.01299	15	30	15	462	50.1
CHID1	0.251	0.635	0.472	0.586	-2	-0.656	-1.079	-0.771	-1.1258617	-0.9251193	0.608	0.034144	0	10.57269	5	8	5	454	51
CLSTN3	0.138	0.194	0.633	0.38	-2.86	-2.369	-0.659	-1.394	-1.8196567	-1.8815105	0.984	0.034327	0	11.19247	8	12	8	956	106
RPSA	0.591	0.723	0.293	0.445	-0.76	-0.468	-1.769	-1.167	-1.0406681	-0.9628409	0.564	0.034504	0	10	2	4	2	300	33.3
HIST1H2AK	0.087	0.409	0.414	0.298	-3.52	-1.289	-1.272	-1.749	-1.9569644	-1.5186561	1.064	0.0348	0	35.38462	5	13	3	130	14.1
IGFBP4	0.109	0.375	0.289	0.544	-3.19	-1.413	-1.789	-0.878	-1.8188547	-1.6013279	0.991	0.034952	0	36.43411	7	15	7	258	27.9
H2AFY	0.107	0.339	0.503	0.387	-3.22	-1.561	-0.996	-1.369	-1.786085	-1.4649811	0.984	0.035945	0	33.06452	10	16	10	372	39.6
XP32	0.388	0.646	0.792	0.412	-1.36	-0.631	-0.338	-1.277	-0.9024657	-0.9538593	0.499	0.036244	0.007	8	2	2	2	250	26.2
RPL15	0.397	0.542	0.528	0.166	-1.33	-0.884	-0.933	-2.591	-1.4353036	-1.1332043	0.796	0.036641	0	14.70588	3	4	3	204	24.1
VCL	0.22	0.419	0.71	0.471	-2.18	-1.257	-0.495	-1.087	-1.2558607	-1.1715083	0.7	0.037073	0	10.22928	11	15	11	1134	123.7
COL2A1	0.169	0.557	0.167	0.527	-2.56	-0.843	-2.556	-0.923	-1.7214412	-1.739237	0.969	0.037981	0	3.026227	4	6	4	1487	141.7
FN1	0.114	0.102	0.431	0.504	-3.13	-3.291	-1.214	-0.988	-2.1548122	-2.1704083	1.222	0.038768	0	51.67728	91	357	2	2355	259

	AR(16F16/DMSO)				Log(2) AR(16F16/DMSO)				Log(2)Mean	Log(2)Median	Log(2)	Two-tailed	Exp.				# Unique		
Gene Name	n=1	n=2	n=3	n=4	n=1	n=2	n=3	n=4	AR	AR	Std.Dev	T.Test	q-value	Coverage	# Peptides	# PSMs	Peptides	# AAs	MW [kDa]
IGFBP7	0.09	0.396	0.33	0.456	-3.47	-1.337	-1.6	-1.132	-1.8850447	-1.4682455	1.075	0.039243	0	59.21986	18	110	18	282	29.1
ANOS1	0.21	0.568	0.658	0.32	-2.25	-0.817	-0.602	-1.642	-1.3287691	-1.2297063	0.762	0.039878	0	11.17647	6	12	6	680	76.2
CHAD	0.234	0.477	0.772	0.349	-2.1	-1.067	-0.374	-1.517	-1.2641487	-1.292274	0.728	0.040304	0	9.470752	3	4	3	359	40.5
CLSTN1	0.146	0.157	0.515	0.55	-2.77	-2.676	-0.956	-0.864	-1.8165717	-1.8158096	1.049	0.040491	0	33.63914	38	121	38	981	109.7
AREG	0.133	0.603	0.307	0.45	-2.91	-0.73	-1.702	-1.151	-1.6229768	-1.4264779	0.945	0.0414	0	17.51825	4	5	4	274	30.2
RAB1	0.156	0.363	0.556	0.542	-2.68	-1.463	-0.847	-0.883	-1.4691345	-1.172934	0.857	0.041606	0	32.65306	5	13	5	147	16.8
APLP2	0.13	0.218	0.572	0.507	-2.95	-2.197	-0.805	-0.981	-1.7325747	-1.5887005	1.019	0.042461	0	35.38663	27	78	26	763	86.9
CARS	0.238	0.529	0.642	0.579	-2.07	-0.918	-0.638	-0.789	-1.1039602	-0.8534163	0.655	0.043361	0	10.75402	8	12	8	809	92
CYR61	0.179	0.429	0.548	0.594	-2.48	-1.221	-0.868	-0.753	-1.331413	-1.0444724	0.794	0.04387	0	9.186352	3	5	3	381	42
LDHA	0.233	0.726	0.447	0.534	-2.1	-0.463	-1.162	-0.904	-1.1573664	-1.0332132	0.692	0.044192	0.001	11.74699	4	4	4	332	36.7
RPL13	0.183	0.535	0.682	0.287	-2.45	-0.903	-0.553	-1.803	-1.4264702	-1.3531214	0.86	0.045187	0	27.96209	7	9	7	211	24.2
RPS13	0.277	0.701	0.448	0.673	-1.85	-0.512	-1.16	-0.57	-1.0238145	-0.8652144	0.625	0.046636	0	36.42384	7	10	7	151	17.2
FLNA	0.194	0.327	0.685	0.562	-2.37	-1.611	-0.546	-0.831	-1.3388681	-1.220533	0.821	0.047063	0	15.187	31	42	29	2647	280.6
APOB	0.293	0.164	0.757	0.425	-1.77	-2.606	-0.402	-1.235	-1.5038516	-1.5038058	0.926	0.047604	0	2.542187	13	22	9	4563	515.2
F13A1	0.176	0.765	0.402	0.387	-2.51	-0.387	-1.314	-1.37	-1.3943528	-1.3421305	0.868	0.048797	0	4.508197	3	5	3	732	83.2
S100A8	0.272	0.718	0.583	0.575	-1.88	-0.478	-0.773	-0.8	-0.9818272	-0.786326	0.614	0.049354	0.003	8.571429	1	2	1	105	11.7
LOC392748	0.215	0.352	0.834	0.44	-2.21	-1.504	-0.261	-1.184	-1.2909698	-1.3440462	0.81	0.049854	0	14.18919	2	5	2	148	16.9
APOC3	0.216	0.511	0.574	0.654	-2.21	-0.97	-0.804	-0.612	-1.1490707	-0.8866646	0.723	0.050098	0	13.67521	1	4	1	117	12.8
PPIB	0.172	0.393	0.531	0.66	-2.54	-1.346	-0.912	-0.6	-1.3492179	-1.1293051	0.849	0.050215	0	59.72222	16	41	15	216	23.7
HDGFRP3	0.179	0.497	0.524	0.612	-2.48	-1.008	-0.935	-0.709	-1.2830093	-0.9713837	0.808	0.050269	0	14.28571	3	5	3	203	22.6
TINAGL1	0.108	0.383	0.384	0.593	-3.21	-1.384	-1.382	-0.753	-1.6810931	-1.3830224	1.059	0.050284	0	18.41542	6	10	6	467	52.4
PCOLCE2	0.264	0.868	0.445	0.46	-1.92	-0.204	-1.168	-1.12	-1.1029016	-1.144166	0.702	0.051635	0	15.42169	5	6	5	415	45.7
COL1A2	0.183	0.272	0.833	0.418	-2.45	-1.879	-0.262	-1.258	-1.4631312	-1.5684602	0.938	0.052516	0	5.856515	6	8	6	1366	129.2
TARS	0.215	0.542	0.785	0.321	-2.22	-0.884	-0.349	-1.641	-1.273348	-1.2623732	0.824	0.053675	0	22.26833	16	28	16	723	83.4
MYH9	0.155	0.312	0.713	0.496	-2.69	-1.678	-0.488	-1.011	-1.4668481	-1.3445434	0.95	0.053832	0	28.92857	58	75	57	1960	226.4
GLG1	0.169	0.27	0.598	0.663	-2.56	-1.888	-0.741	-0.593	-1.4466197	-1.3145558	0.943	0.054708	0	15.69126	17	24	17	1179	134.5
IQGAP1	0.255	0.414	0.734	0.664	-1.97	-1.272	-0.45	-0.591	-1.0714518	-0.9314224	0.7	0.054955	0	8.630054	14	16	14	1657	189.1
SPTBN1	0.31	0.473	0.921	0.502	-1.69	-1.079	-0.12	-0.996	-0.9709585	-1.0371618	0.646	0.057459	0	4.395604	9	10	9	2366	274.7
ANXA1	0.336	0.805	0.71	0.37	-1.57	-0.313	-0.492	-1.433	-0.9531928	-0.9626314	0.643	0.059297	0.001	11.56069	4	5	4	346	38.7
CCT3	0.195	0.703	0.517	0.523	-2.36	-0.509	-0.956	-0.936	-1.1897182	-0.9459103	0.806	0.059888	0	13.34489	7	8	7	577	63.5
RPS23	0.262	0.322	0.92	0.492	-1.93	-1.633	-0.12	-1.024	-1.1770268	-1.3284874	0.799	0.060247	0	20.97902	3	4	3	143	15.8
ANXA2	0.313	0.643	0.799	0.584	-1.68	-0.638	-0.323	-0.776	-0.8537383	-0.7071517	0.581	0.06053	0	46.0177	19	42	19	339	38.6
ACTR2	0.143	0.485	0.589	0.52	-2.8	-1.044	-0.766	-0.942	-1.3889561	-0.9930794	0.95	0.061357	0	17.25888	6	7	5	394	44.7
EL52	0.358	0.531	0.891	0.643	-1.48	-0.913	-0.167	-0.637	-0.7997499	-0.7748178	0.55	0.061961	0	41.80328	33	66	16	732	84.6
RPS11	0.18	0.383	0.853	0.421	-2.47	-1.384	-0.229	-1.247	-1.3333998	-1.3157211	0.918	0.062287	0	43.67089	8	10	8	158	18.4
MYL12A	0.24	0.394	0.912	0.475	-2.06	-1.344	-0.136	-1.073	-1.1529587	-1.2083377	0.795	0.062515	0	23.72881	4	5	4	177	20.4
RPS19	0.212	0.713	0.575	0.522	-2.24	-0.488	-0.8	-0.938	-1.1166431	-0.8688953	0.772	0.062954	0	38.8535	9	17	9	157	17.3
LGALS3BP	0.232	0.26	0.956	0.438	-2.11	-1.945	-0.064	-1.191	-1.3270724	-1.5682684	0.932	0.065189	0	17.77778	11	15	11	585	65.3

	AR(16F16/DMSO)				Log(2) AR(16F16/DMSO)				Log(2)Mean	Log(2)Median	Log(2)	Two-tailed	Exp.				# Unique		
Gene Name	n=1	n=2	n=3	n=4	n=1	n=2	n=3	n=4	AR	AR	Std.Dev	T.Test	q-value	Coverage	# Peptides	# PSMs	Peptides	# AAs	MW [kDa]
VCP	0.184	0.457	0.639	0.648	-2.44	-1.129	-0.646	-0.625	-1.210087	-0.8877724	0.852	0.065609	0	23.20099	16	22	16	806	89.3
ARPC5	0.248	0.495	0.714	0.696	-2.01	-1.013	-0.485	-0.523	-1.0079278	-0.7682872	0.71	0.065697	0	25.16556	6	8	5	151	16.3
ARPC2	0.196	0.523	0.531	0.727	-2.35	-0.935	-0.913	-0.461	-1.1653522	-0.9235872	0.822	0.065816	0	30	10	19	10	300	34.3
EIF4A1	0.238	0.717	0.651	0.541	-2.07	-0.481	-0.617	-0.887	-1.0143705	-0.7522239	0.725	0.068017	0	16.25616	6	9	6	406	46.1
RAN	0.194	0.352	0.907	0.464	-2.36	-1.506	-0.141	-1.107	-1.2795357	-1.306421	0.923	0.069349	0	19.23077	4	8	4	234	26.8
RPL14	0.205	0.96	0.432	0.319	-2.29	-0.059	-1.207	-1.65	-1.3011121	-1.4284858	0.939	0.069529	0.001	13.63636	2	3	2	220	23.8
ARPC4-TTLL3	0.321	0.843	0.58	0.659	-1.64	-0.246	-0.786	-0.601	-0.8185811	-0.693558	0.593	0.070016	0	24.86188	5	11	5	181	21
CLEC11A	0.211	0.369	0.803	0.625	-2.25	-1.437	-0.317	-0.678	-1.1699759	-1.0579016	0.857	0.071847	0	12.0743	3	3	3	323	35.6
VIL2	0.266	0.533	0.729	0.74	-1.91	-0.908	-0.454	-0.433	-0.9268156	-0.6808507	0.693	0.075268	0	22.1843	17	44	5	586	69.4
CASP14	0.399	0.886	0.736	0.619	-1.32	-0.175	-0.436	-0.692	-0.6569643	-0.5639884	0.493	0.075847	0	14.87603	3	3	3	242	27.7
PRMT1	0.174	0.919	0.391	0.43	-2.53	-0.121	-1.358	-1.216	-1.3052122	-1.286935	0.983	0.076703	0.001	5.121294	2	3	2	371	42.4
C8B	0.262	0.871	0.22	0.614	-1.93	-0.2	-2.141	-0.705	-1.2449281	-1.3191631	0.942	0.077441	0.001	3.384095	2	3	2	591	67
RPS14	0.171	0.752	0.522	0.509	-2.55	-0.411	-0.937	-0.973	-1.2174207	-0.9550076	0.924	0.077982	0	32.45033	5	9	5	151	16.3
LDHB	0.284	0.727	0.717	0.641	-1.81	-0.46	-0.48	-0.64	-0.8487707	-0.5602399	0.649	0.079258	0.007	5.988024	2	2	2	334	36.6
RPS26	0.107	0.695	0.548	0.319	-3.22	-0.525	-0.865	-1.651	-1.565982	-1.2579897	1.201	0.079814	0	33.91304	3	5	3	115	13
NOV	0.097	0.666	0.407	0.462	-3.37	-0.586	-1.302	-1.113	-1.5918837	-1.2071349	1.222	0.079933	0	25.77031	7	12	7	357	39.1
EPRS	0.207	0.287	1.055	0.41	-2.27	-1.802	0.077	-1.285	-1.3207196	-1.5431158	1.016	0.080314	0	8.134921	10	11	10	1512	170.5
HNRPR	0.154	0.721	0.382	0.628	-2.7	-0.471	-1.4	-0.671	-1.3099953	-1.0355014	1.008	0.080366	0	13.90205	8	11	4	633	70.9
ARF5	0.279	0.457	0.449	0.036	-1.84	-1.13	-1.15	-4.807	-2.2330934	-1.4973111	1.748	0.083572	0.001	4.366812	1	2	1	229	25.4
CCT6A	0.25	0.654	0.881	0.432	-2	-0.613	-0.185	-1.21	-1.0021186	-0.9114726	0.787	0.084219	0	10.92279	6	8	6	531	58
AMOT	0.225	0.796	0.421	0.709	-2.15	-0.329	-1.249	-0.495	-1.0562679	-0.872255	0.833	0.084942	0.086	0.738007	1	2	1	1084	118
SERPINB12	0.27	0.701	0.752	0.632	-1.89	-0.512	-0.413	-0.662	-0.8684325	-0.5868143	0.687	0.085528	0	7.654321	3	5	3	405	46.2
RPS9	0.187	0.735	0.732	0.367	-2.42	-0.445	-0.45	-1.446	-1.190981	-0.9480555	0.946	0.086429	0	40.72165	10	15	10	194	22.6
FAM53B	0.107	0.381	0.959	0.269	-3.22	-1.392	-0.061	-1.892	-1.6419413	-1.6421556	1.307	0.086697	0.049	2.606635	1	2	1	422	45.7
COLEC10	0.215	0.739	0.77	0.401	-2.22	-0.435	-0.376	-1.318	-1.0861708	-0.876626	0.867	0.087319	0.001	6.859206	2	3	2	277	30.7
CTSL2	0.193	0.529	0.802	0.571	-2.37	-0.919	-0.319	-0.807	-1.1047437	-0.8632435	0.885	0.087954	0.002	5.389222	2	3	2	334	37.3
RPS6	0.184	0.716	0.76	0.362	-2.44	-0.482	-0.396	-1.466	-1.1967271	-0.9739785	0.962	0.088634	0	21.68675	6	9	6	249	28.7
TCP1	0.187	0.496	0.851	0.536	-2.42	-1.011	-0.233	-0.9	-1.1400093	-0.9558328	0.917	0.088858	0	13.66906	9	11	9	556	60.3
EEF1D	0.253	0.959	0.265	0.611	-1.98	-0.061	-1.931	-0.711	-1.1714278	-1.3208262	0.945	0.089368	0.001	2.725968	2	3	1	697	76.5
RPS3	0.148	0.63	0.633	0.529	-2.75	-0.667	-0.66	-0.918	-1.2498693	-0.792379	1.01	0.089689	0	56.79012	14	31	14	243	26.7
DTD1	0.136	0.53	0.482	0.735	-2.88	-0.916	-1.053	-0.445	-1.3236456	-0.9841022	1.07	0.089825	0	33.97129	4	8	4	209	23.5
HSPA4	0.181	0.165	1.158	0.367	-2.47	-2.599	0.1926	-1.445	-1.5796563	-1.9559041	1.289	0.091652	0.001	4.166667	3	3	3	840	94.3
ALDOA	0.228	0.635	0.612	0.772	-2.13	-0.654	-0.708	-0.374	-0.9669619	-0.6814206	0.79	0.091867	0	56.04396	19	40	15	364	39.4
XRCC6	0.171	0.541	0.136	0.912	-2.55	-0.886	-2.884	-0.133	-1.6138967	-1.7192587	1.319	0.091892	0	21.51067	10	12	10	609	69.8
ITIH3	0.225	0.202	1.011	0.53	-2.15	-2.31	0.0163	-0.916	-1.3410081	-1.5350159	1.099	0.092464	0	6.741573	6	14	6	890	99.8
RPS10	0.216	0.411	0.944	0.58	-2.21	-1.283	-0.084	-0.786	-1.0916311	-1.0347333	0.895	0.092569	0	18.96552	5	10	5	174	19.8
RPS8	0.125	0.587	0.802	0.332	-2.99	-0.768	-0.319	-1.589	-1.4178072	-1.1785615	1.175	0.094808	0	44.71154	8	16	8	208	24.2

	AR(16F16/DMSO)				Log(2) AR(16F16/DMSO)				Log(2)Mean	Log(2)Median	Log(2)	Two-tailed	Exp.				# Unique		
Gene Name	n=1	n=2	n=3	n=4	n=1	n=2	n=3	n=4	AR	AR	Std.Dev	T.Test	q-value	Coverage	# Peptides	# PSMs	Peptides	# AAs	MW [kDa]
RPS18	0.185	0.625	0.84	0.448	-2.44	-0.678	-0.251	-1.16	-1.1318085	-0.9190195	0.947	0.096643	0	42.76316	10	20	10	152	17.7
VEGFC	0.115	0.491	0.647	0.581	-3.11	-1.027	-0.629	-0.782	-1.388158	-0.9047513	1.162	0.096861	0.001	6.443914	3	3	3	419	46.9
P4HB	0.116	0.669	0.549	0.508	-3.11	-0.581	-0.865	-0.978	-1.3828657	-0.921773	1.162	0.09756	0	30.09901	15	22	12	505	56.7
ARPC1B	0.249	0.676	0.803	0.617	-2	-0.564	-0.316	-0.697	-0.8951608	-0.6305566	0.756	0.098568	0	34.67742	11	18	11	372	40.9
AP2A1	0.226	0.749	0.632	0.671	-2.15	-0.417	-0.662	-0.575	-0.9504625	-0.6186632	0.805	0.09915	0	8.802456	9	11	1	977	107.5
AP2B1	0.163	0.818	0.637	0.415	-2.62	-0.29	-0.651	-1.269	-1.2073722	-0.9595828	1.025	0.099742	0	8.09674	9	13	9	951	105.6
RPL18A	0.173	0.608	0.804	0.502	-2.53	-0.718	-0.316	-0.993	-1.1396628	-0.8557594	0.968	0.099977	0	25.56818	4	5	4	176	20.7
RPL13A	0.348	0.657	1.048	0.398	-1.52	-0.605	0.0636	-1.331	-0.8487203	-0.9681099	0.725	0.101174	0.001	9.047619	2	4	2	210	24.2
TUBA4A	0.249	0.637	0.998	0.344	-2.01	-0.651	0	-1.541	-1.0501771	-1.0962579	0.898	0.101401	0	35.26786	11	22	3	448	49.9
RPS3A	0.142	0.692	0.669	0.476	-2.82	-0.532	-0.581	-1.071	-1.2499492	-0.825557	1.072	0.102043	0	42.42424	14	21	14	264	29.9
TPI1	0.331	0.821	0.789	0.655	-1.59	-0.285	-0.341	-0.61	-0.7074476	-0.4754413	0.607	0.102221	0	22.02797	5	7	5	286	30.8
TUBA1A	0.195	0.724	0.771	0.487	-2.36	-0.466	-0.375	-1.038	-1.0598358	-0.7522831	0.915	0.103383	0	41.46341	13	30	5	451	50.1
CCT5	0.206	0.71	0.787	0.518	-2.28	-0.493	-0.349	-0.951	-1.0187707	-0.7219269	0.88	0.103559	0	12.38447	7	7	7	541	59.6
RPS4X	0.13	0.826	0.635	0.324	-2.95	-0.275	-0.656	-1.624	-1.3752572	-1.1401538	1.191	0.104048	0	49.04943	14	23	11	263	29.6
CAPN2	0.288	0.495	0.93	0.723	-1.8	-1.014	-0.105	-0.468	-0.84632	-0.741091	0.736	0.105111	0.001	3.840878	2	2	2	729	83.1
TXLNA	0.221	0.427	1.094	0.48	-2.18	-1.226	0.1263	-1.06	-1.0848425	-1.1433792	0.946	0.105606	0.001	10.98901	3	3	3	546	61.9
DSG1	0.267	0.462	1.183	0.373	-1.91	-1.114	0.2354	-1.419	-1.0509334	-1.2668956	0.917	0.105825	0	11.05815	8	10	8	1049	113.7
NT5C2	0.193	0.757	0.641	0.614	-2.37	-0.402	-0.641	-0.704	-1.0300133	-0.672599	0.904	0.107135	0	5.525847	3	4	3	561	64.9
APOD	0.383	1.056	0.691	0.451	-1.38	0.0792	-0.534	-1.149	-0.746994	-0.841367	0.657	0.107587	0.026	2.790698	1	2	1	215	24.1
KARS	0.222	0.54	0.692	0.843	-2.17	-0.89	-0.534	-0.246	-0.9602951	-0.7117858	0.849	0.108797	0	7.872697	4	5	4	597	68
AHCY	0.24	0.867	0.603	0.648	-2.06	-0.206	-0.731	-0.626	-0.9054043	-0.6784898	0.801	0.108976	0	19.67593	8	11	8	432	47.7
IleRS	0.188	0.236	1.336	0.324	-2.41	-2.082	0.4182	-1.627	-1.4259357	-1.8548344	1.271	0.110541	0	9.929633	10	12	10	1279	146.3
RPL19	0.269	0.637	1.053	0.387	-1.89	-0.651	0.0725	-1.372	-0.9607913	-1.0117859	0.856	0.110543	0.002	8.673469	1	2	1	196	23.5
CLU	0.197	0.617	0.808	0.611	-2.34	-0.697	-0.308	-0.712	-1.0144954	-0.7043245	0.904	0.110568	0	23.83073	9	14	9	449	52.5
PLEC	0.221	0.216	1.136	0.55	-2.18	-2.214	0.1833	-0.861	-1.2667358	-1.5182617	1.153	0.115501	0	3.159693	12	13	12	4684	531.5
CCT8	0.179	0.758	0.702	0.559	-2.48	-0.399	-0.51	-0.84	-1.0568054	-0.6750686	0.966	0.116449	0	31.75182	16	21	16	548	59.6
PDIA5	0.329	0.49	1.21	0.431	-1.6	-1.028	0.278	-1.213	-0.8916343	-1.120907	0.816	0.116656	0.001	5.009634	3	4	3	519	59.6
IPO7	0.29	0.394	1.313	0.346	-1.79	-1.344	0.398	-1.528	-1.064648	-1.4357481	0.992	0.121045	0	2.793834	2	4	2	1038	119.4
RPS29	0.171	0.827	0.705	0.486	-2.55	-0.275	-0.504	-1.04	-1.0909747	-0.7717854	1.021	0.122246	0.009	14.28571	2	4	2	56	6.7
PARP1	0.323	0.86	0.805	0.66	-1.63	-0.218	-0.314	-0.599	-0.6898952	-0.4568099	0.646	0.122459	0.001	4.33925	3	3	3	1014	113
SF3B1	0.329	0.448	1.239	0.482	-1.6	-1.158	0.3055	-1.051	-0.8764153	-1.1040837	0.823	0.123171	0.001	2.300613	2	3	2	1304	145.7
HNRPK	0.157	0.274	1.076	0.6	-2.67	-1.869	0.1042	-0.737	-1.2942113	-1.3030481	1.225	0.125024	0	7.327586	3	5	3	464	51
COL18A1	0.23	0.58	1.174	0.285	-2.12	-0.787	0.2297	-1.81	-1.1212034	-1.298419	1.065	0.12596	0	2.109464	3	4	3	1754	178.1
FAU	0.111	0.558	0.996	0.343	-3.17	-0.842	-0.007	-1.544	-1.3907185	-1.1930042	1.342	0.129898	0.001	10.20408	1	3	1	98	10.9
KRT18	0.272	0.79	0.816	0.674	-1.88	-0.34	-0.303	-0.57	-0.7723257	-0.454701	0.746	0.130203	0	13.02326	6	8	5	430	48
ARPC4	0.213	0.731	0.295	1.022	-2.23	-0.452	-1.766	0.0309	-1.1042815	-1.109121	1.067	0.130372	0	18.10811	6	6	6	370	41.5
CCT7	0.235	0.671	0.927	0.601	-2.09	-0.576	-0.109	-0.736	-0.8775797	-0.6558283	0.851	0.131164	0	20.44199	10	14	10	543	59.3

	AR(16F16/DMSO)				Log(2) AR(16F16/DMSO)				Log(2)Mean	Log(2)Median	Log(2)	Two-tailed	Exp.				# Unique		
Gene Name	n=1	n=2	n=3	n=4	n=1	n=2	n=3	n=4	AR	AR	Std.Dev	T.Test	q-value	Coverage	# Peptides	# PSMs	Peptides	# AAs	MW [kDa]
EIF2A	0.196	0.748	0.926	0.436	-2.35	-0.419	-0.111	-1.199	-1.0197666	-0.8089327	0.998	0.133579	0	18.63248	9	11	9	585	64.9
ACTR3	0.133	0.821	0.681	0.486	-2.92	-0.284	-0.554	-1.042	-1.1988973	-0.7981681	1.187	0.136541	0	26.79426	9	18	9	418	47.3
HNRNPC	0.165	0.397	1.002	0.662	-2.6	-1.332	0.0024	-0.596	-1.1313406	-0.9639543	1.121	0.136822	0	19.60784	7	8	7	306	33.6
EIF5	0.177	0.594	1.093	0.406	-2.5	-0.751	0.1248	-1.302	-1.1062025	-1.0266145	1.097	0.137175	0	34.57077	14	14	14	431	49.2
JUP	0.287	0.624	1.143	0.49	-1.8	-0.681	0.1916	-1.028	-0.8296451	-0.8546506	0.826	0.138199	0	18.92617	11	13	8	745	81.7
RRBP1	0.13	0.551	0.769	0.673	-2.95	-0.86	-0.381	-0.571	-1.1898714	-0.7155878	1.188	0.138975	0	28.8961	16	21	16	1540	165.6
RPS12	0.123	0.769	0.574	0.629	-3.03	-0.38	-0.799	-0.669	-1.2184872	-0.7340307	1.218	0.139181	0	20.45455	3	5	3	132	14.5
TNC	0.29	0.198	1.417	0.404	-1.79	-2.333	0.5078	-1.311	-1.2309366	-1.5492789	1.232	0.139585	0.001	2.373489	4	4	4	2233	244.2
SYNCRIP	0.176	0.933	0.514	0.669	-2.5	-0.099	-0.966	-0.58	-1.037122	-0.7729673	1.04	0.13997	0	17.33547	9	11	5	623	69.6
ACAT1	0.083	0.4	1.228	0.296	-3.59	-1.321	0.2972	-1.755	-1.5909764	-1.5379265	1.596	0.140189	0	24.82436	9	13	9	427	45.2
C1QTNF3	0.19	0.541	0.131	1.248	-2.4	-0.885	-2.962	0.321	-1.4803717	-1.6402744	1.487	0.140504	0.001	5.769231	2	3	2	312	33.8
NACA	0.28	0.712	1.091	0.448	-1.84	-0.491	0.1272	-1.158	-0.8392361	-0.8243369	0.847	0.141669	0	1.395573	2	4	2	2078	205.3
TUBB	0.153	0.821	0.722	0.532	-2.71	-0.285	-0.47	-0.911	-1.0943331	-0.6904014	1.11	0.1431	0	25.45045	10	22	3	444	49.6
EIF1AY	0.177	0.434	1.108	0.606	-2.49	-1.204	0.1479	-0.723	-1.06867	-0.9638271	1.103	0.148124	0	26.38889	5	8	5	144	16.4
SUPT16H	0.162	0.519	1.238	0.392	-2.63	-0.948	0.3069	-1.353	-1.1558993	-1.1500848	1.21	0.152153	0	6.494747	5	5	5	1047	119.8
PLRG1	0.304	0.751	1.019	0.61	-1.72	-0.414	0.0291	-0.713	-0.7034802	-0.563173	0.741	0.153846	0.001	3.696498	2	3	2	514	57.2
CCT5	0.216	0.866	0.782	0.611	-2.21	-0.207	-0.355	-0.712	-0.8716526	-0.5332629	0.919	0.154149	0	13.08411	7	8	7	535	57.5
DSP	0.236	0.575	1.186	0.519	-2.08	-0.799	0.247	-0.946	-0.8949325	-0.872255	0.953	0.157037	0	4.667363	13	18	13	2871	331.6
ASPH	0.249	0.658	1.231	0.35	-2	-0.604	0.2996	-1.513	-0.9556132	-1.0586219	1.018	0.15719	0.001	4.221636	3	4	3	758	85.8
RPL7A	0.195	0.565	1.327	0.306	-2.36	-0.823	0.4092	-1.707	-1.1189291	-1.2646858	1.197	0.158282	0	27.06767	8	12	8	266	30
CDSN	0.193	0.515	1.091	0.622	-2.38	-0.957	0.124	-0.683	-0.9730368	-0.82002	1.042	0.158599	0	6.805293	3	6	3	529	51.5
PDAP1	0.252	0.73	1.037	0.563	-1.99	-0.454	0.0516	-0.829	-0.8051284	-0.6416218	0.868	0.16054	0	27.07182	4	5	4	181	20.6
SF3A1	0.32	0.628	1.248	0.473	-1.64	-0.67	0.3219	-1.082	-0.7681654	-0.8759897	0.829	0.160856	0.001	1.134931	1	2	1	793	88.8
CAP1	0.259	0.931	0.836	0.586	-1.95	-0.104	-0.256	-0.772	-0.7708018	-0.5142272	0.837	0.162851	0	27.36842	14	19	14	475	51.6
ARID1A	0.22	0.988	0.719	0.593	-2.18	-0.017	-0.476	-0.755	-0.8578957	-0.6156893	0.934	0.163662	0.01	0.306346	1	2	1	2285	241.9
NAA15	0.212	0.549	1.345	0.366	-2.24	-0.865	0.4293	-1.45	-1.0307035	-1.157371	1.124	0.164023	0	6.812933	7	8	7	866	101.2
DSC1	0.142	0.336	0.834	0.969	-2.82	-1.575	-0.267	-0.047	-1.1765031	-0.9208347	1.285	0.16449	0	5.592841	4	5	4	894	99.9
CACYBP	0.191	0.777	0.829	0.657	-2.39	-0.364	-0.27	-0.606	-0.9079063	-0.48527	0.999	0.166574	0	44.29825	9	13	8	228	26.2
CLIC1	0.211	0.883	0.748	0.679	-2.25	-0.18	-0.42	-0.559	-0.8513428	-0.4896064	0.943	0.168799	0	29.87552	5	11	5	241	26.9
NARS	0.154	0.9	0.709	0.593	-2.7	-0.153	-0.497	-0.755	-1.025547	-0.6258395	1.142	0.170306	0	31.38686	19	27	19	548	62.9
RPS15A	0.161	0.641	1.255	0.325	-2.63	-0.641	0.3278	-1.62	-1.1409654	-1.1301268	1.273	0.170838	0	43.84615	7	9	7	130	14.8
PRSS3	0.423	0.557	1.159	0.772	-1.24	-0.845	0.2125	-0.372	-0.5615957	-0.6083632	0.627	0.171091	0	8.502024	2	5	1	247	26.5
IGHG1	0.217	0.47	1.195	0.028	-2.21	-1.09	0.2591	-5.139	-2.0440859	-1.6484482	2.296	0.173035	0.001	5.394191	2	2	2	482	52.8
SNRPD2	0.212	0.733	0.84	0.762	-2.23	-0.448	-0.248	-0.392	-0.8305592	-0.4197971	0.94	0.175329	0.001	33.05085	3	3	3	118	13.5
RACK1	0.254	0.873	0.748	0.799	-1.98	-0.196	-0.411	-0.325	-0.7267986	-0.3676979	0.838	0.18104	0.001	7.165109	2	2	2	321	34.9
ACTN4	0.245	0.231	1.554	0.537	-2.03	-2.114	0.6365	-0.898	-1.1015036	-1.46435	1.285	0.18486	0	9.220637	7	10	7	911	104.8

	AR(16F16/DMSO)				Log(2) AR(16F16/DMSO)				Log(2)Mean	Log(2)Median	Log(2)	Two-tailed	Exp.				# Unique		
Gene Name	n=1	n=2	n=3	n=4	n=1	n=2	n=3	n=4	AR	AR	Std.Dev	T.Test	q-value	Coverage	# Peptides	# PSMs	Peptides	# AAs	MW [kDa]
RPS28	0.202	0.717	1.242	0.382	-2.31	-0.48	0.3122	-1.388	-0.9665133	-0.9340296	1.133	0.186671	0.001	17.3913	1	2	1	69	7.8
EEF1G	0.194	0.963	0.823	0.561	-2.37	-0.055	-0.282	-0.832	-0.8841961	-0.5569688	1.042	0.188169	0	13.95881	6	6	6	437	50.1
TUBB4B	0.183	0.781	0.971	0.586	-2.45	-0.356	-0.042	-0.77	-0.9054187	-0.5632157	1.074	0.190458	0	25.39326	10	16	3	445	49.8
ARG1	0.173	0.318	1.494	0.558	-2.53	-1.652	0.5788	-0.842	-1.1122378	-1.247376	1.322	0.191017	0.001	8.385093	3	3	3	322	34.7
EIF2S3	0.219	0.889	0.989	0.519	-2.19	-0.169	-0.016	-0.947	-0.8311761	-0.5581841	0.995	0.19339	0	19.70339	8	13	8	472	51.1
RPL24	0.218	0.682	1.372	0.1	-2.2	-0.551	0.4534	-3.322	-1.4041463	-1.3740113	1.682	0.193512	0	24.84076	5	7	5	157	17.8
ABCF1	0.211	0.911	0.938	0.545	-2.25	-0.134	-0.091	-0.877	-0.8371314	-0.505582	1.006	0.194751	0	12.97935	3	5	3	339	38.3
PGD	0.19	0.836	0.285	1.215	-2.39	-0.258	-1.815	0.2804	-1.0462587	-1.0363852	1.263	0.196102	0	16.14907	7	8	7	483	53.1
PA2G4	0.152	1.116	0.671	0.536	-2.72	0.1584	-0.576	-0.899	-1.0080552	-0.7376659	1.221	0.197315	0	37.56345	14	29	14	394	43.8
ILF2	0.19	1.262	0.671	0.461	-2.39	0.3353	-0.574	-1.117	-0.9370247	-0.8455911	1.14	0.198795	0	23.33333	9	19	9	390	43
EIF2S1	0.215	0.738	1.128	0.56	-2.22	-0.438	0.1722	-0.835	-0.8289976	-0.6364518	1.013	0.20014	0	12.38095	5	5	5	315	36.1
SERPINA1	0.167	0.55	1.294	0.551	-2.58	-0.862	0.3677	-0.858	-0.982682	-0.8602054	1.211	0.203034	0	21.86544	12	18	9	654	72.3
PK	0.239	0.845	1	0.645	-2.06	-0.243	0	-0.632	-0.7344675	-0.4376193	0.923	0.20972	0	42.37288	19	34	19	531	57.9
CFL1	0.38	0.856	0.924	0.871	-1.4	-0.225	-0.114	-0.199	-0.4840435	-0.2121859	0.611	0.211081	0	31.86275	7	15	7	204	22.7
KPNB1	0.186	0.298	1.522	0.645	-2.43	-1.746	0.6041	-0.63	-1.0505555	-1.1880812	1.329	0.21209	0.001	2.054795	2	2	2	876	97.1
EDF1	0.209	0.726	1.037	0.705	-2.26	-0.461	0.0506	-0.505	-0.7927807	-0.4831075	1.007	0.213524	0.001	21.62162	3	4	3	148	16.4
OGN	0.349	1.279	0.602	0.705	-1.52	0.3548	-0.731	-0.505	-0.6004344	-0.6179914	0.771	0.217434	0.001	4.775281	2	3	2	356	40.5
HLA-A	0.314	0.884	1.263	0.258	-1.67	-0.178	0.3321	-1.956	-0.8686973	-0.9253518	1.118	0.217924	0.001	11.60221	2	2	2	181	21.1
TGFBI	0.228	0.581	1.373	0.561	-2.13	-0.784	0.4619	-0.832	-0.8211434	-0.807666	1.059	0.218708	0	10.83455	7	9	7	683	74.6
PRDX2	0.303	0.48	1.447	0.623	-1.72	-1.058	0.5329	-0.684	-0.7331508	-0.8705766	0.947	0.219469	0	23.73737	4	8	3	198	21.9
CFD	0.178	0.377	1.661	0.511	-2.49	-1.409	0.7334	-0.967	-1.0340606	-1.187804	1.342	0.220858	0.007	6.538462	1	2	1	260	27.8
SNRPD3	0.224	0.873	1.088	0.549	-2.16	-0.195	0.1215	-0.866	-0.7749893	-0.5305242	1.011	0.222843	0.001	15.07937	2	4	2	126	13.9
NF110b	0.184	0.795	1.096	0.576	-2.44	-0.331	0.1321	-0.796	-0.85918	-0.563271	1.121	0.222923	0	18.70824	15	31	15	898	95.7
HLA-C	0.176	0.822	1.17	0.483	-2.5	-0.283	0.2274	-1.049	-0.9018964	-0.665844	1.19	0.226679	0	17.21311	4	6	2	366	40.8
NAMPT	0.258	0.974	0.969	0.632	-1.96	-0.037	-0.046	-0.661	-0.6754692	-0.3536191	0.903	0.231496	0	17.51527	8	10	8	491	55.5
ZNF788P	0.386	1.455	0.389	0.705	-1.37	0.5413	-1.361	-0.505	-0.6743583	-0.9328505	0.907	0.233609	0.005	5.405405	1	3	1	259	29.9
MANF	0.245	0.479	1.456	0.651	-2.03	-1.063	0.5416	-0.619	-0.7927835	-0.8412502	1.067	0.233947	0	44.86486	9	16	9	185	21.1
EIF5B	0.206	1.067	0.971	0.538	-2.28	0.0936	-0.041	-0.896	-0.780729	-0.4682976	1.091	0.247857	0	5.081967	5	6	5	1220	138.6
SSRP1	0.195	0.904	1.159	0.567	-2.36	-0.146	0.2119	-0.818	-0.7777654	-0.4821216	1.137	0.264791	0	11.14245	8	9	8	709	81
LMNA	0.19	0.668	1.352	0.643	-2.4	-0.581	0.4354	-0.636	-0.7942429	-0.6085588	1.176	0.269477	0	40.66265	24	37	24	664	74.1
LGALS1	0.248	0.971	0.982	0.733	-2.01	-0.042	-0.026	-0.447	-0.6312886	-0.2443954	0.94	0.271808	0	19.25926	4	7	4	135	14.7
S100A8	0.307	0.788	1.187	0.759	-1.71	-0.343	0.2463	-0.398	-0.5500752	-0.3706583	0.824	0.273875	0	31.1828	3	6	3	93	10.8
RPS2	0.182	1.05	1.279	0.367	-2.46	0.0706	0.3556	-1.447	-0.8699238	-0.6882334	1.322	0.279716	0	36.51877	11	14	11	293	31.3
C4A	0.148	0.502	1.215	0.939	-2.75	-0.995	0.2827	-0.091	-0.8888905	-0.5427549	1.353	0.280415	0	6.594037	12	18	2	1744	192.8
SBDS	0.397	0.554	1.794	0.363	-1.33	-0.852	0.8532	-1.461	-0.6980811	-1.092076	1.067	0.281853	0.006	10.4	2	2	2	250	28.8
PACSIN2	0.28	0.854	1.196	0.691	-1.84	-0.228	0.2582	-0.534	-0.5852491	-0.3811793	0.896	0.282522	0	10.49383	5	5	5	486	55.7
HSPA8	0.225	0.862	1.215	0.644	-2.15	-0.214	0.2808	-0.635	-0.6801497	-0.4246116	1.05	0.285927	0	34.21053	22	40	18	646	70.9
MSN	0.206	0.829	1.198	0.702	-2.28	-0.27	0.2602	-0.51	-0.6996341	-0.3898092	1.101	0.293374	0	53.55286	45	109	33	577	67.8

	AR(16F16/DMSO)				Log(2) AR(16F16/DMSO)				Log(2)Mean	Log(2)Median	Log(2)	Two-tailed	Exp.				# Unique		
Gene Name	n=1	n=2	n=3	n=4	n=1	n=2	n=3	n=4	AR	AR	Std.Dev	T.Test	q-value	Coverage	# Peptides	# PSMs	Peptides	# AAs	MW [kDa]
CAPRIN1	0.154	0.79	1.328	0.619	-2.7	-0.34	0.4099	-0.692	-0.8299949	-0.5158411	1.328	0.299787	0	3.244006	2	4	2	709	78.3
SERPINE2	0.242	1.576	0.806	0.437	-2.05	0.6566	-0.312	-1.193	-0.7239744	-0.7525184	1.161	0.301004	0	17.8392	9	13	9	398	44
CST3	0.192	0.64	1.337	0.8	-2.38	-0.643	0.4214	-0.321	-0.7307846	-0.4820055	1.187	0.305814	0	18.49315	2	4	2	146	15.8
G6PD	0.37	0.841	1.379	0.601	-1.43	-0.249	0.4611	-0.737	-0.4898385	-0.4930426	0.799	0.307654	0	5.048544	2	4	2	515	59.3
IGHA1	0.123	0.653	2.226	0.264	-3.03	-0.615	1.156	-1.919	-1.1011001	-1.2670457	1.799	0.308232	0	8.092486	3	6	3	519	56.4
RDX	0.234	0.765	1.164	0.859	-2.1	-0.386	0.2188	-0.219	-0.6202766	-0.302399	1.016	0.309195	0	36.10169	32	69	20	590	69.3
HMGB2	0.123	0.627	1.174	0.946	-3.02	-0.673	0.2306	-0.08	-0.8859872	-0.3762184	1.473	0.31516	0	36.84211	9	11	7	209	24
GAPDH	0.268	0.674	1.265	0.887	-1.9	-0.569	0.3382	-0.174	-0.5758343	-0.3711858	0.957	0.315193	0	42.08955	11	21	11	335	36
COL4A2	0.068	0.154	3.044	0.581	-3.87	-2.702	1.6041	-0.783	-1.4389122	-1.7428199	2.396	0.315814	0	4.614486	7	10	7	1712	167.4
CCT4	0.205	0.846	1.608	0.438	-2.28	-0.242	0.6849	-1.193	-0.7584358	-0.7174362	1.273	0.319261	0	16.32653	8	8	8	539	57.9
PDIA3	0.131	0.601	1.39	0.818	-2.93	-0.734	0.4747	-0.289	-0.8688188	-0.5114349	1.46	0.319623	0	34.14634	4	9	1	123	13.5
AP2M1	0.146	1.252	1.101	0.478	-2.78	0.3243	0.1385	-1.065	-0.8455073	-0.4632903	1.429	0.321906	0	20.86957	9	13	9	460	52.3
TCEA1	0.15	0.382	2.06	0.647	-2.74	-1.387	1.0432	-0.628	-0.9278377	-1.0074021	1.578	0.324388	0	12.29236	3	3	3	301	33.9
PTGES3	0.288	0.612	1.96	0.414	-1.79	-0.708	0.9687	-1.273	-0.7016461	-0.9903665	1.199	0.326274	0.001	13.93939	2	2	2	165	19.4
TTR	0.196	0.488	1.904	0.634	-2.35	-1.034	0.9274	-0.658	-0.7787515	-0.8459525	1.349	0.331961	0.083	3.243243	1	2	1	185	20.1
NMT1	0.24	1.041	1.251	0.605	-2.06	0.0585	0.3225	-0.724	-0.599855	-0.3329222	1.068	0.34298	0	8.870968	3	5	3	496	56.8
PGK1	0.17	1.178	1.051	0.651	-2.56	0.2367	0.0721	-0.619	-0.7171425	-0.2736587	1.282	0.344756	0	46.52278	16	29	16	417	44.6
SFPQ	0.208	0.631	1.637	0.716	-2.27	-0.664	0.7124	-0.482	-0.6754231	-0.5731138	1.225	0.350557	0.005	2.404526	2	3	2	707	76.1
FKBP3	0.186	0.957	1.27	0.687	-2.43	-0.063	0.3459	-0.541	-0.6708295	-0.3020753	1.224	0.353261	0	29.46429	7	10	7	224	25.2
VIM	0.27	0.688	1.609	0.705	-1.89	-0.54	0.6857	-0.503	-0.561711	-0.5213735	1.053	0.364096	0	28.54077	12	21	10	466	53.6
IGL	0.235	0.316	2.666	0.515	-2.09	-1.662	1.4147	-0.959	-0.8241529	-1.3100265	1.564	0.369277	0	20.9205	3	5	3	239	26.2
SSB	0.133	1.093	1.161	0.705	-2.91	0.1289	0.2159	-0.504	-0.7682741	-0.1877272	1.466	0.371503	0	31.61765	14	21	14	408	46.8
HMGB3	0.184	0.635	1.912	0.61	-2.45	-0.656	0.9355	-0.714	-0.7198549	-0.6846693	1.381	0.373826	0	27.5	6	9	5	200	23
SUB1	0.2	0.577	2.039	0.591	-2.32	-0.794	1.0282	-0.758	-0.7119077	-0.7759081	1.371	0.375269	0	39.55224	5	9	5	134	15.1
S100A13	0.202	0.733	1.891	0.574	-2.31	-0.449	0.9192	-0.802	-0.6597877	-0.6253337	1.326	0.392964	0	55.10204	7	12	7	98	11.5
AHNAK	0.212	0.413	1.804	0.979	-2.24	-1.275	0.8517	-0.031	-0.6736339	-0.6532402	1.361	0.395081	0.001	2.86927	3	4	3	5890	628.7
APEX1	0.196	0.755	1.4	0.943	-2.35	-0.406	0.4854	-0.084	-0.588278	-0.245096	1.23	0.409328	0	47.79874	14	29	14	318	35.5
CSTA	0.333	0.561	2.153	0.541	-1.58	-0.833	1.108	-0.886	-0.5489928	-0.8594957	1.157	0.412485	0	53.06122	6	9	6	98	11
HNRNPA2B1	0.48	0.86	1.631	0.498	-1.06	-0.218	0.7097	-1.008	-0.3940183	-0.6129045	0.83	0.412677	0	16.14731	5	8	4	353	37.4
EECP	0.242	0.279	4.217	0.259	-2.05	-1.842	2.0762	-1.949	-0.9405293	-1.8955236	2.013	0.418985	0.002	7.211538	2	3	2	208	22.7
COL5A3	0.229	0.735	2.753	0.254	-2.13	-0.444	1.4594	-1.976	-0.7723366	-1.2103081	1.671	0.423456	0.005	0.859599	2	3	2	1745	172
LCN1	0.413	0.334	2.453	0.565	-1.28	-1.581	1.2946	-0.823	-0.5967105	-1.0503051	1.299	0.425911	0	19.88636	3	5	3	176	19.2
FBP1	0.231	0.719	1.141	1.319	-2.12	-0.476	0.1888	0.3983	-0.5013947	-0.1435951	1.14	0.44365	0.003	6.804734	2	2	2	338	36.8

	AR(16F16/DMSO)				Log(2) AR(16F16/DMSO)				Log(2)Mean	Log(2)Median	Log(2)	Two-tailed	Exp.				# Unique		
Gene Name	n=1	n=2	n=3	n=4	n=1	n=2	n=3	n=4	AR	AR	Std.Dev	T.Test	q-value	Coverage	# Peptides	# PSMs	Peptides	# AAs	MW [kDa]
HMGA1	0.126	0.886	1.69	0.778	-2.98	-0.175	0.7571	-0.362	-0.6909173	-0.2684188	1.605	0.452616	0	48.59813	7	21	3	107	11.7
ENO1	0.195	1.186	1.282	0.759	-2.36	0.2462	0.3582	-0.398	-0.538696	-0.075801	1.26	0.455344	0	37.32719	15	30	15	434	47.1
ARPC5	0.397	0.659	2.191	0.461	-1.33	-0.601	1.1375	-1.117	-0.4779211	-0.8590789	1.12	0.456032	0	21.56863	3	4	2	153	17
S100	0.304	0.778	1.987	0.57	-1.72	-0.363	0.9903	-0.812	-0.4750235	-0.5873007	1.127	0.461287	0.001	7.017544	2	3	2	114	13.2
HMGB1	0.135	0.602	2.016	0.904	-2.88	-0.733	1.0119	-0.146	-0.6876501	-0.43934	1.634	0.46171	0	32.55814	9	17	8	215	24.9
SARS	0.196	0.602	3.132	0.386	-2.35	-0.732	1.647	-1.372	-0.7019616	-1.0519769	1.702	0.469828	0	6.343284	3	5	3	536	61.3
YWHAZ	0.243	0.571	2.8	0.479	-2.04	-0.808	1.4854	-1.062	-0.6063337	-0.9353319	1.492	0.475903	0	12.19512	3	5	2	246	28
HNRPD	0.473	1.08	1.36	0.679	-1.08	0.1107	0.4438	-0.559	-0.2712461	-0.2239998	0.682	0.484462	0	17.46479	6	13	5	355	38.4
PRH1	1.323	3.595	100	0.117	0.403	1.8458	8.6707	-3.097	1.955662	1.12459238	4.934	0.485872	0	16.60377	1	7	1	265	27.9
HDGF	0.197	1.43	1.305	0.651	-2.35	0.5158	0.3849	-0.62	-0.5165421	-0.1175704	1.321	0.491381	0	52.08333	10	12	10	240	26.8
KRT78	0.223	1.779	1.209	0.492	-2.17	0.8308	0.2711	-1.024	-0.5222444	-0.3764758	1.344	0.493638	0	15.38462	10	14	6	520	56.8
MAP4	0.258	0.502	2.085	0.961	-1.96	-0.996	1.0605	-0.058	-0.4872771	-0.5265732	1.291	0.505048	0	2.481498	5	5	5	2297	245.3
S100A6	0.392	1.405	0.845	0.975	-1.35	0.4903	-0.242	-0.037	-0.2848991	-0.1397148	0.774	0.515204	0.001	34.44444	4	5	4	90	10.2
NPM1	0.177	0.871	1.828	0.907	-2.5	-0.199	0.87	-0.141	-0.4914302	-0.1697726	1.424	0.539605	0	43.87755	12	25	12	294	32.6
MTDH	0.398	1.753	4.132	1.298	-1.33	0.8098	2.0469	0.3764	0.476282	0.59310857	1.396	0.543892	0	11.34021	5	6	5	582	63.8
S100A7	0.268	0.852	1.984	0.735	-1.9	-0.232	0.9887	-0.445	-0.3965388	-0.3381601	1.184	0.550865	0.001	21.78218	2	5	2	101	11.5
COL6A1	0.242	0.392	3.87	0.539	-2.05	-1.352	1.9522	-0.892	-0.5852854	-1.121767	1.757	0.552988	0	6.906615	5	9	5	1028	108.5
NUDC	0.383	0.949	1.488	0.902	-1.38	-0.075	0.5748	-0.149	-0.2583267	-0.112061	0.818	0.572443	0.001	10.57402	3	3	3	331	38.2
CALD1	0.303	0.784	2.123	0.795	-1.72	-0.351	1.0881	-0.331	-0.3292659	-0.3409782	1.148	0.606342	0	6.179067	3	4	3	793	93.2
YBX1	0.085	2.167	1.606	0.664	-3.55	1.1155	0.6823	-0.591	-0.5865532	0.04542546	2.106	0.616344	0	21.12299	4	4	4	374	42
HNRNPAB	0.201	1.06	1.764	0.997	-2.31	0.0834	0.8187	-0.005	-0.3537297	0.03942527	1.357	0.638169	0	20.78313	7	16	6	332	36
PIP	0.261	0.415	4.136	0.637	-1.94	-1.27	2.0483	-0.651	-0.4530507	-0.9607761	1.749	0.640107	0	36.9863	6	10	6	146	16.6
KRT13	0.652	2.012	0.448	0.905	-0.62	1.0084	-1.16	-0.144	-0.2283505	-0.3806443	0.923	0.654743	0	24.67249	14	27	7	458	49.6
KITLG	0.534	0.622	2.593	0.615	-0.9	-0.684	1.3728	-0.703	-0.2298589	-0.693701	1.073	0.697255	0.016	3.296703	1	2	1	273	30.9
NUCKS1	0.276	0.899	7.504	1.659	-1.85	-0.153	2.9107	0.737	0.4098791	0.29177004	1.984	0.70721	0.001	18.107	3	5	3	243	27.3
SHMT2	0.171	1.146	5.523	0.343	-2.55	0.1972	2.4652	-1.543	-0.3568231	-0.6726826	2.197	0.766598	0	18.25397	7	9	7	504	56
HMGN1	0.258	0.749	3.513	0.739	-1.95	-0.416	1.8128	-0.436	-0.248306	-0.4261394	1.551	0.769877	0	54	7	14	7	100	10.7
yfbT	0.648	1.293	0.022	11.59	-0.63	0.3711	-5.47	3.5326	-0.5479259	-0.1271621	3.73	0.788044	0.001	9.502262	1	7	1	221	22.9
HMGN2	0.223	1.389	2.552	0.719	-2.16	0.474	1.3536	-0.473	-0.2023427	0.00032909	1.505	0.805495	0	53.33333	5	8	5	90	9.4
INS-IGF2	0.44	2.932	0.493	1.07	-1.18	1.5517	-1.022	0.0983	-0.13897	-0.4619322	1.263	0.839957	0.006	3.5	1	8	1	200	21.5
NCL	0.218	1.294	4.583	1.229	-2.2	0.3724	2.1963	0.2975	0.1677586	0.33494554	1.803	0.864277	0	28.16901	22	45	22	710	76.6
DCD	0.614	0.794	2.554	0.627	-0.7	-0.333	1.3529	-0.672	-0.0889822	-0.5026632	0.976	0.866916	0	20	4	7	4	110	11.3
POSTN	0.446	1.009	2.9	0.597	-1.16	0.0135	1.5352	-0.745	-0.0901604	-0.3655774	1.188	0.88901	0	6.220096	4	7	1	836	93.3
CCDC158	1.812	1.09	1.276	0.329	0.857	0.1242	0.3528	-1.605	-0.067593	0.23850076	1.07	0.907424	0.027	1.796945	1	3	1	1113	127.1

Bibliography

Adams, E.F., C.J. Newton, H. Braunsberg, N. Shaikh, M. Ghilchik, and V.H. James. 1988. Effects of human breast fibroblasts on growth and 17 beta-estradiol dehydrogenase activity of MCF-7 cells in culture. *Breast Cancer Res. Treat.* 11:165–72.

Al-Mahmood, S., J. Sapiezynski, O.B. Garbuzenko, and T. Minko. 2018. Metastatic and triple-negative breast cancer: challenges and treatment options. *Drug Deliv. Transl. Res.* 8:1483–1507. doi:10.1007/s13346-018-0551-3.

Altieri, F., F. Cairone, F. Giamogante, S. Carradori, M. Locatelli, S. Chichiarelli, and S. Cesa. 2019. Influence of Ellagitannins Extracted by Pomegranate Fruit on Disulfide Isomerase PDIA3 Activity. *Nutrients*. 11:186. doi:10.3390/nu11010186.

dos Anjos Pultz, B., F. Andrés Cordero da Luz, S. Socorro Faria, L. Peixoto Ferreira de Souza, P. Cristina Brígido Tavares, V. Alonso Goulart, W. Fontes, L. Ricardo Goulart, and M. José Barbosa Silva. 2017. The multifaceted role of extracellular vesicles in metastasis: Priming the soil for seeding. *Int. J. Cancer*. 140:2397–2407. doi:10.1002/ijc.30595.

Antoniou, A.N., S. Ford, M. Alphey, A. Osborne, T. Elliott, and S.J. Powis. 2002. The oxidoreductase ERp57 efficiently reduces partially folded in preference to fully folded MHC class I molecules. *EMBO J.* 21:2655–2663. doi:10.1093/emboj/21.11.2655.

Arrigoni, C., S. Bersini, M. Gilardi, and M. Moretti. 2016. In Vitro Co-Culture Models of Breast Cancer Metastatic Progression towards Bone. *Int. J. Mol. Sci.* 17. doi:10.3390/IJMS17091405.

Avgustinova, A., M. Iravani, D. Robertson, A. Fearns, Q. Gao, P. Klingbeil, A.M. Hanby, V. Speirs, E. Sahai, F. Calvo, and C.M. Isacke. 2016. Tumour cell-derived Wnt7a recruits and activates fibroblasts to promote tumour aggressiveness. *Nat. Commun.* 7:10305. doi:10.1038/ncomms10305.

Bae, Y.K., A. Kim, M.K. Kim, J.E. Choi, S.H. Kang, and S.J. Lee. 2013. Fibronectin expression in carcinoma cells correlates with tumor aggressiveness and poor clinical outcome in patients with invasive breast cancer. *Hum. Pathol.* 44:2028–2037. doi:10.1016/J.HUMPATH.2013.03.006.

Balanis, N., M.K. Wendt, B.J. Schiemann, Z. Wang, W.P. Schiemann, and C.R. Carlin. 2013. Epithelial to mesenchymal transition promotes breast cancer progression via a fibronectin-dependent STAT3 signaling pathway. *J. Biol. Chem.* 288:17954–67. doi:10.1074/jbc.M113.475277.

Baroni, S., S. Romero-Cordoba, I. Plantamura, M. Dugo, E. D'Ippolito, A. Cataldo, G. Cosentino, V. Angeloni, A. Rossini, M.G. Daidone, and M. V Iorio. 2016. Exosome-mediated delivery of miR-9 induces cancer-associated fibroblast-like properties in human breast fibroblasts. *Cell Death Dis.* 7:e2312–e2312. doi:10.1038/cddis.2016.224.

Barsky, S.H., and N.J. Karlin. 2005. Myoepithelial Cells: Autocrine and Paracrine Suppressors of Breast Cancer Progression. *J. Mammary Gland Biol. Neoplasia*. 10:249–260. doi:10.1007/s10911-005-9585-5.

Bass, M.D., M.R. Morgan, and M.J. Humphries. 2007. Integrins and syndecan-4 make distinct, but critical, contributions to adhesion contact formation. *Soft Matter*. 3:372. doi:10.1039/b614610d.

Benson, C.S., S.D. Babu, S. Radhakrishna, N. Selvamurugan, and B. Ravi Sankar. 2013. Expression of matrix metalloproteinases in human breast cancer tissues. *Dis. Markers*. 34:395–405. doi:10.3233/DMA-130986.

Berger, A.J., C.M. Renner, I. Hale, X. Yang, S.M. Ponik, P.S. Weisman, K.S. Masters, and P.K. Kreeger. 2019. Scaffold stiffness influences breast cancer cell invasion via EGFR-linked Mena upregulation and matrix remodeling. *Matrix Biol.* doi:10.1016/j.matbio.2019.07.006.

Bhowmick, N.A., E.G. Neilson, and H.L. Moses. 2004. Stromal fibroblasts in cancer initiation and progression. *Nature*. 432:332–7. doi:10.1038/nature03096.

Bierie, B., and H.L. Moses. 2006. TGFβ: the molecular Jekyll and Hyde of cancer. *Nat. Rev. Cancer*. 6:506–520. doi:10.1038/nrc1926.

BIGAGLI, E., L. CINCI, M. D'AMBROSIO, and C. LUCERI. 2019. Transcriptomic Characterization, Chemosensitivity and Regulatory Effects of Exosomes in Spontaneous EMT/MET Transitions of Breast Cancer Cells. *Cancer Genomics - Proteomics*. 16:163–173. doi:10.21873/cgp.20122.

Bissell, M.J., and W.C. Hines. 2011. Why don't we get more cancer? A proposed role of the microenvironment in restraining cancer progression. *Nat. Med.* 17:320–329. doi:10.1038/nm.2328.

Blanco, M.J., G. Moreno-Bueno, D. Sarrio, A. Locascio, A. Cano, J. Palacios, and M.A. Nieto. 2002. Correlation of Snail expression with histological grade and lymph node status in breast carcinomas. *Oncogene*. 21:3241–3246. doi:10.1038/sj.onc.1205416.

Brandi, J., M. Manfredi, G. Speziali, F. Gosetti, E. Marengo, and D. Cecconi. 2018a. Proteomic approaches to decipher cancer cell secretome. *Semin. Cell Dev. Biol.* 78:93–101. doi:10.1016/J.SEMCDB.2017.06.030.

Brandi, J., M. Manfredi, G. Speziali, F. Gosetti, E. Marengo, and D. Cecconi. 2018b. Proteomic approaches to decipher cancer cell secretome. *Semin. Cell Dev. Biol.* 78:93–101. doi:10.1016/J.SEMCDB.2017.06.030.

Broders-Bondon, F., T.H.N. Ho-Bouldoires, M.-E. Fernandez-Sanchez, and E. Farge. 2018. Mechanotransduction in tumor progression: The dark side of the force. *J. Cell Biol.* 217:1571–1587. doi:10.1083/JCB.201701039.

Buchsbaum, R.J., and S.Y. Oh. 2016. Breast Cancer-Associated Fibroblasts: Where We Are and Where We Need to Go. *Cancers (Basel).* 8. doi:10.3390/cancers8020019.

Carbon, S., A. Ireland, C.J. Mungall, S. Shu, B. Marshall, S. Lewis, A. Hub, W. Presence, and W. Group. 2009. AmiGO: online access to ontology and annotation data. *Bioinforma. Appl. NOTE*. 25:288–289. doi:10.1093/bioinformatics/btn615.

Carey, L., E. Winer, G. Viale, D. Cameron, and L. Gianni. 2010. Triple-negative breast cancer: disease entity or title of convenience? *Nat. Rev. Clin. Oncol.* 7:683–692. doi:10.1038/nrclinonc.2010.154.

Carpenter, P.M., A. V. Dao, Z.S. Arain, M.K. Chang, H.P. Nguyen, S. Arain, J. Wang-Rodriguez, S.-Y. Kwon, and S.P. Wilczynski. 2009. Motility Induction in Breast Carcinoma by Mammary Epithelial Laminin 332 (Laminin 5). *Mol. Cancer Res.* 7:462–475. doi:10.1158/1541-7786.MCR-08-0148.

Chakraborty, S., M. Lakshmanan, H.L.F. Swa, J. Chen, X. Zhang, Y.S. Ong, L.S. Loo, S.C. Akıncılar, J. Gunaratne, V. Tergaonkar, K.M. Hui, and W. Hong. 2015. An oncogenic role of Agrin in regulating focal adhesion integrity in hepatocellular carcinoma. *Nat. Commun.* 6:6184. doi:10.1038/ncomms7184.

Chang, J., M.C. Lucas, L.E. Leonte, M. Garcia-Montolio, L.B. Singh, A.D. Findlay, M. Deodhar, J.S. Foot, W. Jarolimek, P. Timpson, J.T. Erler, and T.R. Cox. 2017a. Pre-clinical evaluation of small molecule LOXL2 inhibitors in breast cancer. *Oncotarget*. 8:26066–26078. doi:10.18632/oncotarget.15257.

Chang, T.T., D. Thakar, and V.M. Weaver. 2017b. Force-dependent breaching of the basement membrane. *Matrix Biol.* 57–58:178–189. doi:10.1016/j.matbio.2016.12.005.

Chavez, K.J., S. V Garimella, and S. Lipkowitz. 2010. Triple negative breast cancer cell lines: one tool in the search for better treatment of triple negative breast cancer. *Breast Dis.* 32:35–48.

doi:10.3233/BD-2010-0307.

Chazotte, B. 2010. Labeling Cytoskeletal F-Actin with Rhodamine Phalloidin or Fluorescein Phalloidin for Imaging. *Cold Spring Harb. Protoc.* 2010:pdb.prot4947-pdb.prot4947. doi:10.1101/pdb.prot4947.

Chen, F., Z. Zhao, J. Zhou, Y. Lu, D.W. Essex, and Y. Wu. 2018. Protein disulfide isomerase enhances tissue factor-dependent thrombin generation. *Biochem. Biophys. Res. Commun.* 501:172–177. doi:10.1016/j.bbrc.2018.04.207.

Chu, I.M., A.M. Michalowski, M. Hoenerhoff, K.M. Szauter, D. Luger, M. Sato, K. Flanders, A. Oshima, K. Csiszar, and J.E. Green. 2012. GATA3 inhibits lysyl oxidase-mediated metastases of human basal triple-negative breast cancer cells. *Oncogene*. 31:2017–2027. doi:10.1038/onc.2011.382.

Cohen, M., G. Levy, and Y. Nahmias. 2015. Coculture and Long-Term Maintenance of Hepatocytes. *In* Methods in molecular biology (Clifton, N.J.). 161–173.

Collignon, J., L. Lousberg, H. Schroeder, and G. Jerusalem. 2016. Triple-negative breast cancer: treatment challenges and solutions. *Breast cancer (Dove Med. Press.* 8:93–107. doi:10.2147/BCTT.S69488.

Cory, G. 2011. Scratch-Wound Assay. Humana Press. 25–30.

Costa, E.C., A.F. Moreira, D. de Melo-Diogo, V.M. Gaspar, M.P. Carvalho, and I.J. Correia. 2016. 3D tumor spheroids: an overview on the tools and techniques used for their analysis. *Biotechnol. Adv.* 34:1427–1441. doi:10.1016/J.BIOTECHADV.2016.11.002.

Da Costa, G.G., T.H.B. Gomig, R. Kaviski, K. Santos Sousa, C. Kukolj, R.S. De Lima, C. De Andrade Urban, I.J. Cavalli, and E.M.S.F. Ribeiro. 2015. Comparative Proteomics of Tumor and Paired Normal Breast Tissue Highlights Potential Biomarkers in Breast Cancer. *Cancer Genomics Proteomics*. 12:251–61.

Cox, T.R., A. Gartland, and J.T. Erler. 2012. The pre-metastatic niche: is metastasis random? *Bonekey Rep.* 1:80. doi:10.1038/bonekey.2012.80.

Cox, T.R., A. Gartland, and J.T. Erler. 2016. Lysyl Oxidase, a Targetable Secreted Molecule Involved in Cancer Metastasis. *Cancer Res.* 76:188–192. doi:10.1158/0008-5472.CAN-15-2306.

Cuevas, E.P., P. Eraso, M.J. Mazón, V. Santos, G. Moreno-Bueno, A. Cano, and F. Portillo. 2017. LOXL2 drives epithelial-mesenchymal transition via activation of IRE1-XBP1 signalling pathway. *Sci. Rep.* 7:44988. doi:10.1038/srep44988.

Dai, M., Y. Zhang, M. Yu, and W. Tian. 2016. Therapeutic applications of conditioned medium from adipose tissue. *Cell Prolif.* 49:561–567. doi:10.1111/cpr.12281.

Dai, X., H. Cheng, Z. Bai, and J. Li. 2017. Breast Cancer Cell Line Classification and Its Relevance with Breast Tumor Subtyping. *J. Cancer*. 8:3131–3141. doi:10.7150/jca.18457.

Desgrosellier, J.S., and D.A. Cheresh. 2010. Integrins in cancer: biological implications and therapeutic opportunities. *Nat. Rev. Cancer*. 10:9–22. doi:10.1038/nrc2748.

Dihazi, H., G. Helene Dihazi, A. Bibi, M. Eltoweissy, C.A. Mueller, A.R. Asif, D. Rubel, R. Vasko, and G.A. Mueller. 2013. Secretion of ERP57 is important for extracellular matrix accumulation and progression of renal fibrosis, and is an early sign of disease onset. | *J. Cell Sci.* 126:3649–3663. doi:10.1242/jcs.125088.

Dongre, A., and R.A. Weinberg. 2019. New insights into the mechanisms of epithelial–mesenchymal transition and implications for cancer. *Nat. Rev. Mol. Cell Biol.* 20:69–84. doi:10.1038/s41580-018-0080-4.

Du, H., and G. Che. 2017. Genetic alterations and epigenetic alterations of cancer-associated

fibroblasts. *Oncol. Lett.* 13:3–12. doi:10.3892/ol.2016.5451.

Duffy, M.J. 2002. Urokinase plasminogen activator and its inhibitor, PAI-1, as prognostic markers in breast cancer: from pilot to level 1 evidence studies. *Clin. Chem.* 48:1194–7.

Dunn, G.P., L.J. Old, and R.D. Schreiber. 2004. The Three Es of Cancer Immunoediting. *Annu. Rev. Immunol.* 22:329–360. doi:10.1146/annurev.immunol.22.012703.104803.

Dupont, S., L. Morsut, M. Aragona, E. Enzo, S. Giulitti, M. Cordenonsi, F. Zanconato, J. Le Digabel, M. Forcato, S. Bicciato, N. Elvassore, and S. Piccolo. 2011. Role of YAP/TAZ in mechanotransduction. *Nature*. 474:179–183. doi:10.1038/nature10137.

Eden, E., R. Navon, I. Steinfeld, D. Lipson, and Z. Yakhini. 2009. GOrilla: a tool for discovery and visualization of enriched GO terms in ranked gene lists. *BMC Bioinformatics*. 10:48. doi:10.1186/1471-2105-10-48.

Egeblad, M., E.S. Nakasone, and Z. Werb. 2010. Tumors as Organs: Complex Tissues that Interface with the Entire Organism. *Dev. Cell*. 18:884–901. doi:10.1016/j.devcel.2010.05.012.

Eliyatkın, N., E. Yalçın, B. Zengel, S. Aktaş, and E. Vardar. 2015. Molecular Classification of Breast Carcinoma: From Traditional, Old-Fashioned Way to A New Age, and A New Way. *J. Breast Heal.* 11:59. doi:10.5152/TJBH.2015.1669.

Ellgaard, L., and E.-M. Frickel. 2003. Calnexin, Calreticulin, and ERp57: Teammates in Glycoprotein Folding. *Cell Biochem. Biophys.* 39:223–248. doi:10.1385/CBB:39:3:223.

Elliott, N.T., and F. Yuan. 2011. A review of three-dimensional in vitro tissue models for drug discovery and transport studies. *J. Pharm. Sci.* 100:59–74. doi:10.1002/jps.22257.

Fabregat, A., S. Jupe, L. Matthews, K. Sidiropoulos, M. Gillespie, P. Garapati, R. Haw, B. Jassal, F. Korninger, B. May, M. Milacic, C.D. Roca, K. Rothfels, C. Sevilla, V. Shamovsky, S. Shorser, T. Varusai, G. Viteri, J. Weiser, G. Wu, L. Stein, H. Hermjakob, and P. D'Eustachio. 2018. The Reactome Pathway Knowledgebase. *Nucleic Acids Res.* 46:D649–D655. doi:10.1093/nar/gkx1132.

Ferlay, J., I. Soerjomataram, R. Dikshit, S. Eser, C. Mathers, M. Rebelo, D.M. Parkin, D. Forman, and F. Bray. 2015. Cancer incidence and mortality worldwide: sources, methods and major patterns in GLOBOCAN 2012. *Int. J. cancer*. 136:E359-86. doi:10.1002/ijc.29210.

Foitzik, A., R. Prange, K. Böttcher, and A. Schreiner. 2016. High-Content Screening Opera Phenix High-Content Screening System Technical Performance: Speed Authors.

Fredlund, E., J. Staaf, J.K. Rantala, O. Kallioniemi, Å. Borg, and M. Ringnér. 2012. The gene expression landscape of breast cancer is shaped by tumor protein p53 status and epithelial-mesenchymal transition. *Breast Cancer Res.* 14:R113. doi:10.1186/bcr3236.

Frickel, E.-M., R. Riek, I. Jelesarov, A. Helenius, K. Wuthrich, and L. Ellgaard. 2002. TROSY-NMR reveals interaction between ERp57 and the tip of the calreticulin P-domain. *Proc. Natl. Acad. Sci.* 99:1954–1959. doi:10.1073/pnas.042699099.

Friedrich, J., C. Seidel, R. Ebner, and L.A. Kunz-Schughart. 2009. Spheroid-based drug screen: considerations and practical approach. *Nat. Protoc.* 4:309–324. doi:10.1038/nprot.2008.226.

Gaucci, E., F. Altieri, C. Turano, and S. Chichiarelli. 2013. The protein ERp57 contributes to EGF receptor signaling and internalization in MDA-MB-468 breast cancer cells. *J. Cell. Biochem.* 114:2461–2470. doi:10.1002/jcb.24590.

Giannoni, E., F. Bianchini, L. Masieri, S. Serni, E. Torre, L. Calorini, and P. Chiarugi. 2010. Reciprocal Activation of Prostate Cancer Cells and Cancer-Associated Fibroblasts Stimulates Epithelial-Mesenchymal Transition and Cancer Stemness. *Cancer Res.* 70:6945–6956. doi:10.1158/0008-5472.CAN-10-0785.

Gkretsi, V., and T. Stylianopoulos. 2018. Cell Adhesion and Matrix Stiffness: Coordinating Cancer

Cell Invasion and Metastasis. *Front. Oncol.* 8:145. doi:10.3389/fonc.2018.00145.

Goossens, S., N. Vandamme, P. Van Vlierberghe, and G. Berx. 2017. EMT transcription factors in cancer development re-evaluated: Beyond EMT and MET. *Biochim. Biophys. Acta - Rev. Cancer*. 1868:584–591. doi:10.1016/J.BBCAN.2017.06.006.

Guney, E., and B. Oliva. 2012. Exploiting protein-protein interaction networks for genome-wide disease-gene prioritization. *PLoS One*. 7:e43557. doi:10.1371/journal.pone.0043557.

Guo, Y., X. Ji, J. Liu, D. Fan, Q. Zhou, C. Chen, W. Wang, G. Wang, H. Wang, W. Yuan, Z. Ji, and Z. Sun. 2019. Effects of exosomes on pre-metastatic niche formation in tumors. *Mol. Cancer*. 18:39. doi:10.1186/s12943-019-0995-1.

H.S.Young. 2018. No Title.

Halperin, L., J. Jung, and M. Michalak. 2014. The many functions of the endoplasmic reticulum chaperones and folding enzymes. *IUBMB Life*. 66:318–326. doi:10.1002/iub.1272.

Han, J., W. Lim, D. You, Y. Jeong, S. Kim, J.E. Lee, T.H. Shin, G. Lee, and S. Park. 2019. Chemoresistance in the Human Triple-Negative Breast Cancer Cell Line MDA-MB-231 Induced by Doxorubicin Gradient Is Associated with Epigenetic Alterations in Histone Deacetylase. *J. Oncol.* 2019:1–12. doi:10.1155/2019/1345026.

Härmä, V., H.P. Schukov, A. Happonen, I. Ahonen, J. Virtanen, H. Siitari, M. Åkerfelt, J. Lötjönen, and M. Nees. 2014. Quantification of dynamic morphological drug responses in 3D organotypic cell cultures by automated image analysis. *PLoS One*. 9. doi:10.1371/journal.pone.0096426.

Harris, A.R., P. Jreij, and D.A. Fletcher. 2018. Mechanotransduction by the Actin Cytoskeleton: Converting Mechanical Stimuli into Biochemical Signals. *Annu. Rev. Biophys.* 47:617–631. doi:10.1146/annurev-biophys-070816-033547.

Hatahet, F., and L.W. Ruddock. 2009. Protein Disulfide Isomerase: A Critical Evaluation of Its Function in Disulfide Bond Formation. *Antioxid. Redox Signal.* 11:2807–2850. doi:10.1089/ars.2009.2466.

Hawkins, H.C., and R.B. Freedman. 1991. The reactivities and ionization properties of the active-site dithiol groups of mammalian protein disulphide-isomerase. *Biochem. J.* 275:335–339. doi:10.1042/bj2750335.

Hayashi, M., Y. Yamamoto, M. Ibusuki, S. Fujiwara, S. Yamamoto, S. Tomita, M. Nakano, K. Murakami, K. Iyama, and H. Iwase. 2012. Evaluation of Tumor Stiffness by Elastography Is Predictive for Pathologic Complete Response to Neoadjuvant Chemotherapy in Patients with Breast Cancer. *Ann. Surg. Oncol.* 19:3042–3049. doi:10.1245/s10434-012-2343-1.

Hoffstrom, B.G., A. Kaplan, R. Letso, R.S. Schmid, G.J. Turmel, D.C. Lo, and B.R. Stockwell. 2010. Inhibitors of protein disulfide isomerase suppress apoptosis induced by misfolded proteins. *Nat. Chem. Biol.* 6:900–6. doi:10.1038/nchembio.467.

Holler, E. 2005. Laminin isoform expression in breast tumors. *Breast Cancer Res.* 7:166–7. doi:10.1186/bcr1270.

Hoshino, A., B. Costa-Silva, T.-L. Shen, G. Rodrigues, A. Hashimoto, M. Tesic Mark, H. Molina, S. Kohsaka, A. Di Giannatale, S. Ceder, S. Singh, C. Williams, N. Soplop, K. Uryu, L. Pharmer, T. King, L. Bojmar, A.E. Davies, Y. Ararso, T. Zhang, H. Zhang, J. Hernandez, J.M. Weiss, V.D. Dumont-Cole, K. Kramer, L.H. Wexler, A. Narendran, G.K. Schwartz, J.H. Healey, P. Sandstrom, K. Jørgen Labori, E.H. Kure, P.M. Grandgenett, M.A. Hollingsworth, M. de Sousa, S. Kaur, M. Jain, K. Mallya, S.K. Batra, W.R. Jarnagin, M.S. Brady, O. Fodstad, V. Muller, K. Pantel, A.J. Minn, M.J. Bissell, B.A. Garcia, Y. Kang, V.K. Rajasekhar, C.M. Ghajar, I. Matei, H. Peinado, J. Bromberg, and D. Lyden. 2015. Tumour exosome integrins determine organotropic metastasis. *Nature*. 527:329–335. doi:10.1038/nature15756.

Houthuijzen, J.M., and J. Jonkers. 2018. Cancer-associated fibroblasts as key regulators of the breast cancer tumor microenvironment. *Cancer Metastasis Rev.* 37:577–597. doi:10.1007/s10555-018-9768-3.

Hu, M., J. Yao, L. Cai, K.E. Bachman, F. van den Brûle, V. Velculescu, and K. Polyak. 2005. Distinct epigenetic changes in the stromal cells of breast cancers. *Nat. Genet.* 37:899–905. doi:10.1038/ng1596.

Humphries, J.D., A. Byron, M.D. Bass, S.E. Craig, J.W. Pinney, D. Knight, and M.J. Humphries. 2009. Proteomic Analysis of Integrin-Associated Complexes Identifies RCC2 as a Dual Regulator of Rac1 and Arf6. *Sci. Signal.* 2:ra51–ra51. doi:10.1126/scisignal.2000396.

Hussmann, M., K. Janke, P. Kranz, F. Neumann, E. Mersch, M. Baumann, K. Goepelt, U. Brockmeier, and E. Metzen. 2015. Depletion of the thiol oxidoreductase ERp57 in tumor cells inhibits proliferation and increases sensitivity to ionizing radiation and chemotherapeutics. *Oncotarget*. 6:39247–61. doi:10.18632/oncotarget.5746.

Hutchinson, J.H., M.W. Rowbottom, D. Lonergan, J. Darlington, P. Prodanovich, C.D. King, J.F. Evans, and G. Bain. 2017. Small Molecule Lysyl Oxidase-like 2 (LOXL2) Inhibitors: The Identification of an Inhibitor Selective for LOXL2 over LOX. *ACS Med. Chem. Lett.* 8:423–427. doi:10.1021/acsmedchemlett.7b00014.

Ikenaga, N., Z.-W. Peng, K.A. Vaid, S.B. Liu, S. Yoshida, D.Y. Sverdlov, A. Mikels-Vigdal, V. Smith, D. Schuppan, and Y. V Popov. 2019. Selective targeting of lysyl oxidase-like 2 (LOXL2) suppresses hepatic fibrosis progression and accelerates its reversal. doi:10.1136/gutjnl-2016-312473.

Insua-Rodríguez, J., and T. Oskarsson. 2016. The extracellular matrix in breast cancer. *Adv. Drug Deliv. Rev.* 97:41–55. doi:10.1016/J.ADDR.2015.12.017.

Irvin, W.J., and L.A. Carey. 2008. What is triple-negative breast cancer? *Eur. J. Cancer*. 44:2799–2805. doi:10.1016/j.ejca.2008.09.034.

Ishiguro, T., H. Ohata, A. Sato, K. Yamawaki, T. Enomoto, and K. Okamoto. 2017. Tumor-derived spheroids: Relevance to cancer stem cells and clinical applications. *Cancer Sci.* 108:283–289. doi:10.1111/cas.13155.

Iturbide, A., A. García De Herreros, and S. Peiró. 2015. A new role for LOX and LOXL2 proteins in transcription regulation. *FEBS J.* 282:1768–1773. doi:10.1111/febs.12961.

Izdebska, M., W. Zielińska, D. Grzanka, and M. Gagat. 2018. The Role of Actin Dynamics and Actin-Binding Proteins Expression in Epithelial-to-Mesenchymal Transition and Its Association with Cancer Progression and Evaluation of Possible Therapeutic Targets. *Biomed Res. Int.* 2018:1–13. doi:10.1155/2018/4578373.

Janicke, F., A. Prechtl, C. Thomssen, N. Harbeck, C. Meisner, M. Untch, C.G.J.F. Sweep, H.-K. Selbmann, H. Graeff, M. Schmitt, and German N0 Study Group. 2001. Randomized Adjuvant Chemotherapy Trial in High-Risk, Lymph Node-Negative Breast Cancer Patients Identified by Urokinase-Type Plasminogen Activator and Plasminogen Activator Inhibitor Type 1. *JNCI J. Natl. Cancer Inst.* 93:913–920. doi:10.1093/jnci/93.12.913.

Jaros, J., M. Petrov, M. Tesarova, and A. Hampl. 2017. Revealing 3D Ultrastructure and Morphology of Stem Cell Spheroids by Electron Microscopy. 417–431.

Jayachandran, A., B. Dhungel, and J.C. Steel. 2016. Epithelial-to-mesenchymal plasticity of cancer stem cells: therapeutic targets in hepatocellular carcinoma. *J. Hematol. Oncol.* 9:74. doi:10.1186/S13045-016-0307-9.

Jessop, C.E., S. Chakravarthi, N. Garbi, G.J. Hämmerling, S. Lovell, and N.J. Bulleid. 2007a. ERp57 is essential for efficient folding of glycoproteins sharing common structural domains. *EMBO J.* 26:28–40. doi:10.1038/sj.emboj.7601505.

Jessop, C.E., S. Chakravarthi, N. Garbi, G.J. Hämmerling, S. Lovell, and N.J. Bulleid. 2007b. ERp57 is essential for efficient folding of glycoproteins sharing common structural domains. *EMBO J.* 26:28–40. doi:10.1038/sj.emboj.7601505.

Jia, Y., Y. Chen, Q. Wang, U. Jayasinghe, X. Luo, Q. Wei, J. Wang, H. Xiong, C. Chen, B. Xu, W. Hu, L. Wang, W. Zhao, and J. Zhou. 2017. Exosome: emerging biomarker in breast cancer. *Oncotarget*. 8:41717–41733. doi:10.18632/oncotarget.16684.

Jotzu, C., E. Alt, G. Welte, J. Li, B.T. Hennessy, E. Devarajan, S. Krishnappa, S. Pinilla, L. Droll, and Y.-H. Song. 2011. Adipose tissue derived stem cells differentiate into carcinoma-associated fibroblast-like cells under the influence of tumor derived factors. *Cell. Oncol.* 34:55–67. doi:10.1007/s13402-011-0012-1.

Justice, B.A., N.A. Badr, and R.A. Felder. 2009. 3D cell culture opens new dimensions in cell-based assays. *Drug Discov. Today*. 14:102–107. doi:10.1016/j.drudis.2008.11.006.

Kalluri, R., and R.A. Weinberg. 2009. The basics of epithelial-mesenchymal transition. *J. Clin. Invest.* 119:1420–8. doi:10.1172/JCI39104.

Kalluri, R., and M. Zeisberg. 2006a. Fibroblasts in cancer. *Nat. Rev. Cancer*. 6:392–401. doi:10.1038/nrc1877.

Kalluri, R., and M. Zeisberg. 2006b. Fibroblasts in cancer. *Nat. Rev. Cancer*. 6:392–401. doi:10.1038/nrc1877.

Kaplan, R.N., R.D. Riba, S. Zacharoulis, A.H. Bramley, L. Vincent, C. Costa, D.D. MacDonald, D.K. Jin, K. Shido, S.A. Kerns, Z. Zhu, D. Hicklin, Y. Wu, J.L. Port, N. Altorki, E.R. Port, D. Ruggero, S. V. Shmelkov, K.K. Jensen, S. Rafii, and D. Lyden. 2005. VEGFR1-positive haematopoietic bone marrow progenitors initiate the pre-metastatic niche. *Nature*. 438:820–827. doi:10.1038/nature04186.

Karousou, E., M.L. D'Angelo, K. Kouvidi, D. Vigetti, M. Viola, D. Nikitovic, G. De Luca, and A. Passi. 2014. Collagen VI and hyaluronan: the common role in breast cancer. *Biomed Res. Int.* 2014:606458. doi:10.1155/2014/606458.

Keerthikumar, S., D. Chisanga, D. Ariyaratne, H. Al Saffar, S. Anand, K. Zhao, M. Samuel, M. Pathan, M. Jois, N. Chilamkurti, L. Gangoda, and S. Mathivanan. 2016. ExoCarta: A Web-Based Compendium of Exosomal Cargo. *J. Mol. Biol.* 428:688–692. doi:10.1016/j.jmb.2015.09.019.

Khalili, A.A., and M.R. Ahmad. 2015. A Review of Cell Adhesion Studies for Biomedical and Biological Applications. *Int. J. Mol. Sci.* 16:18149–84. doi:10.3390/ijms160818149.

Kim, B.G., H.J. An, S. Kang, Y.P. Choi, M.-Q. Gao, H. Park, and N.H. Cho. 2011. Laminin-332-Rich Tumor Microenvironment for Tumor Invasion in the Interface Zone of Breast Cancer. *Am. J. Pathol.* 178:373–381. doi:10.1016/J.AJPATH.2010.11.028.

Kim, S.-A., E.K. Lee, and H.-J. Kuh. 2015. Co-culture of 3D tumor spheroids with fibroblasts as a model for epithelial–mesenchymal transition in vitro. *Exp. Cell Res.* 335:187–196. doi:10.1016/j.yexcr.2015.05.016.

Kimbung, S., N. Loman, and I. Hedenfalk. 2015. Clinical and molecular complexity of breast cancer metastases. *Semin. Cancer Biol.* 35:85–95. doi:10.1016/J.SEMCANCER.2015.08.009.

Klein, E.A., L. Yin, D. Kothapalli, P. Castagnino, F.J. Byfield, T. Xu, I. Levental, E. Hawthorne, P.A. Janmey, and R.K. Assoian. 2009. Cell-Cycle Control by Physiological Matrix Elasticity and In Vivo Tissue Stiffening. *Curr. Biol.* 19:1511–1518. doi:10.1016/J.CUB.2009.07.069.

Konstantinovsky, S., B. Davidson, and R. Reich. 2012. Ezrin and BCAR1/p130Cas mediate breast cancer growth as 3-D spheroids. *Clin. Exp. Metastasis*. 29:527–540. doi:10.1007/s10585-012-9468-2.

Kozlov, G., P. Mä, ttä nen, D.Y. Thomas, and K. Gehring. A structural overview of the PDI family of proteins. doi:10.1111/j.1742-4658.2010.07793.x.

Kozlov, G., P. Maattanen, J.D. Schrag, S. Pollock, M. Cygler, B. Nagar, D.Y. Thomas, and K. Gehring. 2006. Crystal structure of the bb' domains of the protein disulfide isomerase ERp57. *Structure*. 14:1331–9. doi:10.1016/j.str.2006.06.019.

Kruger, S., Z.Y.A. Elmageed, D.H. Hawke, P.M. Wörner, D.A. Jansen, A.B. Abdel-Mageed, E.U. Alt, and R. Izadpanah. 2014. Molecular characterization of exosome-like vesicles from breast cancer cells. *BMC Cancer*. 14:44. doi:10.1186/1471-2407-14-44.

Kucharzewska, P., H.C. Christianson, J.E. Welch, K.J. Svensson, E. Fredlund, M. Ringnér, M. Mörgelin, E. Bourseau-Guilmain, J. Bengzon, and M. Belting. 2013. Exosomes reflect the hypoxic status of glioma cells and mediate hypoxia-dependent activation of vascular cells during tumor development. *Proc. Natl. Acad. Sci. U. S. A.* 110:7312–7. doi:10.1073/pnas.1220998110.

Lee, J.L., and C.H. Streuli. 2014. Integrins and epithelial cell polarity. *J. Cell Sci.* 127:3217–25. doi:10.1242/jcs.146142.

Lee, K., H. Park, E.H. Lim, and K.W. Lee. 2011. Exosomes from breast cancer cells can convert adipose tissue-derived mesenchymal stem cells into myofibroblast-like cells. *Int. J. Oncol.* 40:130–138. doi:10.3892/ijo.2011.1193.

LEE, P., N. GHORASHIAN, T. GAIGE, and P. HUNG. 2007. Microfluidic System for Automated Cell-Based Assays. *J. Assoc. Lab. Autom.* 12:363–367. doi:10.1016/j.jala.2007.07.001.

Levental, K.R., H. Yu, L. Kass, J.N. Lakins, M. Egeblad, J.T. Erler, S.F.T. Fong, K. Csiszar, A. Giaccia, W. Weninger, M. Yamauchi, D.L. Gasser, and V.M. Weaver. 2009. Matrix Crosslinking Forces Tumor Progression by Enhancing Integrin Signaling. *Cell*. 139:891–906. doi:10.1016/J.CELL.2009.10.027.

Li, X., J. Yang, L. Peng, A.A. Sahin, L. Huo, K.C. Ward, R. O'Regan, M.A. Torres, and J.L. Meisel. 2017. Triple-negative breast cancer has worse overall survival and cause-specific survival than non-triple-negative breast cancer. *Breast Cancer Res. Treat.* 161:279–287. doi:10.1007/s10549-016-4059-6.

Liang, J., and Y. Shang. 2013. Estrogen and Cancer. *Annu. Rev. Physiol.* 75:225–240. doi:10.1146/annurev-physiol-030212-183708.

Liu, H., M.R. Patel, J.A. Prescher, A. Patsialou, D. Qian, J. Lin, S. Wen, Y.-F. Chang, M.H. Bachmann, Y. Shimono, P. Dalerba, M. Adorno, N. Lobo, J. Bueno, F.M. Dirbas, S. Goswami, G. Somlo, J. Condeelis, C.H. Contag, S.S. Gambhir, and M.F. Clarke. 2010. Cancer stem cells from human breast tumors are involved in spontaneous metastases in orthotopic mouse models. *Proc. Natl. Acad. Sci.* 107:18115–18120. doi:10.1073/pnas.1006732107.

Liu, T., L. Zhou, D. Li, T. Andl, and Y. Zhang. 2019. Cancer-Associated Fibroblasts Build and Secure the Tumor Microenvironment. *Front. Cell Dev. Biol.* 7:60. doi:10.3389/fcell.2019.00060.

Lochter, A., and M.J. Bissell. 1995. Involvement of extracellular matrix constituents in breast cancer. *Semin. Cancer Biol.* 6:165–173. doi:10.1006/SCBI.1995.0017.

Lorenzo, C., C. Frongia, R. Jorand, J. Fehrenbach, P. Weiss, A. Maandhui, G. Gay, B. Ducommun, and V. Lobjois. 2011. Live cell division dynamics monitoring in 3D large spheroid tumor models using light sheet microscopy. *Cell Div.* 6:22. doi:10.1186/1747-1028-6-22.

Luo, K. 2017. Signaling Cross Talk between TGF-β/Smad and Other Signaling Pathways. *Cold Spring Harb. Perspect. Biol.* 9. doi:10.1101/cshperspect.a022137.

Luo, M., M. Brooke, and M.S. Wicha. 2015. Epithelial-Mesenchymal Plasticity of Breast Cancer Stem Cells: Implications for Metastasis and Therapeutic Resistance. *Curr. Pharm. Des.*

21:1301.

Lyons, S.M., E. Alizadeh, J. Mannheimer, K. Schuamberg, J. Castle, B. Schroder, P. Turk, D. Thamm, and A. Prasad. 2016. Changes in cell shape are correlated with metastatic potential in murine and human osteosarcomas. *Biol. Open*. 5:289–99. doi:10.1242/bio.013409.

Malhotra, G.K., X. Zhao, H. Band, and V. Band. 2010. Histological, molecular and functional subtypes of breast cancers. *Cancer Biol. Ther.* 10:955–60. doi:10.4161/cbt.10.10.13879.

Manuel Iglesias, J., I. Beloqui, F. Garcia-Garcia, O. Leis, A. Vazquez-Martin, A. Eguiara, S. Cufi, A. Pavon, J.A. Menendez, J. Dopazo, and A.G. Martin. 2013. Mammosphere Formation in Breast Carcinoma Cell Lines Depends upon Expression of E-cadherin. *PLoS One*. 8:e77281. doi:10.1371/journal.pone.0077281.

Marino, S., K.A. Staines, G. Brown, R.A. Howard-Jones, and M. Adamczyk. 2016. Models of ex vivo explant cultures: applications in bone research. *Bonekey Rep.* 5:818. doi:10.1038/bonekey.2016.49.

Marsh, T., K. Pietras, and S.S. McAllister. 2013. Fibroblasts as architects of cancer pathogenesis. *Biochim. Biophys. Acta*. 1832:1070–8. doi:10.1016/j.bbadis.2012.10.013.

Masjedi, A., V. Hashemi, M. Hojjat-Farsangi, G. Ghalamfarsa, G. Azizi, M. Yousefi, and F. Jadidi-Niaragh. 2018. The significant role of interleukin-6 and its signaling pathway in the immunopathogenesis and treatment of breast cancer. *Biomed. Pharmacother.* 108:1415–1424. doi:10.1016/j.biopha.2018.09.177.

Mathivanan, S., and R.J. Simpson. 2009. ExoCarta: A compendium of exosomal proteins and RNA. *Proteomics*. 9:4997–5000. doi:10.1002/pmic.200900351.

McAnulty, R.J. 2007. Fibroblasts and myofibroblasts: Their source, function and role in disease. *Int. J. Biochem. Cell Biol.* 39:666–671. doi:10.1016/j.biocel.2006.11.005.

McIntosh, J., G. Dennison, J.M.P. Holly, C. Jarrett, A. Frankow, E.J. Foulstone, Z.E. Winters, and C.M. Perks. 2010. IGFBP-3 can either inhibit or enhance EGF-mediated growth of breast epithelial cells dependent upon the presence of fibronectin. *J. Biol. Chem.* 285:38788–800. doi:10.1074/jbc.M110.177311.

Méndez, O., and J. Villanueva. 2015. Challenges and opportunities for cell line secretomes in cancer proteomics. *PROTEOMICS - Clin. Appl.* 9:348–357. doi:10.1002/prca.201400131.

Mitchell, A.L., T.K. Attwood, P.C. Babbitt, M. Blum, P. Bork, A. Bridge, S.D. Brown, H.-Y. Chang, S. El-Gebali, M.I. Fraser, J. Gough, D.R. Haft, H. Huang, I. Letunic, R. Lopez, A. Luciani, F. Madeira, A. Marchler-Bauer, H. Mi, D.A. Natale, M. Necci, G. Nuka, C. Orengo, A.P. Pandurangan, T. Paysan-Lafosse, S. Pesseat, S.C. Potter, M.A. Qureshi, N.D. Rawlings, N. Redaschi, L.J. Richardson, C. Rivoire, G.A. Salazar, A. Sangrador-Vegas, C.J.A. Sigrist, I. Sillitoe, G.G. Sutton, N. Thanki, P.D. Thomas, S.C.E. Tosatto, S.-Y. Yong, and R.D. Finn. 2019. InterPro in 2019: improving coverage, classification and access to protein sequence annotations. *Nucleic Acids Res.* 47:D351–D360. doi:10.1093/nar/gky1100.

Moon, H.-J., J. Finney, L. Xu, D. Moore, D.R. Welch, and M. Mure. 2013. MCF-7 cells expressing nuclear associated lysyl oxidase-like 2 (LOXL2) exhibit an epithelial-to-mesenchymal transition (EMT) phenotype and are highly invasive in vitro. *J. Biol. Chem.* 288:30000–8. doi:10.1074/jbc.C113.502310.

Moussay, E., K. Wang, J.-H. Cho, K. van Moer, S. Pierson, J. Paggetti, P. V. Nazarov, V. Palissot, L.E. Hood, G. Berchem, and D.J. Galas. 2011. MicroRNA as biomarkers and regulators in B-cell chronic lymphocytic leukemia. *Proc. Natl. Acad. Sci.* 108:6573–6578. doi:10.1073/pnas.1019557108.

Muschler, J., and C.H. Streuli. 2010. Cell-matrix interactions in mammary gland development and breast cancer. *Cold Spring Harb. Perspect. Biol.* 2:a003202. doi:10.1101/cshperspect.a003202.

Nath, S., and G.R. Devi. 2016. Three-dimensional culture systems in cancer research: Focus on tumor spheroid model. *Pharmacol. Ther.* 163:94–108. doi:10.1016/j.pharmthera.2016.03.013.

Neophytou, C., P. Boutsikos, and P. Papageorgis. 2018. Molecular Mechanisms and Emerging Therapeutic Targets of Triple-Negative Breast Cancer Metastasis. *Front. Oncol.* 8:31. doi:10.3389/fonc.2018.00031.

O'Brien, K., S. Rani, C. Corcoran, R. Wallace, L. Hughes, A.M. Friel, S. McDonnell, J. Crown, M.W. Radomski, and L. O'Driscoll. 2013. Exosomes from triple-negative breast cancer cells can transfer phenotypic traits representing their cells of origin to secondary cells. *Eur. J. Cancer*. 49:1845–1859. doi:10.1016/j.ejca.2013.01.017.

Ogorevc, E., V. Kralj-Iglic, and P. Veranic. 2013. The role of extracellular vesicles in phenotypic cancer transformation. *Radiol. Oncol.* 47:197–205. doi:10.2478/raon-2013-0037.

Ohashi, K., S. Fujiwara, and K. Mizuno. 2017. Roles of the cytoskeleton, cell adhesion and rho signalling in mechanosensing and mechanotransduction. *J. Biochem.* 161:mvw082. doi:10.1093/jb/mvw082.

Ojha, R., and R.K. Amaravadi. 2017. Targeting the unfolded protein response in cancer. *Pharmacol. Res.* 120:258–266. doi:10.1016/j.phrs.2017.04.003.

Okada, K., H.J. Moon, J. Finney, A. Meier, and M. Mure. 2018. Extracellular Processing of Lysyl Oxidase-like 2 and Its Effect on Amine Oxidase Activity. *Biochemistry*. 57:6973–6983. doi:10.1021/acs.biochem.8b01008.

Oliver, J.D., H.L. Roderick, D.H. Llewellyn, and S. High. 1999a. ERp57 Functions as a Subunit of Specific Complexes Formed with the ER Lectins Calreticulin and Calnexin. *Mol. Biol. Cell*. 10:2573–2582. doi:10.1091/mbc.10.8.2573.

Oliver, J.D., H.L. Roderick, D.H. Llewellyn, and S. High. 1999b. ERp57 functions as a subunit of specific complexes formed with the ER lectins calreticulin and calnexin. *Mol. Biol. Cell*. 10:2573–82. doi:10.1091/mbc.10.8.2573.

Orimo, A., P.B. Gupta, D.C. Sgroi, F. Arenzana-Seisdedos, T. Delaunay, R. Naeem, V.J. Carey, A.L. Richardson, and R.A. Weinberg. 2005. Stromal Fibroblasts Present in Invasive Human Breast Carcinomas Promote Tumor Growth and Angiogenesis through Elevated SDF-1/CXCL12 Secretion. *Cell*. 121:335–348. doi:10.1016/j.cell.2005.02.034.

Palmieri, C., D. Roberts-Clark, A. Assadi-Sabet, R. Coope, M. O'Hare, A. Sunters, A. Hanby, M. Slade, J. Gomm, E. Lam, and R. Coombes. 2003. Fibroblast growth factor 7, secreted by breast fibroblasts, is an interleukin-1beta-induced paracrine growth factor for human breast cells. *J. Endocrinol.* 177:65–81. doi:10.1677/joe.0.1770065.

Paoli, P., E. Giannoni, and P. Chiarugi. 2013. Anoikis molecular pathways and its role in cancer progression. *Biochim. Biophys. Acta - Mol. Cell Res.* 1833:3481–3498. doi:10.1016/j.bbamcr.2013.06.026.

Park, H.J., G. Gusarova, Z. Wang, J.R. Carr, J. Li, K.-H. Kim, J. Qiu, Y.-D. Park, P.R. Williamson, N. Hay, A.L. Tyner, L.F. Lau, R.H. Costa, and P. Raychaudhuri. 2011. Deregulation of FoxM1b leads to tumour metastasis. *EMBO Mol. Med.* 3:21–34. doi:10.1002/emmm.201000107.

Park, J., and J.E. Schwarzbauer. 2014. Mammary epithelial cell interactions with fibronectin stimulate epithelial-mesenchymal transition. *Oncogene*. 33:1649–1657. doi:10.1038/onc.2013.118.

Patanaphan, V., O.M. Salazar, and R. Risco. 1988. Breast cancer: metastatic patterns and their prognosis. *South. Med. J.* 81:1109–12.

Paulus, A., S. Freeby, K. Academia, V. Thulasiraman, T. Wehr, N. Liu, S. Roth, and K. Smith. 2009. Accessing Low-Abundance Proteins in Serum and Plasma With a Novel, Simple

Enrichment and Depletion Method sample preparation.

Perou, C.M., T. Sørlie, M.B. Eisen, M. van de Rijn, S.S. Jeffrey, C.A. Rees, J.R. Pollack, D.T. Ross, H. Johnsen, L.A. Akslen, Ø. Fluge, A. Pergamenschikov, C. Williams, S.X. Zhu, P.E. Lønning, A.-L. Børresen-Dale, P.O. Brown, and D. Botstein. 2000. Molecular portraits of human breast tumours. *Nature*. 406:747–752. doi:10.1038/35021093.

Pez, F., F. Dayan, J. Durivault, B. Kaniewski, G. Aimond, G.S. Le Provost, B. Deux, P. Clezardin, P. Sommer, J. Pouyssegur, and C. Reynaud. 2011. The HIF-1-Inducible Lysyl Oxidase Activates HIF-1 via the Akt Pathway in a Positive Regulation Loop and Synergizes with HIF-1 in Promoting Tumor Cell Growth. *Cancer Res.* 71:1647–1657. doi:10.1158/0008-5472.CAN-10-1516.

Pihlajaniemi, T., R. Myllylä, and K.I. Kivirikko. 1991. Prolyl 4-hydroxylase and its role in collagen synthesis. *J. Hepatol.* 13 Suppl 3:S2-7.

Pirneskoski, A., L.W. Ruddock, P. Klappa, R.B. Freedman, K.I. Kivirikko, and P. Koivunen. 2001. Domains b' and a' of protein disulfide isomerase fulfill the minimum requirement for function as a subunit of prolyl 4-hydroxylase. The N-terminal domains a and b enhances this function and can be substituted in part by those of ERp57. *J. Biol. Chem.* 276:11287–93. doi:10.1074/jbc.M010656200.

Pollock, S., G. Kozlov, M.-F. Pelletier, J.-F. Trempe, G. Jansen, D. Sitnikov, J.J.M. Bergeron, K. Gehring, I. Ekiel, and D.Y. Thomas. 2004. Specific interaction of ERp57 and calnexin determined by NMR spectroscopy and an ER two-hybrid system. *EMBO J.* 23:1020–9. doi:10.1038/sj.emboj.7600119.

Pulido, C., I. Vendrell, A.R. Ferreira, S. Casimiro, A. Mansinho, I. Alho, and L. Costa. 2017. Bone metastasis risk factors in breast cancer. *Ecancermedicalscience*. 11:715. doi:10.3332/ecancer.2017.715.

R.Cailleau, R.Young, M.Olivé, and W. J. Reeves, J. 1974. Breast Tumor Cell Lines From Pleural Effusions. *J. Natl. Cancer Inst.* 53:661–674.

Radisky, E.S., and D.C. Radisky. 2015. Matrix metalloproteinases as breast cancer drivers and therapeutic targets. *Front. Biosci. (Landmark Ed.* 20:1144–63.

Raghavan, M., N. Del Cid, S.M. Rizvi, and L.R. Peters. 2008. MHC class I assembly: out and about. *Trends Immunol.* 29:436–43. doi:10.1016/j.it.2008.06.004.

Ramakrishna, R., and R. Rostomily. 2013. Seed, soil, and beyond: The basic biology of brain metastasis. *Surg. Neurol. Int.* 4:S256-64. doi:10.4103/2152-7806.111303.

Ramos, F.S., L.T.R. Serino, C.M.S. Carvalho, R.S. Lima, C.A. Urban, I.J. Cavalli, and E.M.S.F. Ribeiro. 2015. PDIA3 and PDIA6 gene expression as an aggressiveness marker in primary ductal breast cancer. *Genet. Mol. Res.* 14:6960–6967. doi:10.4238/2015.June.26.4.

Raykhel, I., H. Alanen, K. Salo, J. Jurvansuu, V.D. Nguyen, M. Latva-Ranta, and L. Ruddock. 2007. A molecular specificity code for the three mammalian KDEL receptors. *J. Cell Biol.* 179:1193–204. doi:10.1083/jcb.200705180.

Rellmann, Y., and R. Dreier. 2018. Different Forms of ER Stress in Chondrocytes Result in Short Stature Disorders and Degenerative Cartilage Diseases: New Insights by Cartilage-Specific ERp57 Knockout Mice. *Oxid. Med. Cell. Longev.* 2018:8421394. doi:10.1155/2018/8421394.

Ricciardi, M., M. Zanotto, G. Malpeli, G. Bassi, O. Perbellini, M. Chilosi, F. Bifari, and M. Krampera. 2015. Epithelial-to-mesenchymal transition (EMT) induced by inflammatory priming elicits mesenchymal stromal cell-like immune-modulatory properties in cancer cells. *Br. J. Cancer*. 112:1067–75. doi:10.1038/bjc.2015.29.

Richard, C.L., M.C. Farach-Carson, B. Rohe, I. Nemere, and K.A. Meckling. 2010. Involvement of 1,25D3-MARRS (membrane associated, rapid response steroid-binding), a novel vitamin D

receptor, in growth inhibition of breast cancer cells. *Exp. Cell Res.* 316:695–703. doi:10.1016/J.YEXCR.2009.12.015.

Ringnér, M., E. Fredlund, J. Häkkinen, Å. Borg, and J. Staaf. 2011. GOBO: Gene Expression-Based Outcome for Breast Cancer Online. *PLoS One*. 6:e17911. doi:10.1371/journal.pone.0017911.

Roato, I., and R. Ferracini. 2018. Cancer Stem Cells, Bone and Tumor Microenvironment: Key Players in Bone Metastases. *Cancers (Basel).* 10. doi:10.3390/cancers10020056.

Rodday, B., F. Hirschhaeuser, S. Walenta, and W. Mueller-Klieser. 2011. Semiautomatic Growth Analysis of Multicellular Tumor Spheroids. *J. Biomol. Screen.* 16:1119–1124. doi:10.1177/1087057111419501.

Rodriguez-Pascual, F., and D.A. Slatter. 2016. Collagen cross-linking: insights on the evolution of metazoan extracellular matrix. *Sci. Rep.* 6:37374. doi:10.1038/srep37374.

Rodriguez, H.M., M. Vaysberg, A. Mikels, S. McCauley, A.C. Velayo, C. Garcia, and V. Smith. 2010. Modulation of lysyl oxidase-like 2 enzymatic activity by an allosteric antibody inhibitor. *J. Biol. Chem.* 285:20964–74. doi:10.1074/jbc.M109.094136.

Rosini, S., N. Pugh, A.M. Bonna, D.J.S. Hulmes, R.W. Farndale, and J.C. Adams. 2018. Thrombospondin-1 promotes matrix homeostasis by interacting with collagen and lysyl oxidase precursors and collagen cross-linking sites. *Sci. Signal.* 11:eaar2566. doi:10.1126/SCISIGNAL.AAR2566.

Rottner, K., J. Faix, S. Bogdan, S. Linder, and E. Kerkhoff. 2017. Actin assembly mechanisms at a glance. *J. Cell Sci.* 130:3427–3435. doi:10.1242/jcs.206433.

Sağlam, Ö., Z.S. Ünal, C. Subaşı, E. Ulukaya, and E. Karaöz. 2015. IL-6 originated from breast cancer tissue-derived mesenchymal stromal cells may contribute to carcinogenesis. *Tumor Biol.* 36:5667–5677. doi:10.1007/s13277-015-3241-5.

Salvador, F., A. Martin, C. López-Menéndez, G. Moreno-Bueno, V. Santos, A. Vázquez-Naharro, P.G. Santamaria, S. Morales, P.R. Dubus, L. Muinelo-Romay, R. López-López, J.C. Tung, V.M. Weaver, F. Portillo, and A. Cano. 2017. Lysyl Oxidase-like Protein LOXL2 Promotes Lung Metastasis of Breast Cancer. *Cancer Res.* 77:5846–5859. doi:10.1158/0008-5472.CAN-16-3152.

Sano, R., and J.C. Reed. 2013. ER stress-induced cell death mechanisms. *Biochim. Biophys. Acta*. 1833:3460–3470. doi:10.1016/j.bbamcr.2013.06.028.

Santana-Codina, N., R. Carretero, R. Sanz-Pamplona, T. Cabrera, E. Guney, B. Oliva, P. Clezardin, O.E. Olarte, P. Loza-Alvarez, A. Méndez-Lucas, J.C. Perales, and A. Sierra. 2013. A transcriptome-proteome integrated network identifies endoplasmic reticulum thiol oxidoreductase (ERp57) as a hub that mediates bone metastasis. *Mol. Cell. Proteomics*. 12:2111–25. doi:10.1074/mcp.M112.022772.

Santi, A., F.G. Kugeratski, and S. Zanivan. 2018. Cancer Associated Fibroblasts: The Architects of Stroma Remodeling. *Proteomics*. 18:e1700167. doi:10.1002/pmic.201700167.

Saunders, L.R., and D.R. McClay. 2014. Sub-circuits of a gene regulatory network control a developmental epithelial-mesenchymal transition. *Development*. 141:1503–13. doi:10.1242/dev.101436.

Severino, V., A. Farina, and A. Chambery. 2013. Analysis of secreted proteins. *Methods Mol. Biol.* 1002:37–60. doi:10.1007/978-1-62703-360-2_4.

Shao, Z.-M., M. Nguyen, and S.H. Barsky. 2000. Human breast carcinoma desmoplasia is PDGF initiated. *Oncogene*. 19:4337–4345. doi:10.1038/sj.onc.1203785.

Shen, B., M.K. Delaney, and X. Du. 2012. Inside-out, outside-in, and inside-outside-in: G protein

signaling in integrin-mediated cell adhesion, spreading, and retraction. *Curr. Opin. Cell Biol.* 24:600–6. doi:10.1016/j.ceb.2012.08.011.

Singh, P., C. Carraher, and J.E. Schwarzbauer. 2010. Assembly of fibronectin extracellular matrix. *Annu. Rev. Cell Dev. Biol.* 26:397–419. doi:10.1146/annurev-cellbio-100109-104020.

Sodek, K.L., K.J. Murphy, T.J. Brown, and M.J. Ringuette. 2012. Cell-cell and cell-matrix dynamics in intraperitoneal cancer metastasis. *Cancer Metastasis Rev.* 31:397–414. doi:10.1007/s10555-012-9351-2.

Soki, F.N., S.I. Park, and L.K. McCauley. 2012. The multifaceted actions of PTHrP in skeletal metastasis. *Future Oncol.* 8:803–17. doi:10.2217/fon.12.76.

Song, M.-N., P.-G. Moon, J.-E. Lee, M. Na, W. Kang, Y.S. Chae, J.-Y. Park, H. Park, and M.-C. Baek. 2012. Proteomic analysis of breast cancer tissues to identify biomarker candidates by gel-assisted digestion and label-free quantification methods using LC-MS/MS. *Arch. Pharm. Res.* 35:1839–1847. doi:10.1007/s12272-012-1018-6.

Soysal, S.D., A. Tzankov, and S.E. Muenst. 2015. Role of the Tumor Microenvironment in Breast Cancer. *Pathobiology*. 82:142–52. doi:10.1159/000430499.

Stepensky, D., N. Bangia, and P. Cresswell. 2007. Aggregate Formation by ERp57-Deficient MHC Class I Peptide-Loading Complexes. *Traffic*. 8:1530–1542. doi:10.1111/j.1600-0854.2007.00639.x.

Subramanian, A., P. Tamayo, V.K. Mootha, S. Mukherjee, B.L. Ebert, M.A. Gillette, A. Paulovich, S.L. Pomeroy, T.R. Golub, E.S. Lander, and J.P. Mesirov. 2005. Gene set enrichment analysis: A knowledge-based approach for interpreting genome-wide expression profiles. *Proc. Natl. Acad. Sci.* 102:15545–15550. doi:10.1073/PNAS.0506580102.

Sung, B.H., and A.M. Weaver. 2017. Exosome secretion promotes chemotaxis of cancer cells. *Cell Adh. Migr.* 11:187–195. doi:10.1080/19336918.2016.1273307.

Szklarczyk, D., A.L. Gable, D. Lyon, A. Junge, S. Wyder, J. Huerta-Cepas, M. Simonovic, N.T. Doncheva, J.H. Morris, P. Bork, L.J. Jensen, and C. von Mering. 2019. STRING v11: protein–protein association networks with increased coverage, supporting functional discovery in genome-wide experimental datasets. *Nucleic Acids Res.* 47:D607–D613. doi:10.1093/nar/gky1131.

Tan, W., R. Krishnaraj, and T.A. Desai. 2001. Evaluation of Nanostructured Composite Collagen–Chitosan Matrices for Tissue Engineering. *Tissue Eng.* 7:203–210. doi:10.1089/107632701300062831.

Tang, L., and X. Han. 2013. The urokinase plasminogen activator system in breast cancer invasion and metastasis. *Biomed. Pharmacother.* 67:179–182. doi:10.1016/j.biopha.2012.10.003.

Turano, C., E. Gaucci, C. Grillo, and S. Chichiarelli. 2011. ERp57/GRP58: A protein with multiple functions. *Cell. Mol. Biol. Lett.* 16:539–63. doi:10.2478/s11658-011-0022-z.

Tyan, S.-W., C.-H. Hsu, K.-L. Peng, C.-C. Chen, W.-H. Kuo, E.Y.-H.P. Lee, J.-Y. Shew, K.-J. Chang, L.-J. Juan, and W.-H. Lee. 2012. Breast Cancer Cells Induce Stromal Fibroblasts to Secrete ADAMTS1 for Cancer Invasion through an Epigenetic Change. *PLoS One*. 7:e35128. doi:10.1371/journal.pone.0035128.

Unpublished, H.S.Y. 2018. No Title.

Vader, P., X.O. Breakefield, and M.J.A. Wood. 2014. Extracellular vesicles: emerging targets for cancer therapy. *Trends Mol. Med.* 20:385–393. doi:10.1016/j.molmed.2014.03.002.

Wang, C., S. Xu, Y. Tian, A. Ju, Q. Hou, J. Liu, Y. Fu, and Y. Luo. 2019a. Lysyl Oxidase-Like Protein 2 Promotes Tumor Lymphangiogenesis and Lymph Node Metastasis in Breast Cancer. *Neoplasia*. 21:413–427. doi:10.1016/j.neo.2019.03.003.

Wang, F.T., W.E.I. Sun, J.T. Zhang, and Y.Z. Fan. 2019b. Cancer-associated fibroblast regulation of tumor neo-angiogenesis as a therapeutic target in cancer (Review). *Oncol. Lett.* 17:3055–3065. doi:10.3892/ol.2019.9973.

Wang, M., J. Zhao, L. Zhang, F. Wei, Y. Lian, Y. Wu, Z. Gong, S. Zhang, J. Zhou, K. Cao, X. Li, W. Xiong, G. Li, Z. Zeng, and C. Guo. 2017. Role of tumor microenvironment in tumorigenesis. *J. Cancer*. 8:761–773. doi:10.7150/jca.17648.

Wang, T.-H., S.-M. Hsia, and T.-M. Shieh. 2016. Lysyl Oxidase and the Tumor Microenvironment. *Int. J. Mol. Sci.* 18. doi:10.3390/ijms18010062.

Weidenfeld, K., and D. Barkan. 2018. EMT and Stemness in Tumor Dormancy and Outgrowth: Are They Intertwined Processes? *Front. Oncol.* 8:381. doi:10.3389/fonc.2018.00381.

Weiswald, L.-B., J.-M. Guinebretière, S. Richon, D. Bellet, B. Saubaméa, and V. Dangles-Marie. 2010. In situ protein expression in tumour spheres: development of an immunostaining protocol for confocal microscopy. *BMC Cancer*. 10:106. doi:10.1186/1471-2407-10-106.

Wozniak, M.A., R. Desai, P.A. Solski, C.J. Der, and P.J. Keely. 2003. ROCK-generated contractility regulates breast epithelial cell differentiation in response to the physical properties of a three-dimensional collagen matrix. *J. Cell Biol.* 163:583–95. doi:10.1083/jcb.200305010.

Xiao, Q., and G. Ge. 2012. Lysyl oxidase, extracellular matrix remodeling and cancer metastasis. *Cancer Microenviron.* 5:261–73. doi:10.1007/s12307-012-0105-z.

XIAO, Y.-F., X. YONG, B. TANG, Y. QIN, J.-W. ZHANG, D. ZHANG, R. XIE, and S.-M. YANG. 2016. Notch and Wnt signaling pathway in cancer: Crucial role and potential therapeutic targets (Review). *Int. J. Oncol.* 48:437–449. doi:10.3892/ijo.2015.3280.

Xie, L., Z. Sun, Z. Hong, N.J. Brown, O. V. Glinskii, K. Rittenhouse-Olson, G.A. Meininger, and V. V. Glinsky. 2018. Temporal and molecular dynamics of human metastatic breast carcinoma cell adhesive interactions with human bone marrow endothelium analyzed by single-cell force spectroscopy. *PLoS One*. 13:e0204418. doi:10.1371/journal.pone.0204418.

Xu, J., S. Lamouille, and R. Derynck. 2009. TGF-beta-induced epithelial to mesenchymal transition. *Cell Res.* 19:156–72. doi:10.1038/cr.2009.5.

Xu, S., A.N. Butkevich, R. Yamada, Y. Zhou, B. Debnath, R. Duncan, E. Zandi, N.A. Petasis, and N. Neamati. 2012. Discovery of an orally active small-molecule irreversible inhibitor of protein disulfide isomerase for ovarian cancer treatment. *Proc. Natl. Acad. Sci.* 109:16348–16353. doi:10.1073/pnas.1205226109.

Xu, X., L. Zhang, X. He, P. Zhang, C. Sun, X. Xu, Y. Lu, and F. Li. 2018. TGF-β plays a vital role in triple-negative breast cancer (TNBC) drug-resistance through regulating stemness, EMT and apoptosis. *Biochem. Biophys. Res. Commun.* 502:160–165. doi:10.1016/j.bbrc.2018.05.139.

Yoo, D.Y., S. Bin Cho, H.Y. Jung, W. Kim, K.Y. Lee, J.W. Kim, S.M. Moon, M.-H. Won, J.H. Choi, Y.S. Yoon, D.W. Kim, S.Y. Choi, and I.K. Hwang. 2019. Protein disulfide-isomerase A3 significantly reduces ischemia-induced damage by reducing oxidative and endoplasmic reticulum stress. *Neurochem. Int.* 122:19–30. doi:10.1016/J.NEUINT.2018.11.002.

Yuan, Y., Y.-C. Jiang, C.-K. Sun, and Q.-M. Chen. 2016. Role of the tumor microenvironment in tumor progression and the clinical applications (Review). *Oncol. Rep.* 35:2499–2515. doi:10.3892/or.2016.4660.

Zahir, N., J.N. Lakins, A. Russell, W. Ming, C. Chatterjee, G.I. Rozenberg, M.P. Marinkovich, and V.M. Weaver. 2003. Autocrine laminin-5 ligates alpha6beta4 integrin and activates RAC and NFkappaB to mediate anchorage-independent survival of mammary tumors. *J. Cell Biol.* 163:1397–407. doi:10.1083/jcb.200302023.